Università degli Studi di Messina

Dipartimento di Ingegneria

Dottorato di Ricerca in Ingegneria e chimica dei materiali e delle costruzioni - Ciclo XXXVI
S.S.D.: ICAR/08 - ICAR/09

Modal identification of bridges via cost-effective approaches and advanced decomposition techniques

Author:
Matteo Mazzeo

Coordinator:
Prof. Edoardo Proverbio

Supervisor:
Prof. Roberta Santoro

Co-supervisor:
Prof. Dario De Domenico

Accademic Year 2022-2023

ACKNOWLEDGEMENTS

I sincerely thank my supervisors Prof. Roberta Santoro and Prof. Dario De Domenico for their priceless guidance and support during the years of the PhD. Collaborating with them, I have learned to face the inevitable difficulties that may arise in the research field, improved the quality of my work and honed my critical point of view for the interpretation of the research results.

I wish also to express my gratitude and love to my parents who have always encouraged and supported me throughout the course of all my studies, including this PhD.

ABSTRACT

The present PhD thesis investigates the use of cost-effective strategies in combination with advanced decomposition techniques for the modal characterization of existing bridges. A usual strategy for the health condition assessment of existing structures relies on vibration-based approaches; specifically, the most sought-after ones exploit long-term continuous monitoring records under ambient vibrations, processed via operational modal analysis techniques. However, the costs associated with the network of sensors, its protection and maintenance as well as the time and effort required to carry out the tests and to process large amounts of data make the application of this strategy profitable only in the case of strategic structures. This PhD thesis presents the results of several research studies with the main goal of proposing alternative approaches for the modal identification of existing bridges that mitigate the time and cost-related limitations of current ambient vibration monitoring, making it affordable also to monitor the health conditions of ordinary structures. In this regard, two possible solutions are studied. The first one is based on free vibration tests performed with a limited number of sensors directly mounted on the bridge; the second one explores the possibility of providing an approximate estimation of modal parameters via an indirect approach based on the dynamic response of moving vehicles. Aiming at processing the recorded signals, identification strategies based on two advanced signal decomposition techniques, namely the Variational Mode Decomposition (VMD) and the Empirical Fourier Decomposition (EFD), are presented. The proposed approaches are validated with numerical benchmark applications. Further, their performance is also assessed and compared with other traditional approaches in real case-studies concerning roadway and railway bridges.

Keywords: Bridge modal identification, Damping estimation, Free vibration tests, Vehicle Scanning Method, Variational Mode Decomposition (VMD), Empirical Fourier Decomposition (EFD).

CONTENTS

LIST OF FIGURES

LIST OF TABLES

PUBLICATIONS

This thesis is the outcome of the PhD course started three years ago. Part of this thesis is based on papers (listed here below) already published or under review, in scientific conferences, proceedings and journals. These papers are:

1. **M. Mazzeo**, R. Santoro and A. Di Matteo, "A novel indirect modal identification procedure for bridges based on the dynamic response of moving vehicles", *Journal of Sound and Vibration* (under review).

2. **M. Mazzeo**, D. De Domenico, G. Quaranta, and R. Santoro, "An efficient automatic modal identification method based on free vibration response and enhanced Empirical Fourier Decomposition technique", *Engineering Structures*, vol. 298, p. 117046, 2024.

3. **M. Mazzeo**, D. De Domenico, G. Quaranta, and R. Santoro, "Automatic modal identification of bridges based on free vibration response and variational mode decomposition technique", *Engineering Structures*, vol. 280, p. 115665, 2023.

4. **M. Mazzeo**, D. De Domenico, G. Quaranta, and R. Santoro, "Automatic modal identification of bridges based on free vibrations and advanced signal decomposition techniques," *Vibroengineering Procedia*, vol. 50, pp. 49–55, 09 2023.

5. **M. Mazzeo**, D. De Domenico, G. Quaranta, and R. Santoro, "Modal parameters identification in existing bridges based on free vibration tests", in *Proceedings of 12th International Conference on Structural Dynamics - EURODYN 2023*, 2023.

6. **M. Mazzeo**, D. De Domenico, G. Quaranta, and R. Santoro, "Informed assessment of structural health conditions of bridges based on free-vibration tests", in *Proceedings of 8th International Symposium on Life-Cycle Civil Engineering*, 2023.

7. **M. Mazzeo**, D. De Domenico, G. Quaranta, and R. Santoro, "A novel procedure for damping ratio identification from free vibration tests with application to existing bridge decks", in *European Workshop on Structural Health Monitoring: EWSHM 2022* - vol. 3, pp. 699–708, Springer, 2022.

Other relevant papers produced during the PhD years are the following:

8. De Domenico D., **Mazzeo M.**, Messina D. and Recupero A., "Safety assessment of corroded PC half-joint bridges through an advanced mechanochemical finite element model", in *Proc. of the 3rd CACRCS Workshop Capacity Assessment of Corroded Reinforced Concrete Structure*, 2023.

9. De Domenico D., Maugeri N., Longo P., **Mazzeo M.**, Ricciardi G., Quattrocchi A., Montanini R. and Calabrese L., "Shear deficient RC beams retrofitted with inorganic matrix composites", *9th International Conference on Computational Methods in Structural Dynamics and Earthquake Engineering - COMPDYN 2023*, 2023.

10. Santoro R., **Mazzeo M.** and Failla G., "A computational framework for uncertain locally resonant metamaterial structures", *Mechanical Systems and Signal Processing* Vol. 190, p.110094, 2023.

11. De Domenico D., **Mazzeo M.**, Messina D. and Recupero A., "Experimental and numerical investigation on PC beams with artificially corroded post-tensioned tendons", in *Proc. of the 14th fib international PhD Symposium in Civil Engineering*, 2022.

12. **Mazzeo M.**, Laudani R. and Santoro R., "Uncertainty effect on seismic capacity assessment in the out-of-plane failure mechanisms of masonry structures by probabilistic and non-probabilistic approaches", *Developments in the built environment* (under review).

INTRODUCTION

Aims and motivations

Bridges are strategic structures that play a key role in any infrastructure system, allowing to cover significant distances, thus overcoming obstacles and height gradients easily. Many of these structures, especially in Italy, were built between the 1950s and 1970s [1] and, since in most cases they are approaching their nominal service life, the aspects related to structural aging and material degradation due to environmental factors are becoming significant [2]. Further, some of the existing bridges may be affected by fatigue phenomena that further reduce the service life because of traffic loads significantly differing from design conditions [3–5]. In both cases, it becomes necessary to plan and perform careful monitoring to check the actual state of health and identify any significant possible discrepancy from design conditions. On the other hand, it is not always possible to verify if design assumptions are truly respected in the construction phase or immediately after its completion [6], especially for new bridges with high structural complexity, often dependent on esthetic and architectonic factors.

Based on these considerations, a significant interest in controlling and preserving strategic structures such as bridges contributed to the development of the vibration-based structural health monitoring (SHM) field [7,8]. Structural dynamic identification relies on the extraction of modal parameters that are closely related to the physical properties of the monitored structure [9]: information about modal frequencies allows to establish which conditions may trigger structural resonance phenomena, modal damping ratios provide information on its energy dissipation capacity, whereas mode shapes reflect the boundary conditions as well as its mass and stiffness distribution.

The main application of dynamic identification concerns monitoring the health conditions of the structures [10]: specifically, once a first dynamic characterization of the bridge is available, the corresponding identified modal parameters may be assumed as a baseline for future tests to assess if any possible damage, related to relevant fluctuations from reference values, is taking place [11]. Other significant applications of dynamic identification via dynamic tests are the update of numerical models for new structures [12] or the tuning of vibration control systems to retrofit the existing ones.

The most commonly adopted strategy for dynamic identification of strategic structures like bridges is based on long-term monitoring via permanently installed sensors [13], which records the structural response to ambient vibrations produced for example by wind or vehicular traffic, and the application of Operational Modal Analysis (OMA) methods to process the data and retrieve modal parameters [14, 15]. However, this approach presents some critical issues related to the economic impact associated with the selection of performing sensors able to detect ambient vibration response and their number [16, 17] as well as the costs related to their protection and maintenance [18]. Further, the manual analysis and processing of the enormous amount of data continuously collected by dynamic monitoring are often not realistic since it requires a lot of time [19] and can be only partially handled if automated OMA procedures are adopted. Finally, estimations provided by OMA techniques are less

precise than the counterparts obtained by directly exciting the structure due to the lower signal-to-noise ratio of ambient measurements [20] and not always reliable since the assumptions on which OMA is based may not be entirely satisfied in real-case situations. Therefore, a central problem is represented by the research of alternative, cost-effective vibration-based SHM strategies to achieve reliable modal parameter estimates with limited economic impact for both test setup and data management and to reduce the time necessary to perform the tests and obtain the modal characterization of the structure.

To this aim, this thesis focuses on the research of procedures that meet these needs; two different approaches are investigated: the first one is based on a direct identification strategy where the sensors are directly mounted on the structure and exploit free vibration tests, whereas the second one is based on an indirect approach, where dynamic parameters are deduced from the signals recorded by an instrumented testing vehicle which travels along the bridge during the tests. In both cases, the research is focused on the application of advanced decomposition techniques, which are not limited by the assumptions of OMA methods, to extract the significant modal contributions, in combination with novel methods to retrieve the modal parameters.

The cost-effectiveness of the proposed procedures is justified by some considerations that can be made in comparison with traditional continuous health monitoring based on ambient vibrations. Notably, the investigated approaches involve the sporadic monitoring of the structure and the temporary installation of the sensors, therefore, as opposed to traditional procedures, no additional costs are needed for the maintenance or weather protection of the measuring devices. Further, a network with a limited number of sensors is required for the investigated test methodologies, thus reducing even more the costs of the monitoring campaign: in this regard, it is noted that, theoretically, the installation of a single accelerometer is necessary if only modal frequencies and damping ratios have to be identified. Notably, more economic accelerometers are typically adopted in free vibration tests since the required sensitivity is smaller due to the magnitude of the excitation which is significantly higher than the counterpart in ambient vibrations. It is also noted that no specific equipment is required to produce the excitation, as opposed to forced vibration tests, since an ungauged hammer or a track passing over an artificial step suffice for this need. Finally, the time and subsequently the cost associated with data processing are reduced due to the significantly more compact volume of recordings in comparison with continuous monitoring approaches.

Another significant problem in the dynamic characterization of structures is that traditional modal identification requires the analyst expertise for the proper set of control parameters to obtain reliable results [21]. To limit subjectiveness in the user's input parameters and provide more objective estimates, this research also aims to propose suitable tuning procedures that allow to carry out the dynamic identification in an automatic fashion maintaining reliable results.

Structure of the thesis

Chapter 1 provides general background on the topics of modal analysis, dynamic vibration testing and signal pre-processing.

Chapter 2 offers an overview of the actual state of the art concerning structural

dynamic identification: specifically, the most common procedures developed in the context of OMA are described. Further, the state of the art on advanced decomposition techniques is also presented. This choice is justified by the fact that the thesis deals with novel dynamic identification approaches for bridges based on advanced decomposition methods and their performance comparison with classical OMA approaches to highlight similarities and limitations.

Chapter 3 introduces a novel modal identification approach for the dynamic characterization of bridges from free vibration tests: it exploits the Variational Mode Decomposition (VMD) to isolate all significant modal contributions and the corresponding modal frequencies from a given signal; the modal damping ratios are identified via a noise-robust area ratio-based approach; finally, mode shape vectors are assembled comparing the amplitudes of the same mode contribution at fixed time instants obtained from signal recorded at different locations on the structure. Further, a tuning procedure for the automatic setting of control parameters is also introduced for the proposed strategy.

Chapter 4 compares the performance of the VMD-based approach with an alternative decomposition technique, namely an enhanced version of the Empirical Fourier Decomposition (EFD), in the context of free vibration-based dynamic identification. Specifically, the EFD is improved by introducing an automatic procedure for the selection of the number of frequency partitions. Further, the robustness of the segmentation procedure has been refined using a zero-phase moving average smoothing filtering of the frequency spectrum that mitigates the detrimental effects of noise. The EFD-based approach has the advantage that only one control parameter must be preset, thus allowing easier tuning.

To show how the proposed identification approaches can be successfully applied for the dynamic characterization of existing bridge structures, several diversified case studies are analyzed in chapters 3 and 4, specifying from time to time the peculiarities of each structure and the corresponding identification results in comparison with OMA approaches.

Chapter 5 presents a numerical study on the dynamic identification of bridge structures exploiting an indirect approach based on the Vehicle Scanning Method (VSM). Specifically, this chapter aims to extend and generalize the approach proposed in Chapter 3 to VSM where the dynamic parameters are extracted from signals recorded from an instrumented moving vehicle rather than from the structure itself.

Lastly, in Chapter 6, final considerations are made, critically discussing the main results obtained from the research carried out in the context of this thesis.

CHAPTER 1

BACKGROUND

This chapter provides a general overview of the fundamental concepts related to the dynamic identification of existing structures. The classic models adopted in structural dynamics are herein briefly introduced focusing on the definition of concepts such as modal analysis and modal parameters. Next, the practical counterpart is addressed, introducing different modal testing procedures and describing their pros and cons. Finally, the main aspects of signal validation and pre-processing are recalled, to properly select the response from which modal parameters will be estimated.

1.1 Fundamentals of modal analysis

The models typically adopted to simulate the real behavior of a continuous structure are usually obtained by operating a discretization process. The structure can thus be modeled as a n_m degrees of freedom (DOFs) system made up of lumped masses connected through springs and dampers and its structural dynamic response may be described by the following relation:

$$\mathbf{M}\ddot{\mathbf{u}}(t) + \mathbf{Z}\dot{\mathbf{u}}(t) + \mathbf{K}\mathbf{u}(t) = \tilde{\mathbf{f}}(t) \tag{1.1}$$

where $\mathbf{M}$, $\mathbf{Z}$ and $\mathbf{K}$ are respectively the mass, damping and stiffness matrix, $\mathbf{u}(t)$ is the vector containing each DOF displacement, $\tilde{\mathbf{f}}(t)$ is the forcing vector and a dot over a variable denotes differentiation with respect to time.

Modal analysis is a technique that allows to mathematically describe the dynamic behavior of a structure by exploiting its inherent dynamic properties called modal parameters, i.e. modal frequencies, damping ratios, and mode shapes, which are related to its physical parameters, namely mass, stiffness, and damping [22]. Modal frequencies represent the frequencies at which a multi-degrees-of-freedom structure naturally tends to vibrate when subjected to a small oscillation. The motion patterns followed by the structure at the corresponding natural frequencies represent the associated mode shapes. Consider the most simple case in which the free vibrations of an undamped MDOF structure are studied; the equation of motion is:

$$\mathbf{M}\ddot{\mathbf{u}}(t) + \mathbf{K}\mathbf{u}(t) = \mathbf{0} \tag{1.2}$$

The solution of the system of differential equations in Eq.(1.2) may be expressed in terms of frequency ω_r and phase θ_r as a vector of harmonic functions:

$$\mathbf{u}(t) = \sin(\omega_r t + \theta_r)\boldsymbol{\phi}_r \tag{1.3}$$

Substituting Eq.(1.3) in Eq.(1.2) the following relation is obtained:

$$(\mathbf{K} - \omega_r^2 \mathbf{M})\boldsymbol{\phi}_r = \mathbf{0} \quad \text{with} \quad r = 1, \ldots, N \tag{1.4}$$

which defines the eigenproblem of an undamped MDOF system. The n_m solutions to this problem, namely the eigenvalues and corresponding eigenvectors, are obtained by solving the following:

$$\det(\mathbf{K} - \omega_r^2 \mathbf{M}) = \mathbf{0} \tag{1.5}$$

which is an algebraic equation with n_m roots, namely the squared natural frequencies of the structure ω_r^2 $(r = 1, \ldots, n_m)$. The corresponding eigenvectors $\boldsymbol{\phi}_r$ $(r = 1, \ldots, n_m)$ represent the unscaled deflections of the structure and are referred to as mode shapes. Collecting all the mode shapes into the mode shape matrix $\boldsymbol{\Phi} = [\boldsymbol{\phi}_1, \ldots, \boldsymbol{\phi}_{n_m}]$ the eigenproblem may be re-written as follows:

$$(\mathbf{K} - \boldsymbol{\Omega}^2 \mathbf{M})\boldsymbol{\Phi} = \mathbf{0} \tag{1.6}$$

Even though the eigenvalues matrix is unique, the same is not true for the mode shape matrix, which is subject to an indeterminate scaling factor that affects the eigenvectors' amplitude. The most common assumption for the mode shapes matrix is to be normalized with respect to the mass matrix such that both mass and stiffness matrices are diagonalized:

$$\boldsymbol{\Phi}^{\mathrm{T}} \mathbf{M} \boldsymbol{\Phi} = \mathbf{I} \tag{1.7a}$$

$$\boldsymbol{\Phi}^{\mathrm{T}} \mathbf{K} \boldsymbol{\Phi} = \boldsymbol{\Omega}^2 \tag{1.7b}$$

being $\mathbf{I}$ the identity matrix and $\boldsymbol{\Omega}^2 = \mathrm{diag}[\omega_r^2]$ with $(r = 1, \ldots, n_m)$ the spectral matrix.

Modal analysis is based on the assumption that, if the structure is linear and time-invariant, the vibration response may be expressed as the superposition of n_m modes (see Fig. 1.1) as follows :

$$\mathbf{u}(t) = \sum_{r=1}^{n_m} \boldsymbol{\phi}_r q_r(t) = \boldsymbol{\Phi}\mathbf{q}(t) \tag{1.8}$$

being $q_r(t)$ the rth modal displacement.

Substituting in the equation of motion Eq.(1.8) and exploiting the aforementioned normalization conditions it is possible to express the structural dynamic response as a set of uncoupled second-order differential equations representative of n_m modal SDOF oscillators:

$$\ddot{q}_r(t) + \omega_r^2 q_r(t) = 0 \quad \text{with} \quad (r = 1, \ldots, n_m) \tag{1.9}$$

It is possible to follow the same approach considering the free vibration of a damped structure, described by the following equation of motion:

$$\mathbf{M}\ddot{\mathbf{u}}(t) + \mathbf{Z}\dot{\mathbf{u}}(t) + \mathbf{K}\mathbf{u}(t) = \mathbf{0} \tag{1.10}$$

In this case, by applying the modal projection, the modal damping matrix $\boldsymbol{\Xi}$ is introduced:

$$\boldsymbol{\Xi} = \boldsymbol{\Phi}^{\mathrm{T}} \mathbf{Z} \boldsymbol{\Phi} \tag{1.11}$$

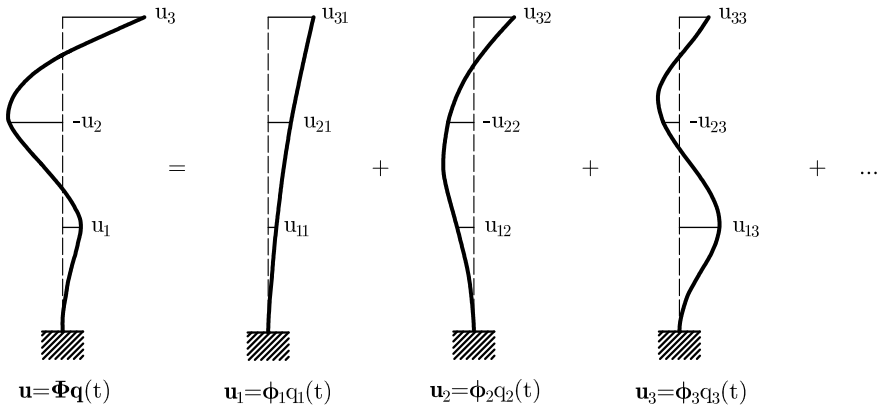

Figure 1.1: Resultant displacement via modal superposition for a 3 DOF system

In general, $\mathbf{\Xi}$ is not diagonal, i.e. the modal projection does not diagonalize the damping matrix, therefore the system of differential equation of motion is not uncoupled. However, for the most common case of classically-damped structure, in which the off-diagonal terms are negligible compared to the ones in the main diagonal, the system can be assumed as uncoupled and the equations of motion in the modal space describe a set of n_m independent SDOF modal oscillators :

$$\ddot{q}_r(t) + \Xi_{rr}\dot{q}_r(t) + \omega_r^2 q_r(t) = 0 \quad \text{with} \quad (r = 1, \ldots, n_m) \tag{1.12}$$

where Ξ_{rr} is the rth term on the main diagonal of $\mathbf{\Xi}$. The most simple solution to model the viscous damping matrix consists of adopting the following expression for the modal damping matrix:

$$\mathbf{\Xi} = \mathbf{\Phi}^{\mathrm{T}}\mathbf{Z}\mathbf{\Phi} = \begin{bmatrix} 2\xi_1\omega_1 & & \\ & \ddots & \\ & & 2\xi_{n_m}\omega_{n_m} \end{bmatrix} \tag{1.13}$$

where ξ_r and ω_r represent the rth modal damping ratio and modal frequency, respectively. The viscous damping matrix is therefore expressed as:

$$\mathbf{Z} = (\mathbf{\Phi}^{\mathrm{T}})^{-1}\mathbf{\Xi}\mathbf{\Phi}^{-1} = \mathbf{M}\mathbf{\Phi}\mathbf{\Xi}\mathbf{\Phi}^{\mathrm{T}}\mathbf{M} \tag{1.14}$$

In this case, the modal matrix $\mathbf{\Phi}$ is also orthogonal to the damping matrix. The main drawback is that the preventive evaluation of the modal matrix is required.

Another common solution is the Rayleigh damping model in which the damping matrix is assumed proportional to the mass and stiffness matrices (see Fig. 1.2) in the form:

$$\mathbf{Z} = \alpha_0\mathbf{K} + \beta_0\mathbf{M} \tag{1.15}$$

Under this assumption, the modal damping ratio can be expressed as follows:

$$\xi_r = \frac{1}{2}\left(\alpha_0\omega_r + \frac{\beta_0}{\omega_r}\right) \tag{1.16}$$

where the two coefficients α_0 and β_0 are obtained imposing that the damping at two modes i and j, whose frequencies define the frequency range of interest, are two assigned values ξ_i and ξ_j respectively:

$$\alpha_0 = \frac{2\omega_j\omega_k(\xi_k\omega_j - \xi_j\omega_k)}{\omega_j^2 - \omega_k^2} \tag{1.17a}$$

$$\beta_0 = \frac{2\xi_j\omega_j - 2\xi_k\omega_k}{\omega_j^2 - \omega_k^2} \tag{1.17b}$$

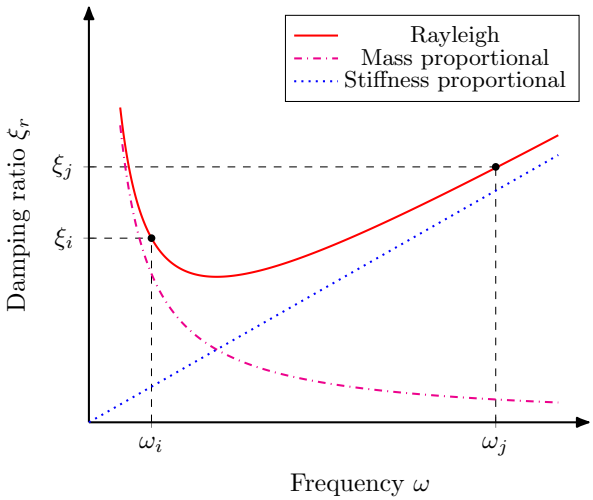

Figure 1.2: Modal damping ratios for models with proportional damping.

It must be pointed out that natural frequencies are of great importance also in the case of forced vibrations. When a damped structure is excited by an external force, the structural response depends on both the modal damping ratios ξ_r and the damped frequencies $\omega_{d,r}$ with $(r = 1, \ldots, n_m)$. The latter are functions of the natural frequencies, i.e. $\omega_{d,r} = \omega_r\sqrt{1-\xi_r^2}$ and for civil structures, which usually are underdamped systems, it holds the assumption $\omega_{d,r} \simeq \omega_r$. Therefore, if the forcing input has a high-frequency content close to at least one of the natural frequencies, the resonance phenomenon might be triggered producing a response with much greater amplitude than the one observed at other exciting frequencies distant from the natural ones.

This concept may be well visualized considering the case of a SDOF oscillator subjected to harmonic excitation: it is possible to define the Magnification Factor as the ratio between the dynamic deflection and the static deflection which would have resulted from the static application of the external load (see Fig. 1.3): it may be observed that approaching the natural frequencies, the amplitude of the response significantly increase; further, the lower the damping ratio, the bigger the magnification rate will be. This, in turn, may produce excessive stress in the structure, thus leading to its collapse. In this regard, an emblematic case is the collapse of the Tacoma bridge because of gusts of wind that blew with frequencies close to that of resonance (see Fig. 1.4).

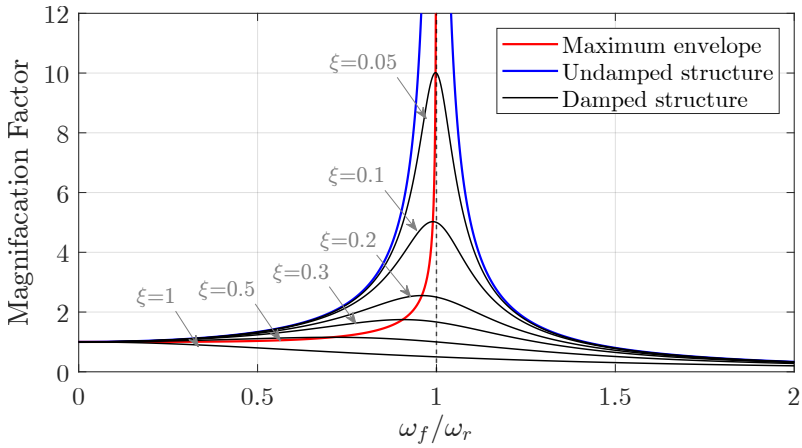

Figure 1.3: Magnification Factor for an SDOF oscillator subjected to harmonic excitation.

Figure 1.4: Collapse of Tacoma Narrow Bridge (1940) due to resonance phenomenon.

1.2 Vibration-based dynamic tests

For both newly constructed and existing structures, it is advisable to measure dynamic properties, i.e. natural frequencies, damping ratios and mode shapes, to better understand the dynamic behavior and ensure structural reliability under serviceability conditions as well as for extreme load scenarios. A vibration-based dynamic test consists of exciting and recording the response of a structure using a network of sensors: the aim is to detect possible variations of dynamic parameters in an existing structure considering at least two discrete points in time. The first one refers to an initial test performed to establish a set of modal parameters assumed as a reference.

Successive test sessions, conducted after a certain period of time, aim at the detection of possible modal parameters variations from the baseline. Therefore, for the monitored structure, conclusions are drawn regarding its health condition according to the observed fluctuations of the modal parameters. The dynamic parameters of a structure are, in fact, functions of its physical properties: any alteration of the latter

due to structural damage is reflected in the alteration of modal parameters. The variation of dynamic properties is thus considered a way to diagnose the structure health condition and assess possible damages [23]. In this context, vibration-based monitoring can complement traditional visual inspection procedures by providing supplementary information especially if the structure is not easily accessible or the possible damage is hidden and not detectable by visual inspections.

Another major application of vibration-based modal testing consists in the update of structural models [12]: the FE model cannot replicate perfectly the real structure behavior because in the modeling some simplifying hypotheses are commonly assumed for both the geometry and the boundary conditions which may divert the analysis result from the real structural behavior. Moreover, the mesh selection and different discretizations may still lead to different results due to possible numerical errors. In this sense, the results from modal identification tests can be exploited to update the FE model toward more realistic results.

Modal testing procedures in bridge SHM have been borrowed from mechanical and aeronautical engineering where dynamic phenomena were researched first: the main difference resides in construction material adopted in bridges, e.g. prestressed concrete, masonry, and composite materials, which have more complex constitutive behavior. Depending on the degree of control over the input excitation, modal parameters can be estimated via the dynamic response produced by ambient, forced or free vibration tests (see Fig. 1.5).

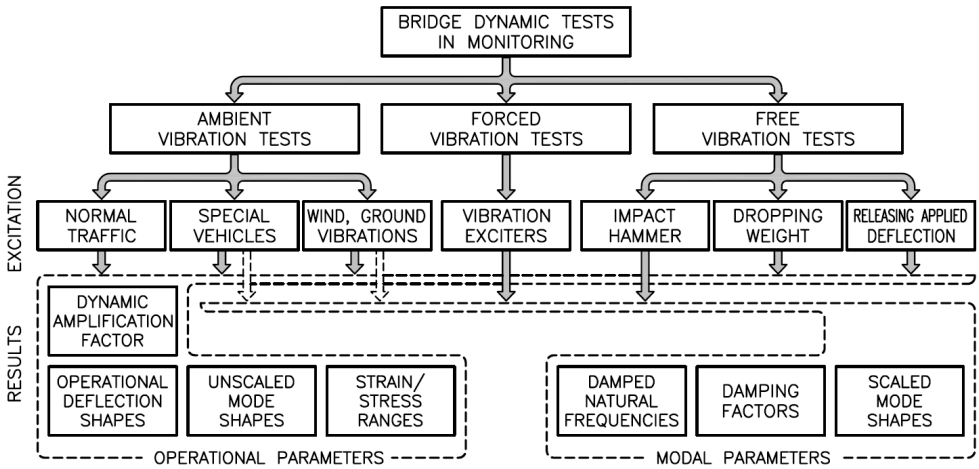

Figure 1.5: Classification of vibration-based tests used for dynamic identification of structures [24].

Forced vibration tests

Forced vibration tests were typically adopted in the field of Experimental Modal Analysis (EMA) for the estimation of modal parameters. This type of testing is especially suitable for stiff bridges that, due to their features, require a higher level of excitation than the one produced by the transit of ordinary traffic or heavy trucks. Notably, if a flexible system such as a footbridge is investigated, excitation may be produced

simply by jumping pedestrians at a specific time pacing. On the other hand, in a bigger or rigid structure, this dynamic load condition is not sufficient to excite the structural modes and, therefore, specific equipment is required, thus making the test more expensive.

The forced vibration test methodology is based on the concept of structural resonance [25]: a harmonic load with a fixed frequency is generated to excite the structure; this operation is repeated varying in small steps the exciting frequency in a fixed range until the structural resonance frequencies are attained. In this case, the acceleration response at the measurement point reaches the highest amplitudes and then starts to decrease as the excitation frequency continues to increase.

The most common solutions to produce forced vibrations in a bridge are instrumented hammers, eccentric mass shakers and linear mass shakers [16]. The excitation technique is highly dependent on the desired intensity of excitation and the bridge's slenderness. Linear mass shakers excite the structure with a combination of steady-

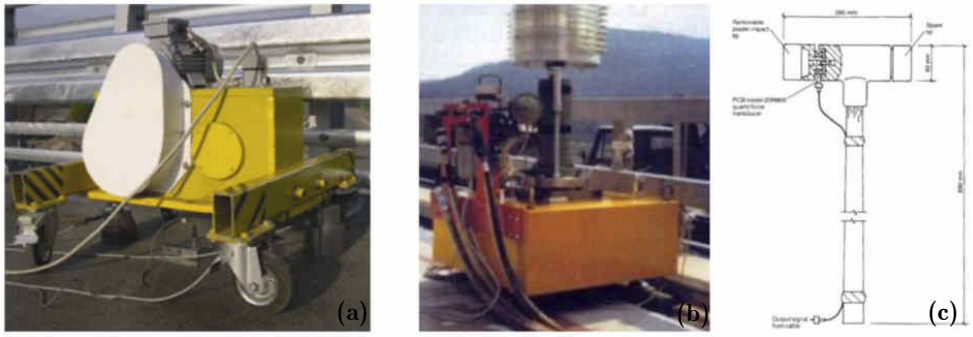

Figure 1.6: Equipment to produce the excitation in forced vibration tests [16]: (a) eccentric mass vibrator; (b) servo-hydraulic shaker; (c) impact hammer tools.

state sinusoidal and transient waves, whereas eccentric mass shakers can only produce harmonic excitation. Both shakers can be used for horizontal or vertical excitation of the structure. Impact hammer usually produces lower excitation levels compared to the shakers and can produce only an impulsive input, therefore it is also considered a way to excite the structure in the context of free vibration tests.

Forced vibration tests allow the accurate control of the excitation features and also achieve high signal-to-noise ratios in the response measurements in comparison with other testing procedures, thus producing more accurate estimates. However, this type of testing is time-consuming because it must be repeated varying the excitation frequency for each mode of interest and, therefore, previous knowledge of structural modal frequencies is required. Moreover, the structure usually must be closed to traffic to allow the testing operation. Even though it is possible to easily excite high frequencies with small shakers, the main limitation of forced vibration tests is due to the difficulty of generating forces large enough to excite a large structure at low frequencies in a controlled way [26]. A possible solution to this problem would be low-frequency massive shakers, however, this choice is usually too expensive due to construction, transport and in-site mounting operations.

Free vibration test

The installation of large permanent sensor networks is becoming popular for the dynamic identification of major structures from the ambient response, however, there exists a large number of constructions that can only be monitored sporadically and in a short time because of budget and technical constraints. In such a case, free vibration tests are especially attractive because they can be performed using a network consisting of a few sensors temporarily installed on the structure in such a way as to limit the duration and cost of the experimental campaign. A free vibration test is typically performed on a civil structure by the application of an impulsive excitation. This test is significantly easier to perform than the forced vibration counterpart and less expensive. It may be carried out by inducing an impulsive response due to the impact of a hammer or the drop of a suspended weight (see Fig. 1.7). An alternative is the sudden release of an applied deflection (see Fig. 1.8): this excitation can be obtained by using a tensioned cable with a fusible connection anchored to the soil and increasing the corresponding tension to the limit or employing a suspended heavy mass that is suddenly disconnected from the structure. In this case, a rough knowledge of the mode shapes is useful because the mass must be hung in a proper location to excite the significant modes [27]. Free vibrations can also be obtained from the passage of a heavy truck on a fixed step in the case of road bridges (see Fig. 1.9) whereas, in the case of railway bridges, the vibrations introduced by the passage of a train may be exploited since at the end of its transit it is observed a residual free vibration response component of the bridge [28, 29].

Free vibration tests are usually performed by introducing an initial perturbation that can induce a response significantly higher than the ambient response (reduced signal-to-noise ratio in comparison with ambient vibrations). Therefore, the sensor specifications for free vibration tests are usually less stringent in comparison with the one adopted in monitoring under ambient excitation due to the higher vibration intensity [30]. Furthermore, the sensors are temporarily installed on the structure resulting in a lower cost in comparison to long-term sensors network exploited for ambient vibration monitoring.

Since free vibration tests can provide accurate estimates of the modal parameters while being rather cheap and easy to implement, they have been performed in many applications. For instance, several free vibration tests have been performed to enable the experimental dynamic characterization of base-isolated buildings [31–33], high-rise buildings [34], masonry towers [35] and ancient tie-rods [36, 37]. The identification of modal features from free vibrations is most popular for bridge monitoring. For example, Cunha et al. [38] have performed free vibration tests to estimate the modal properties of a cable-stayed bridge. The free vibrations for this test have been obtained by releasing a barge attached through a cable. Similarly, Magalhães et al. [39] have performed the dynamic identification of a bridge deck by exploiting its free vibrations due to the sudden rupture of a cable with an attached heavy counterweight. The free vibrations following the passage of a train have been often elaborated for the dynamic identification of railway bridges [14, 29]. Ko et al. [40] have identified the equivalent damping of bridge stay cables equipped with a magnetorheological damper from the free vibration decay following a sinusoidal excitation. Van Nimmen et al. [41] estimated the equivalent damping of a footbridge equipped with a tuned mass damper from its free decay response induced by one person bobbing at the midspan.

The results taken from the free decays of the structural response are generally recognized to be more accurate because the noise influence is smaller and there is no need to make assumptions about the loading conditions [27]. Therefore, when ambient vibration tests are adopted for dynamic identification purposes it is also common to perform supplementary free vibration tests, especially when accurate estimates of damping ratios are required: this depends on the high dispersion observed in literature for damping ratios identified from ambient vibration time series. A limitation of free vibration tests resides in the difficulty in the excitation control for test repeatability purposes: however, this problem becomes less relevant if output-only approaches are considered. The most traditional procedure to analyze the recorded data in free vibration tests consists of the application of band-pass filters to isolate the contributions of the most important modes. Another possible problem when dealing with this type of time series is, therefore, the separation of each modal contribution especially for complex bridge structures with possible closely spaced modes.

Figure 1.7: Type of excitation in a free vibration test: (a) free falling mass [42]; (b) hammer impulse excitation [43].

Figure 1.8: Free vibration test performed on Vasco da Gama cable-stayed bridge [38]: (a) overview of the bridge; (b) eccentrically suspended 60 ton barge; (c) starting cut of hanging Dywidag bar; (d) release of the barge.

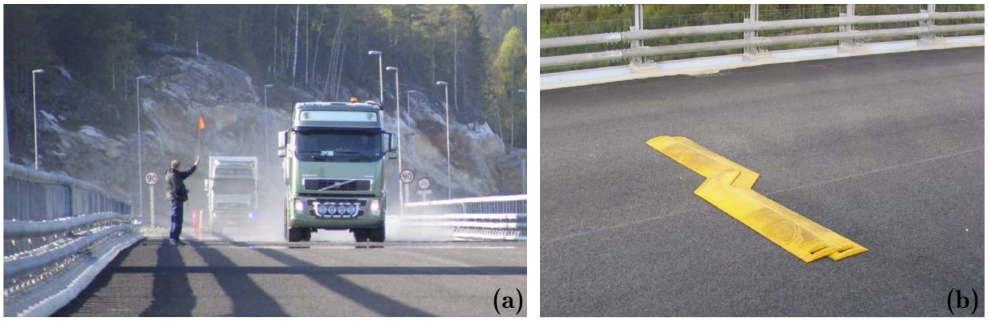

Figure 1.9: Dynamic test performed on the New Svinesund Bridge [44]: (a) Passage of a truck on a road bump fixed on the deck; (b) close-up of the rubber road bump.

Ambient vibration tests

When the dynamic identification of large bridges must be performed, it is usually difficult to excite them artificially using shakers and, therefore, it is preferable to exploit ambient vibrations [45]. Ambient vibration tests do not require specific equipment to excite the structure; different sources of excitation may be exploited such as wind, waves and pedestrian or vehicular traffic. Considering the nature of the input forces, it is not possible to measure or control the excitation which is thus assumed unknown. Therefore, ambient vibration testing implicitly assumes that only response data can be exploited for the estimation of dynamic parameters.

Due to the uncertainty of the input, hypotheses about its nature must be made; ambient excitation is generally modeled as a white noise stationary random process, i.e. the input has a power spectrum that is uniformly spread across the frequency range of interest: any identified parameter associated with significant strong response is representative of a structural mode. The main advantage of this testing approach is that accurate estimations of the modal frequencies and mode shapes can be obtained rapidly and with a reduced cost. Furthermore, the identification is carried out on time series which are representative of the real state of serviceability of the investigated structure. Since no heavy shaker installation is performed, it is not necessary to close the bridge to traffic during the tests. However modal damping ratios identified via ambient vibration tests are sometimes not accurate [14], and therefore complementary tests must be carried out if higher accuracy is needed.

This testing procedure has also some drawbacks: because of the low level of excitation, the accelerometers used for measuring must be highly sensitive, thus increasing the economic impact on the monitoring campaign. An adequate frequency resolution is difficult to obtain when time series with short time spans are used; on the other hand, increasing the frequency resolution by exploiting long time series may reduce the content of useful information due to the low signal-to-noise ratio contained in the timespans characterized by a low-intensity wind or traffic [24]. Moreover, if the structure has an important horizontal mode, the traffic load that is directed in the vertical direction may not be enough to excite it.

Advantages and limitations of vibration-based tests and damage detection

Vibration-based dynamic tests can detect damage dependent on stiffness-related variations in the structure. The main advantage of this approach is that continuous information on the state of the monitored structure is provided at a global level. Notably, it does not require direct assessment of the damaged elements and therefore allows the detection of possible hidden damage or not directly identifiable via visual inspection due to not easily accessible structures. However, this approach has some drawbacks. The main problem is that at least two different monitored states are required to produce a judgment on the structural health condition since a set of baseline values is required: therefore, if the baseline is established on an already damaged structure, only the progression of this deterioration can be captured by this approach. It follows that vibration-based dynamic testing must always be coupled with other complementary SHM approaches as well as visual inspections to properly grasp any pre-existing damage. Another relevant aspect related to vibration-based dynamic tests is that humidity and temperature gradients may induce relevant seasonal variations of the modal parameters. Finally, other drawbacks commonly widespread in the experimental measurements are related to epistemic and aleatory uncertainties as well as systematic errors related to the characteristics and implementation of the monitoring setup.

One of the most common classes of methodologies for damage detection is based on modal frequencies. Specifically, when damage occurs in a structure, a variation of the modal frequencies is expected due to the decrease in its global stiffness. Therefore, a shift in modal frequencies of the monitored structure between two monitored states may be symptomatic of anomalous structural behavior. The first documented attempts to detect damage in structures using frequency shifts are dated to the 1970s [46, 47]. Detection via modal frequencies is limited in the case of low levels of damage due to their poor sensitivity: local changes may be more accurately observed in higher modes frequencies but it is usually not easy to excite them, especially in civil structures [48, 49]. However, damage identification via modal frequencies has been successfully carried out in the case of simple structures such as beams or arches [50, 51]. Similarly in [52] the applicability of modal frequency-based SHM is investigated for a steel railway bridge monitored before and after being retrofitted, quantifying the effect on frequency sensitivity. The use of vibration-based damage detection and monitoring through shifts in natural frequencies is also documented in other relevant publications [47, 53]. Nonetheless, modal frequencies are global parameters [54] and thus they cannot provide any information about the localization of the damage, especially in the case of complex structures [55].

Criteria based on damage identification via modal damping ratios are less common since there is a higher degree of uncertainty on the damping mechanism as well as the sources of damping influencing the structural behavior. Several studies show that in PC and RC structures an increase in damping ratios is expected due to corrosion-induced damage as well as due to the internal friction that is developed when cracks are formed [56,57]. Other documented study damage assessment via modal damping ratios are discussed in [58, 59]. However, it is also observed in the literature [60, 61]that the modal damping ratios extracted from processed vibration data are usually not reliable for damage detection due to the excessive dispersion of the estimates.

Several applications reported in the literature [48, 62] are based on mode shape change because the latter are less influenced by environmental effects than frequen-

cies [63] and can provide information about damage location in the structure. Approaches based on the shift of mode shapes rely on indices such as the Modal Assurance Criterion (MAC) [64] which exploits the orthogonality property of the eigenvectors for the damage assessment or its generalization, namely the Coordinate Modal Assurance Criterion (COMAC) method [62] which also allows to locate the damage via modal node displacements. Studies on the practical application of MAC and COMAC criteria showed that structural changes and the corresponding locations were accurately identified but sometimes false positives were also detected [65–68].

It is worth noting that the effect of small damage on the previously mentioned modal properties is likely to be undetected due to the uncertainties in the experimental procedures. Therefore, to enhance the detection sensitivity, criteria based on higher-order derivatives of mode shapes have been proposed. In this context, one of the most widespread approaches is based on modal curvatures [69]. However, this method has some drawbacks such as the high number of sensors to accurately detect higher modes and the dependency on the number of modes considered [70]. Another modal parameter commonly used for damage assessment is modal flexibility [71]: the method is based on the definition of the flexibility matrix as the inverse of the structural stiffness matrix, which has higher damage sensitivity in comparison with other parameters even if only lower modes are available due to their easy extraction. Applications of this indicator for bridge damage identification purposes are discussed in [72].

1.3 Basics of signal pre-processing and validation

In this section, the main aspects related to the acquisition and validation of the signals recorded during dynamic tests are analyzed.

Aliasing and signal decimation

One of the first settings to be decided in the dynamic testing design is the sampling frequency at which the signals are acquired. The continuous signals obtained by sensors have to be converted into a discrete digital counterpart to be further elaborated; this is achieved by an analog-digital converter (ADC). The proper selection of the sampling frequency influences the accuracy of the signal representation in its digital form. To this aim, Shannon's theorem states that a continuous-time signal may be properly represented by its samples if the sampling frequency F_s is at least twice the highest frequency component $F_{\max}$ of the time signal:

$$F_s \geq 2F_{\max} \tag{1.18}$$

Therefore, the maximum observable frequency (Nyquist frequency) is:

$$F_{\text{Nyquist}} = \frac{F_s}{2} \tag{1.19}$$

If the highest frequency in the band of the analyzed signal is higher than the Nyquist frequency, the aliasing phenomenon occurs [73]: it causes the signal incorrect representation after the digitization process of the continuous signal due to the undersampling in the time domain. Fig. 1.10 shows the case in which a harmonic input

with frequency F_a, applied to ADC, does not satisfy Shannon's theorem. The samples produce an aliased sine wave that maintains the same values at the observation times $k\Delta t = k \cdot 1/F_s$ but has a lower frequency equal to $F_s - F_a$. The energy of the frequency components greater than the Nyquist frequency is forced into the frequency band of the reconstructed signal; therefore, new frequencies, not present in the original signal, appear in the sampled signal after reconstruction (see Fig. 1.11). This in turn makes not distinguishable the actual low-frequency contribution from the aliased one.

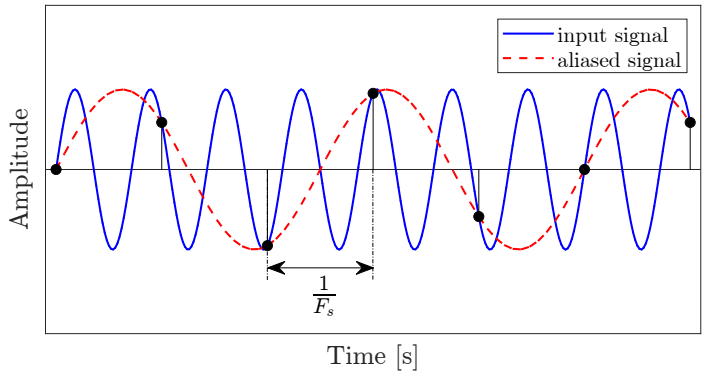

Figure 1.10: Aliasing in the time domain.

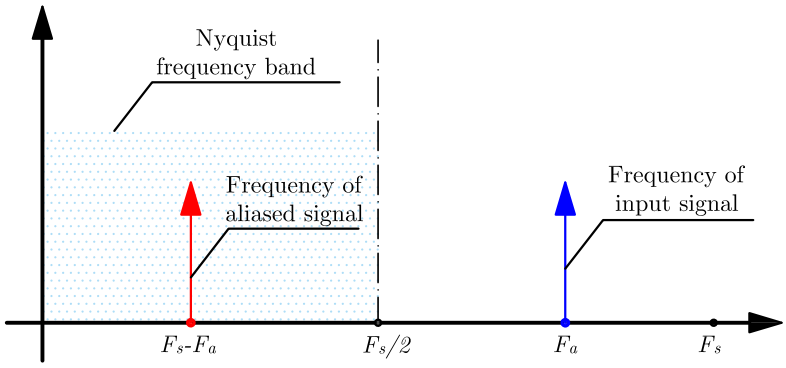

Figure 1.11: Aliasing in the frequency domain.

Aliasing can be minimized if the components above the Nyquist frequency are removed before the analog-to-digital conversion. This theoretically may be achieved by using a low pass filter with a sharp cut-off at $F_s/2$. However, real anti-aliasing filters always have a transition band and, to consider that frequency in this band may also produce aliasing, the cut-off frequency is usually assumed $0.4F_s$. In most of the practical cases, the adopted sampling frequency is much higher than the actual required value, thus producing a large amount of recorded raw data to process. A compression procedure called decimation or down-sampling is therefore exploited to compact the data to be elaborated. The decimation consists of an approximation of the time series that would have been obtained by sampling the signal at a lower rate. The

most simple kind of decimation process is the integer one. First, the high-frequency content is reduced by low pass filtering and subsequently the down-sampling of order Q is carried out on the filtered signal keeping only Qth sample and its integer multiples. Since the under-sampling reduces the sampling frequency, Shannon's sampling theorem likely is no longer satisfied, thus causing the aliasing phenomenon. Therefore, low-pass filtering before the actual decimation process becomes necessary to prevent such an eventuality.

Signals validation

The signal validation has a crucial role in checking if any anomaly affects the raw recordings. This operation allows to check if the signal is suitable for modal identification purposes. Several anomalies may affect the recorded data: the most common ones are noise-related. In these cases, the noise becomes predominant in the signal making it not possible to detect modal parameters. The noise-related phenomena may commonly occur because of the improper setting of the data acquisition system sensitivity, e.g. the sensor's voltage is significantly low in comparison to the one of the analog-digital converter. These anomalies can be easily detected by inspecting the signal frequency spectrum whose peak frequencies are overshadowed by the noise (see Fig. 1.12(a)). Similarly, digital noise effects are detectable by inspecting the time series which may present a series of well-defined constant steps (see Fig. 1.12(b)). Another sensitivity-related problem in data recording is signal clipping (see Fig. 1.12(c)); in this case, the recorded signal saturates the ADC. This effect can be avoided if the maximum input voltage is set high enough without being affected by the noise floor of the converter or by its resolution [26]. Other significant problems that may affect the data are outliers and dropouts; these effects are dependent on system malfunctions and losses of power and can also be detected by signals inspection (see Fig. 1.12(d)).

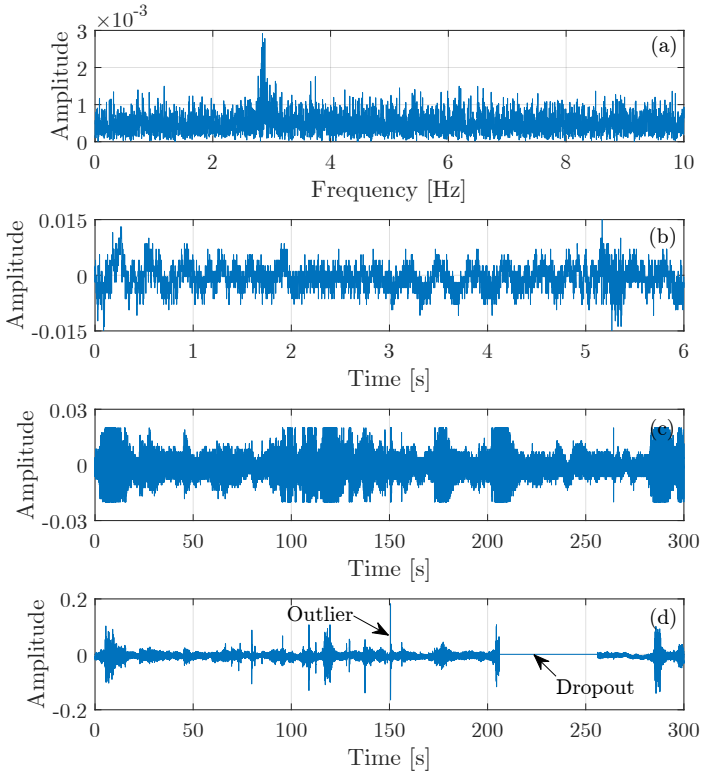

Figure 1.12: Principal data anomalies: (a) frequency spectrum of signal affected by instrumental noise; (b) signal affected by digital noise; (c) signal affected by clipping; (d) signal outliers and dropouts.

Filtering

Once the recorded signals are converted into digital form, they still could be affected by unwanted frequency components which may be eliminated through a digital filtering process. As opposed to the analog counterpart, digital filters are programmed by software and have several advantages such as not being affected by drifting due to temperature and humidity variations as well as not being influenced by manufacturing errors or aging phenomena. An ideal filter typically alters the signal acting in the frequency domain and retaining only the components in the frequency band of interest. Based on the frequency range retained (see Fig. 1.13), the filters are classified in [74]:

- Low-pass filters: retain all the frequencies under a cut-off value and remove higher frequencies;
- High-pass filters: retain all the frequencies higher than a cut-off value and remove lower frequencies;
- Band-pass filters: retain the frequencies contained in a band specified by an upper and a lower value of cut-off frequency;

- Band-stop filters: remove the frequencies contained in a band specified by an upper and a lower value of cut-off frequency.

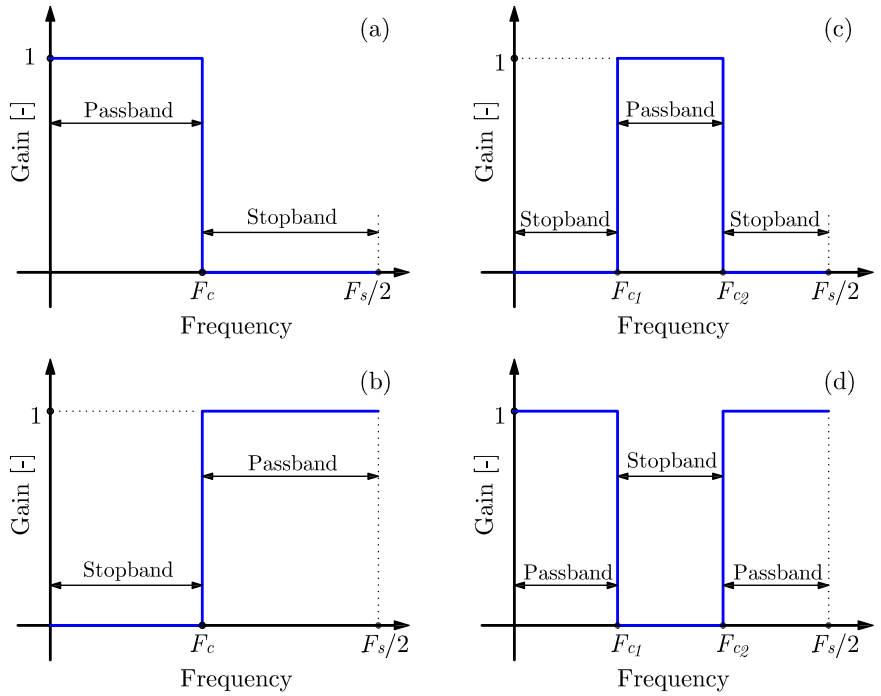

Figure 1.13: Gain for different types of ideal filters: (a) low-pass filter; (b) high-pass filter; (c) band-pass filter; (d) stop-band filter.

An ideal filter does not alter the retained frequency band, therefore its gain is unitary (0 dB) in the pass band and zero ($-\infty$ dB) in the stop band. However, ideal filtering is not possible in practice because a real filter cannot satisfy at the same time all the properties of an ideal one. Notably, a real filter may show variations of the gain in frequency called ripples both in the pass band and stop band as well as a transition band around the cut-off frequency instead of a sharp cut-off (see Fig. 1.14). The choice of the filter is therefore influenced by:

- center frequency: the frequency value at which the filter causes a 3 dB amplitude attenuation. In the case of band-pass and band-stop filters, the center frequency is defined as the geometric mean of the 3 dB attenuation cut-offs;
- roll-off rate: the rate of change of the output of the filter versus frequency;
- the presence of ripple in the pass-band influenced by the filter order;
- phase non-linearity.

Digital filters may be classified based on their impulse response in Finite Impulse Response (FIR) and Infinite Impulse Response (IIR). The former case is characterized

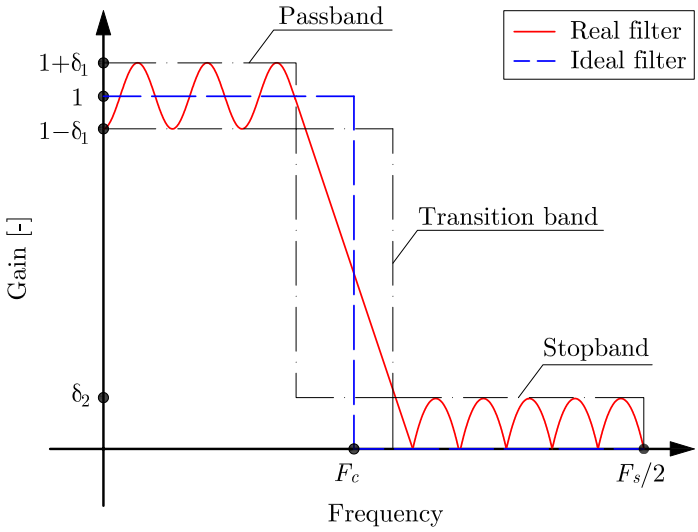

Figure 1.14: Gain behavior of ideal versus real low-pass filter.

by a finite impulse response and the filter output depends only on the current and past input values. In the second case, the impulse response never reaches zero and it extends indefinitely; the filter output is dependent on the actual and past input values as well as the actual and past output values. IIR filters are more efficient than FIR ones due to the fewer coefficients number to reach the same attenuation level, however, the former produces a linear-phase response whereas the latter produces a nonlinear-phase response. In applications such as structural health monitoring where the phase information is not crucial, the advantages of IIR filters may be exploited. Digital IIR filter designs come from the classical analog designs and include the Butterworth, Chebyshev and Elliptic filter types. The basic analog prototype form and the corresponding main features are briefly summarized.

Butterworth filters allow the maximal flatness tending to the ideal case and the 3 dB down frequencies correspond to the cut-off frequencies. On the other hand, a wide transition band characterizes the filter due to the slow roll-off rate. A possible solution to tone down this effect is increasing the filter order since it is proportional to the roll-off rate. The frequency response of this filter is monotonic and no ripples are generated (see Fig. 1.15). Chebyshev Type I filters reach maximal flatness in the stop-band similarly to Butterworth filters but the former achieves a steeper transition between pass-band and stop band than the latter for the same filter order. However, the sharper transition causes the appearance of ripples in the pass-band (see Fig. 1.16). Similarly, Chebyshev Type II filters achieve maximal flatness in the band-pass and have a steeper transition band than Butterworth filters; in this case, the sharper transition causes the appearance of ripples in the stop-band (see Fig. 1.17). Elliptic filters provide the fastest roll rate in the transition band, however, both the pass-band and stop-band are affected by ripples (see Fig. 1.18).

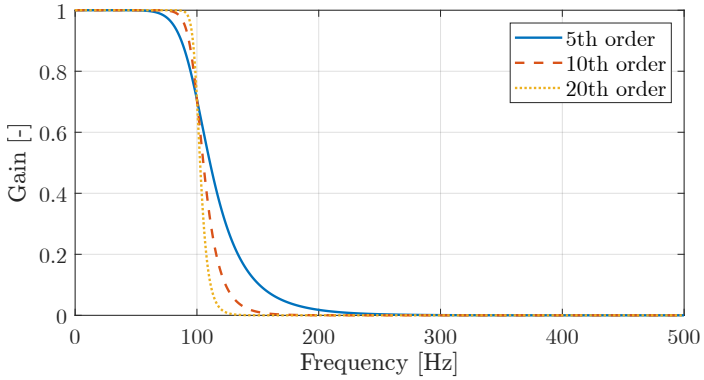

Figure 1.15: Magnitude of the gain over frequencies for a low-pass Butterworth filter, with a cut-off frequency of 100 Hz, varying its order.

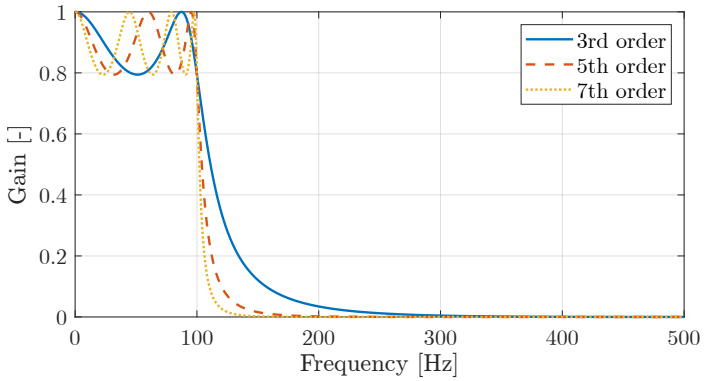

Figure 1.16: Magnitude of the gain over frequencies for a low-pass Chebyshev type I filter, with a cut-off frequency of 100 Hz, varying its order.

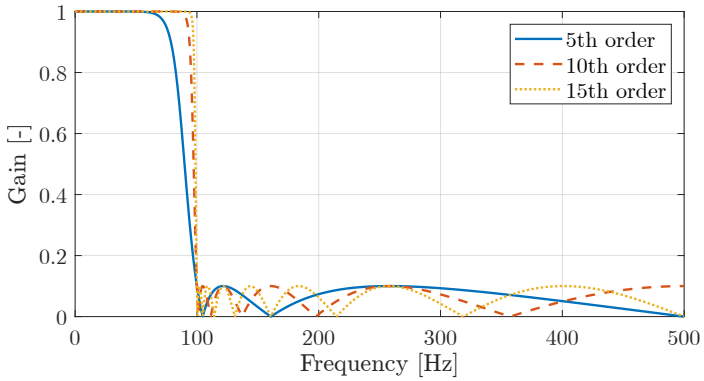

Figure 1.17: Magnitude of the gain over frequencies for a low-pass Chebyshev type II filter, with a cut-off frequency of 100 Hz, varying its order.

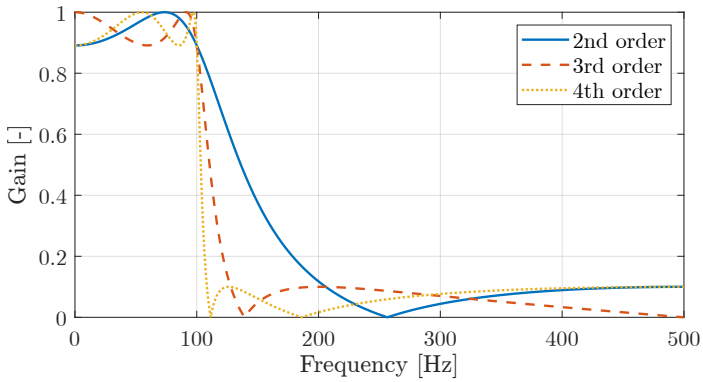

Figure 1.18: Magnitude of the gain over frequencies for a low-pass elliptic filter, with a cut-off frequency of 100 Hz, varying its order.

CHAPTER 2

STATE OF THE ART

This chapter presents a review of the current state of the art in the field of modal identification. As already mentioned in the previous sections, when conducting a vibration-based monitoring campaign, different types of tests can be performed depending on the degree of control on the excitation and, accordingly, different approaches may be followed for the modal parameters identification. When the exciting input on the structure is known and measured, forced vibration tests are carried out and their interpretation is attained using Experimental Modal Analysis (EMA) principles. The most popular approaches are based on the modal identification from the knowledge of the frequency response functions (FRFs), i.e. the relations between the input excitation and the corresponding outputs recorded at the testing locations; a detailed overview of these methods can be found in [75]. However, the application of EMA approaches requires excitation levels that can be only obtained by specific equipment which is not always available. Further, the base assumption that the investigated structure is forced only by the prescribed excitation does not hold well since other actions such as traffic or wind loads may act on it at the same time. These main limitations significantly reduce the applicability of these methods.

On the other hand, when the input is not known or it is not easily measurable, Operational Modal Analysis (OMA) is carried out. The OMA approaches are in part derived from EMA methods by making some specific assumptions on the input excitation.

This chapter will focus on the output-only techniques available in operational conditions due to their high popularity in the context of monitoring large structures such as bridges. When operational forces such as ordinary vehicular traffic, pedestrian loads or wind pressure are considered, classic OMA techniques in the time or frequency domain are adopted. Due to the small magnitude of the excitation, long recordings are usually required to discern the actual ambient vibrations from the noise. Moreover, traditional OMA techniques make certain assumptions on the nature of the excitation [26]:

- It has a wide frequency content, i.e. its frequency spectrum is almost flat in a certain frequency range and therefore it can be assimilated to a white noise input;
- It can be considered a stationary process.

When other sources of excitation are adopted in modal testing, not always these hypotheses are satisfied, thus requiring other approaches. A recent solution is based on advanced decomposition-based strategies in which modal parameters are estimated

once each modal contribution is isolated exploiting a suitable decomposition technique. This approach was originally introduced by Huang et al. [76] which combined the Empirical Mode Decomposition to the Hilbert Spectrum for the time series analysis of non-stationary data.

This chapter, therefore, also reviews the most popular advanced decomposition methods, documented in the current scientific literature, to retrieve modal components from a selected signal as well as suitable techniques for modal frequencies and dampings estimation.

2.1 Time Domain Methods

2.1.1 The continuous-time state-space model

The dynamic behavior of a discretized complex structure with n_m degrees of freedom, forced by the vector $\tilde{\mathbf{f}}(t)$, is described by the equation of motion Eq.(1.1) previously introduced and reported in the following for sake of clarity:

$$\mathbf{M}\ddot{\mathbf{u}}(t) + \mathbf{Z}\dot{\mathbf{u}}(t) + \mathbf{K}\mathbf{u}(t) = \tilde{\mathbf{f}}(t) \tag{2.1}$$

where $\mathbf{u}$, $\dot{\mathbf{u}}$ and $\ddot{\mathbf{u}}$ represent the displacement, velocity and acceleration vectors, respectively, whereas $\mathbf{M}$, $\mathbf{Z}$ and $\mathbf{K}$ are the mass, damping and stiffness matrices (squared matrices with dimensions equal to the number n_m of DOF of the structure). A state space model reduces the second-order differential equation of motion into an equivalent set of two first-order differential equations. It follows that the equation of motion can be expressed in terms of state variables by the introduction of the state vector:

$$\mathbf{x}(t) = \begin{Bmatrix} \mathbf{u}(t) \\ \dot{\mathbf{u}}(t) \end{Bmatrix} \tag{2.2}$$

Combining the equations of motion with the identity

$$\mathbf{M}\dot{\mathbf{u}}(t) = \mathbf{M}\dot{\mathbf{u}}(t) \tag{2.3}$$

and expressing both of them in terms of the state vector introduced in Eq.(2.2), the following set of $2N$ equations is obtained:

$$\dot{\mathbf{x}}(t) = \mathbf{A}_c\mathbf{x}(t) + \mathbf{B}_c\mathbf{f}(t) \tag{2.4}$$

where:

- $\mathbf{A}_c$ is the state matrix of the system in the time-continuous domain with dimensions $2n_m \times 2n_m$:

$$\mathbf{A}_c = \begin{bmatrix} \mathbf{0} & \mathbf{I} \\ -\mathbf{M}^{-1}\mathbf{K} & -\mathbf{M}^{-1}\mathbf{Z} \end{bmatrix} \tag{2.5}$$

- $\mathbf{B}_c$ is the input matrix with dimensions $2n_m \times n_m$:

$$\mathbf{B}_c = \begin{bmatrix} \mathbf{0} \\ \mathbf{M}^{-1} \end{bmatrix} \tag{2.6}$$

- $\mathbf{f}(t)$ is the forcing vector:

$$\mathbf{f}(t) = \begin{bmatrix} \mathbf{0} \\ \tilde{\mathbf{f}}(t) \end{bmatrix} \tag{2.7}$$

being $\mathbf{0}$ and $\mathbf{I}$ the zero and identity matrix, respectively. If the structural response measurements are recorded from l sensors (accelerometers, velocimeters and displacement transducers) at different locations, a set of l observability equations can be associated with the equation of motion:

$$\mathbf{y}(t) = \mathbf{C}_a\ddot{\mathbf{u}}(t) + \mathbf{C}_v\dot{\mathbf{u}}(t) + \mathbf{C}_d\mathbf{u}(t) \tag{2.8}$$

where $\mathbf{C}_a$, $\mathbf{C}_v$ and $\mathbf{C}_d$ are the $l \times n_m$ output location matrices for accelerations, velocities and displacements measured by the adopted sensors, respectively. The former matrices may be exploited to combine couples of displacements to obtain strains, which can be measured on the system using strain gauges. Combining Eqs.(2.1) and (2.8), the second-order representation of an MDOF system in terms of state variables is obtained:

$$\mathbf{y}(t) = \mathbf{C}_c\mathbf{x}(t) + \mathbf{D}_c\mathbf{f}(t) \tag{2.9}$$

where:

- $\mathbf{C}_c$ is the output influence matrix in the continuous-time domain and has dimensions $l \times 2n_m$:

$$\mathbf{C}_c = \begin{bmatrix} \mathbf{C}_d - \mathbf{C}_a\mathbf{M}^{-1}\mathbf{K} & \mathbf{C}_v - \mathbf{C}_a\mathbf{M}^{-1}\mathbf{C}_c \end{bmatrix} \tag{2.10}$$

- $\mathbf{D}_c$ is the direct transmission matrix, which relates applied forces to measured accelerations, with order $l \times n_m$:

$$\mathbf{D}_c = \mathbf{C}_a\mathbf{M}^{-1} \tag{2.11}$$

  If the measures are only displacements and velocities, there is no direct transmission being $\mathbf{D}_c = \mathbf{0}$.

The set made up of the state space equations Eq.(2.4) and the observability equation Eq.(2.9) defines the continuous-time state-space model. This model is characterized by the existence of an infinite number of equivalent state-space representations for a given system [77]: the experimental test allows establishing only one of these infinite realizations. For each of these realizations, a set of modal parameters can be extracted from the state matrix $\mathbf{A}_c$ [78]. The latter can be rewritten as follows:

$$\mathbf{A}_c = \mathbf{\Psi}_c\mathbf{\Lambda}_c\mathbf{\Psi}_c^{-1} \tag{2.12}$$

being $\mathbf{\Lambda}_c$ and $\mathbf{\Psi}_c$ the eigenvalues and eigenvectors matrices related to the state matrix $\mathbf{A}_c$ respectively, which have the following form:

$$\mathbf{\Lambda}_c = \begin{bmatrix} \mathbf{\Lambda} & \mathbf{0} \\ \mathbf{0} & \mathbf{\Lambda}^* \end{bmatrix}, \mathbf{\Psi}_c = \begin{bmatrix} \mathbf{\Theta} & \mathbf{\Theta}^* \\ \mathbf{\Theta\Lambda} & \mathbf{\Theta}^*\mathbf{\Lambda}^* \end{bmatrix} \tag{2.13}$$

where the superscript * is the complex conjugate operator. $\mathbf{\Lambda}$ and $\mathbf{\Theta}$ contain the n_m complex eigenvalues and eigenvectors of second order eigenproblem generated from Eq.(2.1):

$$(\mathbf{M\Lambda}^2 + \mathbf{Z\Lambda} + \mathbf{K})\mathbf{\Theta} = \mathbf{0} \tag{2.14}$$

The damping ratios and circular frequencies are both contained in the complex eigenvalues:

$$\lambda_r, \lambda_r^* = -\xi_r\omega_r \pm \mathrm{j}\omega_r\sqrt{1-\xi_r^2} \quad (r = 1, \ldots, n_m) \tag{2.15}$$

being j the imaginary unit. The imaginary part of λ_r represents the rth natural frequency of the damped system. Because only one subset of the DOF is measured, the observable mode shapes are expressed as:

$$\mathbf{\Phi_c} = \mathbf{C}_c\mathbf{\Psi}_c \tag{2.16}$$

2.1.2 The discrete-time state-space model

The experimental test produces discretized recordings of the structural response of each sensor at discrete time instants; it is thus necessary to convert the continuous-time state-space model into an equivalent discrete model. The solution $\mathbf{x}(t)$ of the system, made up of Eqs.(2.4) and (2.9), can be expressed as follows:

$$\mathbf{x}(t) = e^{\mathbf{A}_c(t-t_0)} + \int_{t_0}^{t} e^{\mathbf{A}_c(t-\tau)}\mathbf{B}_c\mathbf{f}(\tau)d\tau \tag{2.17}$$

where t_0 represents the initial time instant at which the force acts on the system. Considering the discrete time instants $t_k = (k+1)\Delta t$, Eq. (2.17) may be also evaluated in the discrete form and the continuous-time state-space model is therefore converted in the discrete-time state-space one which has the following expression:

$$\begin{cases} \mathbf{x}_{k+1} = \mathbf{A}\mathbf{x}_k + \mathbf{B}\mathbf{f}_k \\ \mathbf{y}_k = \mathbf{C}\mathbf{x}_k + \mathbf{D}\mathbf{f}_k \end{cases} \tag{2.18}$$

where $\mathbf{x}_k = \mathbf{x}(k\Delta t)$ represents the discrete-time state vector containing displacements and velocities, whereas $\mathbf{y}_k$ and $\mathbf{f}_k$ are the sampled input and output respectively. Under the zero-order hold assumption (ZOH), i.e. time functions constant between two consecutive samples, the continuous-time and discrete-time matrices are related by the following expressions [77]:

$$\begin{aligned} \mathbf{A} &= e^{\mathbf{A}_c\Delta t} \\ \mathbf{B} &= \int_{t_0}^{\Delta t} e^{\mathbf{A}_c}d\tau\mathbf{B}_c = [\mathbf{A} - \mathbf{I}]\mathbf{A}_c^{-1}\mathbf{B}_c \\ \mathbf{C} &= \mathbf{C}_c \\ \mathbf{D} &= \mathbf{D}_c \end{aligned} \tag{2.19}$$

The model described by Eq.(2.18) is deterministic because, until now, a deterministic force has been considered. To describe the real case based on the acquisition of experimental data, a stochastic component must be added to the model. Considering that in OMA the input represented by $\mathbf{f}_k$ is not measured, i.e. the contributions related to $\mathbf{B}$ and $\mathbf{D}$ matrices are neglected, the system response is only influenced by two stochastic components modeled as zero-mean stationary white noise processes:

- $\mathbf{w}_k$ is a $2n_m \times 1$ vector containing the process noise due to the inaccuracy of the model which in the absence of $\mathbf{f}_k$ takes its role and becomes the input that drives the dynamics of the system;

- $\mathbf{v}_k$ is a $l \times 1$ vector containing the measurement noise due to sensor inaccuracies and takes into account the direct disturbance of the response system.

Hence, the discrete-time stochastic state-space model (counterpart of the deterministic model represented by Eq.(2.18)) takes the following expression:

$$\begin{cases} \mathbf{x}_{k+1} = \mathbf{A}\mathbf{x}_k + \mathbf{w}_k \\ \mathbf{y}_k = \mathbf{C}\mathbf{x}_k + \mathbf{v}_k \end{cases} \tag{2.20}$$

In Eq.(2.20), $\mathbf{A}$ transforms the current state of the system $\mathbf{x}_k$ in the following one $\mathbf{x}_{k+1}$, whereas the product between the observation matrix $\mathbf{C}$ and the state vector provides the observable part of the state. The aim is to determine the state matrix $\mathbf{A}$ and the output matrix $\mathbf{C}$ to obtain the modal parameters of the system. Modal parameters of discrete and continuous-time state-space models are related by the following expression:

$$\mathbf{A} = e^{\mathbf{A}_c \Delta t} = e^{\boldsymbol{\Psi}\boldsymbol{\Lambda}_c\boldsymbol{\Psi}^{-1}\Delta t} = \boldsymbol{\Psi} e^{\boldsymbol{\Lambda}_c \Delta t}\boldsymbol{\Psi}^{-1} = \boldsymbol{\Psi}\boldsymbol{\Lambda}_d\boldsymbol{\Psi}^{-1} \tag{2.21}$$

where:

- $\boldsymbol{\Lambda}_d = \text{diag}(\mu_r)$, $r = 1, ..., n$ (being n the model order) is the diagonal matrix which contains the discrete-time complex eigenvalues of $\mathbf{A}_d$ obtained solving the problem $\mathbf{A}\boldsymbol{\Psi} = \boldsymbol{\Psi}\boldsymbol{\Lambda}_d$;
- $\boldsymbol{\Psi}$ is a $n \times n$ squared matrix whose columns are the system eigenvectors $\boldsymbol{\psi}_r$ of $\mathbf{A}$.

The eigenvalues μ_r in the discrete-time domain are related to the eigenvalues λ_r in the continuous-time domain by the following relationship:

$$\mu_r = e^{\lambda_r \Delta t} = e^{(-\xi_r\omega_r + \mathrm{j}\omega_r\sqrt{1-\xi_r^2})\Delta t} \tag{2.22}$$

The eigenvalues λ_r in the time-continuous domain represent the modal circular frequencies ω_r of the system and are therefore evaluated as follows:

$$\lambda_r = \frac{ln(\mu_r)}{\Delta t} \tag{2.23}$$

The modal damping ratios are evaluated according to the structural dynamics:

$$\xi_r = -\frac{\text{Re}(\lambda_r)}{|\lambda_r|} \tag{2.24}$$

The mode shapes of the system are the columns of the matrix $\boldsymbol{\Phi}$ which may be evaluated as follows:

$$\boldsymbol{\Phi} = \mathbf{C}\boldsymbol{\Psi} \tag{2.25}$$

The state space model (Eq.(2.20)) is only applicable for linear systems that do not have time-varying changes in their characteristics. Furthermore, the only way to obtain an optimal estimate of a state space model based on measured system response is to require that the system response is a realization of a zero-mean Gaussian distributed stochastic process. In other words, in the applied stochastic framework, the system

response is modeled by a stationary stochastic process $\mathbf{x}_k$, therefore the covariance state matrix $\boldsymbol{\Sigma}$ is independent by the time instant k:

$$\boldsymbol{\Sigma} = E[\mathbf{x}_k \mathbf{x}_k^{\mathrm{T}}] \tag{2.26}$$

where the superscript T indicates the transposition operator. Since the system response of the linear state space model is a Gaussian stochastic process, this implies that $\mathbf{w}_k$ and $\mathbf{v}_k$ are zero mean Gaussian stochastic processes as well:

$$\begin{aligned} E[\mathbf{x}_k \mathbf{w}_k^{\mathrm{T}}] &= \mathbf{0} \\ E[\mathbf{x}_k \mathbf{v}_k^{\mathrm{T}}] &= \mathbf{0} \end{aligned} \tag{2.27}$$

Further, since the input processes $\mathbf{w}_k$ and $\mathbf{v}_k$ are unknown, the simplest assumption is to consider two correlated zero-mean Gaussian white noise processes, defined by their covariance matrices $\mathbf{Q}$, $\mathbf{R}$ and $\mathbf{S}$ as:

$$E\left[\begin{bmatrix}\mathbf{w}_p \\ \mathbf{v}_p\end{bmatrix}\begin{bmatrix}\mathbf{w}_q^{\mathrm{T}} & \mathbf{v}_q^{\mathrm{T}}\end{bmatrix}\right] = \begin{bmatrix}\mathbf{Q} & \mathbf{S} \\ \mathbf{S}^{\mathrm{T}} & \mathbf{R}\end{bmatrix}\delta_{pq} \tag{2.28}$$

being δ_{pq} the Kronecker's delta function. The outputs correlation matrix for a time lag $\tau = i \cdot \Delta t$ is determined as follows [79]:

$$\mathbf{R}_i = E[\mathbf{y}_{k+i}\mathbf{y}_k^{\mathrm{T}}] \tag{2.29}$$

Properly combining Eq.(2.20) with Eqs.(2.26)-(2.29), after some mathematical manipulations, the following properties are achieved:

$$\begin{aligned} \boldsymbol{\Sigma} &= \mathbf{E}[\mathbf{x}_k \mathbf{x}_k^{\mathrm{T}}] = \mathbf{A}\boldsymbol{\Sigma}\mathbf{A}^{\mathrm{T}} + \mathbf{Q} \\ \mathbf{G} &= \mathbf{E}[\mathbf{x}_{k+1}\mathbf{y}_k^{\mathrm{T}}] = \mathbf{A}\boldsymbol{\Sigma}\mathbf{C}^{\mathrm{T}} + \mathbf{S} \end{aligned} \tag{2.30}$$

where $\boldsymbol{\Sigma}$ is the covariance matrix of the state $\mathbf{x}_k$ whereas $\mathbf{G}$ is the covariance matrix between the system response $\mathbf{y}_k$ and the updated state vector $\mathbf{x}_{k+1}$ called next-state output covariance matrix. Furthermore, the output covariance matrix of $\mathbf{y}_k$ for any arbitrary time lag $\tau = i \cdot \Delta t$ can be expressed in terms of the system matrices as:

$$\begin{aligned} \mathbf{R}_0 &= \mathbf{E}[\mathbf{y}_k \mathbf{y}_k^{\mathrm{T}}] = \mathbf{C}\boldsymbol{\Sigma}\mathbf{C}^{\mathrm{T}} + \mathbf{R} \\ \mathbf{R}_i &= \mathbf{E}[\mathbf{y}_{k+i}\mathbf{y}_k^{\mathrm{T}}] = \mathbf{C}\mathbf{A}^{i-1}\mathbf{G} \end{aligned} \tag{2.31}$$

The model presented in this section represents the framework from which the subspace identification approaches stem.

2.1.3 Stochastic Subspace Identification

The formulations based on the previously introduced state space model are usually referred to as Stochastic Subspace Identification (SSI) methods. These parametric models represent, nowadays, the most adopted solution in civil engineering for modal identification purposes in the time domain. Depending on the way the system is identified two main SSI methods may be distinguished: if output correlations are exploited in the model identification process, the Covariance Driven Stochastic Subspace

Identification (SSI-COV) method is adopted; alternatively if recorded time series are directly exploited using projections, Data-Driven Stochastic Subspace Identification (SSI-Data) method is used. These techniques are closely related and if the former has a lower computational cost in terms of time elapsed, the latter can provide additional information if proper post-processing is carried out.

Covariance-Driven Stochastic Subspace Identification

The Covariance Driven Stochastic Subspace Identification (SSI-COV) method [78] is based on the use of the outputs covariance matrix or equivalently of the outputs correlation matrix (because the signals are assumed as zero-mean ones) to identify the system defined as in Eq.(2.20). The time-discretized measured responses are organized in the output matrix:

$$\mathbf{Y} = \begin{bmatrix} \mathbf{y}(\Delta t) & \mathbf{y}(2\Delta t) & \dots & \mathbf{y}(n_t \Delta t) \end{bmatrix} \tag{2.32}$$

where n_t is the number of points of the time series. Each term in $\mathbf{Y}$ is a column vector that contains, at a given discrete time instant, the recorded response at each sensor location. The first step in SSI-COV is the estimation of the output correlation matrices; only a discrete number of samples are recorded in a dynamic test, therefore only an estimate of each correlation matrix $\tilde{\mathbf{R}}$ can be calculated. The estimated correlation matrix $\tilde{\mathbf{R}}_i$, for a predefined ith time lag ($i\Delta t$), has the following expression:

$$\tilde{\mathbf{R}}_i = \frac{1}{n_t - i} \mathbf{Y}_{(1|n_t-i)} \mathbf{Y}^{\mathrm{T}}_{(i|n_t)} \tag{2.33}$$

where $\mathbf{Y}_{(1|n_t-i)}$ is obtained from the $l \times n_t$ data matrix $\mathbf{Y}$ by the elimination of the last i columns whereas $\mathbf{Y}_{(i|n_t)}$ is obtained removing the first i columns from the data matrix $\mathbf{Y}$. Repeating this procedure for each time-lag the correlation matrices for all the discrete frequencies are obtained. The estimated correlations are collected in the following Toeplitz matrix:

$$\mathbf{T}_{(1|i)} = \begin{bmatrix} \tilde{\mathbf{R}}_i & \tilde{\mathbf{R}}_{i-1} & \dots & \tilde{\mathbf{R}}_1 \\ \tilde{\mathbf{R}}_{i+1} & \tilde{\mathbf{R}}_i & \dots & \tilde{\mathbf{R}}_2 \\ \vdots & \vdots & \ddots & \vdots \\ \tilde{\mathbf{R}}_{2i-1} & \tilde{\mathbf{R}}_{2i-2} & \dots & \tilde{\mathbf{R}}_i \end{bmatrix} \tag{2.34}$$

Under the assumption that all the l measured DOF are considered, each correlation matrix has dimensions $l \times l$. If the number of elements removed in each column to calculate $\tilde{\mathbf{R}}_i$ is equal to i, the Toeplitz matrix has dimensions $l \cdot i \times l \cdot i$. For the identification of a system of order n, the following condition must be satisfied:

$$l \cdot i \geq n \tag{2.35}$$

It is possible to express each correlation block matrix $\tilde{\mathbf{R}}_i$ by exploiting Eq.(2.31) as the product of two matrices:

$$\mathbf{T}_{(1|i)} = \begin{bmatrix} \mathbf{C} \\ \mathbf{CA} \\ \vdots \\ \mathbf{CA}^{i-1} \end{bmatrix} \begin{bmatrix} \mathbf{A}^{i-1}\mathbf{G} & \dots & \mathbf{AG} & \mathbf{G} \end{bmatrix} = \mathbf{O}_i \mathbf{\Gamma}_i \tag{2.36}$$

where $\mathbf{O}_i$ is the observability matrix and has dimensions $l \cdot i \times n$ whereas $\mathbf{\Gamma}_i$ is the controllability matrix with dimensions $n \times l \cdot i$. If the condition in Eq.(2.35) is satisfied, the system is both observable and controllable and the rank of $\mathbf{T}_{1|i}$ is equal to n (which represents the order of the model to be identified). Further, to obtain the state matrix $\mathbf{A}$, another matrix decomposition is considered. Specifically, the singular value decomposition (SVD) of the block Toeplitz matrix is expressed as follows:

$$\mathbf{T}_{(1|i)} = \mathbf{U}\mathbf{S}\mathbf{V}^{\mathrm{T}} = \begin{bmatrix}\mathbf{U}_1 & \mathbf{U}_2\end{bmatrix} \begin{bmatrix}\mathbf{S}_1 & \mathbf{0} \\ \mathbf{0} & \mathbf{0}\end{bmatrix} \begin{bmatrix}\mathbf{V}_1^{\mathrm{T}} \\ \mathbf{V}_2^{\mathrm{T}}\end{bmatrix} \tag{2.37}$$

where $\mathbf{U}$ and $\mathbf{V}$ represent the unitary matrices containing the left and right singular vectors whereas $\mathbf{S}$ is the singular values matrix.

The rank of the decomposed matrix is equal to the number of non-zero singular values: under the condition of Eq.(2.35), the rank is equal to n. Comparing Eq.(2.36) to Eq. (2.37), the observability and controllability matrices can be expressed in terms of the SVD output using the following partition:

$$\begin{aligned}\mathbf{O}_i &= \mathbf{U}_1\mathbf{S}_1^{1/2} \\ \mathbf{\Gamma}_i &= \mathbf{S}_1^{1/2}\mathbf{V}_1^{\mathrm{T}}\end{aligned} \tag{2.38}$$

which implies that they can be directly derived once the covariance matrices of measured output signals are obtained. It is worth noticing that alternative formulations of SSI-COV consider pre-multiplying and post-multiplying the Toeplitz matrix by some weighting matrices modifying the state space basis in which the model is defined [79]; the above-discussed formulation assumes as weights the identity matrix. Once the matrices defined in Eq.(2.38) are evaluated the model may be identified by calculating the state space model matrices $\mathbf{A}$ and $\mathbf{C}$. There are two possible ways to evaluate the state matrix $\mathbf{A}$: the first method is based on the decomposition property of the shifted Toeplitz matrix whereas the second one is the observability matrix method. In the first approach, the one-lag shifted Toeplitz matrix has the following expression:

$$\mathbf{T}_{(2|i+2)} = \begin{bmatrix}\tilde{\mathbf{R}}_{i+1} & \tilde{\mathbf{R}}_i & \dots & \tilde{\mathbf{R}}_2 \\ \tilde{\mathbf{R}}_{i+2} & \tilde{\mathbf{R}}_{i+1} & \dots & \tilde{\mathbf{R}}_3 \\ \vdots & \vdots & \ddots & \vdots \\ \tilde{\mathbf{R}}_{2i} & \tilde{\mathbf{R}}_{2i-1} & \dots & \tilde{\mathbf{R}}_{i+1}\end{bmatrix} \tag{2.39}$$

Applying the SVD decomposition to Eq.(2.39), the state matrix $\mathbf{A}$ is retrieved:

$$\mathbf{A} = \mathbf{O}_i^{+}\mathbf{T}_{(2|i+1)}\mathbf{\Gamma}_i^{+} = \mathbf{S}_1^{-1/2}\mathbf{U}_1^{\mathrm{T}}\mathbf{T}_{(2|i+1)}\mathbf{V}_1\mathbf{S}_1^{-1/2} \tag{2.40}$$

where the superscript $+$ is referred to the Moore-Penrose pseudo-inverse operation on non-squared matrix [80]. The second method [81] exploits the shift in the observability matrix. Introducing the matrices $\mathbf{O}_i^{\downarrow}$ and $\mathbf{O}_i^{\uparrow}$ obtained by removing the last and first l rows respectively from $\mathbf{O}_i$:

$$\mathbf{O}_i^{\downarrow} = \begin{bmatrix}\mathbf{C} \\ \mathbf{CA} \\ \vdots \\ \mathbf{CA}^{i-2}\end{bmatrix}, \mathbf{O}_i^{\uparrow} = \begin{bmatrix}\mathbf{CA} \\ \mathbf{CA}^2 \\ \vdots \\ \mathbf{CA}^{i-1}\end{bmatrix} \tag{2.41}$$

it is possible to relate them according to the following expression:

$$\mathbf{A} = (\mathbf{O}_i^{\downarrow})^{+}\mathbf{O}_i^{\uparrow} \tag{2.42}$$

The estimation of the output matrix $\mathbf{C}$ is also carried out following two possible procedures. The first method is based on the consideration that the first block row of the observability matrix $\mathbf{O}_i$ is precisely the matrix $\mathbf{C}$. The second method is based on considering the first block row of the Toeplitz matrix in Eq.(2.34); under the condition expressed by Eq.(2.35) and applying the SVD, it holds:

$$\mathbf{C} = \mathbf{T}_{(1|i)}^{1}\mathbf{V}_1\mathbf{S}_1^{-1/2} \tag{2.43}$$

Once $\mathbf{A}$ and $\mathbf{C}$ are determined all the modal parameters can be evaluated according to Eqs.(2.22) - (2.25). As previously mentioned the solution is not unique depending on the system order.

Data-Driven Stochastic Subspace identification

SSI-COV algorithm assumes that covariance functions are known and raw output data does not play any role irrespective of whether it is available or not. On the other hand, SSI-Data explicitly requires the availability of raw data. The method exploits numerical robust techniques such as QR-factorization, SVD and the least squares method. In the Data-Driven SSI algorithm, instead of calculating the covariances between outputs as in SSI-COV, the projections of the row space of future outputs into the row space of past outputs are calculated to remove the noise. The state vector estimation is carried out using Kalman filter [82], which provides the optimal prediction of the state vector. It is this requirement that necessitates the availability of raw output time data. The Kalman filter aims at producing an optimal prediction $\hat{\mathbf{x}}_k$ of the state $\mathbf{x}_k$ at the discrete-time t_k by utilizing the observations of the outputs up to time t_{k-1} and the available system matrices together with the known noise covariances. Therefore, the initial problem defined by Eq.(2.20) may be rewritten in the form:

$$\begin{cases} \hat{\mathbf{x}}_k = \mathbf{A}\hat{\mathbf{x}}_{k-1} + \boldsymbol{\kappa}_{k-1}\mathbf{e}_{k-1} \\ \mathbf{y}_{k-1} = \mathbf{C}\hat{\mathbf{x}}_{k-1} + \mathbf{e}_{k-1} \end{cases} \tag{2.44}$$

where $\boldsymbol{\kappa}$ is the Kalman gain matrix which gives information about the noise on the system due to the white noise excitation and $\mathbf{e}$ is a vector called innovation which indicates the part of the measured response $\mathbf{y}$ which cannot be predicted by the one step-ahead predictor $\hat{\mathbf{y}}$. From Eq.(2.44), a recursive relation for the state estimation is obtained:

$$\hat{\mathbf{x}}_k = \mathbf{A}\hat{\mathbf{x}}_{k-1} + \boldsymbol{\kappa}_{k-1}(\mathbf{y}_{k-1} - \mathbf{C}\mathbf{x}_{k-1}) \tag{2.45}$$

where the gain matrix is given by the following expression:

$$\boldsymbol{\kappa}_{k-1} = (\mathbf{G} - \mathbf{A}\mathbf{P}_k\mathbf{C}^{\mathrm{T}})(\mathbf{R}_0 - \mathbf{C}\mathbf{P}_{k-1}\mathbf{C}^{\mathrm{T}})^{-1} \tag{2.46}$$

The gain matrix depends on $\mathbf{R}_0$ (see Eq.(2.31)), related to statistical variability of the noise on the measured signal, and on $\mathbf{P}_k$ which is the Kalman state covariance matrix. The latter can be evaluated from the resolution of the Riccati's equation:

$$\mathbf{P}_k = \mathbf{A}\mathbf{P}_{k-1}\mathbf{A}^{\mathrm{T}} + (\mathbf{G} - \mathbf{A}\mathbf{P}_{k-1}\mathbf{C}^{\mathrm{T}})(\mathbf{R}_0 - \mathbf{C}\mathbf{P}_{k-1}\mathbf{C}^{\mathrm{T}})^{-1}(\mathbf{G} - \mathbf{A}\mathbf{P}_{k-1}\mathbf{C}^{\mathrm{T}})^{\mathrm{T}} \tag{2.47}$$

The Kalman filter state sequence $\hat{\mathbf{X}}_i$ is the matrix that contains the state estimates obtained from the output data at the previous i time instants. Assuming that the filter is started at j different time instants, it assumes the form:

$$\hat{\mathbf{X}}_i = \begin{bmatrix} \hat{\mathbf{x}}_i & \hat{\mathbf{x}}_{i+1} & \dots & \hat{\mathbf{x}}_{i+j-1} \end{bmatrix} \tag{2.48}$$

The idea at the basis of the technique is that the Kalman filter state estimates may be expressed as a linear combination of the rows of certain block Hankel matrices containing the raw data.

The data-driven algorithm starts from the construction of the block Hankel matrix related to the discretized measurements; it is a rectangular block matrix expressed in the following form:

$$\mathbf{Y}_{(0|2i-1)} = \frac{1}{\sqrt{j}} \left[\begin{array}{cccc} \mathbf{y}_0 & \mathbf{y}_1 & \cdots & \mathbf{y}_{j-1} \\ \mathbf{y}_1 & \mathbf{y}_2 & \cdots & \mathbf{y}_j \\ \vdots & \vdots & \ddots & \vdots \\ \mathbf{y}_{i-1} & \mathbf{y}_i & \cdots & \mathbf{y}_{i+j-2} \\ \hline \mathbf{y}_i & \mathbf{y}_{i+1} & \cdots & \mathbf{y}_{i+j-1} \\ \mathbf{y}_{i+1} & \mathbf{y}_{i+2} & \cdots & \mathbf{y}_{i+j} \\ \vdots & \vdots & \ddots & \vdots \\ \mathbf{y}_{2i-1} & \mathbf{y}_{2i} & \cdots & \mathbf{y}_{2i+j-2} \end{array}\right] = \left[\frac{\mathbf{Y}_{(0|i-1)}}{\mathbf{Y}_{(i|2i-1)}}\right] = \left[\frac{\mathbf{Y}_p}{\mathbf{Y}_f}\right] \tag{2.49}$$

The Henkel matrix $\mathbf{Y}$ has dimensions $2l \cdot i \times j$, being i the considered number of time lag, l the number of recording channels and it is assumed $j \to \infty$ in the theoretical formulation whereas $j = n_t - 2i + 1$ in practice. The output data are scaled by a factor $1/\sqrt{j}$ to be consistent with the definition of correlation. The Henkel matrix can be considered made up of two block matrices: $\mathbf{Y}_p$ is the block matrix related to signals acquired in the past whereas $\mathbf{Y}_f$ is the block matrix related to signals acquired in the future time. Another equivalent partition of the Henkel matrix can be considered by switching the ith row of measurements from the future matrix to the past matrix which are now labeled as $\mathbf{Y}_f^-$ and $\mathbf{Y}_p^+$ respectively:

$$\mathbf{Y}_{(0|2i-1)} = \left[\frac{\mathbf{Y}_{(0|i)}}{\mathbf{Y}_{(i+1|2i-1)}}\right] = \left[\frac{\mathbf{Y}_p^+}{\mathbf{Y}_f^-}\right] \tag{2.50}$$

The method is based on the evaluation of the row space of the state $\hat{\mathbf{X}}_i$ and the column space of the observability matrix $\mathbf{O}_i$ only from the knowledge of the output signal $\mathbf{Y}$. Once $\hat{\mathbf{X}}_i$ and $\mathbf{O}_i$ are known, the state matrices $\mathbf{A}$ and $\mathbf{C}$ can be evaluated, and the identification process is completed. The projection may be seen as a conditional mean which, for the Gaussian process, is described by its covariances. Considering that the shifted data matrices also define covariances, the orthogonal projection of the row space of future outputs on the row space of past outputs may be computed exploiting the QR factorization of the data Hankel matrix and it may be expressed as follows [79,82]:

$$\mathbf{P}_i = \frac{\mathbf{Y}_f}{\mathbf{Y}_p} = \mathbf{Y}_f \mathbf{Y}_p^{\mathrm{T}} (\mathbf{Y}_p \mathbf{Y}_p^{\mathrm{T}})^{+} \mathbf{Y}_p \tag{2.51}$$

Assuming that the system is both observable and controllable the main theorem of SSI allows to write the projection matrix as the product between the observability matrix

and the Kalman filter state sequence:

$$\mathbf{P}_i = \mathbf{O}_i \hat{\mathbf{X}}_i = \begin{bmatrix} \mathbf{C} \\ \mathbf{CA} \\ \vdots \\ \mathbf{CA}^{i-1} \end{bmatrix} \begin{bmatrix} \hat{\mathbf{x}}_i & \hat{\mathbf{x}}_{i+1} & \dots & \hat{\mathbf{x}}_{i+j-1} \end{bmatrix} \tag{2.52}$$

The orthogonal projection may also be decomposed by SVD after pre-multiplying for the weighting matrix $\mathbf{W}_1$ with dimensions $li \times li$ and post-multiplying for the weighting matrix $\mathbf{W}_2$ with dimensions $j \times j$:

$$\mathbf{W}_1 \mathbf{P}_i \mathbf{W}_2 = \begin{bmatrix} \mathbf{U}_1 & \mathbf{U}_2 \end{bmatrix} \begin{bmatrix} \mathbf{S}_1 & \mathbf{0} \\ \mathbf{0} & \mathbf{0} \end{bmatrix} \begin{bmatrix} \mathbf{V}_1^{\mathrm{T}} \\ \mathbf{V}_2^{\mathrm{T}} \end{bmatrix} = \mathbf{U}_1 \mathbf{S}_1 \mathbf{V}_1^{\mathrm{T}} \tag{2.53}$$

The number of non-zero singular values represents the model order n, which is also correspondent to the dimension of the projected raw space. Depending on the selected algorithm, different expressions can be adopted for the weighted matrices; the choice allows writing the projection using a different basis. The Principal Component (PC) algorithm assumes that the weighted matrices have the following form:

$$\begin{aligned} \mathbf{W}_1 &= \mathbf{I} \\ \mathbf{W}_2 &= \mathbf{Y}_p^{\mathrm{T}} \left(\frac{1}{j} \mathbf{Y}_p \mathbf{Y}_p^{\mathrm{T}} \right)^{-1/2} \mathbf{Y}_p \end{aligned} \tag{2.54}$$

In the Unweighted Principal Component (UPC) algorithm, the weight matrices are assumed equal to the identity matrix:

$$\mathbf{W}_1 = \mathbf{W}_2 = \mathbf{I} \tag{2.55}$$

In the Canonical Variate Algorithm (CVA), the singular values of the weighted projection matrix represent the cosines of the principal angles between the row space of the past outputs $\mathbf{Y}_p$ and the row space of the future outputs $\mathbf{Y}_f$; the selected weighted matrices in the algorithm are:

$$\begin{aligned} \mathbf{W}_1 &= \left(\frac{1}{j} \mathbf{Y}_p \mathbf{Y}_p^{\mathrm{T}} \right)^{-1/2} \\ \mathbf{W}_2 &= \mathbf{I} \end{aligned} \tag{2.56}$$

From Eq.(2.53) the following relations hold:

$$\begin{aligned} \mathbf{W}_1 \mathbf{O}_i &= \mathbf{U}_1 \mathbf{S}_1^{1/2} \\ \hat{\mathbf{X}}_i \mathbf{W}_2 &= \mathbf{S}_1^{1/2} \mathbf{V}_1^{\mathrm{T}} \end{aligned} \tag{2.57}$$

The same procedure can be applied to define the orthogonal projection $\mathbf{P}_{i-1}$ leading to an estimate of the Kalman state sequence $\hat{\mathbf{X}}_{i+1}$:

$$\hat{\mathbf{X}}_{i+1} = \mathbf{O}_{i-1}^{+} \mathbf{P}_{i-1} \tag{2.58}$$

Once the state sequence estimates are evaluated by SVD decomposition, the state matrices $\mathbf{A}$ and $\mathbf{C}$ can be obtained. Specifically, the initial problem can be rewritten in the following form [83]:

$$\begin{bmatrix} \hat{\mathbf{X}}_{i+1} \\ \mathbf{Y}_{i|i} \end{bmatrix} = \begin{bmatrix} \mathbf{A} \\ \mathbf{C} \end{bmatrix} \hat{\mathbf{X}}_i + \begin{bmatrix} \boldsymbol{\rho}_w \\ \boldsymbol{\rho}_v \end{bmatrix} \tag{2.59}$$

where $\mathbf{Y}_{i|i}$ is the ith block-row of the Hankel matrix whereas $\boldsymbol{\rho}_w$ and $\boldsymbol{\rho}_v$ are the Kalman filter residuals which are uncorrelated with the state estimation $\hat{\mathbf{X}}_i$. It is possible to solve this set of equations by the least squares method obtaining an asymptotically unbiased estimate of $\mathbf{A}$ and $\mathbf{C}$ in the form [84]:

$$\begin{bmatrix} \mathbf{A} \\ \mathbf{C} \end{bmatrix} = \begin{bmatrix} \hat{\mathbf{X}}_{i+1} \\ \mathbf{Y}_{i|i} \end{bmatrix} \hat{\mathbf{X}}_i^{+} \tag{2.60}$$

Once the state matrices are determined, the identification is completed by evaluating the modal parameters using Eqs.(2.22) $-$ (2.25).

System order estimation

Stochastic subspace methods require the knowledge of the order of the system n for the identification of the modal parameters. When an order n for the system is established, n eigenvectors will be retrieved from the state matrix $\mathbf{A}$, but rarely all of them will be real modes of the structure; in fact, purely numerical modes may also be identified. These mathematical modes result from the overestimation of the model order; they are created to allow the mathematical description of the measurements, which are affected by biases due to several reasons such as measurement noise, computational noise or modeling inaccuracies. The best way to discern real modes from numerical ones consists in the evaluation of a stabilization plot (see Fig. 2.1). This procedure is based on the fact that proper modes are related only to the features of the structure and are not dependent on the numerical process, so they will be constantly identified independently by the order assumed for the system. The stabilization diagram presents modal frequencies identified for all the system modes varying the model order. The frequencies that will be repeated consistently varying the model order give information about the real modes and about a reasonable value to assume for the model order. The approach is based on the over-specification of the order of the model, which is set large enough to ensure the identification of all physical modes. The stability of each mode is established considering the following three criteria associated with two consecutive orders of the system:

1. The scatter between the identified frequencies of two consecutive model orders must be under 1%:
$$\frac{|\nu_n - \nu_{n+1}|}{f_n} < 0.01 \tag{2.61}$$

2. The scatter between damping ratios of two consecutive model orders must be lower than 5%:
$$\frac{|\xi_n - \xi_{n+1}|}{\xi_n} < 0.05 \tag{2.62}$$

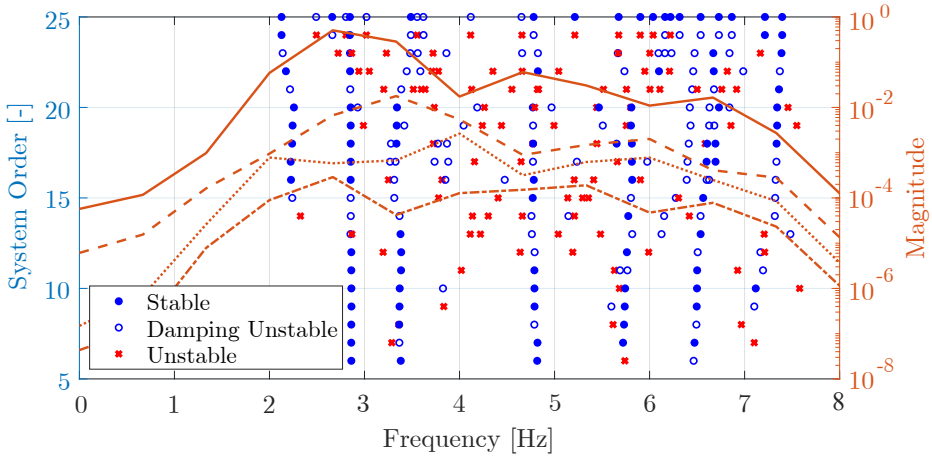

Figure 2.1: Stabilization plot for SSI method applied to an existing bridge vibration response.

3. The comparison of the same mode shape at two consecutive model orders due to Modal Assurance Criterion (MAC) must satisfy the following relationship:

$$1 - \text{MAC}[\boldsymbol{\phi}_n, \boldsymbol{\phi}_{n+1}] < 0.02 \tag{2.63}$$

If all the previous conditions are satisfied the mode is considered stable. Another possible criterion rests on the fact that civil structures are usually underdamped and the frequencies that define their behavior must be in complex conjugate pairs: frequencies that don't have the conjugate must be excluded because related to spurious modes.

2.1.4 Natural Excitation Technique

The Natural Excitation Techniques (NExT) is a class of procedures developed in the 1990s for output-only modal identification [85]. These methods have importance from a historical perspective because they revolutionized the OMA; the main applications in OMA before NExT consisted in the analysis of PSD functions and the identification of Operational Deflection Shapes (ODS) [26]. The ODS are generally a combination of several mode contributions, and they can be assumed as an estimate of mode shapes only if one mode is dominant at the considered frequencies. If the modes are closely spaced the respective contributions cannot be neglected and the ODS becomes a superposition of multiple modes. The introduction of NExT procedures allowed a more accurate analysis for close frequencies and also the actual extraction of mode shapes instead of operative deflection shapes. These methods were first developed in deterministic input-output modal analysis and applied to the impulse response function experimentally determined. Subsequently, the methodology was extended to OMA considering the analysis of correlation functions due to ambient vibrations. One of the first applications in the output-only case was the dynamic identification of vertical-axis wind turbines in operating conditions [86] where the excitation could not be easily measured and only the output response could be recorded. NExT procedures are based on the common assumption that auto and cross-correlation functions of the output

signals recorded from the operating structure can be expressed as sums of exponential decaying harmonics. Each sinusoidal component corresponds to a structural mode and its own frequency and damping ratio can be easily evaluated. The difference in the approaches is related to the possible different choices of the adopted method to analyze the correlation functions. The method consists of four phases:

1. Acquisition of data recorded from sensors mounted on the structure;
2. Evaluation of the autocorrelation and cross-correlation functions using standard techniques;
3. Use of a time-domain method on the correlation functions for the estimation of modal parameters; typically, three possible techniques can be alternatively used: Polyreference Least Square Complex Exponential (LSCE) method [87], Ibrahim Time Domain (ITD) method [88] and Eigensystem Realization Algorithm (ERA) [89];
4. Estimation of the mode shapes from the knowledge of the other modal parameters.

The result at the base assumption of the NExT procedure relies on the elaborations of cross-correlation functions for a discretized system. Given a linear system with n_m degrees of freedom, the measured response functions $\mathbf{y}(t)$ may be written as the superposition of the modal basis $\mathbf{\Phi}$ (see Eq.(1.8)) as follows:

$$\mathbf{y}(t) = \sum_{r=1}^{n_m} \boldsymbol{\phi}_r q_r = \mathbf{\Phi}\mathbf{q}(t) \tag{2.64}$$

where $\mathbf{q}(t)$ is the vector of modal coordinates and $\mathbf{\Phi}$ is a matrix collecting the n_m eigenmodes solution of the following eigenvalue problem:

$$(\mathbf{K} - \omega_r \mathbf{M})\boldsymbol{\phi}_r = \mathbf{0} \tag{2.65}$$

Using the modal superposition relation, the equation of motion for the rth mode can be expressed as follows:

$$\ddot{q}_r(t) + 2\xi_r\omega_r\dot{q}_r(t) + \omega_r^2 q_r(t) = \frac{1}{m_r}\boldsymbol{\phi}_r^{\mathrm{T}}\mathbf{f} \tag{2.66}$$

The measured response at the ith point due to the load applied at the kth point, namely $y_{ik}(t)$ can be expressed, through the Duhamel integral, in the following form:

$$y_{ik}(t) = \sum_{r=1}^{n_m} \phi_{ri}\phi_{rk} \int_{-\infty}^{t} f_k(\tau) g_r(t-\tau) d\tau \tag{2.67}$$

where ϕ_{ri} is the ith component of the rth mode shape,

$$g_r(t) = \frac{1}{m_r\omega_r\sqrt{1-\xi_r^2}} e^{-\xi_r\omega_r t} \sin\left(\omega_r\sqrt{1-\xi_r^2}t\right) \tag{2.68}$$

Assuming the load to be impulsive, i.e. the force $f(\tau)$ may be considered as a Dirac's Delta function at $\tau = 0$, the measured response at the point i due to an input impulse

at the point k can be expressed as the summation of n_m modal unitary impulse responses:

$$y_{i,k}(t) = \sum_{r=1}^{n_m} \frac{\phi_{ri}\phi_{rk}}{m_r\omega_r\sqrt{1-\xi_r^2}} e^{-\xi_r\omega_r t} \sin\left(\omega_r\sqrt{1-\xi_r^2}t\right) \tag{2.69}$$

The cross-correlation between two responses $y_{i,k}(t)$ and $y_{j,k}(t)$ with a time delay T due to the white noise input in the point k is defined as follows:

$$R_{y_i y_j,k}(T) = E[y_{i,k}(t+T)y_{j,k}(t)] \tag{2.70}$$

where $E[\cdot]$ is the expectation operator. Substituting Eq.(2.69) into Eq.(2.70) the correlation function assumes the following form:

$$R_{y_i y_j,k}(T) = E\left[\sum_{r=1}^{n_m}\sum_{s=1}^{n_m} \phi_{ri}\phi_{rk}\phi_{sj}\phi_{sk} \int_{-\infty}^{t}\int_{-\infty}^{t+T} g_r(t+T-\sigma)g_s(t-\tau)f_k(\sigma)f_k(\tau)d\sigma d\tau\right] \tag{2.71}$$

being σ an integration variable. The previous equation can be re-written considering the properties of the operator $E[\cdot]$ as follows:

$$R_{y_i y_j,k}(T) = \sum_{r=1}^{n_m}\sum_{s=1}^{n_m} \phi_{ri}\phi_{rk}\phi_{sj}\phi_{sk} \int_{-\infty}^{t}\int_{-\infty}^{t+T} g_r(t+T-\sigma)g_s(t-\tau)E[f_k(\sigma)f_k(\tau)]d\sigma d\tau \tag{2.72}$$

Assuming that white noise is exciting the system, it holds:

$$R_{f_k f_k}(\tau-\sigma) = E[f_k(\sigma)f_k(\tau)] = \alpha_k\delta(\tau-\sigma) \tag{2.73}$$

where α_k is a constant and δ is the Dirac Delta function. Exploiting the previous equation and making a change on the integration variable, i.e., $\lambda = t-\sigma$, the cross-correlation function assumes the following form:

$$R_{y_i y_j,k}(T) = \sum_{r=1}^{n_m}\sum_{s=1}^{n_m} \alpha_k\phi_{ri}\phi_{rk}\phi_{sj}\phi_{sk} \int_0^{\infty} g_r(\lambda+T)g_s(\lambda)d\lambda \tag{2.74}$$

After some mathematical manipulation, it follows:

$$R_{y_i y_j,k}(T) = \sum_{r=1}^{n_m} G_{ijk,r}e^{-\xi_r\omega_r T}\cos\left(\omega_r\sqrt{1-\xi_r^2}T\right) + H_{ijk,r}e^{-\xi_r\omega_r T}\sin\left(\omega_r\sqrt{1-\xi_r^2}T\right) \tag{2.75}$$

where $G_{ijk,r}$ and $H_{ijk,r}$ are functions independent by T and have the following expressions:

$$\begin{aligned} G_{ijk,r} &= \sum_{s=1}^{n_m} \frac{\alpha_k\phi_{ri}\phi_{rk}\phi_{sj}\phi_{sk}}{m_r m_s\sqrt{1-\xi_r^2}\omega_r}\left(\frac{I_{rs}}{J_{rs}^2+I_{rs}^2}\right) \\ H_{ijk,r} &= \sum_{s=1}^{n_m} \frac{\alpha_k\phi_{ri}\phi_{rk}\phi_{sj}\phi_{sk}}{m_r m_s\sqrt{1-\xi_r^2}\omega_r}\left(\frac{J_{rs}}{J_{rs}^2+I_{rs}^2}\right) \end{aligned} \tag{2.76}$$

where it is assumed:

$$\begin{aligned} I_{rs} &= 2\sqrt{1-\xi_r^2}\omega_r(\xi_r\omega_r + \xi_s\omega_s) \\ J_{rs} &= (1-\xi_s^2)\omega_s^2 - (1-\xi_r^2)\omega_r^2 + (\xi_r\omega_r + \xi_s\omega_s)^2 \end{aligned} \tag{2.77}$$

Eq.(2.75) highlights that cross-correlation functions can be expressed as a linear combination of exponential decaying harmonics; the form of this equation is similar to the unitary impulse response function of the initial system expressed by Eq.(2.69). This result, therefore, implies that the cross-correlation functions can be processed by time domain identification techniques for the estimation of modal features. Similar considerations hold for auto-correlation functions. Even though NExT procedures provided a significative improvement in the output-only identification, they have been progressively replaced by more robust subspace methods because of certain limitations; for instance, the ITD method produces spurious modes that are not real, due to the lack of noise truncating mechanisms. Furthermore, the extraction of higher modes requires a repeated application of filters to the data which can lead to a time-consuming process [15].

2.1.5 Random Decrement Technique

The random decrement technique (RDT) is an alternative method for the estimation of correlation functions used in combination with other time domain methods in OMA for the identification of modal parameters [15]. The method was first introduced in the 1960s as a procedure to estimate the correlation function from a signal while it was being measured [90]. A mathematical formulation of RDT is proposed in [91] for the case of a SDOF system excited by zero mean Gaussian white noise. In the beginning, only auto random decrement (RD) signatures could be calculated, then Ibrahim [92] presented a method to calculate also the cross RD signatures and the method was perfected by Asmussen [93]. The technique allows the identification from the evaluation of Random Decrement (RD) signature functions. The structural response to a random input is made up of a deterministic part and a random one: averaging enough samples of the same random response, the deterministic component of the response can be obtained. The resulting signal from the application of the RD signature technique to a random response output of a structure can be interpreted as a free decay response and, therefore, can be processed by any covariance-driven identification methods. The RD signature is the average of a collection of segments extracted from the same time history [91] that are characterized by the same initial condition. This is done to avoid averaging out the deterministic part of the response. In this method, the initial conditions are called triggering conditions and the discrete-time instants of the response in which they are satisfied are defined triggering points. Different triggering conditions can be considered such as the crossing level of a threshold or the sign of the slope crossing; the amplitude and the slope of the response signal at each triggering point represent the initial displacement and velocity of the system respectively; this implies that a triggering condition can be seen as the application of a specific initial condition on the considered system. For a given measured response function $y(t)$, the RD signature can be expressed as follows:

$$D_{yy}(\tau) = E[y(t+\tau)|C_y(t)] \tag{2.78}$$

where $C_y(t)$ represents the triggering condition. The estimate of the RD signature for a discretized signal, averaging N_b segments, has the following expression:

$$D_{yy}(\tau) = \frac{1}{N_b} \sum_{n=1}^{N_b} y(t_n + \tau) | C_y(t_n) \tag{2.79}$$

Similarly, the cross-signature between two signals $y_j(t)$ and $y_k(t)$ is:

$$D_{y_j y_k}(\tau) = \frac{1}{N_b} \sum_{n=1}^{N_b} y_j(t_n + \tau) | C_{y_k}(t_n) \tag{2.80}$$

The most general triggering condition is given as [94]:

$$C_y(t) = \{a_1 \leq y(t) \leq a_2, b_1 \leq \dot{y}(t) \leq b_2\} \tag{2.81}$$

where a_1, a_2 and b_1, b_2 can be any value between the minimum and maximum values of the signal and its derivative. In the most general case of triggering condition, under the assumptions of a linear system excited by a stationary zero-mean Gaussian process the RD signature is estimated as a linear combination of the correlation function $R_{yy}(\tau)$ and its derivative $\dot{R}_{yy}(\tau)$:

$$D_{yy}(\tau) = \frac{R_{yy}(\tau)}{\sigma_y^2} \tilde{a} - \frac{\dot{R}_{yy}(\tau)}{\sigma_y^2} \tilde{b} \tag{2.82}$$

where σ_y^2 is the variance of the triggering process whereas $\tilde{a}$ and $\tilde{b}$ are scaling constants representing, respectively, the mean of the response function and the mean of its derivative at all the triggering points. If the chosen triggering condition influences only the triggering process, an RD signature proportional to the correlation function is obtained whereas if the triggering condition is only related to the derivatives of the triggering process, an RD signature proportional to the derivative of the correlation function is obtained. The measured dynamic response of a structure may be expressed as the sum of three contributions, namely a step response dependent on the displacement, an impulse response dependent on velocity and a third term dependent on the random external excitation as follows:

$$y(t) = y(0)d(t) + \dot{y}(0)\dot{d}(t) + h(t - \tau) \times f(\tau) \tag{2.83}$$

where $d(t)$ is the free vibration response for the conditions $y(0) = 1$, $\dot{y}(0) = 0$; $v(t)$ is the free vibration response for $u(0) = 0$, $\dot{u}(0) = 1$; $h(t)$ is the unit impulse response function and $\tau \in [0, t]$ the lower and upper limits for the convolution operator.

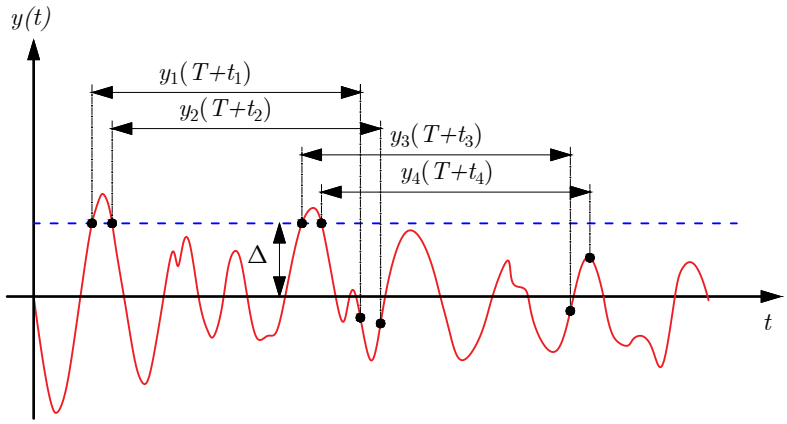

Figure 2.2: Definition of trigger threshold Δ and sample interval T.

Considering the signal in Fig. 2.2, for the simplest triggering condition, the steps followed by RDT are listed below:

1. Select the sampling interval T and the triggering condition, e.g. the trigger threshold Δ. At each time instant $t_i (i = 1, ..., N_b)$ when the threshold is crossed, the corresponding responses of duration T, namely $y_i(t_i + T)$, can be retrieved.

2. Shift the sampled response to base time $t = 0$, obtaining the sampled responses (see Fig 2.3). Under the assumption that both the excitation $f(t)$ and the response $y(t)$ are zero-mean stationary stochastic processes, the expectation of the sampled signal is the following:

$$E[y_i(t)] = \Delta \cdot d(t) \tag{2.84}$$

   Therefore, the free vibration response may be expressed as the expectation of the sampled signal $y_i(t)$ for the initial conditions $y(0) = \Delta$, $\dot{y}(0) = 0$.

3. The random-decrement free-vibration response $D_{yy}(t)$ may be expressed as the average of all sampled signals:

$$D_{yy}(t) \simeq \frac{1}{N_b} \sum_{i=1}^{N_b} y_i(t_i + T) \tag{2.85}$$

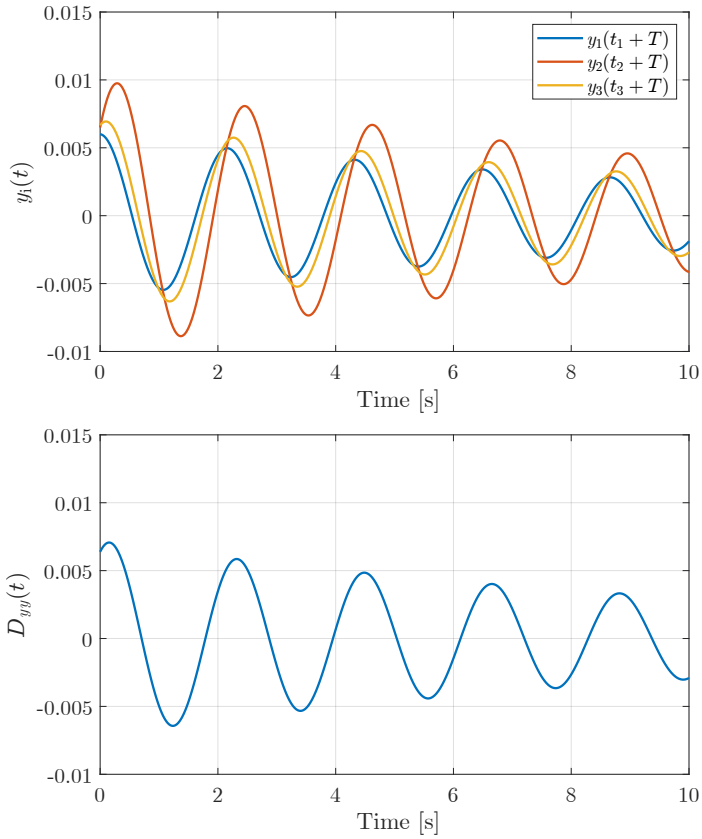

Figure 2.3: Sampled responses (top) and free-decay response obtained after processing by the RDT (bottom).

2.2 Frequency Domain Methods

2.2.1 Peak-picking

An early method for output-only modal identification purposes in the frequency domain is the Peak Picking (also called Basic Frequency Domain method - BFD) [95,96]. It assumes that the structural damping is low and also each mode influences the structural response in a narrow frequency band around the modal frequency, i.e. the vibrational modes are well separated. This method is the most undemanding and allows to identify only modal frequencies and modal shapes from the knowledge of the spectral density matrix of the response. The identification of natural frequencies is carried out manually picking the frequencies at each significative peak present in the spectral density function associated with the response. Considering the hypothesis of a frequency band in which only one mode is significative, e.g. the rth mode, the measured response function is expressed as follows:

$$\mathbf{y}(t) \simeq \boldsymbol{\phi}_r q_r(t) \tag{2.86}$$

being $q_r(t)$ the modal coordinate of the rth mode. The correlation matrix associated with the structural response is:

$$\mathbf{R_{yy}}(\tau) = E[\mathbf{y}(t+\tau)\mathbf{y}(t)^{\mathrm{T}}] = R_{q_r q_r}\boldsymbol{\phi}_r\boldsymbol{\phi}_r^{\mathrm{T}} = E[q_r(t+\tau)q_r(t)]\boldsymbol{\phi}_r\boldsymbol{\phi}_r^{\mathrm{T}} \tag{2.87}$$

where $R_{q_r q_r}$ is the modal auto-correlation function for the rth mode. Once the correlation matrix is known, the spectral density matrix is evaluated as:

$$\mathbf{G_{yy}}(\omega) = \frac{1}{2\pi}\int_{-\infty}^{\infty}\mathbf{R_{yy}}(\tau)e^{-\mathrm{j}\omega t}d\tau = G_{q_r q_r}(\omega)\boldsymbol{\phi}_r\boldsymbol{\phi}_r^{\mathrm{H}} \tag{2.88}$$

where $G_{q_r q_r}(\omega)$ is the auto spectral density function of the modal coordinate, and the superscript H denotes the operations complex conjugate and transpose. Considering the assumptions of the method and Eq.(2.88), the spectral density matrix $\mathbf{G_{yy}}(\omega)$ has a rank equal to one: this implies that at the resonance frequency, every column gives an estimation of the modal shape. Each column differs by others by a scaling factor because in OMA the input is not known. Subsequently, the trace of $\mathbf{G_{yy}}(\omega)$ is evaluated at each sampled frequency; the frequencies in correspondence with the peaks of this function then must be selected as modal frequencies.

The main drawback of the method is the possible misleading results in the presence of closely spaced modes [97] because it is not valid anymore the assumption of a single dominant mode in each frequency band. Moreover, this approach cannot identify modal damping ratios; in the past to overcome this limitation, the approach was used in combination with the half-power bandwidth method but it has been shown in the literature that damping estimation was inaccurate [98]. The problem of closely spaced modes may be quite common for real structures, thus more accurate methodologies were developed to achieve better modal identification performances in the frequency domain.

2.2.2 Frequency Domain Decomposition

The Frequency Domain Decomposition technique (FDD) was introduced by Brincker et al. [99] to overcome the drawbacks of the Peak-picking method in the presence of closely spaced modes. The idea behind the method consists of performing an approximate decomposition of the system response into a set of independent SDOF systems, one for each mode. Let it be l the number of monitored degrees of freedom of the system (equal to the number of sensors in the layout): for each one of them a discrete time history made up of n_t points, namely $y_i(t)$, $i = 1, \ldots, l$, is recorded. It is possible to evaluate for each discrete circular frequency, the spectral density matrix of the system response functions which is a square matrix of order l and has the following expression:

$$\mathbf{G}_{YY}(\omega) = \begin{bmatrix} \mathrm{PSD}_{11}(\omega) & \ldots & \mathrm{CPSD}_{1l}(\omega) \\ \vdots & \ddots & \vdots \\ \mathrm{CPSD}_{l1}(\omega) & \ldots & \mathrm{PSD}_{ll}(\omega) \end{bmatrix} \tag{2.89}$$

where $\mathrm{PSD}_{ii}(\omega)$ represents the power spectral density function for the ith recorded signals and $\mathrm{CPSD}_{ij}(\omega)$ represents the cross power spectral density function between the ith and jth signals. The unknown input signals are related to the measured output signal by [73]:

$$\mathbf{G}_{YY}(\omega) = \mathbf{H}^{*}(\omega)\mathbf{G}_{FF}(\omega)\mathbf{H}^{\mathrm{T}}(\omega) \tag{2.90}$$

where $\mathbf{H}(\omega)$ is the frequency response function (FRF) matrix, $\mathbf{G_{FF}}(\omega)$ is the input's PSD matrix and the superscript $*$ indicates the complex conjugate. The FRF matrix can be also expressed in poles and residues form as:

$$\mathbf{H}(\omega) = \sum_{r=1}^{n_m} \left(\frac{\mathbf{R}_r}{\mathrm{j}\omega - \lambda_r} + \frac{\mathbf{R}_r^*}{\mathrm{j}\omega - \lambda_r^*} \right) \tag{2.91}$$

where n_m is the number of modes, $\lambda_r = -\xi_r\omega_r + \mathrm{j}\omega_r\sqrt{1-\xi_r^2}$ is the rth pole (usually present in complex conjugate pairs) which contains the information about both the rth resonance frequency and damping ratio and $\mathbf{R}_r$ is the residue matrix which has the following expression:

$$\mathbf{R}_r = \boldsymbol{\phi}_r \boldsymbol{\gamma}_r^{\mathrm{T}} \tag{2.92}$$

where $\boldsymbol{\phi}_r$ is the rth mode shape and $\boldsymbol{\gamma}_r$ is the modal participation vector associated with the rth mode. If all the measurement points are considered in the calculations, $\mathbf{H}(\omega)$ becomes a squared matrix and $\boldsymbol{\phi}_r = \boldsymbol{\gamma}_r$. Considering Eqs.(2.90) - (2.92), and under the assumption of Gaussian white noise as input for the system, the PSD matrix of the output can be expressed as:

$$\mathbf{G}_{YY}(\omega) = \sum_{r=1}^{n_m}\sum_{s=1}^{n_m} \left(\frac{\mathbf{R}_r}{\mathrm{j}\omega - \lambda_r} + \frac{\mathbf{R}_r^*}{\mathrm{j}\omega - \lambda_r^*} \right) \mathbf{G}_{FF} \left(\frac{\mathbf{R}_s}{\mathrm{j}\omega - \lambda_s} + \frac{\mathbf{R}_s^*}{\mathrm{j}\omega - \lambda_s^*} \right)^{\mathrm{H}} \tag{2.93}$$

Using the Heaviside partial fraction theorem and considering only the contribution of dominant modes at the given frequency, the following expression for $\mathbf{G}_{YY}$ is obtained [100]:

$$\mathbf{G}_{YY}(\omega) = \sum_{r=1}^{\tilde{n}_m} \left(\frac{d_r \boldsymbol{\phi}_r \boldsymbol{\phi}_r^{\mathrm{T}}}{\mathrm{j}\omega - \lambda_r} + \frac{d_r^* \boldsymbol{\phi}_r^* \boldsymbol{\phi}_r^{\mathrm{H}}}{\mathrm{j}\omega - \lambda_r^*} \right) \tag{2.94}$$

In Eq.(2.94) the index $\tilde{n}_m < n_m$ highlights the fact that only dominant modes are relevant at a given frequency, furthermore the equation gives a direct relationship between measured data through $\mathbf{G}_{YY}(\omega)$ and modal parameters $\boldsymbol{\phi}_r$ and λ_r. The expression presented in Eq.(2.94) is equivalent to performing, for each discrete frequency, a single-valued decomposition (SVD) on the response PSD matrix $\mathbf{G}_{YY}(\omega)$. Considering that in the SVD, for a Hermitian and positive definite matrix, it holds $\mathbf{U}$=$\mathbf{V}$, the decomposition can be written as follows:

$$\mathbf{G}_{YY}(\omega) = \mathbf{V}\boldsymbol{\Sigma}\mathbf{V}^{\mathrm{H}} \tag{2.95}$$

where $\boldsymbol{\Sigma}$ is the $l \times l$ diagonal matrix collecting the singular values in descending order and $\mathbf{V}$ is the matrix that collects in each column the singular vectors of $\mathbf{G}_{YY}(\omega)$:

$$\begin{aligned} \boldsymbol{\Sigma} &= \begin{bmatrix} \sigma_1 & 0 & \dots & 0 \\ 0 & \sigma_2 & \dots & 0 \\ \vdots & \vdots & \ddots & \vdots \\ 0 & 0 & \dots & \sigma_l \end{bmatrix} \\ \mathbf{V} &= \begin{bmatrix} \mathbf{v}_1 & \mathbf{v}_2 & \dots & \mathbf{v}_l \end{bmatrix} \end{aligned} \tag{2.96}$$

This procedure is repeated for each discretized frequency line and each singular value is plotted against each corresponding discretized frequency. In [99] it is shown that

the singular values are estimates of the auto spectral density of the SDOF systems in modal coordinates, and near the resonance peak the singular vectors provide an estimate of the mode shape for each resonance frequency. Approaching a resonance frequency, only one mode contributes to the response, thus the sum in Eq.(2.94) has only one term; this implies that in the SVD there is only a dominant singular value which is the first due to the descending order assumed in the construction of $\mathbf{\Sigma}$ and the corresponding singular vector is an approximate estimation of the mode shape. For the rth resonance frequency it holds $\omega \to \omega_r$ and therefore:

$$\mathbf{G}_{YY}(\omega) = \sigma_1 \mathbf{v}_1 \mathbf{v}_1^{\mathrm{H}} \tag{2.97}$$

and the mode shape vector is expressed as:

$$\tilde{\boldsymbol{\phi}}_r = \mathbf{v}_1(\omega_r) \tag{2.98}$$

where the superscript $\sim$ means, once again, that the modal shape is an estimate and not the exact value. For repeated or coupled modes the peak selection must be performed not only on the first singular value plot but also on the second one whereas for closely spaced but not coincident modes is sufficient the peak selection on the first singular value plot. For the practical application of the method, the main steps of the FDD technique are summarized as follows:

1. Estimation of the spectral density matrices $\mathbf{G}_{YY}(\omega)$ from the raw time series data for each frequency line;
2. Singular value decomposition of the spectral density matrices;
3. If multiple test setups are available, average the first singular value of all test setups and perform the same operation for the other singular values;
4. Peak picking on the average singular values. For well-separated modes, the peaks must always be picked on the first singular value plot. For repeated modes, and sometimes for closely spaced modes the peak picking is performed also on the second singular value, the third singular value, etc. . . ;
5. The frequencies at each peak of the first singular value plot are the modal frequencies and the corresponding first singular vectors are the modal shapes.

The FDD method allows accurate identification of both modal frequencies and modal shapes even for closely spaced or repeated modes, however, its major limitation is the impossibility of identifying modal damping ratios. Furthermore, the accuracy of natural frequency estimates in FDD is related to the frequency resolution [15]: long records of the structural response to ambient vibrations provide high-quality singular value plots as a result of spectra characterized by a large number of averages and a fine frequency resolution (in the order of 0.01 Hz).

2.2.3 Enhanced Frequency Domain Decomposition

The Enhanced Frequency Domain Decomposition (EFDD) is an extension of the FDD procedure that allows better accuracy in the identification of modal frequency (independent on the frequency resolution) and mode shapes as well as the identification

of modal damping ratio which is not possible in the FDD [101, 102]. The method is based on the conversion of the PSD function in the time domain at resonance frequencies; modal damping ratios are evaluated performing the logarithmic decrement of the corresponding normalized auto-correlation function. The first step in the method consists of the application of the FDD procedure on the signals using the peak picking procedure to select the resonance frequencies ω_r and mode shapes $\tilde{\boldsymbol{\phi}}_r$. For each peak frequency, the corresponding SDOF-spectral bell function must be evaluated in order to identify the modal parameters: it represents the selection of the points of the singular value spectra with similar singular vectors. For the generic rth mode, the SDOF-spectral bell is evaluated by performing a correlation analysis, based on the MAC [64]: the higher the similarity between the compared vectors, the higher the MAC factor will be, tending to the unity if perfect correspondence is achieved. In this specific case, the singular vector associated with the selected rth peak frequency $\tilde{\boldsymbol{\phi}}_r = \mathbf{v}_1(\omega_r)$ is compared with the singular vectors $\mathbf{v}_q$ at the nearby frequencies and the MAC factor assumes the following form:

$$\mathrm{MAC}(\mathbf{v}_q, \tilde{\boldsymbol{\phi}}_r) = \frac{\left|\mathbf{v}_q^{\mathrm{H}} \tilde{\boldsymbol{\phi}}_r\right|^2}{(\mathbf{v}_q^{\mathrm{H}} \mathbf{v}_q)(\tilde{\boldsymbol{\phi}}_r^{\mathrm{H}} \tilde{\boldsymbol{\phi}}_r)} \tag{2.99}$$

The rth SDOF Spectral Bell function will be made up of all the retained singular values in the vicinity of the peak which satisfies the condition that the MAC between their correspondent singular vectors and the one at the rth resonance peak is larger than a fixed MAC rejection level. Typically, the MAC rejection level is assumed equal to 0.8. The method produces a better estimate of the modal shape; in fact, the information carried by the corresponding singular vector of each point of the SDOF spectral bell function is combined and this is achieved by the calculation of a weighted average multiplying the singular vectors with their corresponding singular values. This implies that the closer the singular vectors are to the peak frequency of the SDOF spectral bell, the more weight it has on the mode shape estimate. Once each SDOF spectral bell function is evaluated, the corresponding approximated SDOF correlation functions in the time domain are obtained by performing the Inverse Fourier Transform. The SDOF correlation functions are windowed to exclude the initial and final parts because they are affected by non-linearities induced by noise. The modal damping ratios can be evaluated on the windowed signals by the application of the logarithmic decrement method. For the rth mode, it holds [103]:

$$\delta_r = \frac{2}{p} ln \left(\frac{r_{0r}}{|r_{pr}|} \right) \tag{2.100}$$

where r_{0r} is the initial value of the correlation function and r_{pr} is the pth extrema. The parameter δ_r can also be obtained by expressing the windowed function in a logarithm plane where it will result in a straight line whose slope $\tilde{m}$ can be calculated and consequently $\delta_r = \tilde{m}\Delta t$ being Δt the time windows of the SDOF correlation function. The kth modal damping ratio is:

$$\xi_r = \frac{\delta_r}{\sqrt{4\pi^2 + \delta_r}} \tag{2.101}$$

The damped resonance frequency is simply obtained by the evaluation of the slope for the straight line obtained in the graph which plots the number of times the correlation function crosses the zero axis against the time in the considered time window. From the knowledge of both damped frequencies and damping ratios it is possible to evaluate the natural frequencies as follows:

$$\nu_r = \frac{\nu_{d,r}}{\sqrt{1-\xi_r^2}} \tag{2.102}$$

where ν_r is the natural frequency and $\nu_{d,r}$ is the damped frequency for the rth mode.

2.3 Modal Identification through adaptive decomposition methods

Classic OMA identification methods both in the time domain and frequency domain are the most popular solution for modal identification, straightforward in implementation and easy to interpret. These conventional techniques allow the processing of a given signal providing information about the frequency content and its time localization with a certain degree of accuracy which depends on the specific assumptions at the base of the considered method. However, the application of these methodologies is limited when systems with closely spaced modes or high damping ratios are investigated. Another important limitation dwells in the assumptions at the base of OMA such as the linear behavior of the structure and stationarity of the recorded response. Decomposition techniques based on Fourier analysis or wavelet analysis are usually referred to as "rigid methods" because they are expansion-based; the choice of a proper set of basis functions becomes difficult without information about the signal to be analyzed, especially for complex ones and can lead to subjective assumptions about their features. Usually, real signals recorded in vibrating MDOF structure are quite complex to analyze: this is mainly due to the noise, distortion effects possibly related to existing damages (which can produce non-linearity) and also the possible non-stationarity of the signal. The stationarity assumption loses its validity, especially for aging structures under ambient or seismic excitation [104]. Huang et al. [76, 105] highlight how the conventional Fourier-based approaches may yield distorted, indirect, or incomplete information about nonlinear and non-stationary time series. Furthermore, in problems like modal identification of large civil structures such as tall buildings or long-span bridges, closely spaced modes can occur, and Fourier transform-based methods are not applicable requiring linear lightly damped structure with well-separated modal frequencies [106]. Therefore, the identification of modal parameters requires a class of suitable decomposition algorithms that allows the decomposition of an arbitrary multicomponent signal into its mono-component parts in an accurate way. Modal parameter identification methods based on time-frequency analysis have recently become a popular research topic because it is possible to obtain information both in time and frequency simultaneously for a given signal and possible nonlinearities or non-stationarity can be handled. Hence, several adaptive mode decomposition methods have been recently formulated; these techniques are "flexible" in the description of an arbitrary signal, being not limited by the preliminary choice of the set of basis functions. The good data adaptability is related to the way these

methods are defined: usually, they are empirically based or exploit certain analytical principles which support the way they operate. The domain in which the decomposition occurs depends on the specifics of the technique and it may be the time, frequency or time-frequency domain. The retrieved unimodal components should be independent of each other and must recreate the initial signal via the superposition effect; they should also respect certain sparsity conditions that depend on the particular method considered. The most well-known approaches among the many solutions proposed in the scientific literature, are here briefly recalled and detailed in the following sections. The most widespread adaptive method is the Empirical Mode Decomposition (EMD) used in combination with the Hilbert-Huang transform and it has been extensively used for modal identification in engineering problems, however, some limitations related to mode mixing phenomena and end effects limit its performance. Another popular technique is the Empirical Wavelet Transform (EWT) which decomposes a multi-component signal on the base of the segmentation of the correspondent frequency spectrum and the application of a wavelet filter bank. EWT also suffers from mode-mixing problems in the case of signals with closely spaced modes due to the nature of the transition phase of each filter of the bank. The Variational Mode Decomposition is a method based on mathematical foundations and the generalization of the concept of Wiener filter: it decomposes the signal non-recursively and extracts the modes concurrently, overcoming limitations of EMD related to noise sensitivity and mode-mixing effects. Another recent adaptive method is the Empirical Fourier Decomposition (EFD) which overcomes the mode mixing and the trivial components problems of EWT by the introduction of an improved segmentation technique of the Fourier spectrum and the use of a zero-phase filter bank.

2.3.1 Empirical Mode Decomposition (EMD)

The Empirical Mode Decomposition (EMD) is one of the first algorithms able to handle the isolation of mono-component contributions from a multi-component nonlinear and non-stationary target signal. EMD has been exploited for a wide range of problems in several fields: specifically, common applications in structural engineering concern system identification, structural control and damage assessment. One of the most rife applications deals with the modal identification of MDOF systems using EMD and it has been addressed by different authors [107, 108]. Yu and Ren [109] applied EMD to an arch bridge under ambient excitation to identify modal parameters and compared the results with the ones obtained from typical methodologies used in OMA showing good accordance. Similarly, He et al. [110] used EMD in combination with RDT on a steel truss bridge under ambient vibrations. Chen [106] performed the modal identification for a long-span bridge with closely spaced modes under wind load exploiting EMD. Yang and Lee [111] identified modal frequencies using EMD on indirect measurement done by sensors mounted on a vehicle moving along the bridge and studied the effect of vehicle damping on the extracted signal. Dhakal and Malla [112] used indirect measurements for modal frequency identification on a steel railroad bridge and validated the results with a finite element model. In several studies EMD is used for the evaluation of possible structural damage: Xu and Chen [113] analyzed a three-story model under different kinds of excitation and exploited the method for the identification of location and severity of the damage; Bradley et al. [114]

studied the damage identification problem for beams under moving load; Lofrano et al. [115] exploited EMD to assess the localized damage of a structure in free vibration conditions; Bisheh et al. [116] studied the damage detection for a cable-stayed bridge analyzing the IMFs extracted by this method.

The EMD was introduced by Huang et al. [76] and it is based on the decomposition of the signal into a finite collection of amplitude and frequency modulated (AM-FM) mono-component signals called Intrinsic Mode Functions (IMFs). The IMFs have not an analytical formulation due to the empirical nature of the algorithm and preserve the information about their variable instantaneous frequencies and amplitudes; the same is not true for components obtained through Fourier transform-based methods. The IMFs are defined in a way that must satisfy the two following conditions:

1. The number of extreme points (maxima and minima) must be equal or at most differ by one with respect to the number of zero-crossing points in each IMF;

2. The mean between the upper and lower envelopes, called local mean, must be equal to zero.

The procedure exploited in the EMD to identify the IMFs is composed of two loops: the inner one necessary to obtain a residual part that satisfies IMFs properties and the outer one which must be iterated on the updated signal until all the significant IMFs are extracted from the signal. In detail, the inner loop is reported in its general form for the kth IMF extraction and consists of the following steps:

1. Selection of the initial signal $y(t)$, and setting of the index $j = 1$;

2. Detection of the extreme points (local maxima and minima) of the signal;

3. Evaluation of upper and lower envelopes of the signal using cubic splines to interpolate the extreme points, respectively labeled as $U_j(t)$ and $L_j(t)$ (see Fig. 2.4);

4. Evaluation of the local mean, i.e. $m_j(t) = [U_j(t) + L_j(t)]/2$.

5. Construction of the prototype of IMF: $c_j(t) = y(t) - m_j(t)$.

If stop criteria for IMF sifting are respected then the effective IMF is $v_k(t) = c_j(t)$ whereas if the conditions are not met the procedure is repeated from point 2 adopting as the new signal the IMF prototype $c_j(t)$: the inner loop is iterated until the IMF prototype is an actual IMF.

This process described in the inner loop is called sifting because it separates the finest local mode from the data at each loop and it has two effects: smoothing of the uneven amplitudes and elimination of riding waves. The sifting procedure can therefore be regarded as an iterative way of removing the asymmetry between the upper and lower envelopes to transform the original signal into an amplitude-modulated one [117]. Once an IMF is produced from the inner loop, the outer loop consists in:

1. Initialization of the signal;

2. Extraction of the kth IMF (inner loop);

3. Construction of the residual signal $r_k(t) = y(t) - \sum_{k=1}^{K} v_k(t)$;

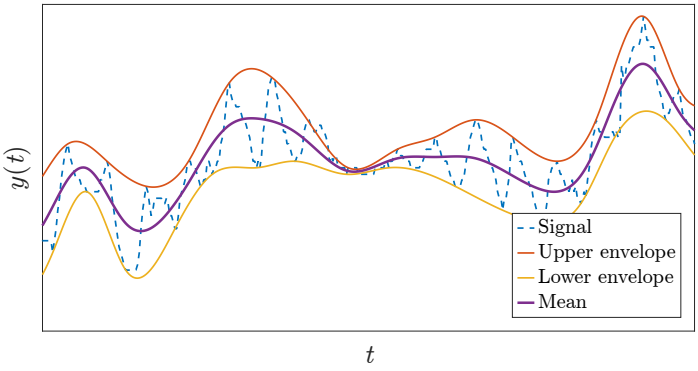

Figure 2.4: Construction of envelopes via cubic spline interpolation.

4. If $r_k(t)$ satisfies the stopping criteria for EMD (this is achieved when $k = K$), then $r_K(t)$ is the final residual signal and the decomposition is over, otherwise other IMFs must be extracted from the residue which will be used in the inner loop as the new input signal.

In this way it is possible to decompose the signal as the sum of a finite number of IMFs and a residue function:

$$y(t) = \sum_{k=1}^{K} v_k(t) + r_K(t) \tag{2.103}$$

Usually, a common criterion adopted for terminating the sifting procedure is based on the normalized standard deviation on two consecutive sifting results:

$$\sum_{t=0}^{T} \frac{(y_i(t) - y_i(t+1))^2}{y_i^2(t)} < \varepsilon \tag{2.104}$$

where ε is a tolerance threshold.

Figure 2.5 summarizes the steps followed by the method. Due to the way the sifting process is defined, the IMFs are extracted following the order of frequency content from the highest to the lowest one and finally the residue [118]. Another possible interpretation of the EMD procedure is the result of a filter bank [119, 120] made up of bandpass filters designed to isolate mono-component signals. The method is relatively simple in the application, does not require prior knowledge of the source of the analyzed signal and allows the analysis of classes of signals which other methods cannot handle. EMD is therefore a data-driven technique and it can identify the optimal mode number, without any external input, based on the local features of the signal.

However, the method has also several issues which may significantly influence the decomposition performance. One of the main problems resides in the fact that EMD lacks a theoretical foundation: indeed it works according to an algorithm and the performance is influenced by details in its implementation [117]. Another drawback of the method is related to the mode mixing phenomenon [121, 122]: this can manifest in an IMF consisting of oscillations at widely disparate frequency scales or, for

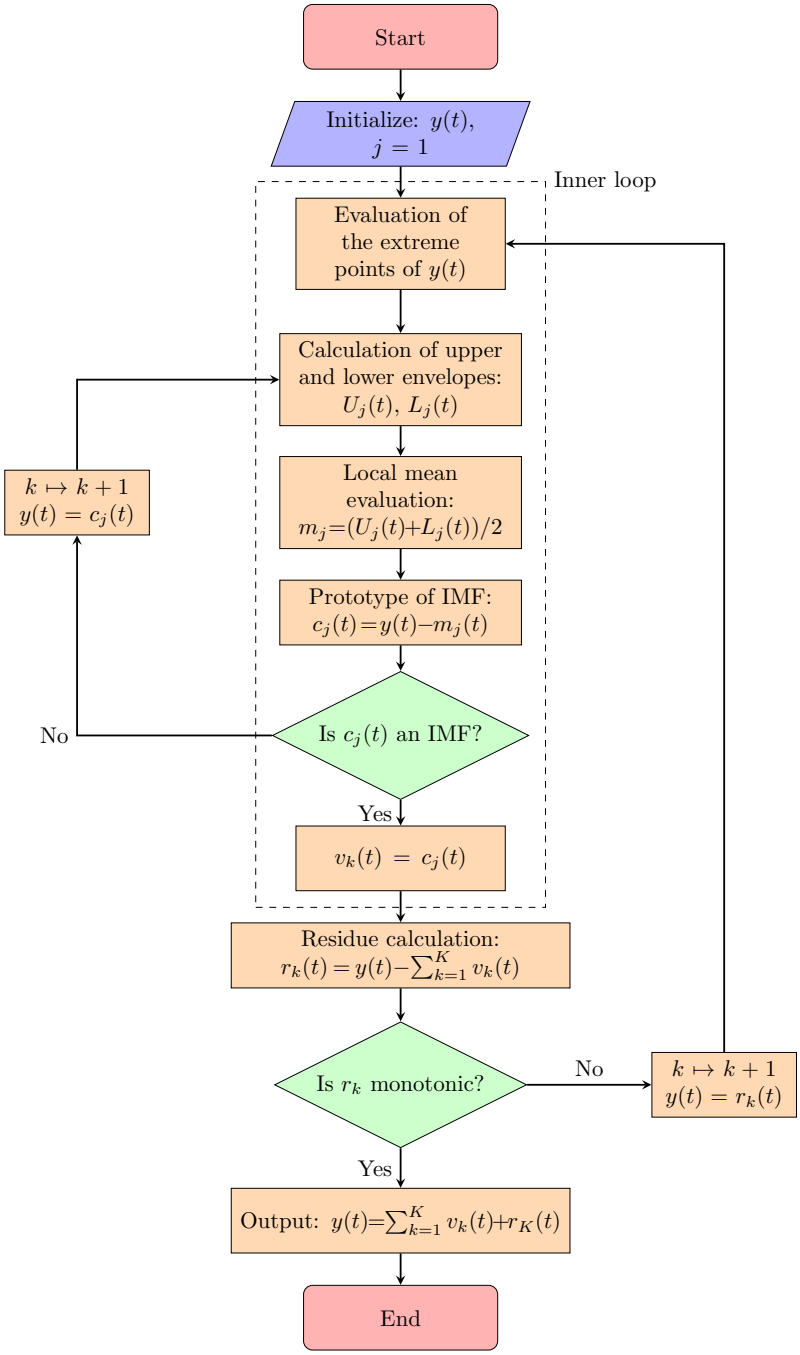

Figure 2.5: Algorithm of Empirical Mode Decomposition.

closely spaced modes, in an IMF containing multiple components at close frequencies. Specifically, in the latter case, the algorithm struggles to distinguish each mode con-

tribution in a narrow-band frequency range and tends to unify them. This problem leads to difficulty in the physical interpretation of the identified set of IMFs. The mode mixing is also strictly related to the weak robustness of EMD against the noise [123]; notably, the latter may produce fictitious extreme points that will be considered in the interpolation phase of the algorithm, thus spoiling the decomposition results: a slight change of signal to noise ratio (SNR) may determine a whole different set of IMFs. EMD, like every adaptive algorithm, is dependent on the frequency resolution of the data. In fact, a real signal is a continuous function but is always acquired in a discrete-time format [117]; depending on the setting of the sampling frequency, an extreme point contained in the real signal may not be present in the actual discrete recording thus undermining the decomposition performance in the envelopes evaluation phase. A common solution to this aspect consists in over-sampling which improves the decomposition performance limiting also possible over-sifting problems. EMD is also significantly influenced by the choice of several settings [124] such as the adopted stopping criterion, the kind of interpolation exploited in the envelope estimation and the boundary conditions; therefore, it does not exist a unique decomposition for the target signal. The envelopes are commonly determined via interpolation using cubic splines with good results, although this choice is computationally burdensome: other possible solutions are proposed in the literature to speed up the process however they often produce over-sifting problems. The boundary conditions have a significant role in the decomposition performance. Notably, the spline fitting leads to fluctuations at the ends of the dataset; if the starting and ending points of the signal are considered as knots in the envelopes, swings of the spline interpolation in the current IMF extraction may occur which propagates in the selection of all the following components [124]. This problem is handled by padding procedures at the extremes or using windowing functions. A possible solution to the problem of mode mixing in EMD has been addressed by Wu and Huang [121] who proposed a noise-assisted procedure called Ensemble Empirical Mode Decomposition (EEMD). This method consists of considering several trials in each of which a white noise of fixed amplitude is added to the initial signal. Due to this addition throughout the whole decomposition process, mode mixing is effectively reduced. The EEMD repeatedly decomposes the signals thus obtained into a series of IMFs for each trial, by applying the original EMD process. Considering an adequate number of trials, the added noise is therefore eliminated by averaging the ensemble of IMFs at the same position related to each trial leaving only the real IMFs. The loop on which is based the algorithm is the following:

1. Generation of a new time series by adding the white noise to the signal $y_i(t) = y(t) + w_i(t)$;
2. Decomposition of this new signal $y_i(t)$ using EMD;
3. Repetition of steps 1-2 for the fixed number of trials considering different components of white noise;
4. Evaluation of the ensemble mean corresponding to each IMF.

The accuracy of this procedure highly depends on the number of trials considered for the ensemble mean and the amplitude of the white noise; theoretically an infinite number of trials provides the exact evaluation for the IMFs, however considering a

finite number the obtained IMFs are partially affected by the added noise and thus a limited amplitude of the white noise must be considered. Suggested values for white noise amplitude and number of trials are respectively 20% of the standard deviation of the signal and a few hundred.

2.3.2 Variational Mode Decomposition (VMD)

The Variational Mode Decomposition (VMD) is a technique that allows isolating concurrently and in a non-recursive way unimodal components, labeled as IMFs, from a multicomponent target signal [125]. The method exploits the concepts of Hilbert transform, Wiener filtering and harmonic mixing. This technique has been used mainly in applications related to fault diagnosis in mechanical parts [126–128], however recently it has also been exploited in the seismic field [129], in civil structures modal identification [29, 130, 131]. An alternative definition of IMFs is formulated for this technique: the requirements of the original definition still must be satisfied, however, other conditions are enforced, thus providing a restrictive version of EMD's IMFs. In detail, recalling the IMF form as an AM-FM signal, i.e. $v_k = A_k(t)\cos(\phi_k(t))$, the following requirements must be met:

1. The envelope of instantaneous amplitudes $A_k(t)$ must be non-negative: $A_k(t) \geq 0$;

2. The instantaneous phase $\phi_k(t)$ must be a non-decreasing function, therefore the first order time derivative must be non-negative: $\phi_k^{'}(t) \geq 0$;

3. Both the envelope $A_k(t)$ and the instantaneous frequency $\phi_k^{'}(t)$ must vary much slower than the phase $\phi_k(t)$.

The last requirement implies that on a sufficiently long interval in the form $[t-\Delta t, t+\Delta t]$ with $\Delta t \simeq 2\pi/\phi_k^{'}(t)$ the kth IMF can be considered as a harmonic function with instantaneous amplitude $A_k(t)$ and instantaneous frequency $\phi_k^{'}(t)$. This definition ensures that the IMFs are well characterized in terms of sparsity property by their bandwidths: they are assumed as narrow banded components mostly compact around a center frequency. For this reason, the IMFs thus defined are also called Band Limited Intrinsic Mode Functions (BLIMFs). This new definition satisfies the EMD requirements, however, the opposite is usually not true because EMD's IMFs may have wide support containing several frequency peaks. VMD algorithm achieves the adaptive signal decomposition considering a variational framework in which the bandwidth associated with each component is assessed searching for the optimal solution of a constrained variational problem. The optimization process is performed in the frequency domain. Each mode is iteratively evaluated as the result of a narrow-band Wiener filter applied to the signal estimation residual of all other modes; the Wiener filter is calculated considering the current value in the iteration of the center frequency and, after the IMF estimation, the latter is re-estimated as the center of gravity of the IMF power spectrum. Therefore, VMD produces a segmentation of the Fourier spectrum to isolate all the modal components of the signal. In detail, the assessment of the bandwidth for each mode is carried out through the following steps:

1. The analytical signal is evaluated for each kth IMF using the Hilbert-Huang transform operator $\mathcal{H}[\cdot]$:

$$v_k^{\mathrm{A}}(t) = v_k(t) + \mathrm{j}\mathcal{H}[v_k(t)] = \left[\delta(t) + \frac{\mathrm{j}}{\pi t}\right] \tag{2.105}$$

2. The frequency spectrum of the mode is shifted to the baseband, by mixing with an exponential function tuned to the respective estimated central frequency:

$$v_k^{\mathrm{M}}(t) = \left[\left(\delta(t) + \frac{\mathrm{j}}{\pi t}\right) * v_k(t)\right] e^{-\mathrm{j}\omega_k t} \tag{2.106}$$

3. Each mode bandwidth BW_k is estimated by computing the H_1 Gaussian smoothness of the demodulated signal (i.e., the squared L^2-norm of the gradient):

$$\mathrm{BW}_k = \left\| \partial \left\{ \left[\left(\delta(t) + \frac{\mathrm{j}}{\pi t}\right) * v_k(t)\right] e^{-\mathrm{j}\omega_k t} \right\} \right\|_2^2 \tag{2.107}$$

Based on these steps, the following constrained variational problem is obtained:

$$\begin{gathered} \min_{\substack{v_1(t),\ldots,v_K(t) \\ \omega_1,\ldots,\omega_K}} \left\{ \sum_{k=1}^{K} \left\| \partial_t \left[\left(\delta(t) + \frac{\mathrm{j}}{\pi t}\right) * v_k(t)\right] e^{-\mathrm{j}\omega_k t} \right\|_2^2 \right\} \\ \text{s.t.} \quad \sum_{k=1}^{K} v_k(t) = v(t) \end{gathered} \tag{2.108}$$

where ∂_t is the gradient operator and $\|\cdot\|_2$ is the L^2-norm operator. Different methods can be used to solve the optimization problem in Eq.(2.108). By using a quadratic penalty term and the Lagrange multipliers technique to enforce the constraints, the search for the solution to this variational problem leads to the following augmented Lagrangian function:

$$\begin{aligned} \mathcal{L}(v_1(t), \ldots v_K(t), \omega_1 \ldots \omega_K, \lambda) = \alpha \sum_{k=1}^{K} \left\| \partial_t \left[\left(\delta(t) + \frac{\mathrm{j}}{\pi t}\right) * v_k(t)\right] e^{-\mathrm{j}\omega_k t} \right\|_2^2 \\ + \left\| v(t) - \sum_{k=1}^{K} v_k(t) \right\|_2^2 + \left\langle \lambda, v(t) - \sum_{k=1}^{K} v_k(t) \right\rangle \end{aligned} \tag{2.109}$$

where α is the quadratic penalty factor, λ is the Lagrangian multiplier and $\langle\cdot\rangle$ is the L^2-inner product. The solution of the governing constrained problem is thus equivalent to the evaluation of the saddle point of the augmented Lagrangian function. This can be achieved using the Alternating Direction Method of Multipliers (ADMM), which solves two sub-optimization problems. By minimizing the augmented Lagrangian function and moving into the spectral domain, the following problem is obtained:

$$\begin{aligned} \hat{v}_k^{n+1}(\omega) = \underset{\hat{v}_k(\omega)}{\operatorname{argmin}} \Bigg\{ \alpha \left\| \mathrm{j}\omega \left[(1 + \operatorname{sgn}(\omega + \omega_k)\, \hat{v}_k(\omega + \omega_k)) \right] \right\|_2^2 \\ + \left\| \hat{v}(\omega) - \sum_{k=1}^{K} \hat{v}_k(\omega) + \frac{\hat{\lambda}}{2} \right\|_2^2 \Bigg\} \end{aligned} \tag{2.110}$$

where the symbol $\hat{}$ hereinafter refers to the quantities expressed in the frequency domain (ω being the pulsation variable) whereas n is the iteration counter. The solution for this problem is:

$$\hat{v}_k^{n+1}(\omega) = \frac{\hat{v}(\omega) - \sum_{k \neq j} \hat{v}_j(\omega) + \frac{\hat{\lambda}}{2}}{1 + 2\alpha \left(\omega - \omega_k\right)^2} \tag{2.111}$$

The real component of the inverse Fourier transform finally yields the corresponding version in the time domain. The same procedure for the evaluation of central pulsation leads to the following problem:

$$\omega_k^{n+1} = \underset{\omega_k}{\operatorname{argmin}} \left\{ \int_0^\infty \left(\omega + \omega_k\right)^2 \left|\hat{v}_k(\omega)\right|^2 \mathrm{d}\omega \right\} \tag{2.112}$$

which has the following solution:

$$\omega_k^{n+1} = \frac{\int_0^\infty \omega \left|\hat{v}_k(\omega)\right|^2 \mathrm{d}\omega}{\int_0^\infty \left|\hat{v}_k(\omega)\right|^2 \mathrm{d}\omega} \tag{2.113}$$

The Lagrangian multiplier is updated as follows:

$$\hat{\lambda}^{n+1} = \hat{\lambda}^n + \chi \left[\hat{v}(\omega) - \sum_{k=1}^{K} \hat{v}_k^{n+1}(\omega) \right] \tag{2.114}$$

where χ is a noise tolerance parameter. The procedure stops once the following convergence criterion is satisfied:

$$\sum_{k=1}^{K} \frac{\left\| \hat{v}_k^{n+1}(\omega) - \hat{v}_k^n(\omega) \right\|_2^2}{\left\| \hat{v}_k^n(\omega) \right\|_2^2} < \varepsilon \tag{2.115}$$

where ε is the selected tolerance. The extracted component $v_k(t)$ corresponds to the contribution to the free vibration response attributable to the kth mode of vibration whereas ω_k is the estimate of the associated natural frequency. The VMD algorithm is summarized in Fig. 2.6. An advantage of VMD is that, unlike EMD-based methods, it achieves a decomposition in a non-recursive way extracting the modes concurrently: in this way, an error balancing among the IMFs can be taken into account during the sub-optimization loop. VMD may be interpreted as a signal decomposition technique with a wavelet-packet transform filter bank structure, significantly different from the EMD filter bank interpretation. This implies that VMD is an adaptive method with more refinement time-frequency divisions [132] and therefore it can better capture features of closely spaced modes. As previously mentioned the IMFs extracted using EMD are not bandlimited whereas, on the contrary, the ones obtained from VMD are limited in bandwidth thus allowing a proper single-mode decomposition [125]. The major drawback of the VMD method is that its performance is highly dependent on the proper tuning of two main parameters, namely the number of IMFs to be extracted K and the penalty factor α. The other involved parameters (i.e., the convergence threshold ε and the noise tolerance parameter χ) have much less influence. On the

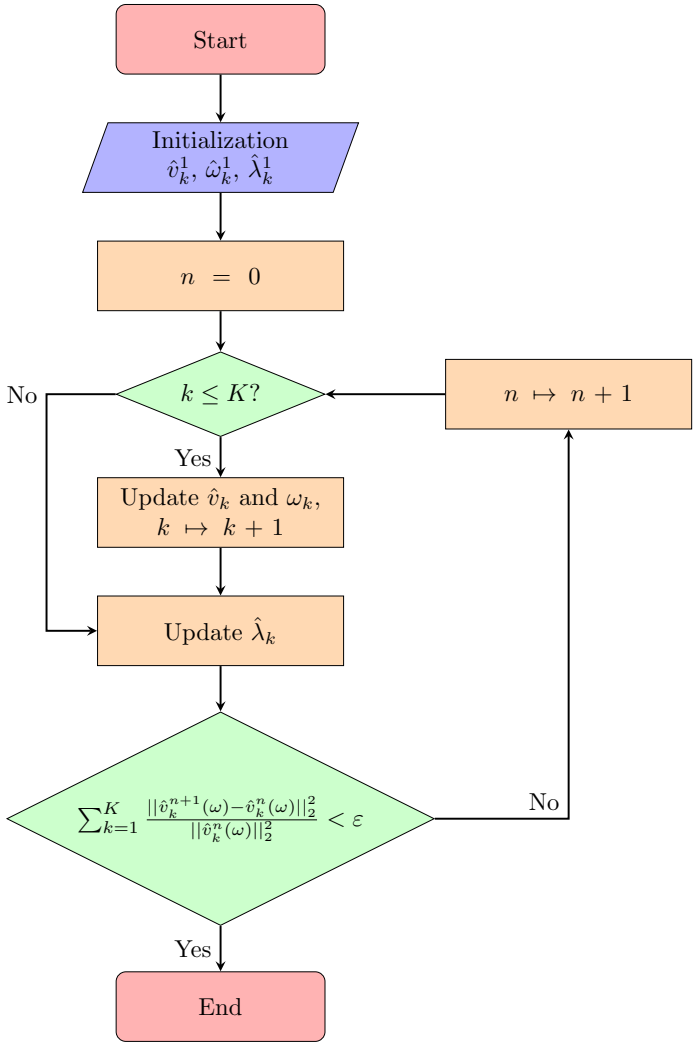

Figure 2.6: Algorithm of Variational Mode Decomposition

one hand, the number of IMFs K is related to loss or redundancy of information: it establishes how many modes can be retrieved from the initial signal. If K_0 is the (generally unknown) exact number of IMFs, three possibilities may occur when assigning K:

- if $K < K_0$ then mixed modes are produced (i.e., the identified IMFs have components with different frequencies). In this case, each instantaneous central frequency tends to fluctuate instead of being constant;
- if $K > K_0$ then the signal is over-decomposed into redundant IMFs (i.e., the contribution of one mode is split into several IMFs);
- $K = K_0$ the exact number of modes are extracted from the signal.

On the other hand, the penalty factor is a regularization term related to the fidelity of the original signal reconstruction which influences the IMFs bandwidth [123,128] as follows:

- if the value of α is too small, the bandwidth may be overestimated: the smaller α is assumed, the wider the bandwidth of the filter will be. This, in turn, causes the aliasing phenomenon. Further, more background noise and interference components will be included in the frequency range defined by the filter cut-off frequencies;
- if the value of α is too large, then the resulting modes are likely to be distorted thus determining a loss of fidelity in signal reconstruction.

To overcome the VMD parameters selection problem, several studies have been conducted to find the optimal value of these parameters by adopting different procedures. The first attempts were based on finding the optimum value of K neglecting the influence of penalty factor on the decomposition performance: Yang et al. [133] proposed a criterion based on cross-correlation coefficients to estimate adaptively the number of IMFs. Lian et al. [134] estimated the optimal number of modes following an algorithm that combines the effects of several parameters, namely energy loss coefficient, kurtosis and permutation entropy. Similarly, Wang et al. [135] proposed an optimization procedure for K which is based on permutation entropy. If the influence between mode number K and the penalty factor α must be considered, a popular strategy to determine them concurrently is based on metaheuristic optimization methods; the effect of the parameters on VMD performance is taken into account considering a suitable fitness function and obtaining the optimum as its extremal point. A metaheuristic optimization algorithm can provide a solution to an optimization problem, especially, in the cases of imperfect information or limited computation capacity [136]. The metaheuristic methods consist of two parts, namely the exploration process, which investigates promising parts of the domain in which the optimum may be reached, and the exploitation process which builds the local search capability around the promising regions. Metaheuristic algorithm can be divided into three classes:

- evolutionary inspired algorithms: these algorithms try to imitate the natural evolution and the rules of the biological world. In the exploration stage, the progress of the search process is started with a randomly generated population which is then evolved over several successive generations. The optimizer of the exploration stage revolves around design parameters that must be random to globally explore the promising solution search space. The most popular examples of this family are Genetic programming and Genetic algorithm [137];
- physics-based algorithms: these algorithms try to imitate real physical phenomena; the most common example is the gravitational search algorithm;
- swarm intelligence algorithms: these algorithms are based on mimicking the social behavior of swarms of creatures in nature. This is the most popular family of algorithms used in metaheuristic optimization problems in recent years. A typical example of this family is particle swarm optimization [138].

However, the optimal couple of parameters obtained from these procedures is highly influenced by the choice of the fitness function and the performance may vary significantly depending on the choice of the specific optimization algorithm. Notably, it is unlikely to find a single algorithm that performs well on most optimization problems, because of the specific circumstances, requirements, constraints and implementation scenarios.

2.3.3 Empirical Wavelet Transform (EWT)

The Empirical Wavelet Transform (EWT) is an adaptive decomposition method proposed by Gilles in 2013 [139]. The method exploits the interpretation of the wavelet decomposition as the application of a filter bank to the signal to be analyzed. The adaptability is attained considering that the filter cut-off frequencies may vary depending on where the information contained in each signal's component spectrum is located in the frequency domain. The segmentation process starts normalizing the signal frequency domain to $[0, \pi]$ and consists of detecting the boundaries of each one of the contiguous frequency partitions, i.e. $[\omega_{n-1}, \omega_n]$ with $n = 1, \ldots, N$, where the assumptions $\omega_0 = 0$ and $\omega_N = \pi$ are made. Moreover, a symmetric transition zone centered in ω_n with width $2\tau_n$ is defined for each filter (see Fig. 2.7). Considering ω_0

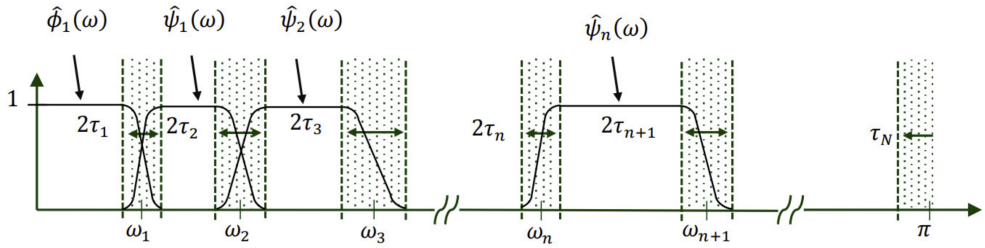

Figure 2.7: Partitioning of the frequency domain (from [140]).

and ω_N fixed values, $N-1$ frequency boundaries must be determined; to do so all the local maxima in the frequency spectrum must be detected and subsequently sorted in descending order. Assuming that M local maximum points are found two possible cases can be considered:

- If $M > N$ only the highest $N-1$ local maxima and the corresponding frequencies $[\Omega_1, \ldots, \Omega_N]$ are kept.
- If $M < N$ the signal has fewer modes than expected, all the maxima and the correspondent frequencies are kept, therefore $M+1$ is assumed as the maximum number of frequency partitions that can be obtained.

The boundaries of each frequency partition are therefore evaluated as follows:

$$\omega_n = \frac{\Omega_{n-1} + \Omega_n}{2} \quad \forall n \in [1, N-1] \tag{2.116}$$

The next step in the procedure consists of the construction of a suitable family of wavelets for the decomposition. The nth empirical wavelet may be interpreted as the

band-pass filter defined on the nth frequency partition. Exploiting this interpretation and following the generation method of Meyer's wavelets [141], a set of piecewise-defined functions is defined as follows: mutually orthogonal trigonometric functions are considered in the transition phases where the boundary frequencies are located and unitary constant value is assumed elsewhere.

The family of wavelets thus generated is made up of an empirical scaling function $\phi_1(\omega)$ and a set of empirical wavelets $\psi_n(\omega)$ having the following analytical form in the frequency domain (referred to as $\hat{\phi}_1(\omega)$ and $\hat{\psi}_n(\omega)$, respectively):

$$\hat{\phi}_1(\omega) = \begin{cases} 1 & \text{if } |\omega| \leq \omega_1 - \tau_1 \\ \cos\left[\frac{\pi}{2}\beta(x)\left(\frac{1}{2\tau_1}(\tau_1 + |\omega| - \omega_1)\right)\right] & \text{if } \omega_1 - \tau_1 \leq |\omega| \leq \omega_1 + \tau_1 \\ 0 & \text{otherwise} \end{cases}$$

$$\hat{\psi}_n(\omega) = \begin{cases} 1 & \text{if } \omega_n + \tau_n \leq |\omega| \leq \omega_{n+1} + \tau_{n+1} \\ \cos\left[\frac{\pi}{2}\beta(x)\left(\frac{1}{2\tau_{n+1}}(\tau_{n+1} + |\omega| - \omega_{n+1})\right)\right] & \text{if } \omega_{n+1} - \tau_{n+1} \leq |\omega| \leq \omega_{n+1} + \tau_{n+1} \\ \sin\left[\frac{\pi}{2}\beta(x)\left(\frac{1}{2\tau_n}(\tau_n + |\omega| - \omega_n)\right)\right] & \text{if } \omega_n - \tau_n \leq |\omega| \leq \omega_n + \tau_n \\ 0 & \text{otherwise} \end{cases} \tag{2.117}$$

where $\beta(x)$ is an arbitrary function that satisfies the following conditions:

$$\beta(x) = \begin{cases} 1 & \text{if } x < 0 \\ 0 & \text{if } x > 1 \end{cases} \qquad \beta(x) + \beta(1-x) = 1 \ \forall x \in [0,1] \tag{2.118}$$

The expression adopted for $\beta(x)$ in this method $\forall x \in [0,1]$ is the following [141]:

$$\beta(x) = x^4(35 - 84x + 70x^2 - 20x^3) \tag{2.119}$$

The parameter τ_n is calculated as follows:

$$\tau_n = \gamma\omega_n \tag{2.120}$$

where γ is a term that avoids the overlap between boundaries of $\hat{\phi}_1(\omega)$ and $\hat{\psi}_n(\omega)$ and it is evaluated as:

$$\gamma = \frac{R-1}{R}\min_n\left(\frac{\omega_{n+1} - \omega_n}{\omega_{n+1} + \omega_n}\right) \tag{2.121}$$

being R the number of discrete samples in the signal. The signal can be therefore decomposed using as a basis the empirical wavelets as follows:

$$\tilde{y}(t) = W_y^{\varepsilon}(0,t) * \phi_1(t) + \sum_{n=1}^{N-1} W_y^{\varepsilon}(n,t) * \psi_n(t) \tag{2.122}$$

where * is the convolution operator and the coefficients $W_y^{\varepsilon}(0,t)$ and $W_y^{\varepsilon}(n,t)$ are called approximation coefficient function and detail coefficient function respectively

and are determined as follows:

$$\begin{aligned} W_y^{\varepsilon}(0,t) &= \mathcal{F}^{-1}\left(\hat{y}(\omega)\hat{\phi}_1(\omega)\right) = \int_{-\omega_1-\tau_1}^{\omega_1+\tau_1} f(\tau)\overline{\phi_1(t-\tau)}d\tau \\ W_y^{\varepsilon}(n,t) &= \int_{-\omega_{n+1}-\tau_{n+1}}^{\tau_n-\omega_n} y(\tau)\overline{\psi_n(t-\tau)}d\tau + \int_{\omega_n-\tau_n}^{\omega_{n+1}+\tau_{n+1}} y(\tau)\overline{\psi_n(t-\tau)}d\tau \end{aligned} \tag{2.123}$$

being $\mathcal{F}^{-1}[\cdot]$ the Inverse Fourier Transform. The decomposed part of the signal may be therefore expressed as follows:

$$\begin{aligned} y_0(t) &= W_y^{\varepsilon}(0,t) * \phi_1(t) \\ y_n(t) &= W_y^{\varepsilon}(n,t) * \psi_n(t) \end{aligned} \tag{2.124}$$

The adaptive partitioning of the Fourier domain significantly influences the decomposition performance; the main shortcoming of EWT is related to the difficult estimation of proper frequency boundaries. This is due to a twofold reason:

1. If the signal to be decomposed is significantly disturbed, i.e. the signal has a low signal-to-noise (SNR) ratio, trivial components may be extracted in the process leading to errors in the detection of modes. Usually in this case, the first decomposed component obtained via EWT is a trivial residue signal: because of this inclusion in the set of modal components, it is difficult to determine without prior knowledge of the signal the exact number of components to be considered in the extraction process. This aspect is especially true in the case of noisy and non-stationary signals [142]: local maximum points produced by the noise and the non-stationary components may be mistakenly considered in the peak selection, thus producing a wrong segmentation (see Fig. 2.8).

2. The transition phase related to each boundary frequency of the filter bank may produce interference between contiguous components, especially in the case of closely spaced modes thus originating mode-mixing phenomena.

A big research effort has been made in the literature to improve the performance of this method. Several works [143, 144] dealt with the problem of noisy signals and the possibility of removing the requirement of a high SNR for the signal to apply EWT; other studies focused on improving the time-frequency representation for non-stationary signals, e.g. by exploiting the Fourier-Bessel series expansion method [145]. Even though some improvements have been achieved, EWT still struggles to overcome the previously mentioned drawbacks.

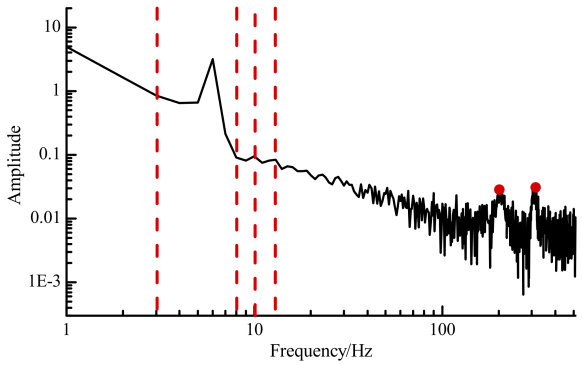

Figure 2.8: Spectrum segmentation of a noisy non-stationary signal (from [142]).

2.3.4 Empirical Fourier Decomposition (EFD)

The EFD technique is an adaptive decomposition method introduced recently by Zhou et al. [146] to overcome the limitations typically recognized in the other methods based on Fourier Transform such as EWT [139] and Fourier Decomposition Method (FDM) [147]. Notably, the EWT performance worsens in the case of noisy signals due to an unexpected signal segmentation, which may affect the estimation of the instantaneous frequencies and select trivial components. Similarly, FDM results have shown to be inconsistent when different frequency scan techniques are adopted to decompose the signal. The EFD technique allows the decomposition of a multi-modal signal into its uni-modal components and consists of two main steps, namely a spectrum segmentation procedure and the construction of a zero-phase filter bank. The segmentation procedure aims at producing N frequency partitions of the frequency spectrum of the signal to be analyzed whereas the zero-phase filter bank is required to perform the actual decomposition.

The segmentation process is carried out within a normalized frequency domain $[0, \pi]$. Therefore, signal frequency lines must be also normalized. Initially, the boundaries of the N contiguous frequency partitions, namely $[\omega_{n-1}, \omega_n]$, are detected. Unlike other decomposition techniques that exploit the spectrum segmentation (e.g., EWT), the frequencies ω_0 and ω_N that define the boundary of the first and last frequency partition are not necessarily equal to 0 and π, respectively. Fourier spectrum magnitudes at 0 and π are evaluated through an adaptive process and are sorted together with other local maxima in decreasing order. The first N frequencies corresponding to the largest maximum magnitudes detected in the signal spectrum are sorted in descending order and are denoted as $\{\Omega_1, ..., \Omega_N\}$. Furthermore, it is assumed $\Omega_0 = 0$ and $\Omega_{N+1} = \pi$. For each pair of consecutive frequencies Ω_n and Ω_{n+1}, the partition is determined by picking the frequency value ω_n at which a global minimum is attained as follows:

$$\omega_n = \begin{cases} \underset{\omega}{\operatorname{argmin}} \hat{X}_n(\omega) & \text{if } 0 \leq n \leq N \text{ and } \Omega_n \neq \Omega_{n+1} \\ \Omega_n & \text{if } 0 \leq n \leq N \text{ and } \Omega_n = \Omega_{n+1} \end{cases} \tag{2.125}$$

where $\hat{X}_n(\omega)$ is the Fourier spectrum amplitude between Ω_n and Ω_{n+1} whereas ω is

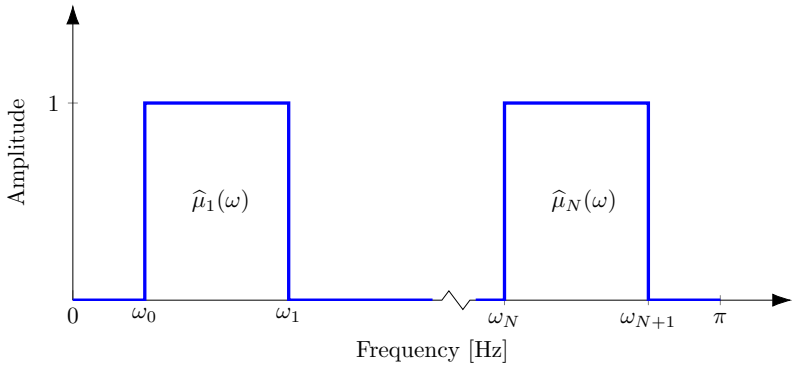

Figure 2.9: Zero-phase filter bank used in the EFD technique.

the frequency variable.

The second step of the procedure consists of the construction of a filter bank to perform the decomposition. Zero-phase filters are considered to avoid possible interference due to their transition phases, which can produce mode-mixing effects. The zero-phase filter bank is designed based on the frequency partitions obtained after the segmentation. Hence, the boundary frequencies of each partition identify the cut-off frequencies. Each zero-phase filter is a bandpass filter with no transition phase operating on a given frequency partition $[\omega_{n-1}, \omega_n]$ with unitary amplitude in the frequency domain (Fig. 2.9):

$$\hat{\mu}_n = \begin{cases} 1 & \text{if } \omega_{n-1} \leq |\omega| \leq \omega_n \\ 0 & \text{otherwise} \end{cases} \tag{2.126}$$

The zero-phase filter retains most of the Fourier spectrum contribution in the given partition and remaining spectral components out of the cut-off frequency range are eliminated. Let $\hat{f}(\omega)$ be the Fourier transform of the signal to be analyzed, the generic filtered component has the following expression:

$$\hat{y}_n(\omega) = \hat{\mu}(\omega)\hat{y}(\omega) = \begin{cases} \hat{y}(\omega) & \text{if } \omega_{n-1} \leq |\omega| \leq \omega_n \\ 0 & \text{otherwise} \end{cases} \quad \forall n \in [1, N] \tag{2.127}$$

The modal component can be expressed in the time domain using the inverse Fourier Transform operator $\mathcal{F}^{-1}[\cdot]$ as follows:

$$y_n(t) = \mathcal{F}^{-1}[\hat{y}_n(\omega)] = \int_{-\omega_n}^{-\omega_{n+1}} \hat{y}_n(\omega) e^{\mathrm{j}\omega t} \mathrm{d}\omega + \int_{\omega_n}^{\omega_{n+1}} \hat{y}_n(\omega) e^{\mathrm{j}\omega t} \mathrm{d}\omega \tag{2.128}$$

where t is the time variable. The reconstructed signal is obtained by simply summing up the extracted components:

$$\tilde{y}(t) = \sum_{n=1}^{N} y_n(t) \tag{2.129}$$

Central frequencies of all the segments are extracted as the frequency values in the Fourier spectrum at which the first N highest local maxima are attained.

2.4 Modal identification via Hilbert transform

The Hilbert transform [76] is a useful tool to gather information in terms of time-frequency content from the modal components once they are extracted from the recorded time series using one of the above-mentioned adaptive decomposition methods. Given a generic signal $y(t)$, the operator Hilbert transform $H[\cdot]$ is defined as the convolution between the signal and $1/\pi t$ with the following expression:

$$\mathcal{H}[y(t)] = y(t) * \frac{1}{\pi t} = \frac{1}{\pi}\text{p.v.}\int_{-\infty}^{\infty} \frac{y(\tau)}{t-\tau} d\tau \tag{2.130}$$

In Eq.(2.130) an improper integral is introduced: the integrand has a singularity and the limits of integration are infinite. Therefore, the actual Hilbert transform is defined considering the Cauchy principal value of the integral in Eq.(2.130) and can be rewritten as follows:

$$\mathcal{H}[y(t)] = \frac{1}{\pi}\lim_{\varepsilon\to 0^+}\left(\int_{t-1/\varepsilon}^{t-\varepsilon} \frac{y(\tau)}{t-\tau} d\tau + \int_{t+\varepsilon}^{t+1/\varepsilon} \frac{y(\tau)}{t-\tau} d\tau\right) \tag{2.131}$$

The Hilbert transform can be interpreted in the frequency domain as an operator which imparts a phase shift of $\pm\pi/2$ radians to every frequency component of a function, the sign of the shift is dependent on the sign of the frequency. The Hilbert transform has also a crucial role in the construction of the signal analytical representation. For a given time series the analytic signal is defined as a complex-valued function with the following form:

$$y^{\text{A}}(t) = y(t) + \text{j}\mathcal{H}[y(t)] = a(t)e^{\text{j}\theta(t)} \tag{2.132}$$

The analytic signal is characterized by a unilateral spectrum with non-negative frequencies only. The use of the analytic signal is based on the consideration that the negative frequency components of the spectrum in a real-valued signal can be neglected without loss of information since it holds the Hermitian symmetry property; moreover, this choice allows easier mathematical manipulations on the signal. The complex exponential term $e^{\text{j}\theta(t)}$ describes the rotation of the complex signal in time, being $\theta(t)$ the phase, whereas the time-varying amplitude is described by the real envelope $a(t)$. Notably, if the change of signal amplitude in time is slow enough, for the Bedrosian's theorem the associated analytic signal possesses the same amplitude function $a(t)$. The instantaneous phase $\theta(t)$ is calculated as:

$$\theta(t) = \arctan\frac{\mathcal{H}[y(t)]}{y(t)} \tag{2.133}$$

The instantaneous frequency is expressed as follows:

$$\omega = \frac{d\theta(t)}{dt} \tag{2.134}$$

whereas the envelope of the instantaneous amplitudes is:

$$\rho(t) = \sqrt{y^2(t) + (\mathcal{H}[y(t)])^2} \tag{2.135}$$

The Hilbert-Huang transform is an effective method to study the dynamic characteristics of a structure with linear behavior [148, 149]. Let $v_k(t)$ be the kth SDOF modal

component extracted using any adaptive decomposition method from the recorded structural response. Assuming that the latter is the result of a free vibration test, the extracted modal components $v_k(t)$ with $k = 1, \ldots, K$ are also free vibration signals which mathematically may be described as follows:

$$v_k(t) = \rho_k e^{-\xi_k \omega_{n,k} t} \cos\left(\omega_{d,k} t + \phi_k\right) \tag{2.136}$$

By applying the Hilbert transform the corresponding analytic signal is:

$$v_k^{\mathrm{A}} = v_k(t) + \mathrm{j}\mathcal{H}[v_k(t)] = a_k(t) e^{\mathrm{j}\theta_k(t)} \tag{2.137}$$

where $a_k(t)$ and $\theta_k(t)$ denote the kth instantaneous amplitude and phase angle, respectively, which have the following form:

$$a_k(t) = \rho_k e^{-\xi_k \omega_{n,k} t} \tag{2.138a}$$

$$\theta_k(t) = \omega_{d,k} t + \phi_k \tag{2.138b}$$

Taking the logarithm of Eq.(2.138a) it holds:

$$\ln a_k(t) = -\xi_k \omega_{n,k} t + \ln \rho_k \tag{2.139}$$

Taking the first derivative of Eq.(2.138b) it holds:

$$\omega_{d,k} = \frac{d\theta_k(t)}{dt} \tag{2.140}$$

Therefore, the kth modal damped frequency can be obtained from Eq.(2.140) as the slope of the phase angle $\theta_k(t)$ versus the time t plot. Furthermore, the value $-\xi_k \omega_{n,k}$ may be obtained from Eq.(2.139) as the slope of the decaying amplitude $\ln a_k(t)$ versus time t plot. Using the linear least-square method the above-mentioned slopes can be computed as parameters that define the corresponding fitting curves. The kth natural frequency $\omega_{n,k}$ and damping ratio ξ_k may be evaluated as follows:

$$\omega_{n,k} = \sqrt{s_{\theta,k}^2 + s_{a,k}^2} \tag{2.141a}$$

$$\xi_k = \sqrt{\frac{s_{a,k}^2}{s_{\theta,k}^2 + s_{a,k}^2}} \tag{2.141b}$$

where $s_{\theta,k}$ and $s_{a,k}$ are the slopes of the phase angle $\theta_k(t)$ and decaying amplitude $\ln a_k(t)$ versus time plot, respectively. For each modal component, it is also possible to represent both instantaneous frequency and amplitude as functions of time in a three-dimensional plot, in which the amplitude can be contoured on the time-frequency plane, providing the Hilbert amplitude spectrum. To plot the correspondent Hilbert spectrum $H_k(\omega, t)$, which provides the localization of the density of energy both in time and frequency, the instantaneous amplitude is replaced by its squared value.

2.5 Damping estimation from free vibration responses

This section presents the most common methods currently available in the scientific literature to estimate the modal damping ratios of a given structure considering that a free vibration response recorded signal is available. The direct exploitation of the decay curve is only valid for the estimation of the structural damping of a single vibration mode, e.g. in the case of SDOF systems or for a structure where the excitation source is strong enough to excite only the first mode. In general, when dealing with MDOF systems, it is necessary an additional data processing step, i.e. filtering, to retrieve the corresponding uni-modal components from the recorded time series. However, in the case of closely spaced modes, a classic filtering process is not enough to extract the correct modal contributions. In these cases, the structural damping must be estimated by adaptive methods, able to handle simultaneously multiple vibration modes. All the methods herein discussed are formulated for SDOF systems and may be subsequently extended to MDOF structures once the uni-modal components are retrieved using the above-mentioned decomposition techniques: the performance in damping estimation is therefore influenced by the decomposition performance of the adopted method for the signal processing.

Half-power bandwidth method

The half-power bandwidth method is one of the simplest procedures for the damping ratio estimation: it has been extensively used for both single-degree-of-freedom (SDOF) and multi-degree-of-freedom (MDOF) structures with linear viscous damping. Consider an SDOF oscillator forced with a harmonic excitation: it is possible to express the displacement response function $\hat{y}(\omega)$ in adimensional form as follows:

$$\hat{y}(\omega) = \frac{1}{\sqrt{(1-r^2)^2 + (2\xi r)^2}} \tag{2.142}$$

being $r = \omega/\omega_n$ the ratio between the generic frequency ω and the system natural frequency ω_n and ξ its damping ratio. The modulus of the response function attained at resonance is $|\hat{y}(\omega_r)| = 1/2\xi\sqrt{1-\xi^2}$; if ξ is small enough (i.e., $\xi \to 0$), the assumption $r \simeq 1$ is valid and it may be simplified as $|\hat{y}(\omega_n)| = 1/2\xi$. This condition is coincident with the estimation of the response function at the natural frequency i.e., $\omega = \omega_n$. The half-power bandwidth method is based on finding two points called half-power frequency points at two frequencies ω_1 and ω_2, close to the response peak with $\omega_1 < \omega_r < \omega_2$, such that the following condition is satisfied (see Fig. 2.10):

$$|\hat{y}(\omega_1)| = |\hat{y}(\omega_2)| = \frac{1}{\sqrt{2}} \cdot \frac{1}{2\xi} \tag{2.143}$$

Enforcing this condition on the response function the following equation is obtained:

$$r^4 - 2(1-2\xi^2)r^2 + (1-8\xi^2) = 0 \tag{2.144}$$

The solution of this equation provides two roots, namely $r_1 = \omega_1/\omega_n$ and $r_2 = \omega_2/\omega_n$, and therefore the two half-power frequency points may be obtained. The damping ratio estimation may be carried out once ω_1, ω_2 and ω_n are known, making proper

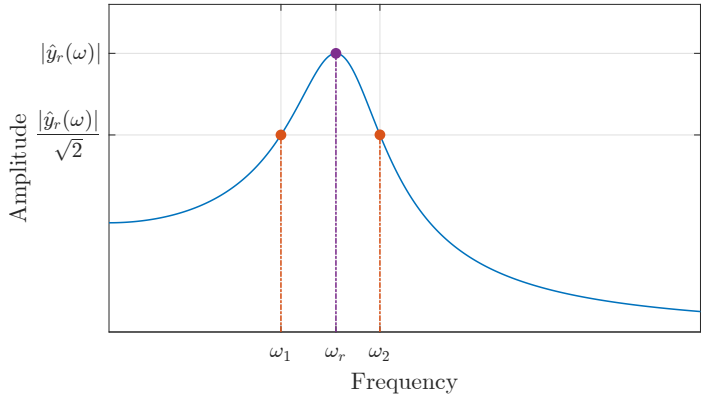

Figure 2.10: The half-power bandwidth method for the estimation of the damping ratio.

assumptions. Depending on the latter, different approximate expressions for the damping ratio may be obtained. The solution of Eq.(2.144) under the conditions of positive real roots, i.e., $\xi < 1/2\sqrt{2} = 0.353$, is:

$$r_i^2 = \left(\frac{\omega_i}{\omega_n}\right)^2 = (1 - 2\xi^2) \pm 2\xi\sqrt{1 + \xi^2} \quad \text{for} \quad i = 1, 2 \tag{2.145}$$

If $\xi \ll 1$ and neglecting higher order terms, the roots assume the following form:

$$r_i^2 = 1 \pm 2\xi \tag{2.146}$$

Using binomial expansion for both roots and summing them up, it holds $r_2 - r_1 = 2\xi$ and therefore:

$$\xi \simeq \frac{\omega_2 - \omega_1}{2\omega_n} \tag{2.147}$$

When the frequency response function is experimentally or numerically obtained the damping ratio can be calculated using the frequency peak $\omega_r = \omega_n\sqrt{1 - 2\xi^2}$. Similarly to the previous case, the following relation holds:

$$\frac{\omega_2 - \omega_1}{\omega_r} \simeq \frac{2\xi}{\sqrt{1 - 2\xi^2}} \tag{2.148}$$

and for small values of ξ it follows:

$$\xi \simeq \frac{\omega_2 - \omega_1}{2\omega_r} \tag{2.149}$$

Eq.(2.149) is the relation commonly adopted for the damping ratio estimation for the SDOF system. In the case of the MDOF system this approach may be applied if it is guaranteed that the modal frequencies are widely spaced, the structure has a response dominant first mode and $\xi < 0.20$ (i.e., the assumption $\omega_n \simeq \omega_r$ is valid). The accuracy of the estimation provided by Eq.(2.149) decreases if an acceleration frequency response function is adopted instead of a displacement one: in this case, the damping estimations for an MDOF structure are reliable if $\xi \leq 0.15$ [150]. If

the structure presents closely spaced modes, the possible coupling causes the method to fail to provide reliable estimates due to different values assumed by the peak and half power frequencies between the global frequency response and each mode one (see Fig. 2.11). The limitations of applicability of this method to MDOF structures are investigated in [151, 152].

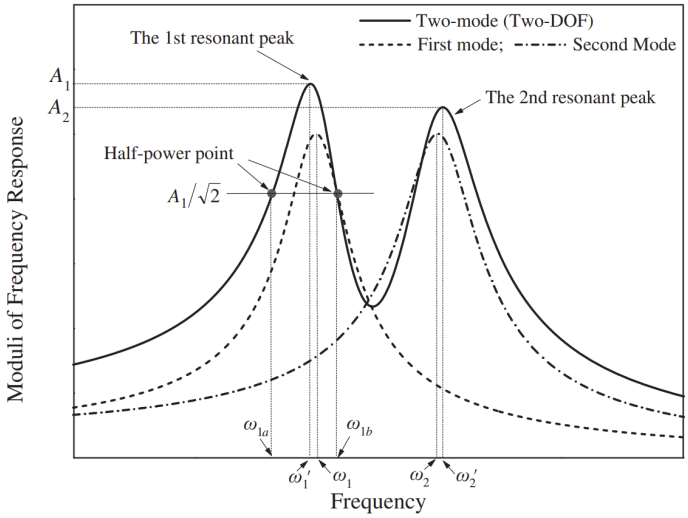

Figure 2.11: Schematic response of a two-DOF system with closely spaced modes (from [152]).

Logarithmic decrement method

The logarithmic decrement method is based on the consideration that for an under-damped linear SDOF system the time response (displacement, velocity or acceleration) is expressed in the form:

$$y(t) = \rho e^{-\xi\omega t} cos(\omega_d t + \theta) \tag{2.150}$$

being ρ and θ the amplitude and phase, dependent on the initial conditions, ω is the natural frequency and $\omega_d = \omega\sqrt{1-\xi^2}$ the corresponding damped frequency and ξ is the damping ratio. The time interval between two adjacent response peaks can be expressed as follows:

$$T_d = \frac{2\pi}{\omega\sqrt{1-\xi^2}} \tag{2.151}$$

and the logarithmic decrement δ may be defined as the natural logarithm of the ratio between two consecutive response peaks (see Fig. 2.12):

$$\delta = \ln\frac{y_n}{y_{n+1}} = \xi\omega T_d \tag{2.152}$$

Combining Eq.(2.151) and Eq.(2.152) the logarithmic decrement assumes the following form:

$$\delta = \frac{2\pi\xi}{\sqrt{1-\xi^2}} \tag{2.153}$$

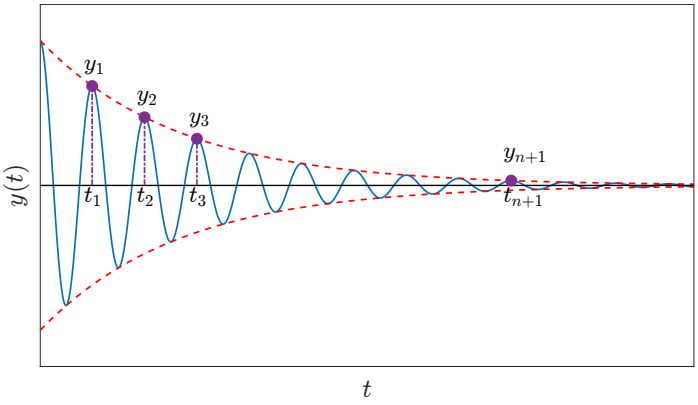

Figure 2.12: Free vibration response for an SDOF system.

which for small values of ξ, i.e., $\sqrt{1-\xi^2} \simeq 1$, may be approximated as follows:

$$\delta = \ln \frac{y_1}{y_2} \simeq 2\pi\xi \tag{2.154}$$

If the first $n+1$ local peaks are considered, the logarithmic decrement may be also expressed as follows:

$$\delta = \frac{1}{n} \ln \frac{y_1}{y_{n+1}} \tag{2.155}$$

where it is exploited the property:

$$\frac{y_1}{y_2} = \frac{y_2}{y_3} = \ldots = \frac{y_n}{y_{n+1}} = e^{\delta} \tag{2.156}$$

For small values of the damping ratio the previous relations provide the same logarithmic decrement (see Fig. 2.13).

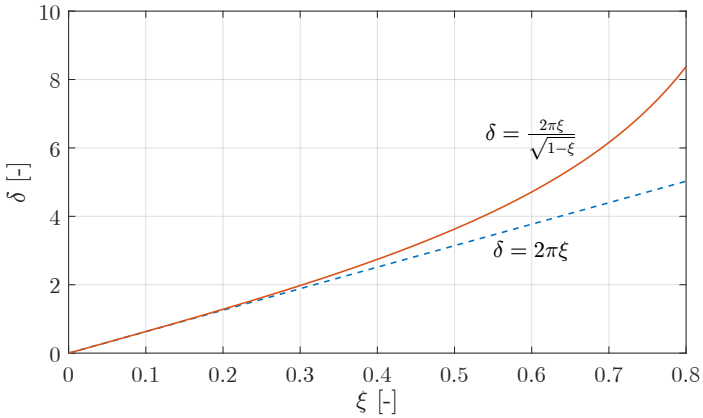

Figure 2.13: Damping ratio versus logarithmic decrement

From Eq.(2.153) and Eq.(2.154) the exact and approximate expressions for the damping ratio may be obtained:

$$\xi = \frac{\delta}{\sqrt{\delta^2 + 4\pi^2}} \tag{2.157a}$$

$$\xi \simeq \frac{\delta}{2\pi} \tag{2.157b}$$

Eq.(2.157) is valid also when a free vibration acceleration recording is considered for the damping ratio estimation; this is particularly useful in the dynamic identification context because the most common type of signal acquired from testing campaigns are accelerations. For MDOF systems, the free response may be expressed as a finite sum of damped modal harmonics functions:

$$y(t) = \sum_{r=1}^{N} \rho_r e^{-\xi_r \omega_r t} \cos\left(\omega_r \sqrt{1-\xi_r^2}\, t + \theta_r\right) \tag{2.158}$$

being ξ_r and $\omega_r\sqrt{1-\xi_r^2}$ the damping ratio and damped modal frequency of the rth mode and N the total number of modes. The logarithmic decrement method may be therefore applied once each mode harmonic signal is isolated. The method becomes less precise when the recorded response is affected by noise: the latter may produce significant local distortion at the peaks thus inhibiting the correct logarithmic decrement estimations.

Area-ratio based damping ratio estimation

This method was introduced by Huang et al. [153]. Consider the time history of the free vibration response of the SDOF system which has the analytic form expressed in Eq.(2.150): suppose that it has $2N+1$ zero-crossing points at the discrete time instants $t_1, t_2, \ldots, t_{2N+1}$ and $2N$ areas enclosed by it and the time axis, namely $A_1, A_2, \ldots, A_N$ (see Fig. 2.14).

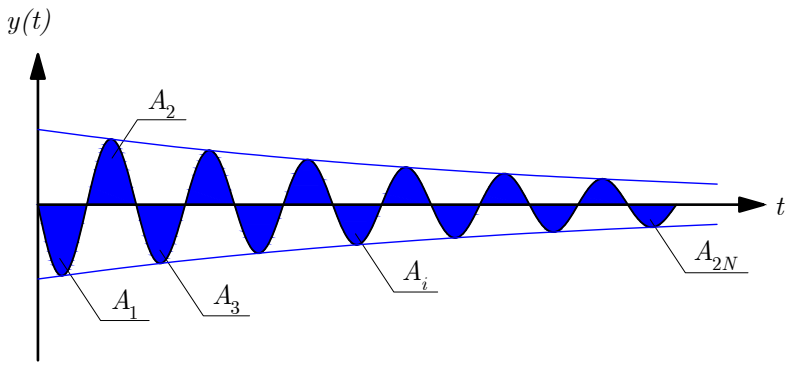

Figure 2.14: Areas enclosed by the SDOF free vibration response.

It is possible to express the first two areas A_1 and A_2 as follows:

$$A_1 = \int_0^{\frac{T_d}{2}} |u(t+t_1)|dt = \rho e^{-\xi\omega t_1} \int_0^{\frac{T_d}{2}} |e^{-\xi\omega t} \sin(\omega_d t + \theta + \omega_d t_1)|dt \tag{2.159a}$$

$$A_2 = \int_0^{\frac{T_d}{2}} \left| u\left(t + t_1 + \frac{T_d}{2}\right) \right| dt = \rho e^{-\xi\omega t_1} e^{-\xi\omega\frac{T_d}{2}} \int_0^{\frac{T_d}{2}} |e^{-\xi\omega t} \sin\left(\omega_d t + \theta + \omega_d t_1\right)| dt \tag{2.159b}$$

Combining Eq.(2.159a) and Eq.(2.159b) it holds:

$$A_2 = A_1 e^{-\xi\omega\frac{T_d}{2}} \tag{2.160}$$

and similarly:

$$A_{2N} = A_{2N+1} e^{-\xi\omega\frac{T_d}{2}} \tag{2.161}$$

Therefore the following ratio between the sum of the N odd-numbered areas and the sum of the N even-numbered areas can be written as follows:

$$R_1 = \frac{A_1 + A_3 + \ldots + A_{2N-1}}{A_2 + A_4 + \ldots + A_{2N}} = \frac{A_1 + A_3 + \ldots + A_{2N-1}}{(A_1 + A_3 + \ldots + A_{2N-1}) e^{-\xi\omega\frac{T_d}{2}}} = e^{\pi\xi/\sqrt{1-\xi^2}} \tag{2.162}$$

Taking natural logarithm to the base e to both sides of Eq.(2.162), the damping ratio may be expressed as:

$$\xi = \frac{1}{\sqrt{1 + \left(\frac{\pi}{R_1}\right)^2}} \tag{2.163}$$

Alternatively, the following ratio between the sum of the first N areas and the sum of the second N areas can be written as follows:

$$R_2 = \frac{A_1 + A_2 + \ldots + A_N}{A_{N+1} + A_{N+2} + \ldots + A_{2N}} = \frac{A_1 + A_2 + \ldots + A_N}{(A_1 + A_2 + \ldots + A_N) e^{-\xi\omega N T_d}} = e^{2N\pi\xi/\sqrt{1-\xi^2}} \tag{2.164}$$

The damping ratio can therefore be written as follows:

$$\xi = \frac{1}{\sqrt{1 + \left(\frac{2N\pi}{R_2}\right)^2}} \tag{2.165}$$

This area ratio-based damping identification method turns out to be very robust to the noise as demonstrated in [30]. To extend this method to MDOF structures, it is required the correct extraction of the SDOF modal contribution from the recorded signal, which may be achieved using any decomposition technique.

CHAPTER 3

BRIDGES DYNAMIC IDENTIFICATION BASED ON FREE VIBRATION RESPONSE AND VARIATIONAL MODE DECOMPOSITION TECHNIQUE

3.1 Introductory remarks

The easy access to sensing devices and data acquisition technologies facilitated the large diffusion of dense monitoring systems that can permanently record the dynamic response of critical buildings and infrastructures under serviceability conditions. The processing of the recorded data allows to assess the structure integrity over time through the estimation of the modal parameters in serviceability conditions. The latter are closely related to the physical properties of the structure such as mass, stiffness and energy dissipation, and their variation over time may be used as a tool for damage detection. Further, the estimation of modal frequencies, damping ratios and mode shapes play a crucial role in structural model updating [12] and diagnostic [23].

Specifically, when ambient vibrations are processed for output-only modal analysis, operational modal analysis (OMA) techniques are adopted. The applicability of these methodologies, already introduced in Chapter 2, is vastly documented in the literature for bridge dynamic identification purposes. In this context, in [154] and [155] is discussed the performance of the most common OMA approaches for the modal identification of suspension and cable-stayed bridges, whereas similar considerations are done in [156] for a PC post-tensioned bridge. A comparative analysis of OMA methods with application to real structures is also carried out in [157] and [158]. Whelan et al. [159] exploit OMA for the health monitoring of a highway bridge excited by vehicular traffic and ambient conditions; a comparison between FDD and SSI techniques is carried out showing that the latter allows the extraction of more mode shapes with higher accuracy. Hong et al. [160] study the effect of the wind on the response of an existing suspension bridge performing the identification of its dynamic characteristics by processing field measurements with data-driven SSI; the information is used to update a FE model that shows accurate predictions of the wind response. Ubertini et al. [161] propose a robust automated modal identification procedure based on SSI methods and clustering analysis and discuss its application for the dynamic identification of a historic iron arch bridge and a long-span footbridge. In [102, 162, 163] the application of EFDD to bridge structures for the estimation of modal damping ratios is discussed, showing that the poor frequency resolution of the data as well as the presence of closely spaced modes influence the performance of the method leading to their overestimation. Castellanos-Toro et al. [164] estimate modal frequencies of a vast variety of structures including vehicular, pedestrian and railway bridges using ambient

vibration tests processed via OMA. Specifically, data are recorded using smartphones and processed using NExT and SSI techniques, showing that these devices are suitable systems for the modal identification of flexible structures. Lorenzoni et al. [14] analyze five different typologies of road and railway bridges, i.e. steel trusses, steel box, multi-girder reinforced concrete, masonry and reinforced concrete arch bridges, using ambient vibration recordings obtained during a continuous monitoring campaign. The data is processed adopting different OMA identification techniques both in frequency and time domain for the evaluation of the quality of the modal estimates. Further, the influence of structural typologies, length of acquired time histories and ambient noise, loading and environmental effects on the dynamic identification are addressed. Rainieri et al. [10] discuss about dynamic identification of several bridge structures highlighting the capability of vibration-based techniques in combination with OMA in supporting the design and management of bridge structures. Specifically, SSI and EFDD methods are adopted in this paper for the FE model validation, the formulation of empirical relations for the fundamental frequency estimation of RC arch bridges and for vibration serviceability assessment of pedestrian bridges. Further, automatic OMA procedures for the bridge continuous monitoring are reviewed, remarking on their attractiveness for full-scale bridge application. Zini et al. [165] analyze the signal recorded during a dynamic test campaign performed on a short-span RC bridge with half-joints in Italy adopting SSI-COV and RD technique; the study specifically aims at investigating the quality of modal damping ratio estimates accounting for the minimum signal length to identify unbiased damping, the effects of the properties of the signals and the dependency from the vibration amplitude.

However, continuous monitoring may not always be a feasible solution since the installation and maintenance cost of the sensors is justified only in the case of large structures. Nonetheless, the need to collect information on dynamic behavior also exists in the case of less important structures that can only be monitored sporadically due to economic, technical or practical limitations. In this sense, monitoring via free vibration tests is a suitable solution since it can be carried out using a limited number of sensors, temporarily installed on the examined structure, whose required sensitivity is lower in comparison with the case of environmental vibrations. These aspects, combined with the limited amount of time required to perform the tests, make free vibration tests an economic and rapid solution. Even though free vibration responses tend to rapidly decay in most real cases, the measured response amplitude will be higher than the ambient vibrations counterpart since an actual initial perturbation is introduced in the structure; this allows obtaining more accurate estimates of the modal parameters which are less affected by the noise. Depending on how the free response is induced and/or which component of the bridge is tested, it might require a temporary closure of the infrastructure and the corresponding authorization by deputed authorities. To deal with these practical issues, free vibration tests can be arranged together with other activities that require a temporary bridge closure, such as exceptional maintenance or retrofitting interventions, static tests, or inspections following accidental extreme events.

There are numerous cases documented in the literature related to the dynamic identification of structures by free vibration tests. In this regard, Clemente et al. [166] as well as Tomaszkiewicz and Owerko [167] assess the modal parameters of cable-stayed bridges exploiting the free vibrations produced by a heavy truck driving over a

bar placed on the paving. Further, Huang et al. [168] use the impulsive excitation due to the sudden braking of a truck traveling along an inclined direction to test under free vibrations an arch bridge and identify its modal features. Miyashita and Nagai [169] estimate the modal damping ratio of a glass footbridge via a single wireless accelerometer mounted at the deck midspan. Li et al. [170] identify the modal damping ratios of the cables within a cable-stayed bridge from their free vibration response. Quaranta et al. [171] estimate the modal damping ratios of a prototype composite glubam-steel truss bridge from the free vibration response induced by removing suddenly a mass suspended at the midspan of the bottom chord.

Commonly, damping ratio estimation is one of the most complex tasks in the dynamic characterization of structures since a significant scattering is generally observed in its values if alternative testing methods and identification techniques are adopted [27]. In this context, the logarithmic decrement technique results by far the most common method currently used for damping identification when free vibration responses are considered [167, 169–171]. Despite the well-known limitations, improvements to this method continue to be developed. For example, Tomaszkiewicz and Owerko [167] exploit nonlinear regression methods to reduce the detrimental effect of noise, whereas Little and Mann [172] propose an analytical relation for the optimal selection of the number of periods to be used in the logarithmic decrement method. Further, in the case of multi-modal signals, it is required the use of band-pass filters to isolate all the detectable modes and subsequently apply to them the logarithmic decrement technique [167, 171, 173]. In this regard, Nakutis and Kaškonas [174] highlight that the construction of the filters is a non-trivial task that largely depends on the filter parameters selected by the user, thus preventing the use of logarithmic decrement in an automatic fashion. In addition, it is observed in [27] that this approach fails in the case of dynamic responses characterized by closely spaced modes. An alternative approach for damping ratio estimation purposes has been developed by Huang et al. [153] and it is based on the ratio of the areas enclosed by the free response; the main feature of this damping identification approach is its high robustness against noise. The same method has also been investigated by Santoshkumar and Khasawneh [175], who numerically evaluate the optimal number of cycles to be used to minimize the uncertainty in damping estimation. However, similar issues to the logarithmic decrement technique are observed in the case of multi-modal signals since the isolation of the unimodal contribution is still required. To cope with this issue, advanced signal decomposition techniques may be exploited in place of traditional filtering (and its inherent limitations).

Specifically, one of the most effective techniques is the Variational Mode Decomposition (VMD) [125]. Recent studies adopted this method as an extraction tool for signal modal components in the dynamic identification framework, both in experimental models and real structures [130, 131, 176]. However, neither their feasibility nor the impact of the involved control parameters has been ever investigated when estimating the multi-modal damping ratios by means of the area ratio-based method in the framework of automatic modal identification of structures based on free vibration response.

The content of this chapter is based on studies recently conducted by the Author on this topic [30, 177, 178]. Specifically, in Section 3.2 it is presented the proposed approach for the identification of natural frequencies, modal damping ratios and mode

shapes of bridges from the free vibration response. The methodology is based on an automatically tuned version of the variational mode decomposition technique in combination with the area ratio-based damping identification approach. In Section 3.3 the proposed method is validated by assuming a synthetic benchmark signal which includes two closely spaced modes. The performance of the presented approach is critically examined through a comparison with the standard logarithmic decrement technique. Finally, in Section 3.4, three real case studies are examined. The first case-study deals with the complete modal identification of a prestressed concrete girder bridge deck. The second case study is concerned with cables damping identification of a cable-stayed bridge, by also presenting a comparison with damping estimates obtained by alternative techniques based on ambient vibrations. Incidentally, the analysis of the experimental data for this second case study also allowed the quantification of relaxation losses of the stay-cables. Finally, the third case-study exploits the proposed procedure for the dynamic characterization of a series of PC overpasses from an extensive monitoring campaign based on free vibration tests. The peculiarity of these structures resides in the static configuration commonly adopted in the 1970s for overpass construction, which consists of decks with dapped-end girders (Gerber scheme) connected at the abutments through Mesnager hinges. The experimental results are critically compared with numerical previsions of two different FE models considering the investigation of the effects of boundary conditions and material properties on the result performance.

3.2 Variational mode decomposition-based identification

This Section illustrates all the steps of the proposed procedure for the output-only modal identification of civil constructions based on their free vibration response. Although the proposed procedure is general and can be applied to any construction type, the present study is restricted to the dynamic characterization of bridges, where the acquisition of the experimental free vibration response is most common. The methodology exploits a suitable decomposition technique to isolate the modal components of the response and to estimate the corresponding modal frequencies, while the area ratio-based approach is finally implemented to identify the modal damping ratios. The mode shapes identification is also addressed. An important feature of the proposed procedure is that it can be implemented in a fully automatic fashion (i.e., without significant limitations regarding the characteristics of the structures and avoiding subjectiveness in the user's input parameters).

3.2.1 Automatic optimal tuning of the variational mode decomposition technique

The generic structural response to be analyzed is first decomposed in order to extract all embedded relevant components. Among the available techniques for this goal, the Hilbert-Huang transform [76], also known as empirical mode decomposition (EMD), is widely adopted in structural monitoring [179]. The EMD is not supported by a rigorous mathematical derivation and several applications have demonstrated that it is rather sensitive to noise and sampling. These issues motivated the development of several variants of the original EMD technique over the years. An important issue of the EMD technique is its poor reliability in separating close modes, which is a significant limitation for automatic large-scale applications. Taking this into account, in the present work the signal to be analyzed is decomposed by means of the VMD technique [125]. Previous applications of the VMD technique have shown that it is able to extract efficiently the embedded components, largely irrespective of their relative amplitudes and how close they are.

The VMD technique extracts the relevant components from the selected signal $v(t)$ as amplitude-frequency-modulated functions called intrinsic mode functions (IMFs) $v_k(t)$, and also provides the corresponding central frequency ω_k (i.e., the frequency value around which the frequency content of the IMF is concentrated).

An exhaustive description of VMD has been formerly presented in Chapter 2. As already previously mentioned, the performance of the VMD technique is highly dependent on the proper tuning of two main parameters, namely the number of IMFs to be extracted K and the penalty factor α. The other involved parameters (i.e., the convergence threshold ε and the noise tolerance parameter χ) have much less influence.

A rough estimate of the number of IMFs K can be readily achieved considering the number of significant peaks in the Fourier transform of the signal. However, if noise contamination is large or for closely spaced peaks, the choice of K becomes more complex and subjective. Therefore, an automatic procedure for the optimal tuning of K and α is implemented. Given a starting range of possible values for K, i.e. $[K_{\min}, K_{\max}]$, the implemented procedure is based on the consideration that the

higher K is assumed, the narrower each mode bandwidth becomes. Consequently, the central frequencies get closer and modes mixing can happen. Hence, the best value of K is the one that maximizes the distance between each central frequency. This condition can be quantified using the correlation measure. For each value of $\tilde{K} \in [K_{\min}, K_{\max}]$, the correlation between two sampled IMFs $v_k(t_p)$ and $v_{k+1}(t_p)$ (t_p being the sampling time instant) is calculated as follows:

$$\rho_{k,k+1} = \frac{\sum_{p=1}^{P} \left(v_k\left(t_p\right) - \mu_{v_k}\right)\left(v_{k+1}\left(t_p\right) - \mu_{v_{k+1}}\right)}{\sqrt{\sum_{p=1}^{P}\left(v_k\left(t_p\right) - \mu_{v_k}\right)^2}\sqrt{\sum_{p=1}^{P}\left(v_{k+1}\left(t_p\right) - \mu_{v_{k+1}}\right)^2}} \tag{3.1}$$

where μ_{v_k} is the mean value of the kth IMF and P the total number of samples. For each value of α within a starting range $[\alpha_{\text{start}}, \alpha_{\text{end}}]$, the corresponding optimal value of K is determined as follows:

$$K = \underset{K_{\min} \leq \tilde{K} \leq K_{\max}}{\operatorname{argmin}} \left\{ \frac{1}{\tilde{K} - 1} \sum_{k=1}^{\tilde{K}-1} \rho_{k,k+1} \right\} \tag{3.2}$$

and a stabilization diagram is thus obtained by collecting all the couples (α, K). So doing, it is possible to observe that K will assume a stable value within the interval $[\alpha_{\min}, \alpha_{\max}] \subseteq [\alpha_{\text{start}}, \alpha_{\text{end}}]$, which is the sought number of IMFs to adopt in the VMD procedure. Once K is determined, the optimal penalty factor α must be selected. In fact, such value is still unknown and the sensitivity of K with respect to α has been only evaluated so far. Therefore, for each value of $\tilde{\alpha} \in [\alpha_{\min}, \alpha_{\max}]$, two parameters are evaluated for each kth IMF, namely the power spectrum information entropy $\text{PSIE}_k(\tilde{\alpha})$ and the uncorrelation factor $\text{UC}_k(\tilde{\alpha})$. The first parameter is directly proportional to the bandwidth whereas the latter is inversely proportional to the reconstruction performance. These parameters are evaluated as follows [29]:

$$\text{PSIE}_k(\tilde{\alpha}) = -\sum_{\ell=0}^{L} \frac{S_{v_k}\left(\omega_\ell\right)}{\sum_{\ell=0}^{L} S_{v_k}\left(\omega_\ell\right)} \ln\left[\frac{S_{v_k}\left(\omega_\ell\right)}{\sum_{\ell=0}^{L} S_{v_k}\left(\omega_\ell\right)}\right] \tag{3.3}$$

$$\text{UC}_k(\tilde{\alpha}) = 1 - \frac{\sum_{\ell=0}^{L} S_v\left(\omega_\ell\right) S_{v_k}\left(\omega_\ell\right) - \frac{\sum_{\ell=0}^{L} S_v\left(\omega_\ell\right) \sum_{\ell=0}^{L} S_{v_k}\left(\omega_\ell\right)}{L+1}}{\sqrt{\sum_{\ell=0}^{L} S_v^2\left(\omega_\ell\right) - \frac{\left(\sum_{\ell=0}^{L} S_v^2\left(\omega_\ell\right)\right)^2}{L+1}}\sqrt{\sum_{\ell=0}^{L} S_v^2\left(\omega_\ell\right) - \frac{\left(\sum_{\ell=0}^{L} S_{v_k}^2\left(\omega_\ell\right)\right)^2}{L+1}}} \tag{3.4}$$

where S_v and S_{v_k} are the power spectrum of the signal v and that of the kth IMF v_k, respectively (ω_ℓ being the spectral line and L the total number of spectral lines). An average value for these parameters is then evaluated:

$$\overline{\text{PSIE}}(\tilde{\alpha}) = \frac{\sum_{k=1}^{K} \text{PSIE}_k(\tilde{\alpha})}{K} \tag{3.5}$$

$$\overline{\text{UC}}(\tilde{\alpha}) = \frac{\sum_{k=1}^{K} \text{UC}_k(\tilde{\alpha})}{K} \tag{3.6}$$

After the following normalization:

$$\overline{\overline{\text{PSIE}}}(\tilde{\alpha}) = \frac{\overline{\text{PSIE}}(\tilde{\alpha}) - \min_{1 \leq k \leq K} \text{PSIE}_k(\tilde{\alpha})}{\max_{1 \leq k \leq K} \text{PSIE}_k(\tilde{\alpha}) - \min_{1 \leq k \leq K} \text{PSIE}_k(\tilde{\alpha})} \tag{3.7}$$

$$\overline{\overline{\mathrm{UC}}}(\tilde{\alpha}) = \frac{\overline{\mathrm{UC}}(\tilde{\alpha}) - \min_{1\leq k\leq K} \mathrm{UC}_k(\tilde{\alpha})}{\max_{1\leq k\leq K} \mathrm{UC}_k(\tilde{\alpha}) - \min_{1\leq k\leq K} \mathrm{UC}_k(\tilde{\alpha})} \tag{3.8}$$

the optimal value of α is evaluated as follows:

$$\alpha = \underset{\alpha_{\min}\leq\tilde{\alpha}\leq\alpha_{\max}}{\operatorname{argmin}} \left\{ \overline{\overline{\mathrm{PSIE}}}(\tilde{\alpha}) + \overline{\overline{\mathrm{UC}}}(\tilde{\alpha}) \right\} \tag{3.9}$$

3.2.2 Robust damping identification

The modal damping ratio corresponding to each IMF v_k is evaluated by means of the area ratio-based method [153]. To this end, the best result is obtained by processing only the part of the signal v that follows the largest absolute peak value, so as to mitigate the effect of noise and to limit the influence of concurrent vibrations (i.e., ambient excitation). Although the method can be applied to all signals recorded by means of a sensor network, for the same reasons, the best results are expected from the signal that exhibits the largest peak value.

Therefore, assuming that v_k has $2N_k+1$ zero-crossing points, it is possible to detect the $2N_k$ regions enclosed between v_k and the time axis whose areas are denoted as $A_{1,k}, \ldots, A_{i,k}, \ldots, A_{2N,k}$ (see Fig. 3.1). So doing, the damping ratio corresponding to

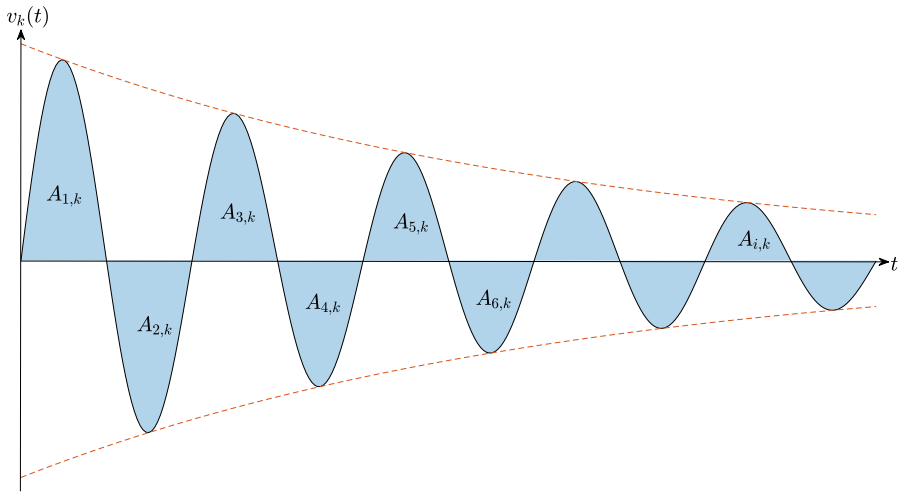

Figure 3.1: Detection of the regions enclosed between the kth IMF and the time axis for the application of the area ratio-based damping identification technique.

v_k is obtained in closed form as follows [153]:

$$\xi_k = \frac{1}{\sqrt{1 + (2N_k\pi/R_k)^2}} \tag{3.10}$$

where

$$R_k = \ln\left[\frac{\sum_{i=1}^{N_k} A_{i,k}}{\sum_{i=N_k+1}^{2N_k} A_{i,k}}\right] \tag{3.11}$$

It is noted that R_k can be numerically evaluated by applying any quadrature method for the estimation of $A_{i,k}$.

This area ratio-based damping identification method turns out to be very robust to the noise. Indeed, in the standard implementation of the logarithmic decrement technique, the accuracy of the damping identification depends on local maxima and minima values of the time history, which may be largely influenced by local fluctuations due to the noise. By using the area values, the detrimental effect of the noise is strongly mitigated. Furthermore, the number of cycles that minimizes the uncertainty in damping estimation can be established following the recommendations by Santoshkumar and Khasawneh [175].

3.2.3 Mode shapes identification

The identification of the mode shapes is based on the elaboration of the free vibration response recorded from all the available sensors [130]. Let t_p^{peak} be the time instant corresponding to a local (maximum or minimum) peak value of the kth IMFs extracted by decomposing the free vibration response recorded from all the sensors in the network (see Fig. 3.2). If $v_k^{(s)}(t_p^{\text{peak}})$ is the local (maximum or minimum) peak value at t_p^{peak}

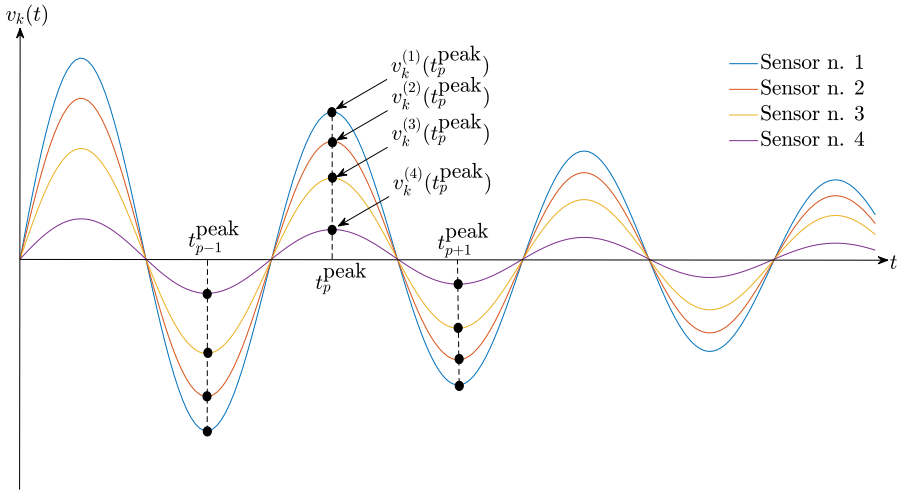

Figure 3.2: Mode shape identification based on the kth IMFs extracted from the free vibration responses recorded at different sensor positions.

of the kth IMF obtained from the sth sensor (S being the total number of sensors in the network), then the kth mode shape vector ϕ_k is expressed as follows:

$$\phi_k = \left\{ v_k^{(1)}(t_p^{\text{peak}}) \quad v_k^{(2)}(t_p^{\text{peak}}) \quad \dots v_k^{(s)}(t_p^{\text{peak}}) \quad \dots v_k^{(S)}(t_p^{\text{peak}}) \right\}^\top \tag{3.12}$$

The normalized mode shape vector is thus obtained as follows:

$$\overline{=}{\phi}_k = \left\{ v_k^{(1)}(t_p^{\text{peak}}) \quad v_k^{(2)}(t_p^{\text{peak}}) \quad \dots v_k^{(s)}(t_p^{\text{peak}}) \quad \dots v_k^{(S)}(t_p^{\text{peak}}) \right\}^\top / \max_{1 \le s \le S} \left| v_k^{(s)}(t_p^{\text{max}}) \right| \tag{3.13}$$

Theoretically, the ratio between the peak values of the kth IMF obtained from a couple of sensors is constant in time. However, noise and/or sampling may distort randomly the peak value of the kth IMF. In order to alleviate this issue, the normalized mode shape vector given by Eq.(3.13) is also calculated for all significant local (maximum or minimum) peaks at $\ldots, t_{p-2}^{\text{peak}}, t_{p-1}^{\text{peak}}, t_{p}^{\text{peak}}, t_{p+1}^{\text{peak}}, t_{p+2}^{\text{peak}}, \ldots$ (see Fig. 3.2), and each component of the mode shape vector is then estimated as the average value of the obtained results.

3.3 Numerical validation

While the robustness against the noise of the area ratio-based damping identification method has been already pointed out for uni-modal applications, the effectiveness of such a technique for multi-modal applications has to be investigated yet. In view of large-scale applications, besides the impact of the automatic tuning of the control parameters involved in the signals decomposition stage, such validation cannot neglect that some resulting modes can be eventually close to each other. As a matter of fact, close modes are not as common, but they sometimes occur in civil structural monitoring applications [180]. Therefore, the present numerical application especially aims at evaluating the effectiveness of the proposed computational framework to deal with automatic modal identification even in the case of close modes.

To this end, the following (noise-free) synthetic signal is considered:

$$\begin{aligned} y(t) = y_1(t) + y_2(t) + y_3(t) = & 10\mathrm{e}^{-0.025\cdot 6\pi t}\sin\left(6\pi t + \frac{\pi}{2}\right) \\ & + 40\mathrm{e}^{-0.040\cdot 34\pi t}\sin\left(34\pi t + 1\right) \\ & + 45\mathrm{e}^{-0.030\cdot 38\pi t}\sin\left(38\pi t + 0.3\pi\right) \end{aligned} \tag{3.14}$$

The adopted expression for the synthetic signal $y(t)$ given by Eq.(3.14) as well as its frequency spectrum in Fig. 3.3 highlight that it embeds three spectral components, two of which are rather close to each other. The proposed computational framework has been thus applied to this synthetic signal, assuming that the optimal values of K and α fall in the ranges $[2, 8]$ and $\left[1, 10^5\right]$, respectively, in agreement with general previous applications of the VMD technique [29, 131, 136, 181–183] (the same ranges will be adopted for the following experimental applications as well). The automatic search for the optimal values of K and α is also reported in Fig. 3.3. The stabilization diagram in Fig. 3.3 shows that the true number of IMFs $K = 3$ has been identified whereas it results $\alpha = 1,538$. Figure 3.4 illustrates the IMFs automatically extracted according to the implemented computational framework and compares them with the theoretical harmonic counterpart $y_i(t)$ (with $i = 1, .., 3$) of the synthetic signal $y(t)$. Results in Tab. 3.1 demonstrate that frequencies and damping ratios associated with the three components of the analyzed synthetic signal are well identified, thereby confirming the correctness of the implemented procedure.

Table 3.2 compares the damping ratio values identified according to the proposed procedure and the estimates obtained by means of the logarithmic decrement technique. According to common practice, band-pass filters are adopted in combination with the logarithmic decrement technique in order to isolate each mode. Herein, Butterworth band-pass filters are designed as follows: cut-off frequencies range equal to

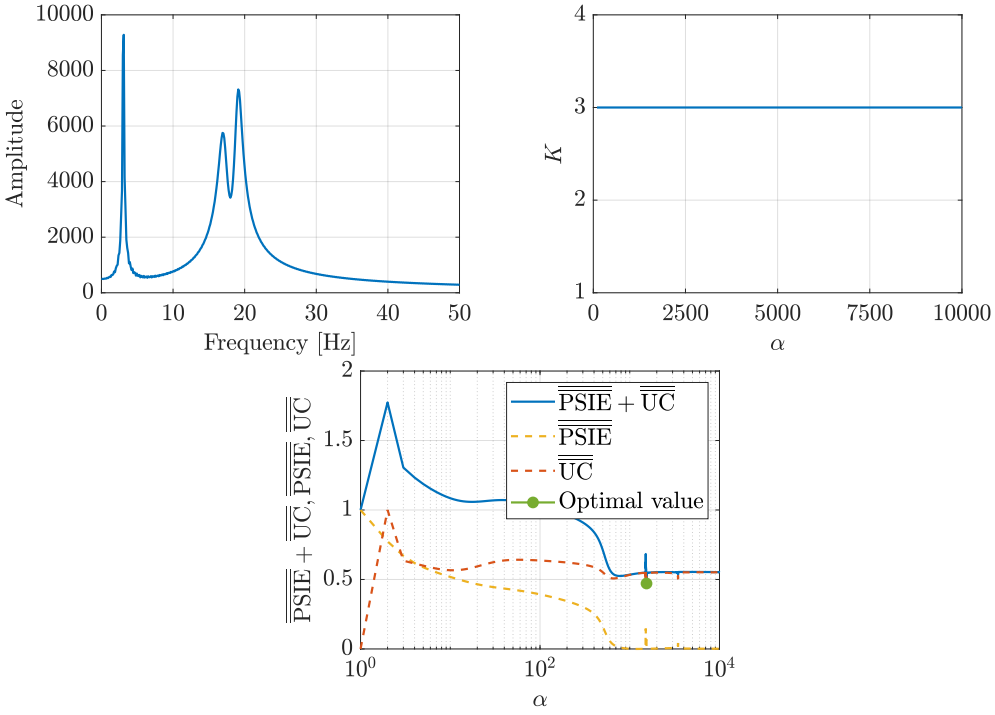

Figure 3.3: Frequency spectrum of the considered synthetic signal (top-left), stabilization diagram related to the automatic identification of the number of IMFs (top-right) and automatic evaluation of the optimal penalty factor (bottom).

Table 3.1: Comparison between estimated and reference values of frequencies and damping ratios for the analyzed synthetic signal.

Mode Number	Frequency [Hz]		Damping [-]	
	Identified	Theoretical	Identified	Theoretical
1	3.24	3	0.0251	0.025
2	16.33	17	0.0402	0.040
3	18.92	19	0.0302	0.030

1-6.5 Hz, 9.2-18 Hz and 18-30 Hz (Case 1); cut-off frequencies equal to ±1 Hz the frequency values corresponding to the peaks in the signal frequency spectrum (Case 2); cut-off frequencies equal to ±2 Hz the frequency values corresponding to the peaks in the signal frequency spectrum (Case 3). Results in Tab. 3.2 confirm that the standard application of the logarithmic decrement technique together with the band-pass filtering for multi-modal damping identification is very sensitive to the filter parameters, as already pointed out by Nakutis and Kaškonas [174]. Additionally, its accuracy performance notably worsens when dealing with closely-spaced modes, as emphasized in previous works [27]. Conversely, Tab. 3.2 demonstrates that the implemented approach leads to the accurate damping ratios identification from multi-modal signals

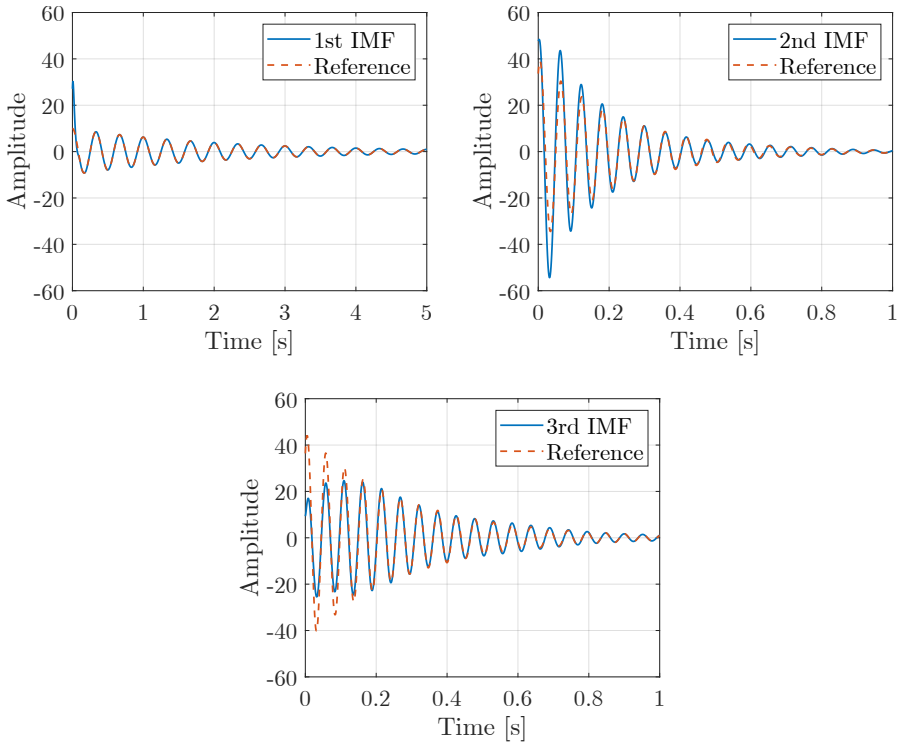

Figure 3.4: IMFs extracted from the synthetic signal compared to reference components of the original multi-modal signal.

even when close modes occur, without requiring any feedback by the user.

Table 3.2: Comparison between estimated and reference values of frequencies and damping ratios for the analyzed synthetic signal.

Mode Number	Logarithmic decrement			This study
	Case 1	Case 2	Case 3	
1	0.025 (1.2%)	0.027 (6.8%)	0.018 (28.0%)	0.025 (0.4%)
2	0.021 (47.3%)	0.041 (3.5%)	0.016 (59.8%)	0.040 (0.5%)
3	0.048 (60.0%)	0.055 (82.0%)	0.029 (2.7%)	0.030 (0.7%)

In the proposed benchmark test, it seems that the identification of the damping ratio is more accurate than the frequency estimation. The reason is twofold: 1) according to the VMD technique, the frequencies are extracted from a numerical optimization problem (in terms of central frequencies) and, consequently, are affected by numerical precision tolerances; 2) the damping affects the signal and represents a disturbing factor of the IMFs' frequency spectra, thus reducing the precision of its peak detection. However, these issues have limited influence on damping ratio identification if the number of areas in the proposed approach is properly increased.

3.4 Experimental applications

The effectiveness of the presented framework for the automatic modal identification of bridges based on free vibration response is now discussed in the present Section with reference to experimental case-studies. They deal with very common applications of free vibration tests on bridges, namely the complete modal identification of bridge decks, the identification of stress and damping of the cables in cable-stayed bridges and the dynamic characterization of a series of overpasses with dapped-end girders. For all the investigated cases, access to the raw data used in the analysis was granted due to past and ongoing technical consultancies and research projects involving the University of Messina and external bodies that deal with structural health monitoring.

3.4.1 Prestressed concrete girder bridge decks of the Longano viaduct

The first case-study deals with the bridge deck of the Longano viaduct (Fig. 3.5). It belongs to the A20 highway connecting the cities of Messina and Palermo in Sicily (Italy), and it is made up of two separate roadways (one for each of the two traffic directions).

Figure 3.5: Overview of the Longano viaduct.

The structural scheme of the bridge deck consists of three simply supported spans. The lateral spans are 29 m long while the central one is 30 m long, thereby resulting a total length equal to 88 m (Fig. 3.6). The deck of each roadway is composed by 4 prestressed concrete I-shaped girders. Their spacing is equal to 2.75 m while their width and height are equal to 0.70 m and 1.65 m, respectively. The girders are structurally collaborating by means of five transverse diaphragms (two near the supports and three along the span) and by an overlying reinforced concrete slab (having thick and width equal to 20 cm and 11 m, respectively). Each girder has 42 pretensioned steel 0.6" strands, of which 10 are inclined through deviators placed 8 m far from the supports whereas the remaining ones are located in the bottom flange (26), in the top flange (4) and in the web (2). The girders are simply supported on neoprene bearings, according to the most common structural scheme adopted in Italy for bridges built in the 1960s-1970s. The abutments have heights equal to 6 m and 7 m, and they are made of reinforced concrete. The piers have circular cross-section with radius equal to 1.10 m. They are 5.5 m and 6 m tall and are made of reinforced concrete with spiral stirrups consisting of Dywidag prestressing bars with a diameter equal to 32 mm.

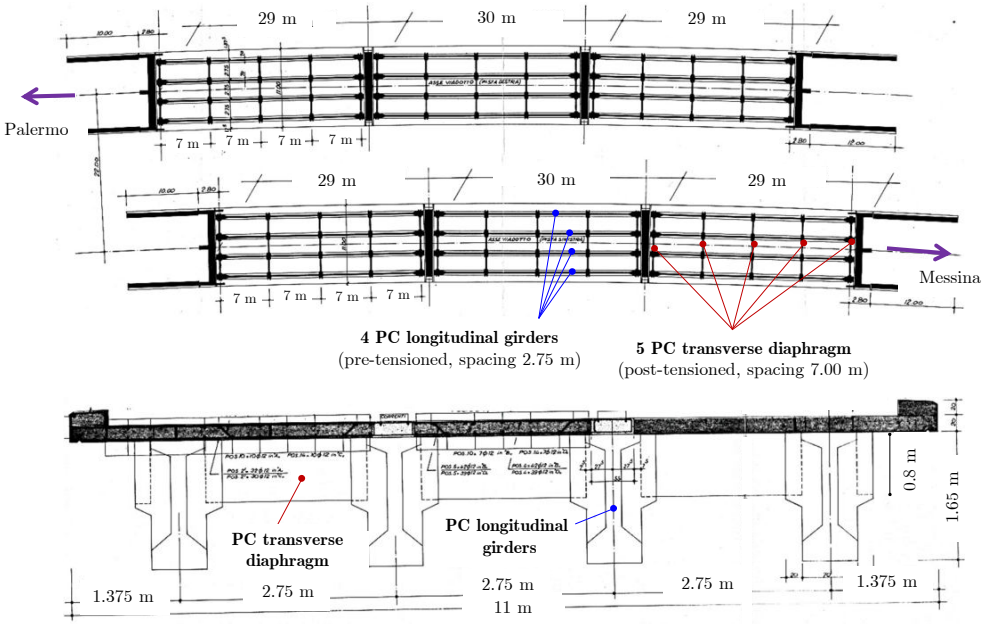

Figure 3.6: Original design drawings of the Longano viaduct: horizontal section of the bridge deck (top) and transverse section of the bridge deck (bottom).

Low-cost free vibration tests were performed on the bridge deck of the Longano viaduct in order to identify its modal parameters [43]. The main goal of this rapid dynamic monitoring campaign was the identification of the bridge damping as well as the validation of a finite element (FE) model of the bridge through the comparison between predicted and estimated natural frequencies and mode shapes. The sensors layout for the tested span is reported in Fig. 3.7. It employs three couples of accelerometers (sensitivity equal to 1 V/g) that were anchored at 1/4, 1/2 and 3/4 of the span length in symmetric positions with respect to the roadway axis. Signal acquisition was conducted with a sampling frequency equal to 1 kHz. Free vibration response was induced by an impulsive load produced by the transit of a three-axle heavy truck with gross weight equal to 347 kN passing on an artificial step having a height equal to 12 cm (Figs. 3.7-3.8). The bridge was closed to vehicular traffic during the tests and the heavy truck crossed multiple times the bridge deck in each road direction with the aim of obtaining multiple recordings to extract reliable results. Figures 3.9 and 3.10 show a selection of the accelerations recorded during free vibration tests and their corresponding frequency spectra in both road directions at different locations on the bridge deck.

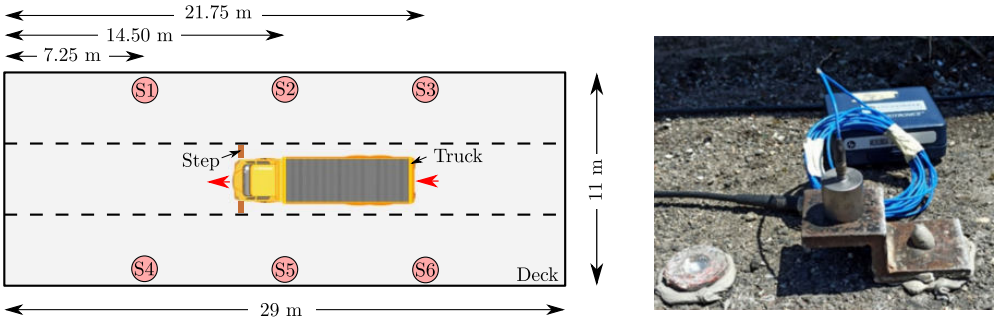

Figure 3.7: Position of the accelerometers S1,. . . ,S6 employed for the dynamic monitoring of the bridge deck (left) and rigid anchorage of the accelerometer (right).

Figure 3.8: Application of an impulsive load by means of the transit of a three-axle truck on a step.

Two distinct series of free vibration tests were performed on each roadway of the structure, one before and another one after the application of a static load. Such static loading test was required in order to check the load-bearing capacity of the bridge deck under the maximum serviceability loads prescribed by the current Italian Technical Code [184], which are different from those at the time of the bridge construction. Specifically, six heavy trucks (with three or four axles), each designated by a unique ID ranging from 1 to 6, were exploited to load the bridge deck during the static testing. Notably, the loads were progressively applied in three stages following a protocol determined prior to the test as shown in Fig. 3.11. The procedure aimed at checking for any signs of cracking or other damage-related occurrences. Performing the dynamic monitoring campaign before and after the static loading tests served to confirm the lack of cracks or any other damage due to application of the static load. Henceforth, the results obtained from the dynamic monitoring campaign performed before and after the application of the static load will be referred to as "pre-static" and "post-static", respectively.

The FE model of the bridge deck is realized with the software SAP2000 [185], using 1D beam elements (6 degrees of freedom per node) with linear material model to describe both prestressed concrete longitudinal girders and transversal diaphragms in serviceability loading conditions. According to previous literature studies [186, 187],

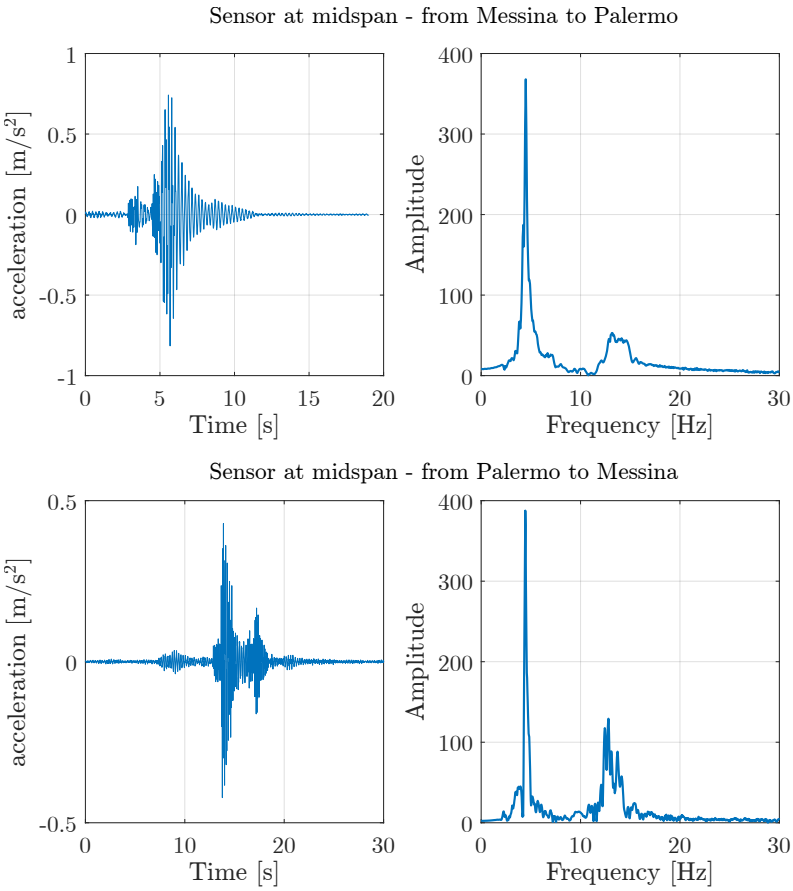

Figure 3.9: Accelerations recorded at midspan during free vibration test on the deck of the roadway from Messina to Palermo and that of the roadway from Palermo to Messina and their corresponding frequency spectra.

the collaborating portion of the overlying reinforced concrete slab (whose effective width b_{eff} is computed according to Eurocode 4 provisions [188]) is included in the cross-sectional characteristics of the girders. Considering the actual simply supported conditions of the bridge deck, ideal pinned restraints are assumed at the two ends of the bridge span, i.e., at the ends of each girder [43]. The membrane stiffening effect produced by transverse diaphragms and overlying slab is simulated through a diaphragm constraint applied to all nodes of the deck. The cross-sectional characteristics of girders and diaphragms are automatically generated through the Section Designer tool integrated in SAP2000 [185]. Mass distribution on the bridge deck includes self-weight of structural elements and dead loads due to road pavement and guardrails. No information about material characterization was available for this structure, therefore design values for concrete of class C35/45 in terms of compressive strength and elastic modulus, i.e. $f_c = 35$ MPa and $E_c = 34625$ MPa, are adopted in the FE model.

The proposed computational framework has been applied to all free vibration responses recorded on the deck before and after the application of the static load. It

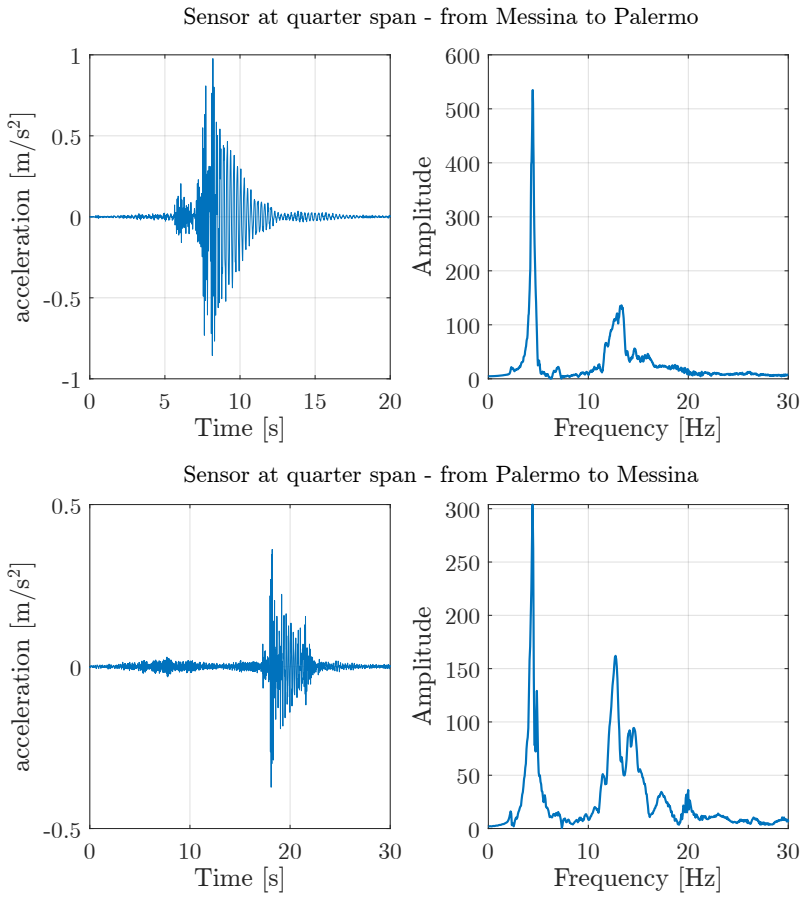

Figure 3.10: Accelerations recorded at quarter span during free vibration test on the deck of the roadway from Messina to Palermo and that of the roadway from Palermo to Messina and their corresponding frequency spectra.

is assumed that the optimal values of K and α fall in the ranges $[2, 8]$ and $\left[1, 10^5\right]$, respectively. As an example, Fig. 3.12 shows the frequency spectra and the automatically extracted IMFs for the free vibration responses recorded on the deck at $1/2$ and $1/4$ of the span length before the static loading test.

Natural frequencies and modal damping ratios identified from the signals recorded by the accelerometers during the free vibration tests performed before and after the static loading test on both roadways are listed in Tab. 3.3 and Tab. 3.4. Tables 3.3 and 3.4 show that the minimal experimental setup allowed the identification of two modes only. The natural frequencies are almost constant, regardless of the considered sensor position and the application of the static load. Specifically, fluctuations of -2.05% and 6.84% are observed for the first two modal frequencies, respectively, from the estimates at midspan following the execution of the static load test; similarly, frequency fluctuations of 1.14% and 1.06% are observed from measurements at the quarter of the span. Modal damping ratios are also fairly constant and their value

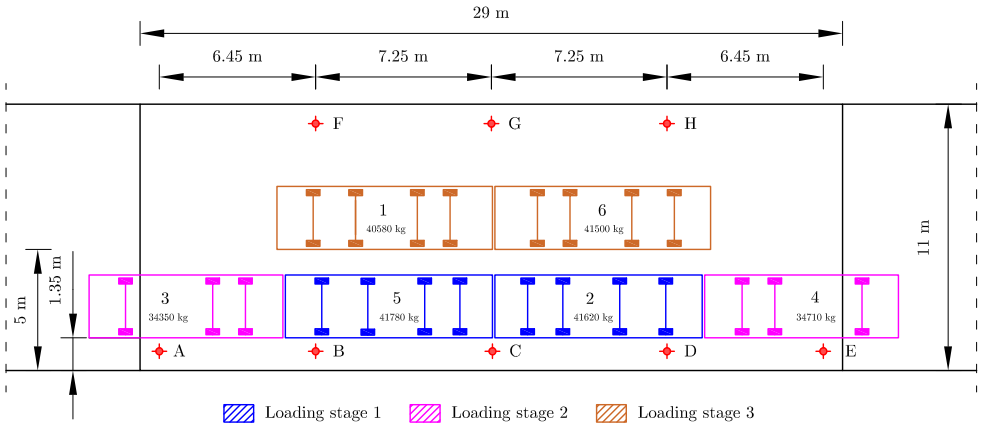

Figure 3.11: Static load tests on the Longano viaduct deck: location of the measurement points of displacement (A-H) and position of heavy trucks in the three loading stages.

is reasonably consistent with the hypothesis of uncracked prestressed concrete cross-section.

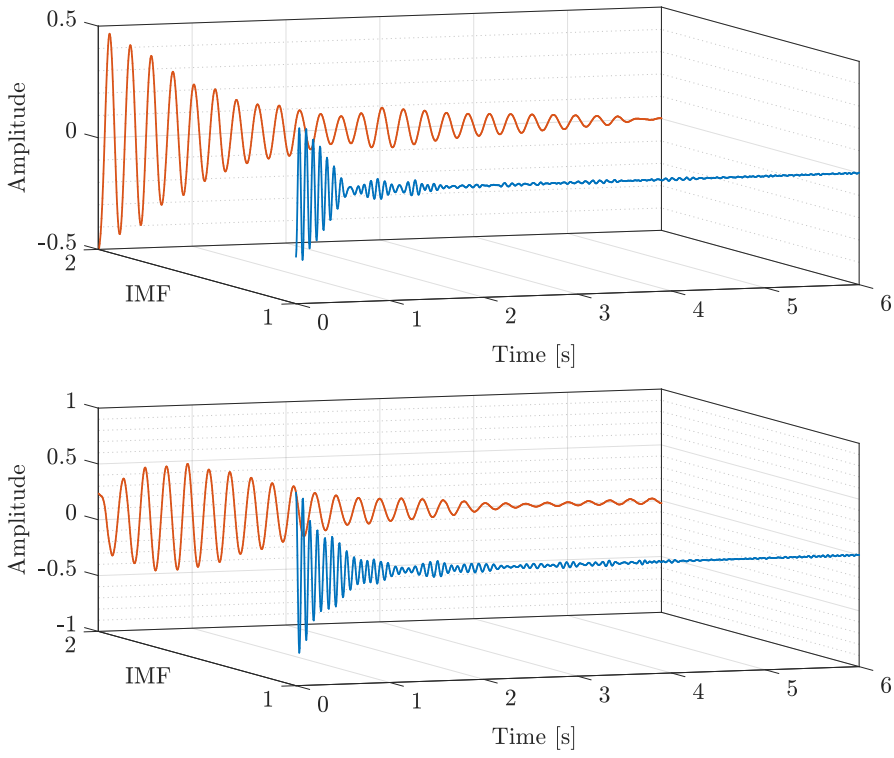

Figure 3.12: Extracted IMFs for the free vibration response recorded on the deck at 1/2 (up) and 1/4 (down) of the span length before the static loading test.

The identified modal damping ratios exhibit a reduced scattering among the different measurements (see also Fig. 3.13).

Table 3.3: Identified natural frequencies and modal damping ratios for the bridge deck along the roadway from Messina to Palermo.

Sensor position	Mode number	Pre-static		Post-static	
		Frequency [Hz]	Damping Ratio [%]	Frequency [Hz]	Damping Ratio [%]
Midspan	1	4.39	3.16	4.48	3.01
	2	13.59	3.43	12.66	2.39
Quarter span	1	4.37	2.85	4.32	3.72
	2	13.17	3.32	13.03	3.59

Table 3.4: Identified natural frequencies and modal damping ratios for the bridge deck along the roadway from Palermo to Messina.

Sensor position	Mode number	Pre-static		Post-static	
		Frequency [Hz]	Damping Ratio [%]	Frequency [Hz]	Damping Ratio [%]
Midspan	1	4.69	2.61	4.49	2.4
	2	13.02	2.67	12.88	2.93
Quarter span	1	4.29	2.86	4.38	2.52
	2	13.55	2.56	12.66	2.36

The estimated modal frequencies are compared to those extracted by peak-picking procedure on the Fourier Transform of the signal, whereas estimated modal damping ratios are compared with the ones obtained with the classic procedure consisting in logarithmic decrement method applied to user-defined band-pass filtered components of the recordings. For this application a 5th order Butterworth band pass filter is adopted. Results listed in Tab. 3.5 show that frequency and damping ratio estimations are consistent with those obtained by means of classic procedures. Finally, Figs. 3.14 and 3.15 as well as Tab. 3.6 show a good agreement between the mode shapes obtained from the numerical FE model of the bridge and the modal displacements identified from the free vibration test before the static loading test.

An objective way to assess the consistency between theoretical and identified mode shapes is the modal assurance criterion (MAC) defined as follows:

$$\mathrm{MAC} = \frac{\left|\sum_{s=1}^{S} \phi_{th,s}\phi_{exp,s}^{*}\right|^{2}}{\sum_{s=1}^{S} \phi_{th,s}\phi_{th,s}^{*} \sum_{s=1}^{S} \phi_{exp,s}\phi_{exp,s}^{*}} \tag{3.15}$$

where S is the total number of sensors in the network, $\phi_{th,s}$ and $\phi_{exp,s}$ are the sth components of the theoretical and experimental mode shape vector, respectively. The higher the similarity between theoretical and experimental mode shapes, the higher

Table 3.5: Comparison of identified modal parameters before static load test in terms of frequencies (VMD vs peak-picking technique) and modal damping ratio (area-based approach vs logarithmic decrement method).

			Frequency [Hz]			Damping Ratio [%]	
Roadway Direction	Sensor position	Mode number	Proposed method	Peak-picking	FEM	Proposed method	Logarithmic decrement
From Messina to Palermo	Midspan	1	4.39	4.48	4.01	3.16	2.85
		2	13.59	13.47	14.11	3.43	3.44
	Quarter span	1	4.37	4.47	4.01	2.85	2.74
		2	13.17	13.11	14.11	3.32	3.41
From Palermo to Messina	Midspan	1	4.69	4.72	4.01	2.61	2.72
		2	13.02	13.10	14.11	2.67	2.57
	Quarter span	1	4.29	4.25	4.01	2.86	2.81
		2	13.55	13.39	14.11	2.56	2.20

MAC factor, which tends to the unity if a perfect correspondence is achieved. Considering the roadway direction from Messina to Palermo, MAC factors of 0.994 and 0.993 are observed for the first and second mode, respectively. Likewise, for the opposite roadway direction (from Palermo to Messina), MAC factors of 0.966 and 0.994 are observed for the first and second mode respectively. Numerical and experimental values of the natural frequencies are also in good agreement. It is noted that the dynamic identification provides very similar results for the two decks of the Longano viaduct. This is consistent with the fact that the bridges have identical structural scheme and age, and also their current conditions are similar. This comparison substantiates the general correctness of the FE model, and the residual difference between numerical and experimental results can be further reduced after suitable model updating.

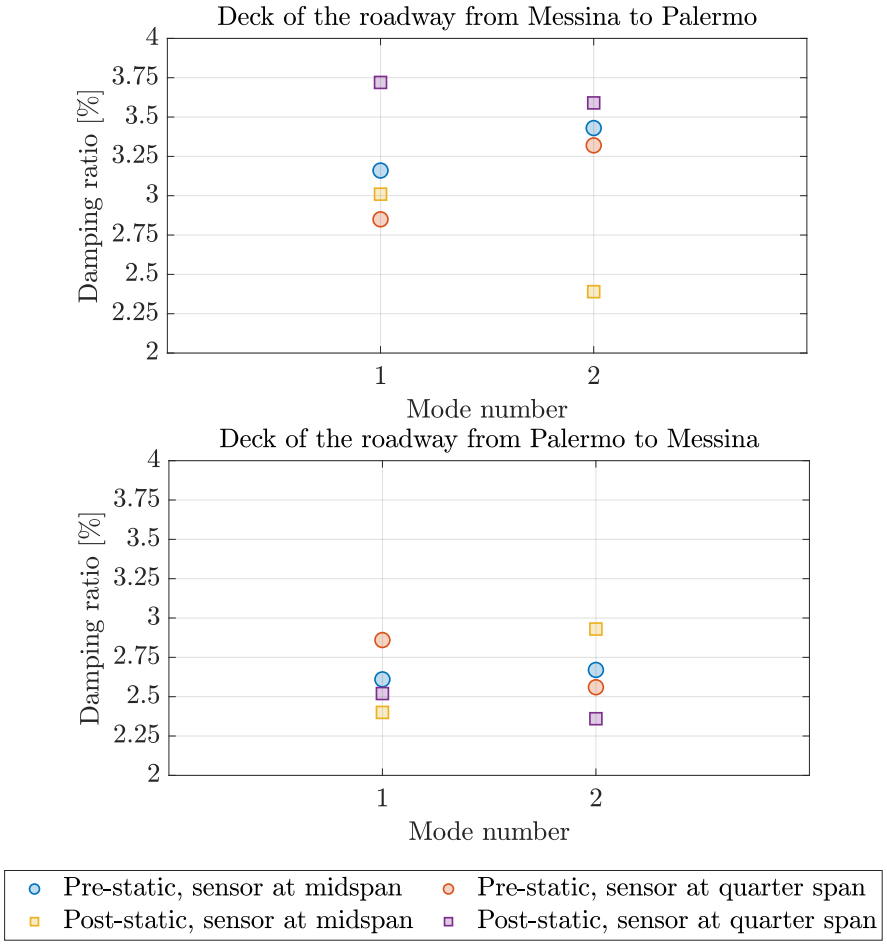

Figure 3.13: Numerical values of the modal damping ratios identified from the free vibration response at different measurement points before and after the static loading test.

Table 3.6: Comparison between numerical mode shapes obtained from a FE model and corresponding modal displacements identified from the free vibration test on the Longano bridge deck fro both roadway direction before the static loading test

	1st mode ($\phi_{1,\mathrm{ID}}$)			2nd mode ($\phi_{2,\mathrm{ID}}$)		
Sensor ID	ME - PA direction	PA - ME direction	FEM	ME - PA direction	PA - ME direction	FEM
S1	-0.66	-0.48	-0.73	0.76	0.72	0.74
S2	-0.89	-0.68	-1.00	0.90	0.92	1.00
S3	-0.73	-0.53	-0.73	0.77	0.79	0.70
S4	-0.58	-0.57	-0.71	0.61	0.63	0.72
S5	-1.00	-1.00	-0.97	1.00	1.00	1.00
S6	-0.70	-0.70	-0.71	0.72	0.74	0.73

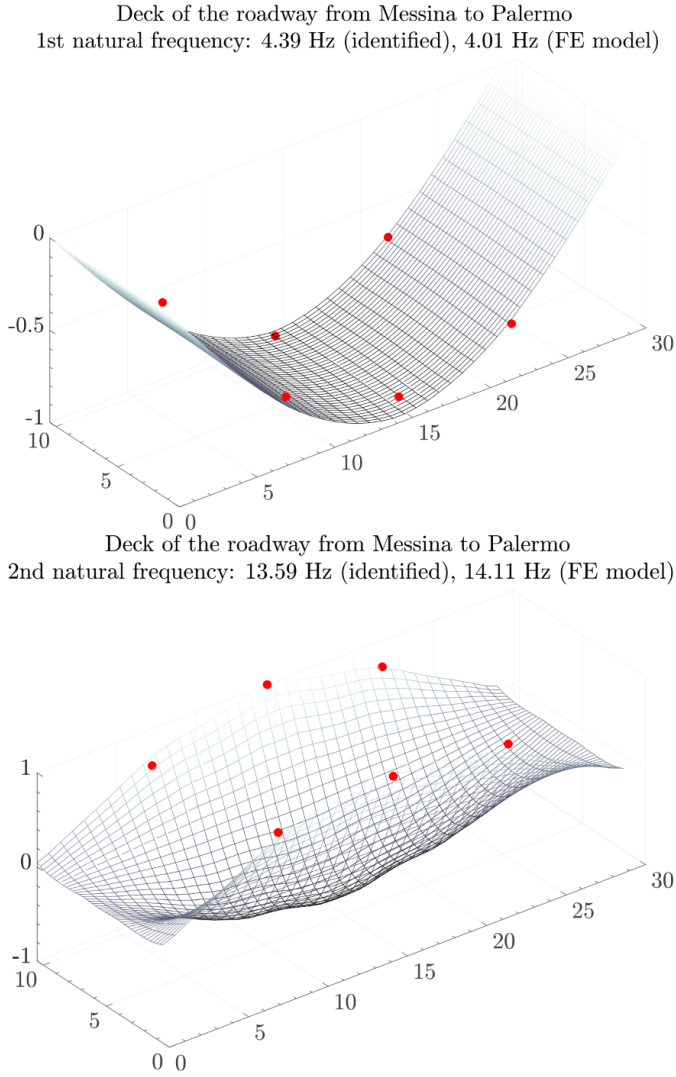

Figure 3.14: Comparison between numerical mode shapes (gray surface) and modal displacements identified from the free vibration test (red dots) on the deck of the roadway from Messina to Palermo before the static loading test.

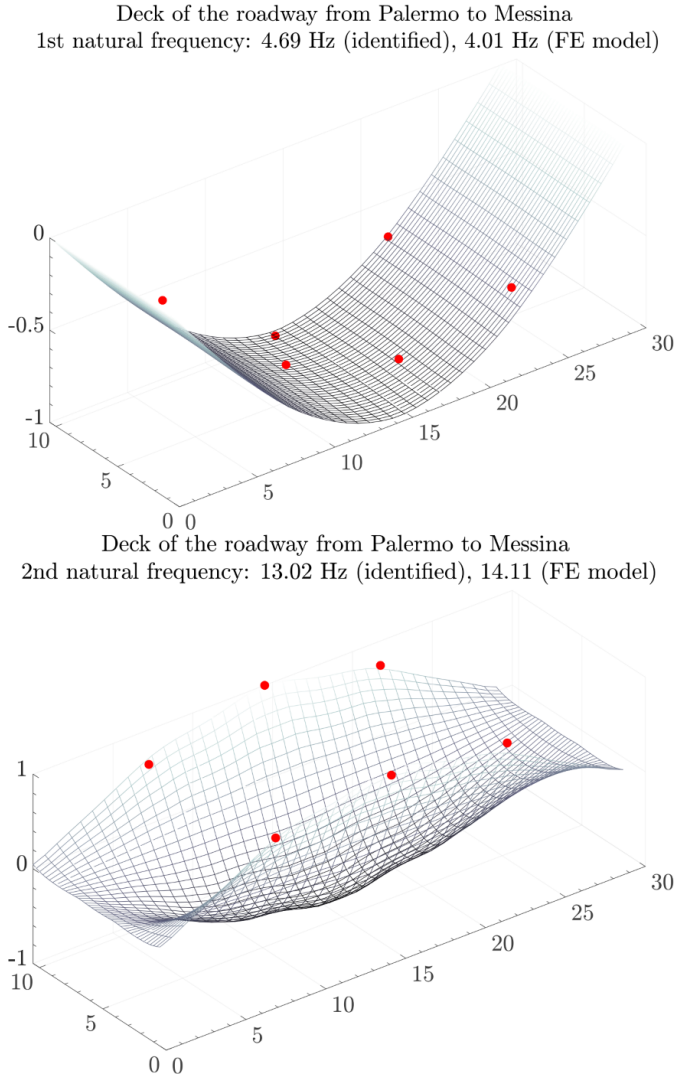

Figure 3.15: Comparison between numerical mode shapes (gray surface) and modal displacements identified from the free vibration test (red dots) on the deck of the roadway from Palermo to Messina before the static loading test.

3.4.2 Cable-stayed bridge over the Garigliano river

The second case-study deals with the cable-stayed bridge over the Garigliano river (Italy), which is part of the highway connecting the cities of Naples and Rome (Fig. 3.16). The bridge was completed on 1993. Its structure has a total length equal to 180 m and is made up of two equal spans. The bridge deck consists of precast, prestressed reinforced concrete multicell block girders with height and width equal to 2.45 m and 26.1 m, respectively.

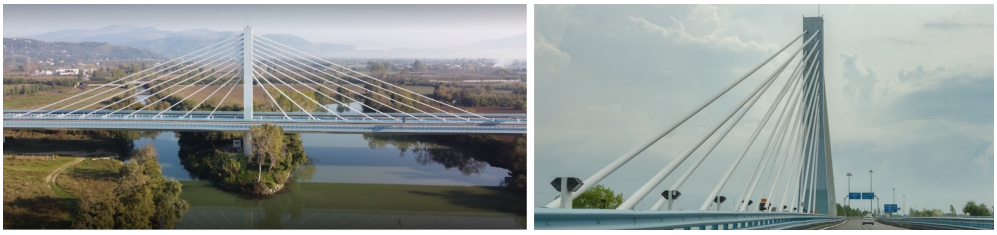

Figure 3.16: Overview of the cable-stayed bridge over the Garigliano river.

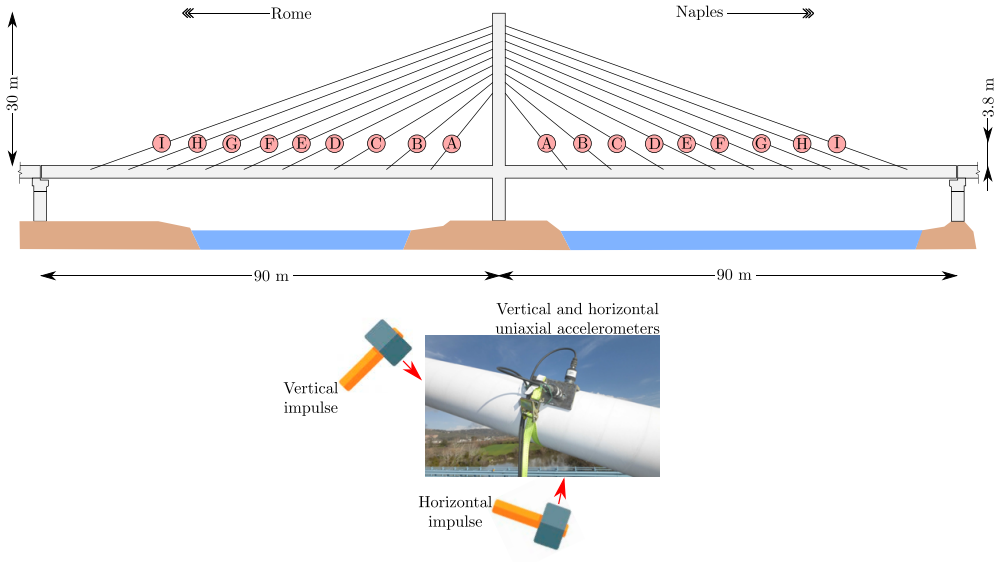

Figure 3.17: Bridge geometry and sensors layout to monitor the dynamic response of the stay-cables under impulse.

The bridge deck includes four prestressing systems. Specifically, three prestressing systems were realized in the longitudinal direction for structural reasons and for assembling the sections, while the fourth one is applied to each precast section along the transverse direction. Each span is simply supported at one end whereas it is constrained to the central pylon on the other end. Furthermore, each span is sustained by 9 couples of cables composed by two parallel elements spaced 1.7 m along the transverse direction. The cables have a variable length (between 23 m and 87.5 m) and

accommodate a variable number of 0.6" galvanized sheathed high-strength prestressing steel strands (between 45 and 55). The pylon is composed of three parts. The first 5 m long segment is made of reinforced concrete and has a linearly variable transverse cross-section (from 4.6 m × 2.5 m to 4 m × 2.5 m). Both second and third segments of the pylon are made of steel. A linearly variable cross-section is adopted up to a height equal to 10 m, where the cross-section has dimensions equal to 2.9 m × 2.5 m. The cross-section is thus constant for the remaining part of the pylon height.

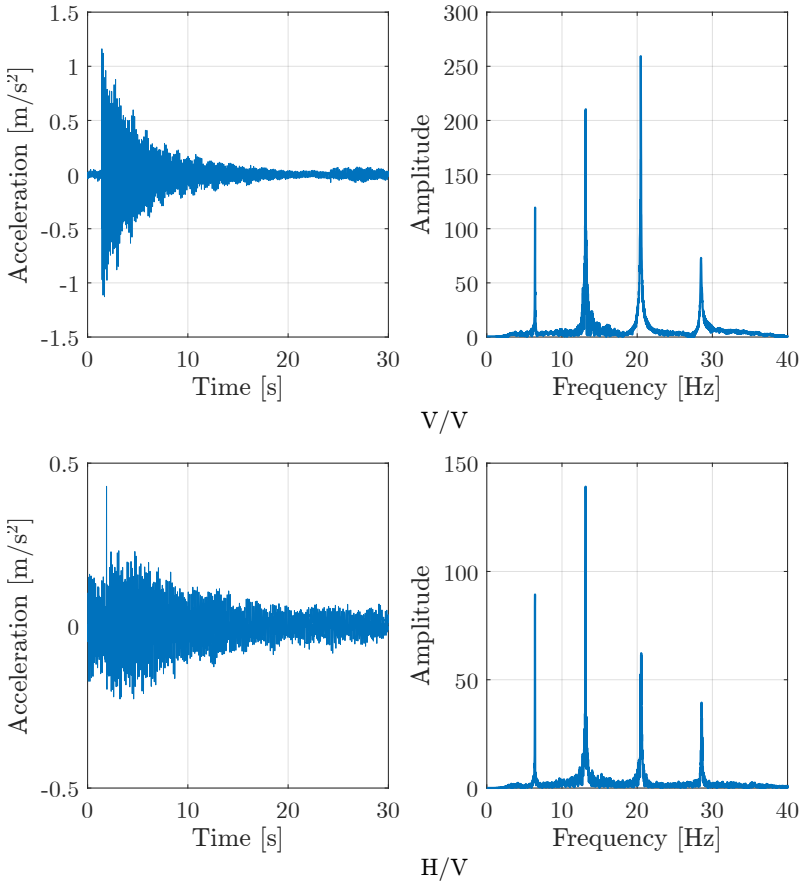

Figure 3.18: Accelerations recorded for the shortest cable on the roadway from Naples to Rome considering different impulse directions and vertical sensor orientations together with corresponding frequency spectra.

This cable-stayed bridge was previously subjected to investigations that mainly focused on the identification of the modal features of deck from its dynamic response under ambient excitation [166,189]. The focus of the present experimental application is on the bridge cables. Because of the large number of stay-cables to be inspected, a campaign of free vibration tests was designed to monitor the cables' condition at low cost and in a short time, with minimal equipment and no inference with the normal operation of the infrastructure. The dynamic response of each stay-cable is recorded by positioning two uniaxial accelerometers (sensitivity 10 V/g) at an average height

equal to 3.8 m from the bridge deck extrados. Each couple of sensors is mounted on the two faces of an L-shaped steel element (Fig. 3.17) in order to acquire both horizontal and vertical accelerations. The steel angle was secured to the stay-cable by means of nylon tightening straps. The dynamic response was recorded with a sampling frequency equal to 200 Hz along the two orthogonal directions under a vertical and horizontal impulse (Fig. 3.17). Henceforth, the labels “V/V" and “V/H" will refer to the results carried out from signals recorded in the vertical and horizontal direction, respectively, under the vertical impulse. Similarly, the labels "H/V" and "H/H" will denote the outputs carried out from signals recorded in the vertical and horizontal direction, respectively, under the horizontal impulse.

Figures 3.18 and 3.19 show a typical set of signals recorded for a cable under different impulse directions and sensor orientations as well as their corresponding frequency spectra. For the sake of conciseness, the dynamic response of the cables on the west side only (along both traffic directions) is discussed in the present study.

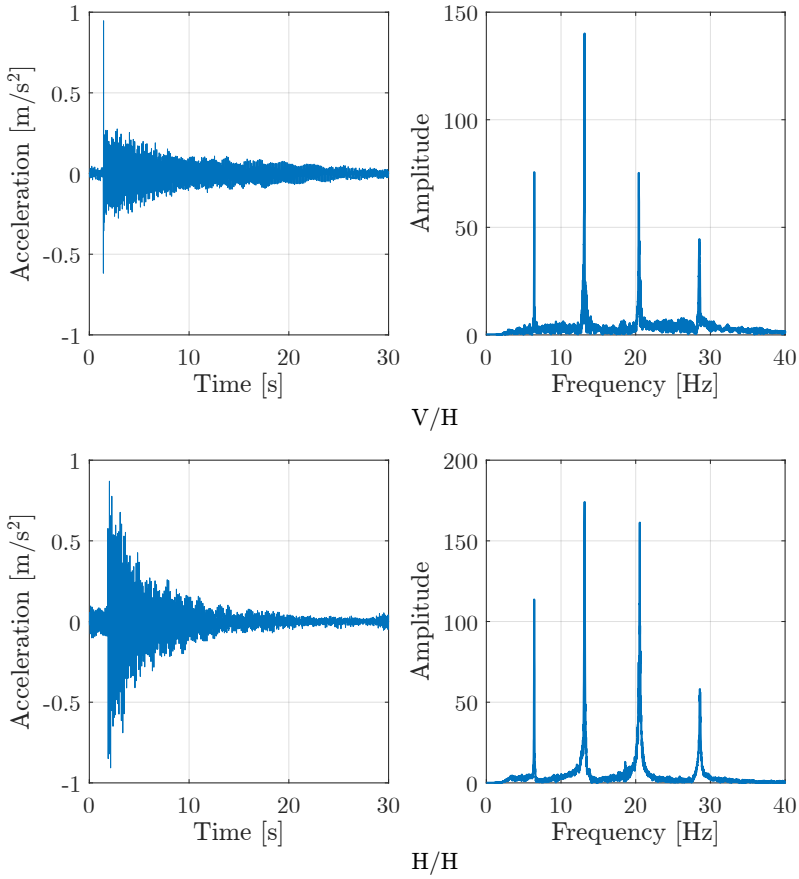

Figure 3.19: Accelerations recorded for the shortest cable on the roadway from Naples to Rome considering different impulse directions and horizontal sensor orientations together with corresponding frequency spectra.

Cables dynamic identification

The proposed computational framework for modal identification based on free vibration response has been applied to all selected signals. It is assumed that the optimal values of K and α fall in the ranges $[2, 8]$ and $\left[1, 10^5\right]$, respectively. As an example, Fig. 3.20 shows the frequency spectrum and the automatically extracted IMFs for the vertical response of the shortest cable on the roadway from Naples to Rome under the vertical impulse.

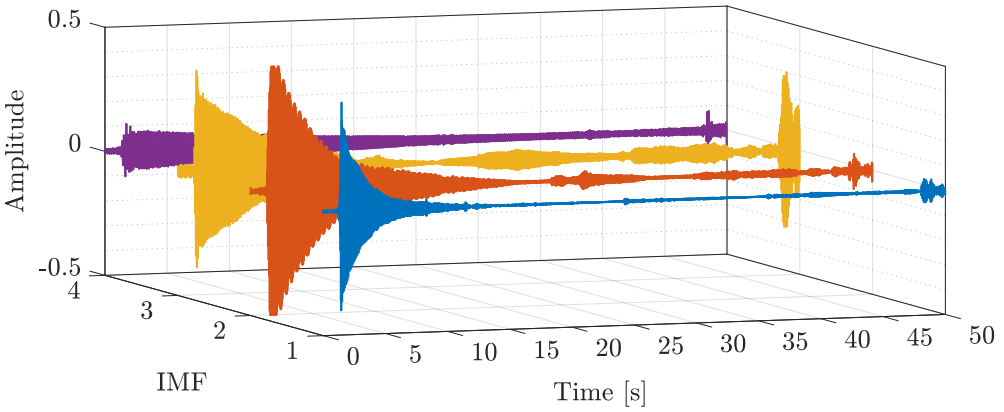

Figure 3.20: Extracted IMFs for the vertical response of the shortest cable on the roadway from Naples to Rome under the vertical impulse.

For each stay-cable, the identified natural frequencies ν_k corresponding to the extracted kth IMF are initially examined in order to estimate the tensile force T by means of alternative formulations. The first relationship is derived from the classical beam theory, and it is an improvement of the simplistic formulation based on the taut string theory. It reads:

$$T = 4ml^2 \left(\frac{\nu_k}{k}\right)^2 - \frac{EJ}{l^2} (k\pi)^2 \tag{3.16}$$

where m and l are mass density and cable length, respectively, whereas EJ is the flexural stiffness of the cable.

Since the underlying simplifications of the beam model may lead to significant errors, two more sophisticated relationships are also considered. One of these more refined formulation is proposed by Zui et al. [190], and it is based on the following two dimensionless parameters:

$$\xi = l\sqrt{\frac{T}{EJ}} \tag{3.17a}$$

$$\Gamma = \frac{0.31\xi + 0.5}{0.31\xi - 0.5}\sqrt{\frac{wl}{128EA\Delta^3 \cos^5 \vartheta}} \tag{3.17b}$$

where w is the cable weight per unit length, EA is the axial stiffness of the cable, ϑ is the cable inclination and Δ is the ratio between sag and cable length. The parameter ξ rules the behavior of the cable: while it behaves like a string for large values of ξ, a beam-like behavior is observed for small values of ξ. The parameter Γ also takes into

account the sag effect: the cable force mainly depends on the first vibrational mode and the effects due to cable sag and inclination are negligible for $\Gamma \geq 3$ while second or higher modes only must be considered otherwise. Therefore, taking ξ and Γ into account, the following formulations apply for $\Gamma \geq 3$:

$$T = \begin{cases} \frac{4w}{g}(\nu_1 l)^2 \left[1 - 2.20\frac{C}{\nu_1} - 0.550\left(\frac{C}{\nu_1}\right)^2\right] & \text{if } \xi \geq 17 \\ \frac{4w}{g}(\nu_1 l)^2 \left[0.865 - 11.6\left(\frac{C}{\nu_1}\right)^2\right] & \text{if } 6 \leq \xi < 17 \\ \frac{4w}{g}(\nu_1 l)^2 \left[0.828 - 10.5\left(\frac{C}{\nu_1}\right)^2\right] & \text{if } 0 \leq \xi < 6 \end{cases} \tag{3.18}$$

while, for $\Gamma < 3$, the following relationships hold:

$$T = \begin{cases} \frac{w}{g}(\nu_2 l)^2 \left[1 - 4.40\frac{C}{\nu_2} - 1.10\left(\frac{C}{\nu_2}\right)^2\right] & \text{if } \xi \geq 60 \\ \frac{w}{g}(\nu_2 l)^2 \left[1.03 - 6.33\frac{C}{\nu_2} - 1.58\left(\frac{C}{\nu_2}\right)^2\right] & \text{if } 17 \leq \xi < 60 \\ \frac{w}{g}(\nu_2 l)^2 \left[0.882 - 85\left(\frac{C}{\nu_2}\right)^2\right] & \text{if } 0 \leq \xi < 17 \end{cases} \tag{3.19}$$

where $C = \sqrt{EJg/(wl)^2}$.

The second refined formulation here considered has been proposed more recently by Fang et al. [191]. In such case, the cable force is related to the natural frequency through the following relationship:

$$T = 4\pi^2 m l^2 \frac{\nu_k}{\gamma_k^2} - \frac{EJ}{l^2}\gamma_k^2 \tag{3.20}$$

where $\gamma_k = k\pi + A\psi_k + B\psi_k^2$, with $\psi_k = \sqrt{EJ/(m\omega_k^2 l^4)}$, $A = -18.9 + 26.2k + 15.1k^2$ and $B = 290$ for $k = 1$ while $B = 0$ for $k \geq 2$. Cables force is calculated assuming an elastic modulus of the prestressing steel equal to 198,000 MPa, whereas the inertia was evaluated considering a quincunx strands configuration into PHED sheaths. The linear weight for the cable was evaluated assuming a linear weight for strands and PHED sheath equal to 1.305 kg/m and 5.68 kg/m, respectively. The density of the grout filling is considered to be equal to 1,440 kg/m^3, and a 95% filling rate is adopted. All relevant cables data are listed in Tab. 3.7. Numerical values of the natural frequency of the stay-cables calculated according to Zui et al. [190] $\nu_{k,\text{Zui et al.}}$ and Fang et al. [191] $\nu_{k,\text{Fang et al.}}$ are listed in Tab. 3.8 (it is pointed out that the parameter Γ by Zui et al. [190] is always much larger than 3, which implies that the cable dynamics mainly depends on the first vibrational mode and the effects due to cable sag and inclination are negligible). Table 3.8 demonstrates that the estimates of the first natural frequency obtained according to Zui et al. [190] and Fang et al. [191] are very close each other. For the first vibrational mode, Fig. 3.21 shows the ratio between the identified natural frequency values $\nu_{k,\text{exp}}$ and those calculated according to Zui et al. [190] $\nu_{k,\text{Zui et al.}}$

Table 3.7: Identified natural frequencies and modal damping ratios for the bridge deck along the roadway from Palermo to Messina.

Stay-cable	Slope [°]	Diameter [mm]	Length [mm]	Area [mm^2]	Inertia [mm^4]	Weight per unit length [N/mm]	Sag-to-cable length ratio
A	50.448	30	17682	6750	15457797	0.979	0.0017
B	38.293	53	25797	6750	15457797	0.979	0.0021
C	30.818	62	34906	8250	19603252	1.071	0.0018
D	26.291	70	44296	8250	19603252	1.071	0.0016
E	24.262	90	51671	8250	19603252	1.071	0.0017
F	22.723	110	59022	8250	19603252	1.071	0.0019
G	21.492	130	66479	8250	19603252	1.071	0.002
H	20.508	155	73921	8250	19603252	1.071	0.0021
I	19.684	230	81456	7050	16839615	0.941	0.0028

and Fang et al. [191] $\nu_{k,\text{Fang et al.}}$. Figures 3.22 and 3.23 show the numerical values of the ratio $\nu_{k,\text{exp}}/\nu_{k,\text{Fang et al.}}$ for higher modes. Missing outputs are due to the fact that either the corresponding mode was not identified or the relevant file is corrupted. It can be observed that there is a very good agreement between experimental and predicted natural frequency values. In particular, predicted values of the natural frequency of the stay-cables are slightly larger than the experimental ones, and the maximum difference is less than 7%.

Table 3.8: Identified natural frequencies and modal damping ratios for the bridge deck along the roadway from Palermo to Messina.

Stay-cable	$\nu_{k,\text{Zui et al.}}$ [Hz]	$\nu_{k,\text{Fang et al.}}$ [Hz]			
	$k=1$	$k=1$	$k=2$	$k=3$	$k=4$
A	6.60	6.68	13.70	21.48	30.33
B	4.32	4.36	8.82	13.52	18.58
C	3.2	3.30	6.65	10.10	13.71
D	2.58	2.59	5.21	7.87	10.60
E	2.21	2.22	4.46	6.71	9.025
F	1.94	1.94	3.90	5.87	7.88
G	1.71	1.72	3.45	5.18	6.94
H	1.53	1.54	3.08	4.63	6.20
I	1.34	1.35	2.70	4.06	5.43

For each stay-cable, the application of the proposed computational framework has allowed the identification of the modal damping ratios from the free vibration response. The results are plotted in Figs. 3.24 and 3.25, where modal damping ratios estimated for each measurement axis and direction of the applied impulsive loads are provided for each stay-cable. Once again, missing results are due to the fact that either the

corresponding mode was not identified or the relevant file is corrupted. For comparison purposes, estimates of modal damping ratios obtained through ambient vibrations on the same cables are reported in Figs. 3.24 and 3.25 by using two methods from the literature, namely the Natural Excitation Technique (NExT) [86] and the Random Decrement Technique (RDT) [92].

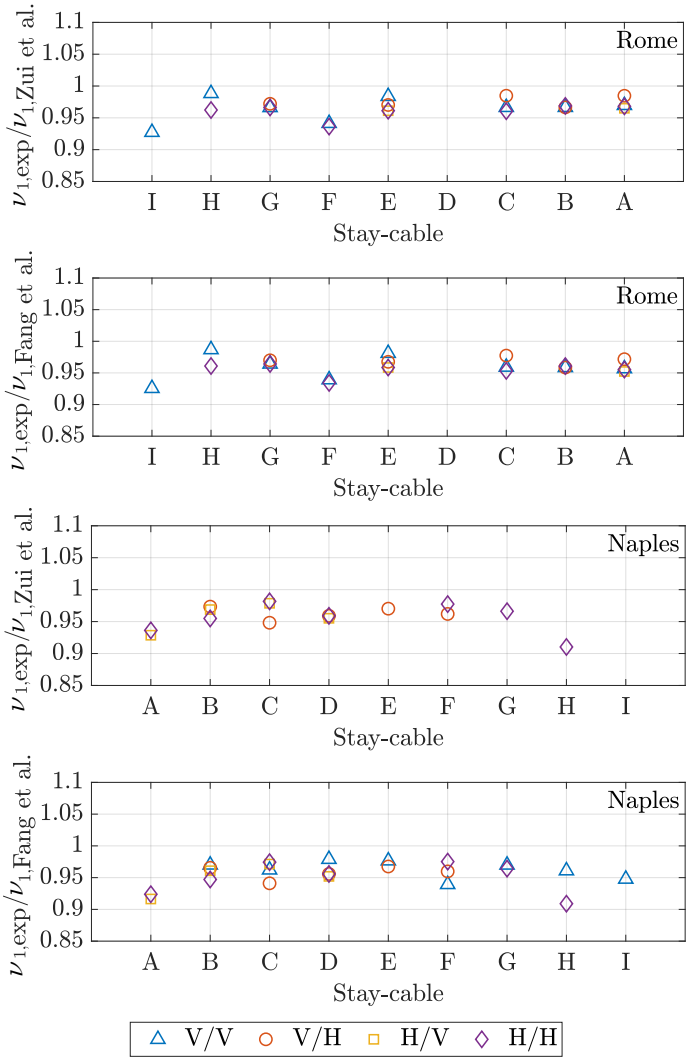

Figure 3.21: Ratio between experimental and predicted natural frequency of the stay-cables for the first vibrational mode.

Figures 3.24 - 3.25 demonstrate that the average value of the modal damping ratio of the stay-cables is almost constant, regardless the mode number. The estimates

obtained from ambient vibrations are slightly higher than those obtained from free vibrations. However, a relatively limited scattering is observed among the different estimates, which slightly increases in some sporadic cases close to the extreme cables characterized by the minimum and maximum frequencies. All damping values fall within the range 0-0.8% in good agreement with previous experimental estimations of the modal damping ratio for the cables of cable-stayed bridges [192]. Based on the results obtained in the two discussed real case-studies, it can be concluded that the proposed method represents a reliable free-vibration-based modal identification tool able to detect reasonable estimates of natural frequencies, mode shapes and damping ratios, and lends itself to an automated implementation with minimal subjectiveness on the parameters' selection.

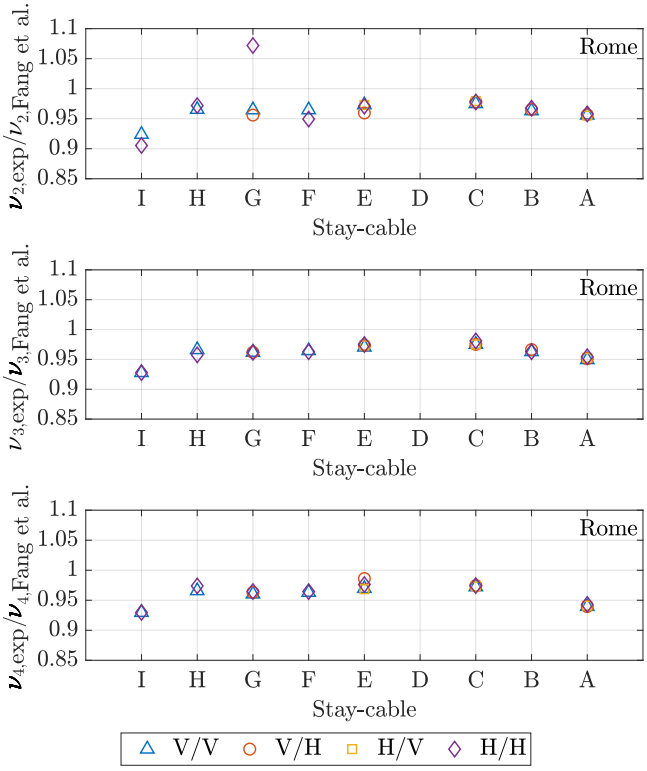

Figure 3.22: Ratio between experimental and predicted natural frequency of the stay-cables for higher vibrational modes (Rome direction).

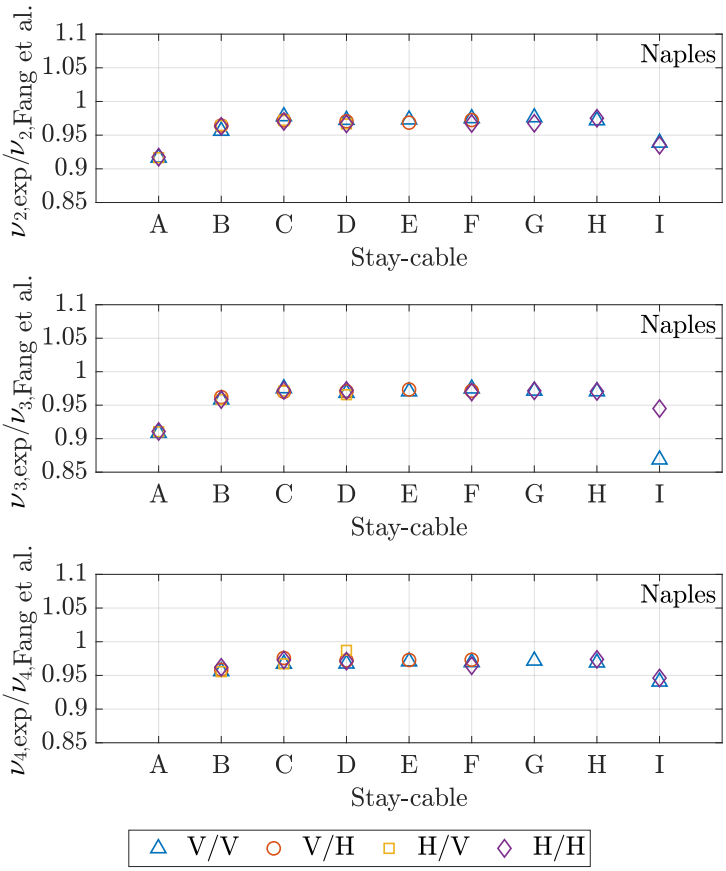

Figure 3.23: Ratio between experimental and predicted natural frequency of the stay-cables for higher vibrational modes (Naples direction).

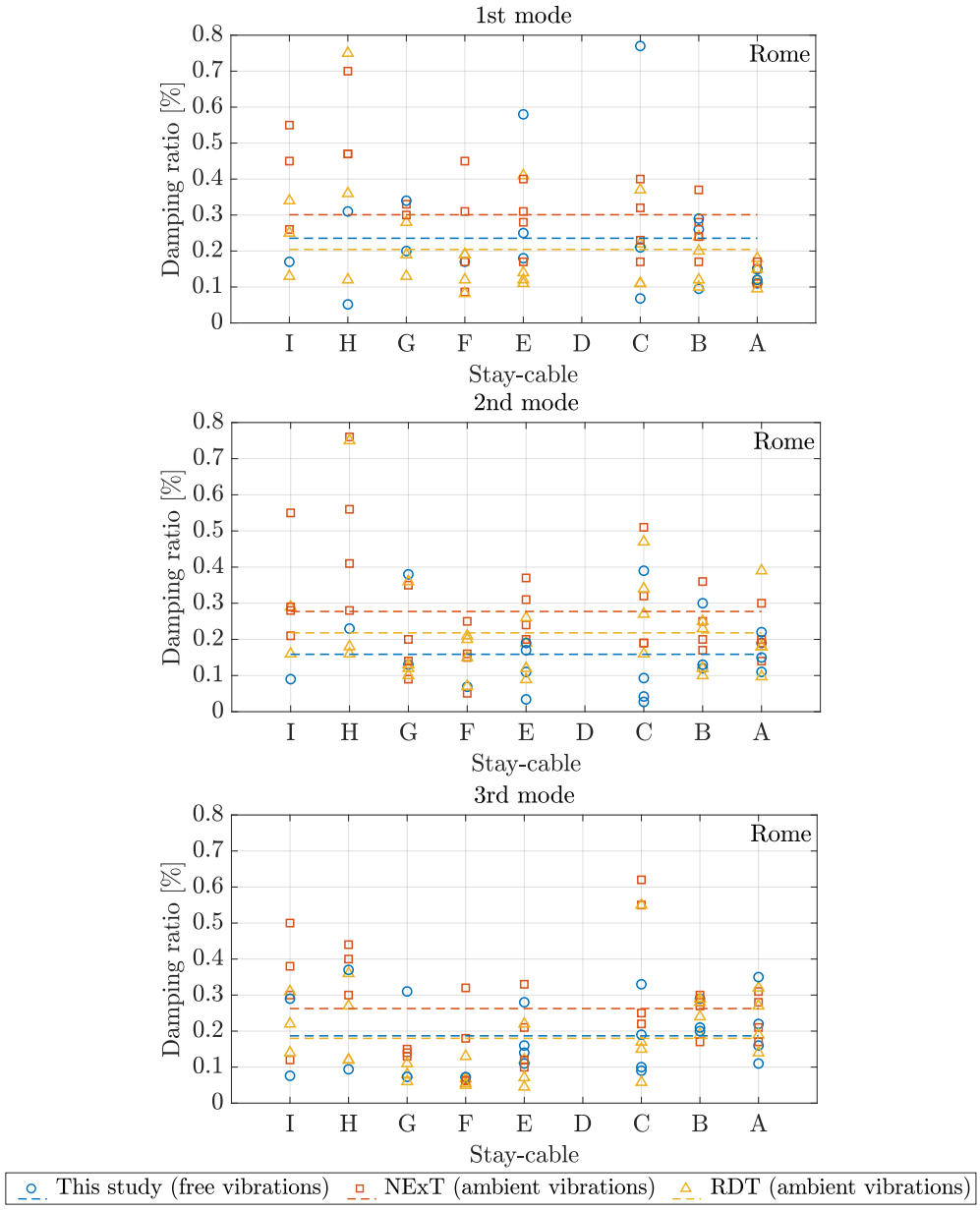

Figure 3.24: Cable modal damping ratios identified under different dynamic loading conditions by means of alternative techniques - Rome direction (the dashed lines denote the average value).

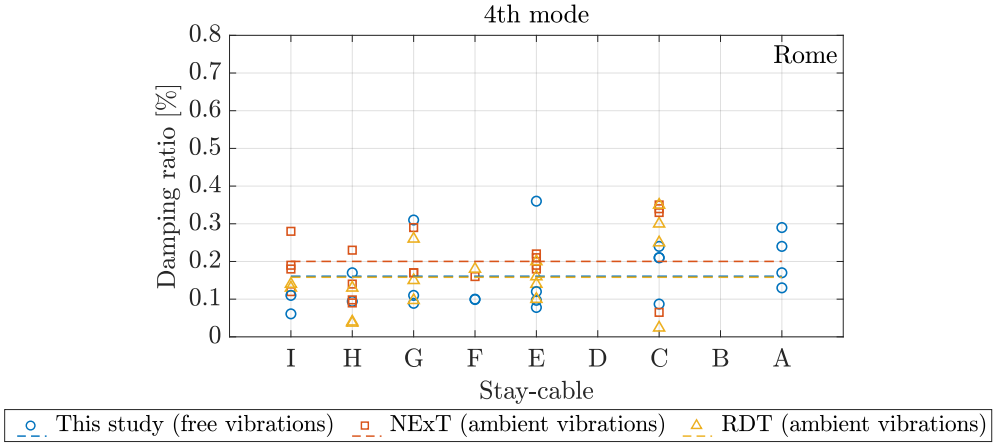

Figure 3.24: Cable modal damping ratios identified under different dynamic loading conditions by means of alternative techniques - Rome direction (the dashed lines denote the average value) (cont).

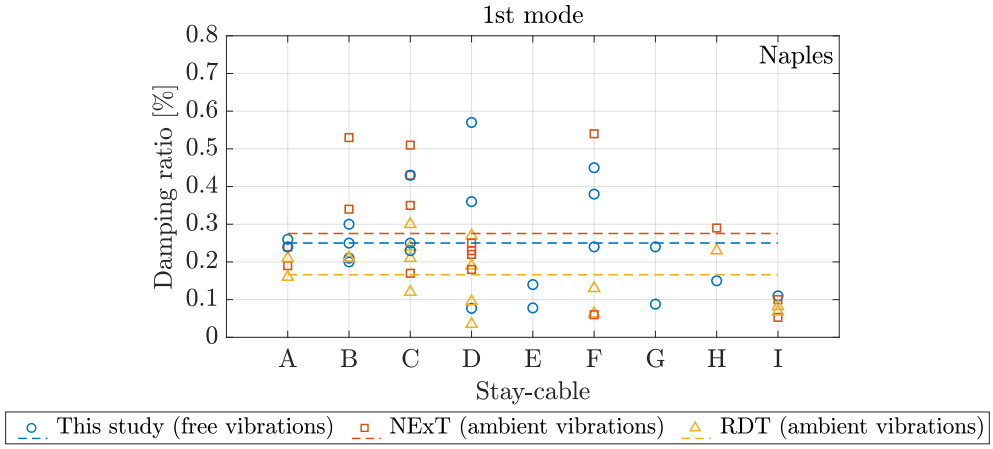

Figure 3.25: Cable modal damping ratios identified under different dynamic loading conditions by means of alternative techniques - Naples direction (the dashed lines denote the average value).

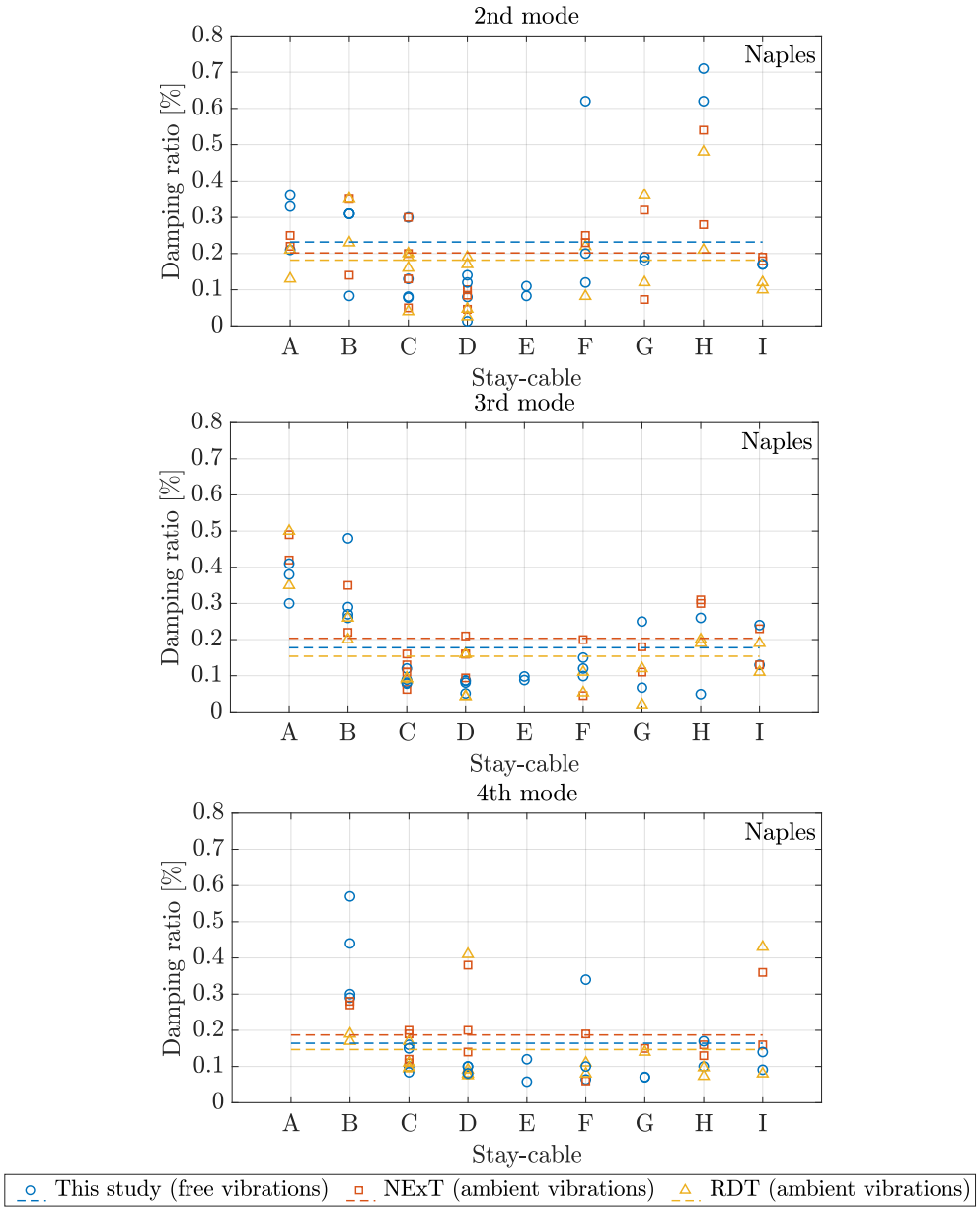

Figure 3.25: Cable modal damping ratios identified under different dynamic loading conditions by means of alternative techniques - Naples direction (the dashed lines denote the average value) (cont).

Cables stress relaxation analysis

Figure 3.26 shows the ratio between estimated cable forces using the above-mentioned models available in the literature and the corresponding values provided in the original design reports. The design range of the cable forces is also highlighted, and it is obtained from the actual design cable force considering all the possible variations due to traffic load and thermal fluctuations.

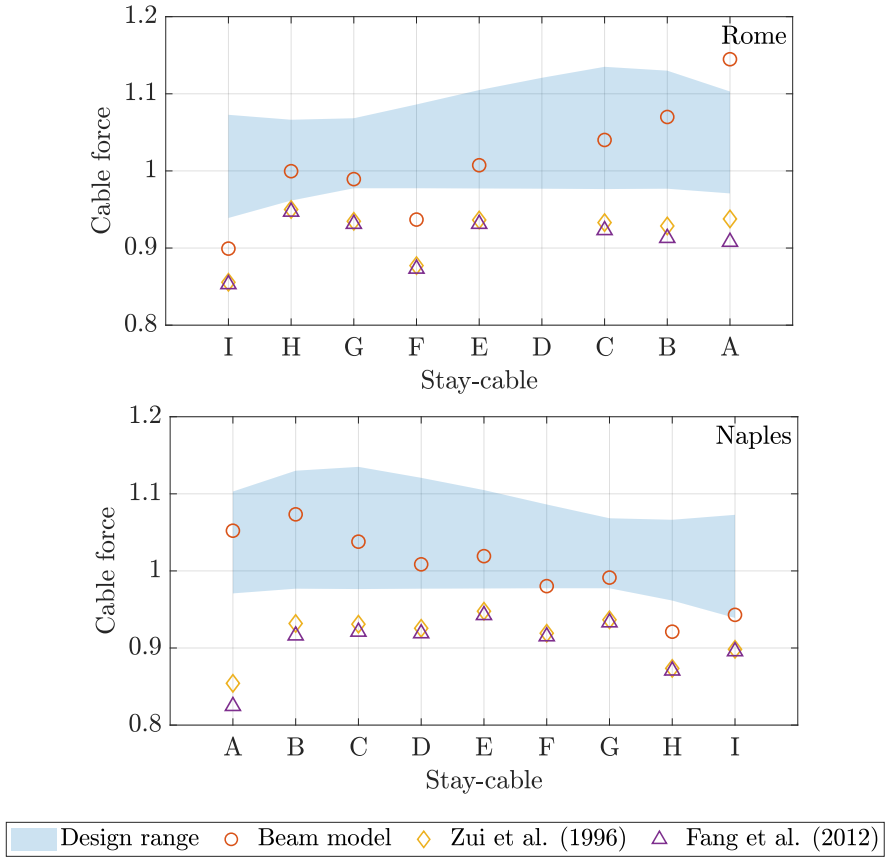

Figure 3.26: Estimated cable forces and corresponding design range accounting for the variations due to traffic load and thermal fluctuations (cables force is normalized with respect to the reference design value).

Specifically, in the original design report, it is considered a conventional fluctuation of ± 150 kg/cm^2 on the actual stress of each cable due to the thermal gradients as well as a fluctuation (different for each cable) ranging between -240 kg/cm^2 and 710 kg/cm^2 due to the traffic load. These values were determined in agreement with the prescription of the Italian technical code available at the time of the bridge construction. The upper and lower bounds of the design range were therefore obtained by adding to the original cable strength the contribution due to the upper and lower bound of the stress fluctuations. A close inspection of the results in Fig. 3.26 may suggest that the beam model leads to estimates of the cable forces in better agreement

with design values than the formulations by Zui et al. [190] and Fang et al. [191]. This, however, conflicts with the well-established evidence by which the beam model is fairly inaccurate because of the simplifications it relies on. Furthermore, it is observed in Fig. 3.26 that the results obtained according to Zui et al. [190] and Fang et al. [191] are very close each other and do not fall within the design range, but are regularly lower than the lower bound. This suggests the need of introducing a further aspect to properly interpret the results in Fig. 3.26. In this sense, it is argued that what is observed in Fig. 3.26 can be explained by taking into account the relaxation phenomenon of the stay-cables.

In order to find a suitable evidence for that, the stress values of the stay-cables are determined in compliance with Eurocode 2 provisions [193] accounting for the relaxation losses.

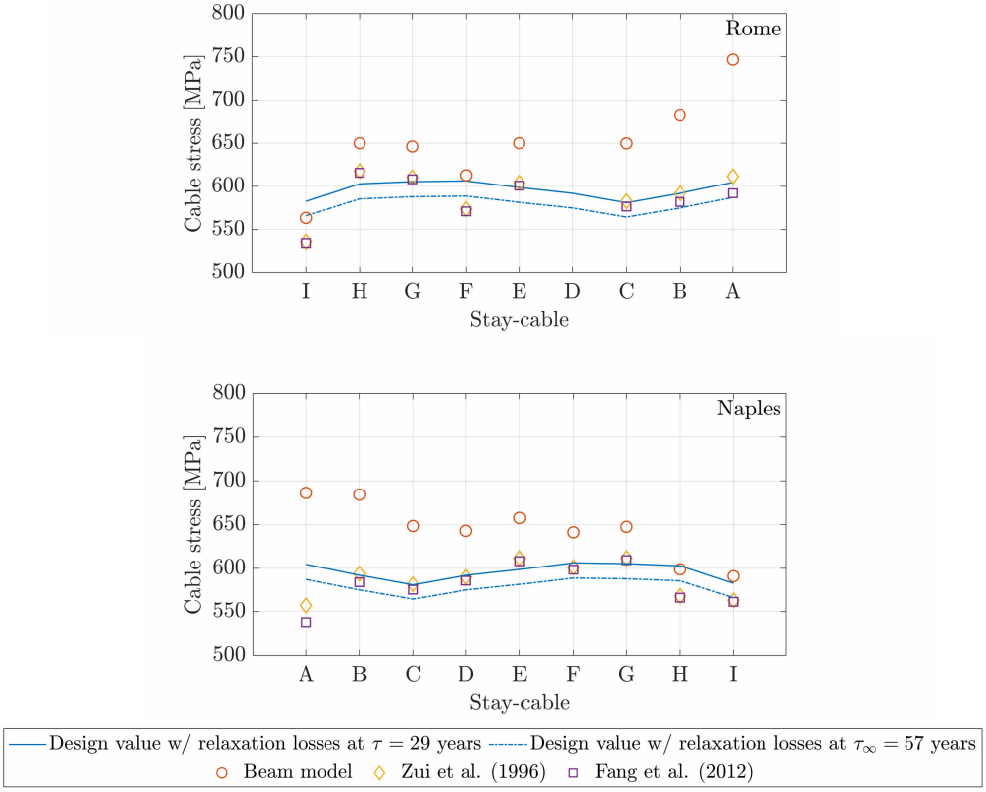

Figure 3.27: Estimated cable stresses and corresponding design values accounting for the relaxation losses.

Accordingly, the relaxation losses for ordinary tendons are calculated as follows:

$$\frac{\Delta\sigma_{pr}}{\sigma_{pi}} = 5.39\varrho_{1000}\mathrm{e}^{6.7\eta}\left(\frac{\tau}{1000}\right)^{0.75(1-\eta)}10^{-5} \tag{3.21}$$

where $\Delta\sigma_{pr}$ is the absolute value of the relaxation loss of the prestress, σ_{pi} is the absolute value of the initial prestress, τ is the time after tensioning, $\eta = \sigma_{pi}/f_{pk}$ is the

stress value normalized with respect to the characteristic value of the tensile strength of the prestressing steel f_{pk}. Finally, ϱ_{1000} is the relaxation loss at 1,000 hours after tensioning for a mean temperature equal to 20 °C, which is equal to 8 for ordinary tendons.

Assuming a tensile strength of the prestressing steel $f_{pk} = 1,700$ MPa, it is estimated from Eq. (3.21) that the relaxation losses are completed at $\tau_\infty = 57$ years. Figure 3.27 shows the stress values of the stay-cables estimated according to the considered models by means of the corresponding experimental natural frequencies. Design cable stress values calculated by subtracting the relaxation losses at $\tau_\infty = 57$ years and $\tau = 29$ years (i.e., the current bridge age) are also shown in Fig. 3.27.

Results in Fig. 3.27 demonstrate that the numerical models by Zui et al. [190] and Fang et al. [191] lead to experimental cable stress values in excellent agreement with design predictions, provided that relaxation losses are properly taken into account. Conversely, the beam model overestimates the stress of the stay-cables and the shorter is the cable, the larger is the error. Notably, the beam model leads to unacceptable errors in force and tension prediction as the cables become shorter or stouter because Eq.(3.16) is derived from an axially-tensioned beam with hinged end boundaries rather than fixed ones.

3.4.3 A 20 Highway overpasses

The third case study investigated in this chapter deals with a series of road overpasses part of the A20 highway, which connects Messina to Palermo (Italy). Dating back to the early 1970s, these bridges were built adopting the Niagara-type structural scheme and consist of two symmetric precast lateral cantilevers of 29 m and a central suspended span between the half joints of 31 m, both in prestressed concrete. Fig. 3.28 shows a representative case of the investigated structures. It's worth noting that the investigated overpasses, and thus the experimental measurements, were divided into two different batches, hereinafter labeled as batch 7 and 9, according to their location in the A20 highway (see Fig. 3.28): this depends also on the fact that the structures of each batch have been realized at different times by two construction companies with different equipment and concrete batching plants.

Figure 3.28: Overview of one of the A20 road overpasses representative of the series investigated in the present study.

Depending on the specific overpass, the deck has a variable width between 6.5 m and 17 m and, correspondingly, it is made up of a variable number of I-shaped post-tensioned girders, ranging from 3 to 8, equally spaced at 2 m. The latter have a variable height section ranging between 1.70 m at midspan and 1.30 m at the abutments and are connected by rectangular-shaped transverse diaphragms and an overlying RC slab with 0.16 m thickness. Figure 3.29 shows the geometry of the most common type among the investigated overpasses, i.e. with a deck made up of 5 girders. Specifically, each girder is reinforced with 6Ø10 longitudinal bars at the top flange and the web, 11Ø10 bars at the bottom flange, and Ø12/15 cm transverse web reinforcement. The girders reinforcement also includes transverse web reinforcement Ø12/15 cm (for the cantilevers) and Ø10/30 cm (for the central beams). Further, each girder is reinforced with parabolic prestressing tendons made of cold-drawn Ø7 steel wires: in the lateral spans, a total of 4 cables per girder are used, 3 of which (32 wires) are anchored at the dapped end and the last one (42 wires) is anchored at the abutment, whereas central span girders have 3 cables (32 wires) are, 2 of which anchored at the dapped end (see Fig. 3.30(a)). The dapped ends (0.70 x 0.90 x 0.75 m) are reinforced with 2Ø24 hangers, 4Ø24 diagonal bars, 6Ø24 longitudinal steel bars (both at top and bottom)

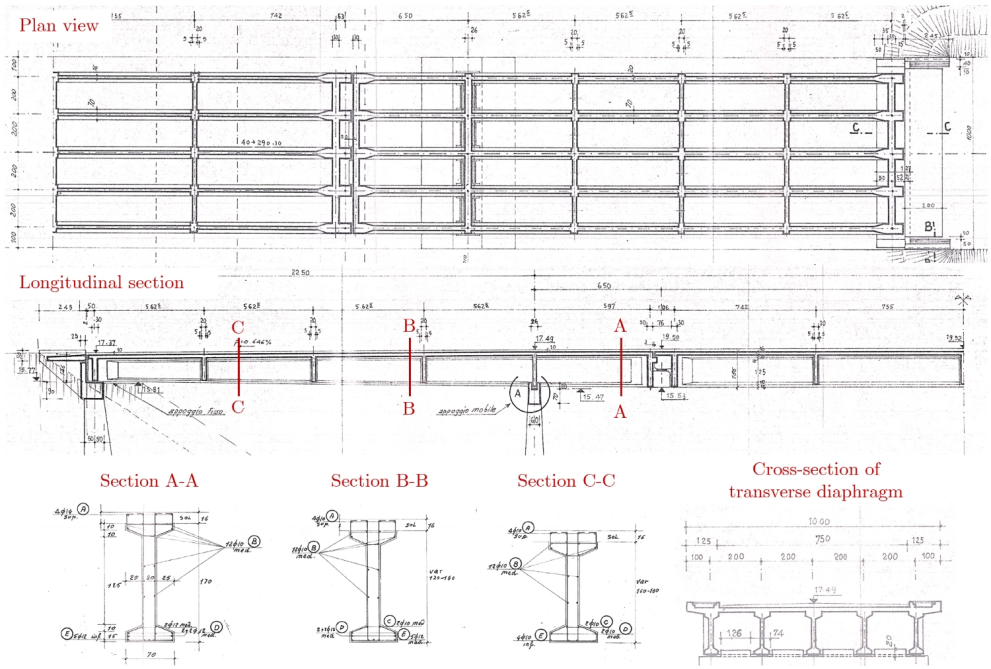

Figure 3.29: Original drawings of one of the investigated overpass (deck made up of 5 girders): (a) plan view of the overpass, (b) longitudinal section of 1/2 girder, (c)transverse sections of one girder at different abscissa and (d) transverse section of the bridge deck.

and stirrups Ø14/15 cm (see Fig. 3.30(b)). Finally, the RC slab is reinforced with 4Ø14 longitudinal bars in the zones above the girders, 6Ø8 longitudinal bars in the remaining parts, and transverse Ø10/25 cm bars for the entire slab width.

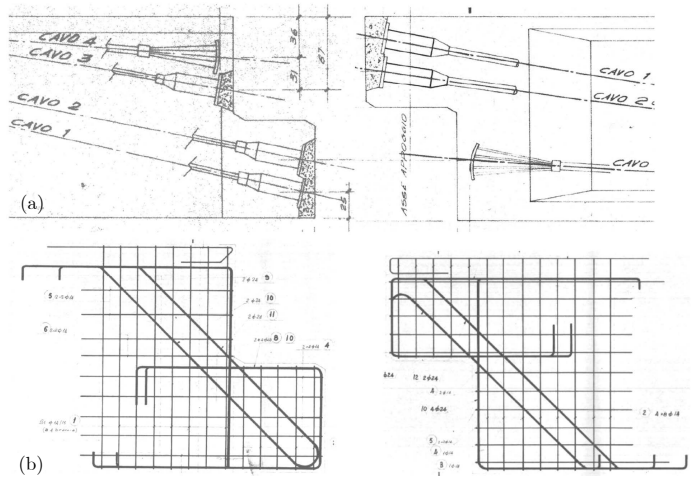

Figure 3.30: Dapped end girders: (a) prestressing cables and (b) longitudinal and transversal reinforcement.

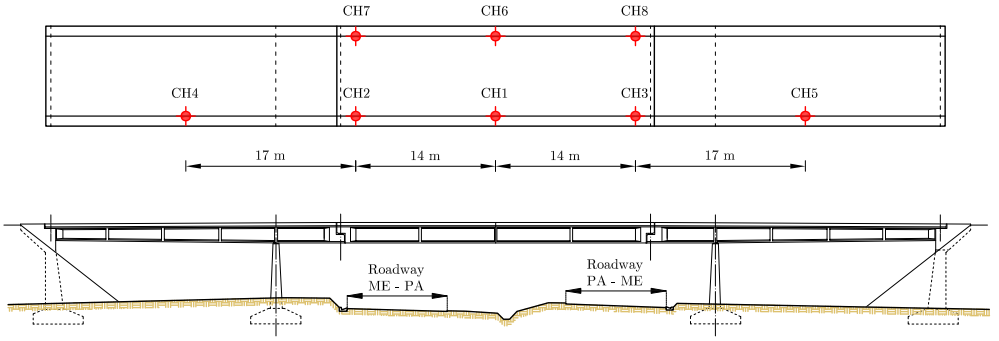

Figure 3.31: Sensors layout on the investigated bridges.

Dynamic identification

Each one of the half-joint bridges has been monitored by performing a campaign of low-cost free vibration tests to assess their actual health condition. Notably, it has been possible to obtain estimates of the modal parameters representative of the serviceability conditions of the structures, which in turn may be also exploited for the indirect estimations of their physical properties. For each examined structure the same test set-up is exploited: it consisted of 8 uniaxial sensors (CH1−CH8) with a sensitivity of 1000 V/g, rigidly anchored to the bridge deck and connected to a 16-bit control unit. The sensors have been arranged favoring the east lane of the overpasses on which a total of five sensors were mounted (CH1−CH5), whereas the remaining three sensors (CH6−CH8) have been placed on the west lane as shown in Fig. 3.31. To perform the tests, the structure was dynamically excited by the transit of a vehicle (gross weight of 35 kN) marching on the deck at an average speed of 50 km/h, and free vibrations were recorded as the vehicle left the structure. The acquisition of the signals was performed considering a sampling frequency of 1kHz. For some of the investigated overpasses, two distinct series of free vibration tests have been carried out, namely before and after the application of a static load. Such a test was carried out to assess the bridge deck's ability to support the load conditions specified by the current Italian Technical Code [184], which differ from those assumed at the time of construction. Notably, the dynamic tests performed between the aforementioned static load application, aimed to assess any possible damage due to lack of bearing capacity which shall be reflected in a fluctuation of the modal parameters. Recorded time series (see Fig. 3.32) have been processed by means of a third-order Butterworth filter to retain the frequency range of interest, i.e. (0.5−15) Hz.

The dynamic identification is carried out by comparing the results of two different approaches, namely the proposed procedure and the Covariance Driven - Stochastic Subspace Identification Method (SSI-COV). Adopting the aforementioned identification procedures, it has been possible to successfully identify up to five modes for the investigated structures. Tables 3.9 and 3.10 compare the identified modal frequencies showing a nice agreement between the estimates obtained from the two identification procedures. Specifically, Tab. 3.9 compares the frequencies before and after the execution of the static tests, showing that negligible frequency variations, under 1% for the first three modes, are observed. Missing results for overpass n.18 are due to the

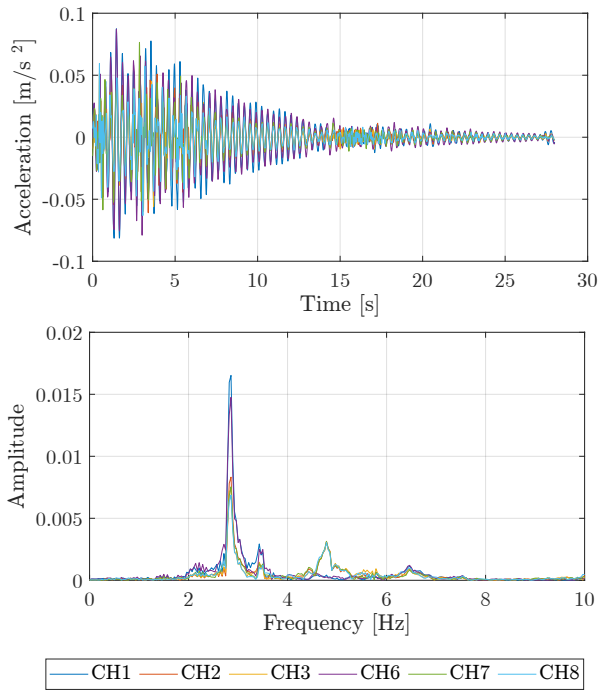

Figure 3.32: Example of the recorded time series on the central span of the overpass (left) and corresponding Fourier transform (right).

fact that the magnitude of the excitation exerted in the dynamic tests did not properly excite the second torsional mode making the estimations unreliable. Further, it is noted from Tab. 3.10 that slightly lower natural frequencies are identified for the overpasses with a higher number of deck girders, as well as that the most significant contribution to the dynamic response falls in the range between 2.6−3.2 Hz, depending on the actual material properties of the investigated structure.

Table 3.9: Identified natural frequencies, before and after (in brackets) the execution of the static load tests and corresponding relative variations, using VMD-based identification method and SSI-COV for the investigated overpasses.

	Overpass n.18 (5 girders)				Overpass n.19 (5 girders)			
Mode	VMD	$\Delta\nu$[%]	SSI-COV	$\Delta\nu$[%]	VMD	$\Delta\nu$[%]	SSI-COV	$\Delta\nu$[%]
1	2.84 (2.86)	0.42	2.86 (2.84)	0.73	2.79 (2.78)	0.36	2.78 (2.76)	0.65
2	3.11 (3.12)	0.16	3.11 (3.08)	1.09	3.12 (3.10)	0.69	3.12 (3.11)	0.32
3	4.87 (4.83)	0.76	4.92 (4.79)	2.62	4.77 (4.78)	0.16	4.73 (4.74)	0.06
4	–	–	–	–	5.79 (5.80)	0.28	5.72 (5.81)	1.66
5	6.54 (6.41)	2.12	6.56 (6.37)	2.92	6.49 (6.37)	1.92	6.47 (6.19)	4.32

It is worth noting that a single value of frequency is obtained for each mode via SSI-COV since it elaborates concurrently all the information provided in the data set, whereas the modal frequencies obtained via the VMD-based identification approach

Table 3.10: Identified natural frequencies using VMD-based identification and SSI-COV for the investigated overpasses.

	Overpass n.7 (8 girders)		Overpass n.12 (5 girders)		Overpass n.15 (7 girders)		Overpass n.17 (5 girders)	
Mode	VMD	SSI-COV	VMD	SSI-COV	VMD	SSI-COV	VMD	SSI-COV
1	2.66	2.71	2.64	2.64	2.74	2.81	2.83	2.85
2	2.85	2.92	3.05	3.06	3.14	3.08	3.41	3.36
3	4.77	4.75	4.56	4.67	4.74	4.66	4.83	4.77
4	5.31	5.27	5.36	5.32	5.27	5.28	5.44	5.76
5	6.61	6.86	6.33	6.41	6.34	6.36	6.47	6.60

are obtained by averaging all the available estimates (one for each signal in the data set). The obtained results have been useful for the development of numerical FE models of the bridge deck, which is addressed in the following subsection.

In addition to natural frequencies, dynamic tests have been also exploited to identify the inherent modal damping ratios. Once again it is pointed out that the estimates obtained via the VMD-based approach are averaged out over the eight available measures (from CH1 to CH8). Specifically, the analysis of the recorded signals allows the identification of modal damping ratios, up to the fifth mode, which are summarized in Figs. 3.33 and 3.34; a reasonable agreement between the two adopted methodologies is reached, even though a bigger scatter is observed if compared with the identified frequencies. Nonetheless, the identified damping ratios are under 3% which is a reasonable order of magnitude for PC structural elements in the elastic phase, thus suggesting that, in serviceability conditions, no significant damage occurred in the bridge deck before the test execution. Further, it is noted that for the overpasses for which pre-static and post-static identification has been performed, the VMD-based identification approach provides more accurate estimates since a limited scatter is observed between the two scenarios if compared with the SSI-COV counterparts.

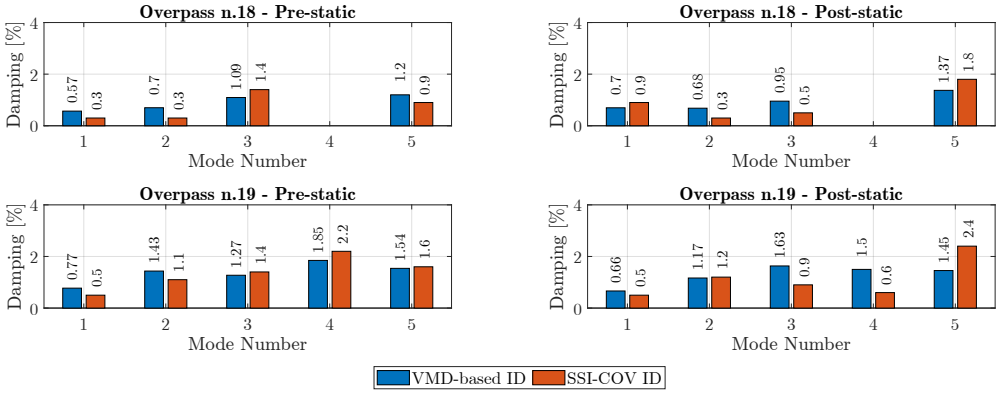

Figure 3.33: Comparison of the identified modal damping ratios, using the VMD-based approach and SSI-COV method, before and after the static tests performed on 5 girders deck overpasses

Finally, the mode shapes have been successfully identified. Even though the number of sensors is limited and it is also not symmetrically installed with respect to the

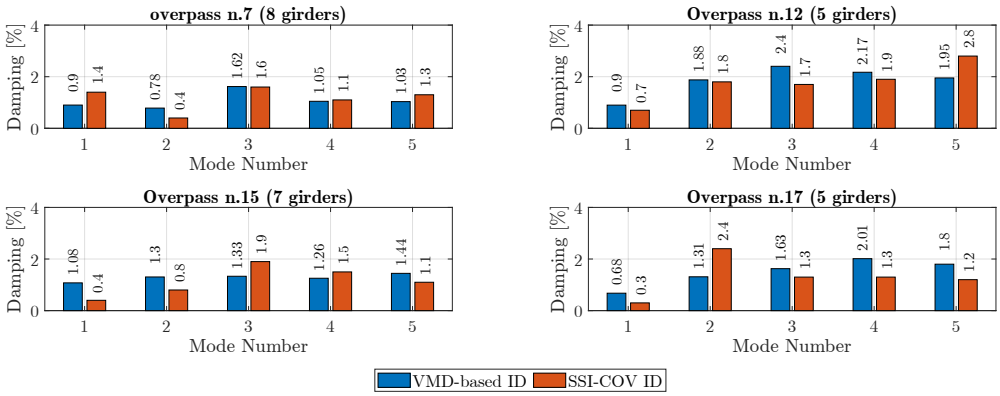

Figure 3.34: Identified modal damping ratios, using the VMD-based approach and SSI-COV method, for deck overpasses with a variable number of girders.

roadway direction, it is possible to assert that the first two modes are representative of the flexural and torsional behavior of the central suspended span, respectively, whereas the successive ones reflect the flexural and torsional behavior at higher modes of the overpass, in which also the cantilevered parts are significantly affected by any dynamic excitation. Figure 3.35 shows the identified mode shapes from the test performed on one of the overpasses; as can be noted, a nice agreement is achieved between the estimated mode shapes with the two methods. To quantify the degree of similarity between estimated modes, the Modal Assurance Criterion (MAC) is adopted (see Eq.(3.15). For the investigated case MAC values equal to 0.999, 0.991, 0.993, 0.901 and 0.970 are observed for the five identified modes, respectively. It is pointed out that negligible differences have been observed between estimated mode shapes before and after the execution of the static loading test.

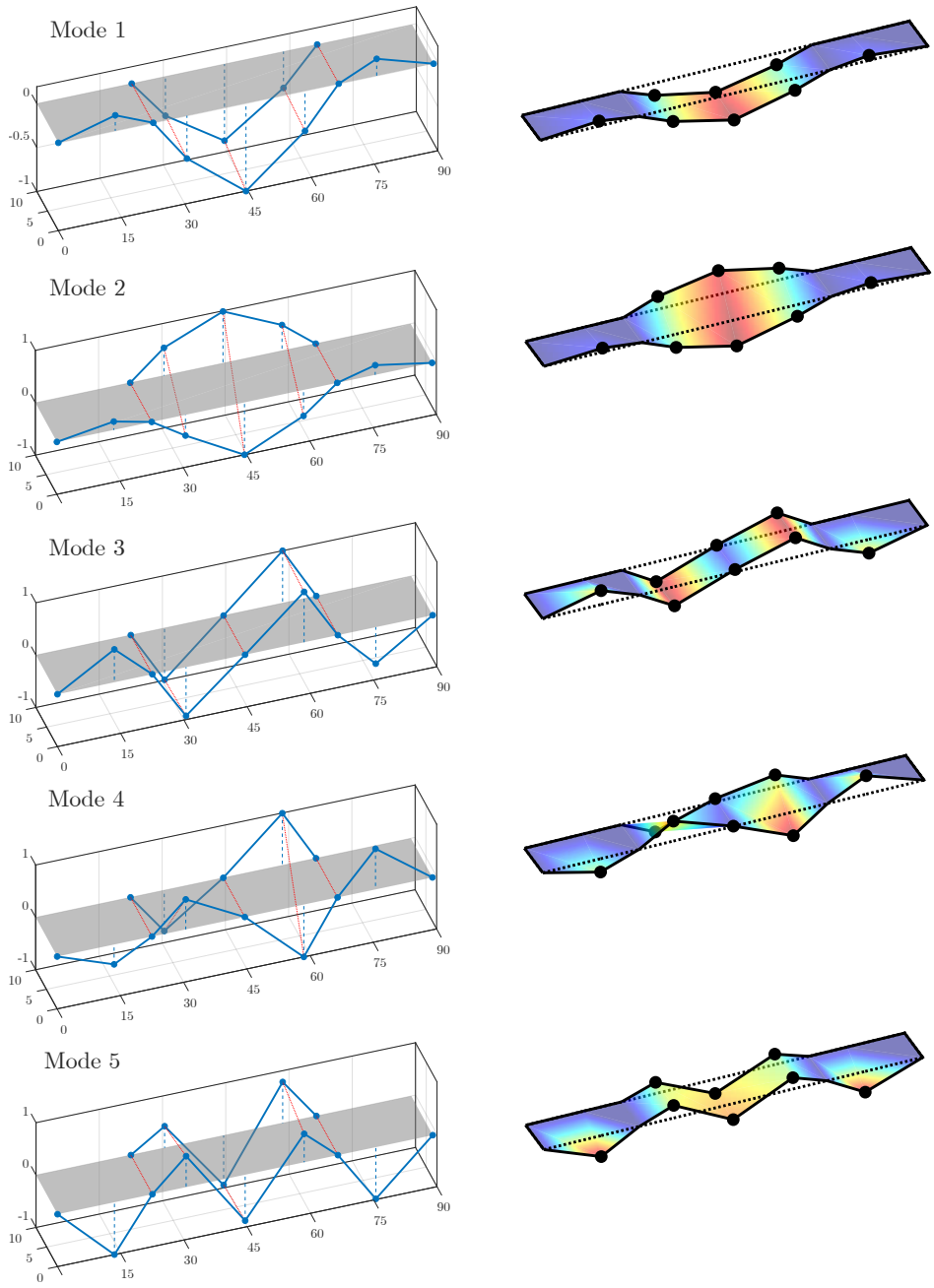

Figure 3.35: First five mode shapes identified via the VMD-based approach (left) and SSI-COV method (right).

Comparative analysis via numerical FE simulations

The identified frequencies and mode shapes of the most common type of overpass (i.e., with a bridge deck made up of 5 girders), estimated via the dynamic identification, are compared with the predictions of simplified FE models. To this aim, two FE models with different degrees of approximation have been realized with the structural analysis program SAP2000 [185].

In the first model (see Fig. 3.37), both longitudinal beams and transverse diaphragms have been modeled using beam elements with six degrees of freedom per node. The sectional properties of girders and diaphragms were automatically associated, once the corresponding sections were defined, through SAP 2000 Section Designer tool [185]. In addition, it is worth noticing that the overlaying RC slab has been modeled in a simplified way, associating each girder with the corresponding collaborating part, whose width was calculated according to Eurocode 4 provisions [188]: this has been attained by including the specific collaborating part in the cross-section parameters of the girders. Further, a diaphragm constraint has been adopted to account for the membrane stiffening effect of the RC slab in the horizontal direction. A sec-

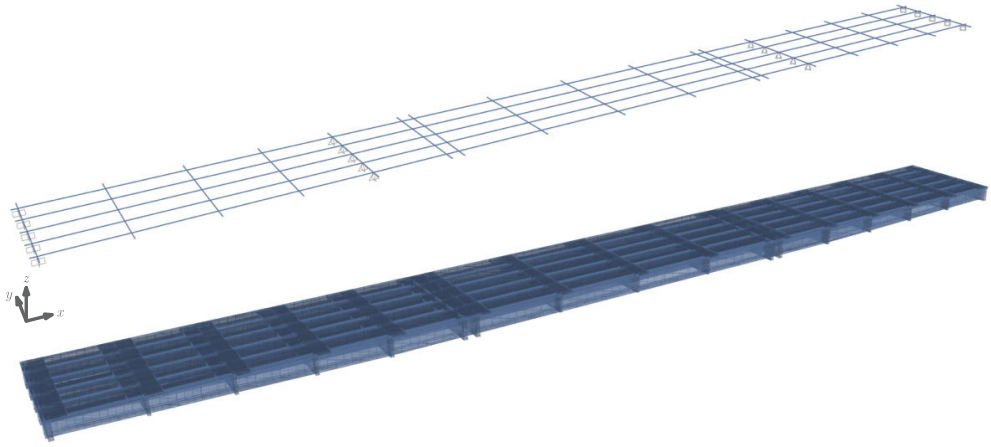

Figure 3.36: FE model of the bridge deck using beam elements with collaborating portion of RC slab: standard view (top) and extruded view (bottom).

ond more refined model (see Fig. 3.36) has been generated using beam elements for both girders and transverse diaphragm, as in the previous case, whereas shell elements have been adopted to simulate the overlaying slab. Specifically, joint offsets have been introduced to connect the latter to the girders: they simulate the actual height difference between the girder centroid and the mid-plane of the slab. In both models, rigid pinned restraints have been assumed at the intermediate pier, thus neglecting both their actual deformability and neoprene bearings one. Further, to simulate the Niagara-type scheme, moment release conditions have been assigned to each beam node at the RC corbels abscissas.

Finally, two different boundary conditions have been considered at the abutments, namely pinned and clamped (rigid) constraints, to assess which one better describes the behavior of the real structure. In that regard, the abutments of the real structure are

connected with the terminal transverses by means of Mesnager hinges (see Fig. 3.38) to avoid the lifting of the deck in the cantilevered spans for full load conditions. Depending on the excitation that the structure has experienced during its life, this constraint may behave as a cross between a clamp if the concrete at the hinge has been cracked and a pin, otherwise.

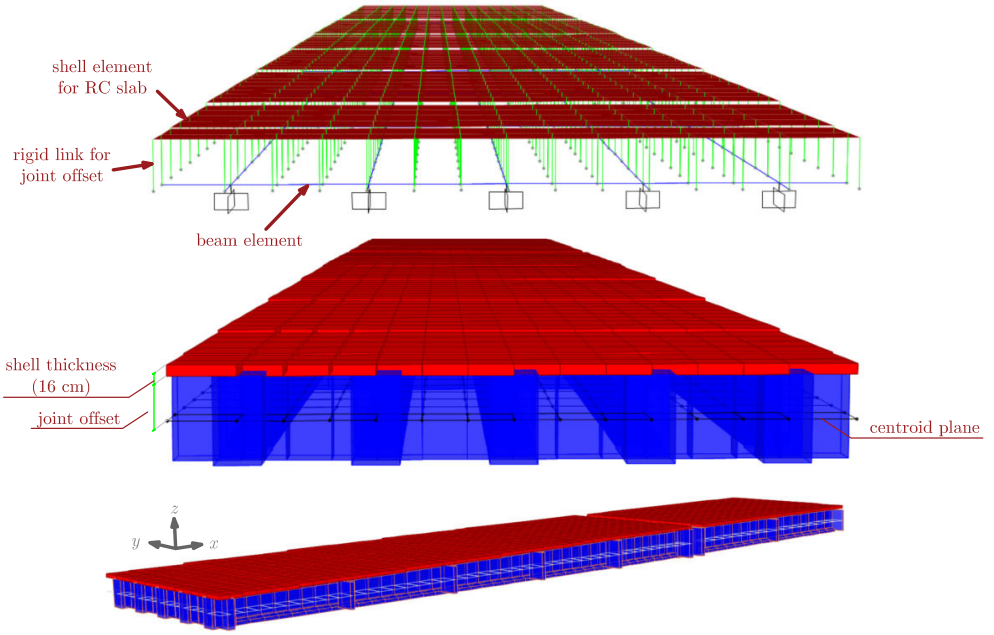

Figure 3.37: View of half of the FE model of the bridge deck modeled using shell elements with joint offset for RC slab and beam elements for longitudinal girders and transverse diaphragms: offset view (top) and extruded view (bottom).

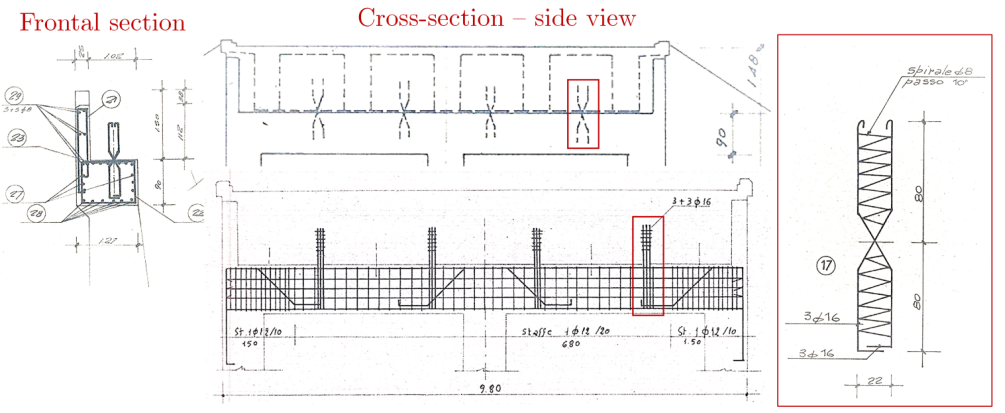

Figure 3.38: Detail of the Mesnager hinges and their positions at the abutment (from the original drawings).

In both models, mass distribution has been evaluated from the bridge deck load analysis, which included the self-weight of structural elements and overloads produced by road pavement and guardrails. A crucial parameter in the evaluation of the modal response of the structure is the concrete elastic modulus E_c since it figures in the stiffness matrix of the associated eigenproblem. Specifically, it can be related to the concrete compressive strength by means of relations proposed by normative codes such as the one proposed by EC2 [193]. Considering the variability of the cubic compressive strength R_c observed in the experimental campaign, it appears reasonable to evaluate modal parameters in the FE model by accounting for the corresponding variability of E_c. Further, since the EC2 relation is both differentiable and invertible, the probability density function (PDF) of the random variable E_c, labeled as $f_{E_c}(E_c)$, may be obtained in closed-form once the corresponding compressive strength PDF is known, i.e. $f_{R_c}(R_c)$, using the probability transform method (PTM) [194]. More details are provided in the next subsection.

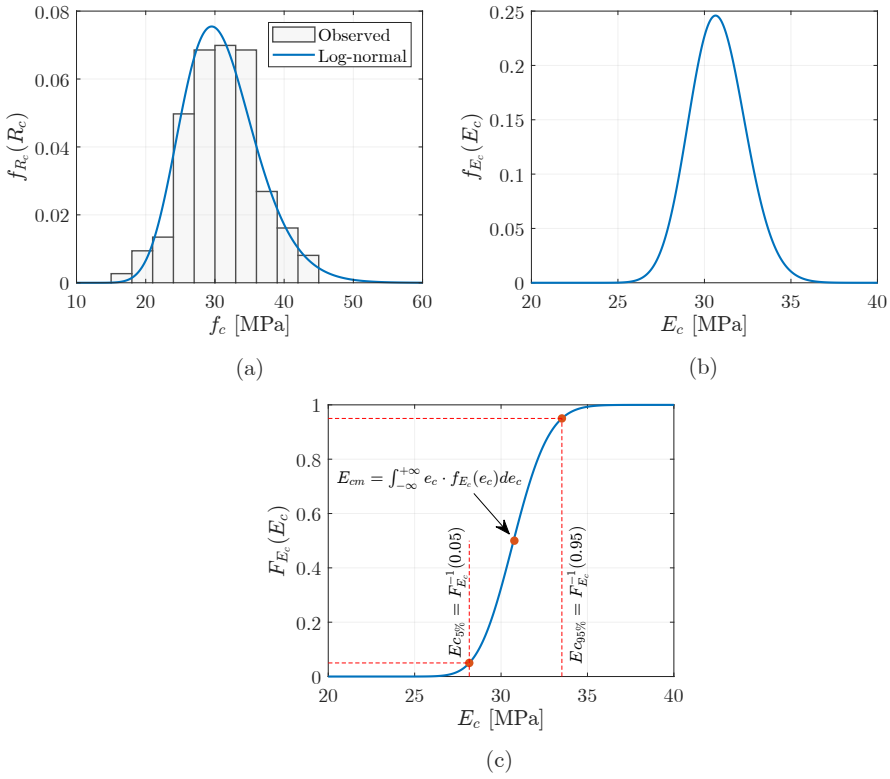

Figure 3.39: Evaluation of concrete elastic modulus via probability transformation method (PTM): (a) evaluation of PDF for concrete compressive strength $f_{R_c}(R_c)$ based on experimental data, (b) evaluation of PDF of elastic modulus $f_{E_c}(E_c)$ based on the knowledge of $f_{R_c}(R_c)$ and (c) determination of elastic modulus fractiles based on the corresponding CDF $F_{E_c}(E_c)$.

Since the relation between E_c and f_c is empirical, to properly consider both the model uncertainty and the material variability, three different values of elastic modulus have been considered in the analysis, namely the mean value E_{cm}, the 5% lower

fractile $E_{c,5\%}$ and the 5% upper one $E_{c,95\%}$. Notably, the fractile values have been obtained by inverting the cumulative distribution function (CDF) of E_c, i.e. $F_{E_c}(E_c)$ as summarized in Fig. 3.39.

Figs. 3.40 and 3.41 summarize the frequencies predicted for the first five modes by the two analyzed models, depending on the specific constraints adopted at the ends and the elastic modulus fractile chosen in the analysis.

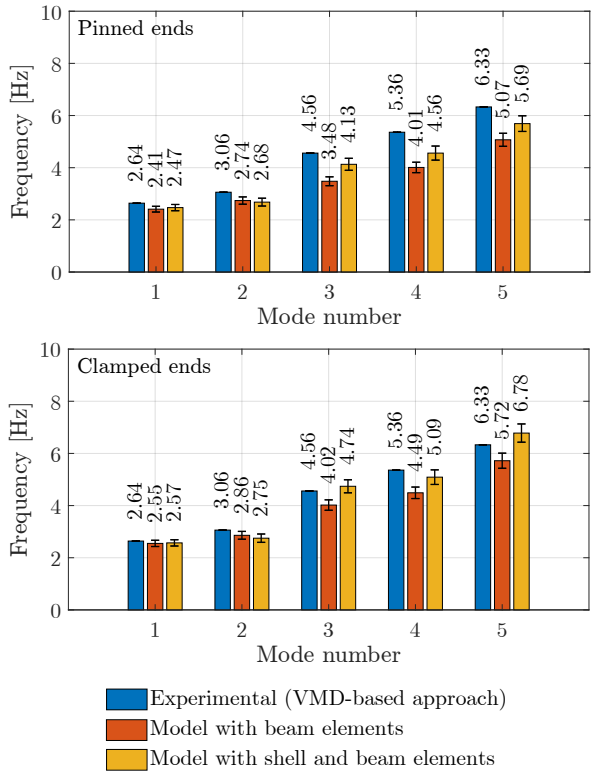

Figure 3.40: Comparison between experimental frequencies and the predicted ones obtained from the FE models, depending on the boundary conditions, for the first five modes. The model has been calibrated using elastic moduli obtained from the experimental measures of compressive strength from batch 7 via PTM.

It is noted that the more refined method provides estimates closer to the experimental results; specifically, the model with clamped ends predicts the closest modal frequencies to the experimental counterpart, thus implying that the Mesnager hinges have not been cracked during the structure life, since they behave similarly to a clamp constraint. Moreover, Fig. 3.42 shows the estimated mode shapes obtained with the more refined method highlighting that a nice agreement with the experimental counterpart is reached. The degree of similarity with the ones obtained with the VMD-based approach is quantified by means of MAC: Tab 3.11 lists the MAC factors observed for the first five modes. It is pointed out that no significant variations in the mode shapes are observed between the two investigated models.

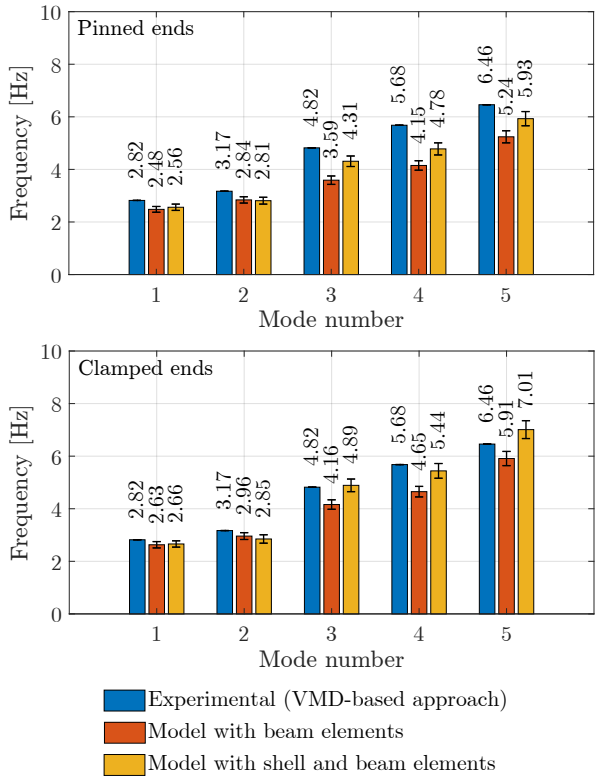

Figure 3.41: Comparison between experimental frequencies and the predicted ones obtained from the FE models, depending on the boundary conditions, for the first five modes. The model has been calibrated using elastic moduli obtained from the experimental measures of compressive strength from batch 9 via PTM.

Table 3.11: MAC factors for quantitative assessment between identified mode shapes via VMD and SSI-COV and predicted ones via the refined FE model.

Mode	MAC factor [-]	
	VMD vs FEM	SSI-COV vs FEM
1	0.992	0.993
2	0.992	0.993
3	0.993	0.986
4	0.938	0.916
5	0.927	0.934

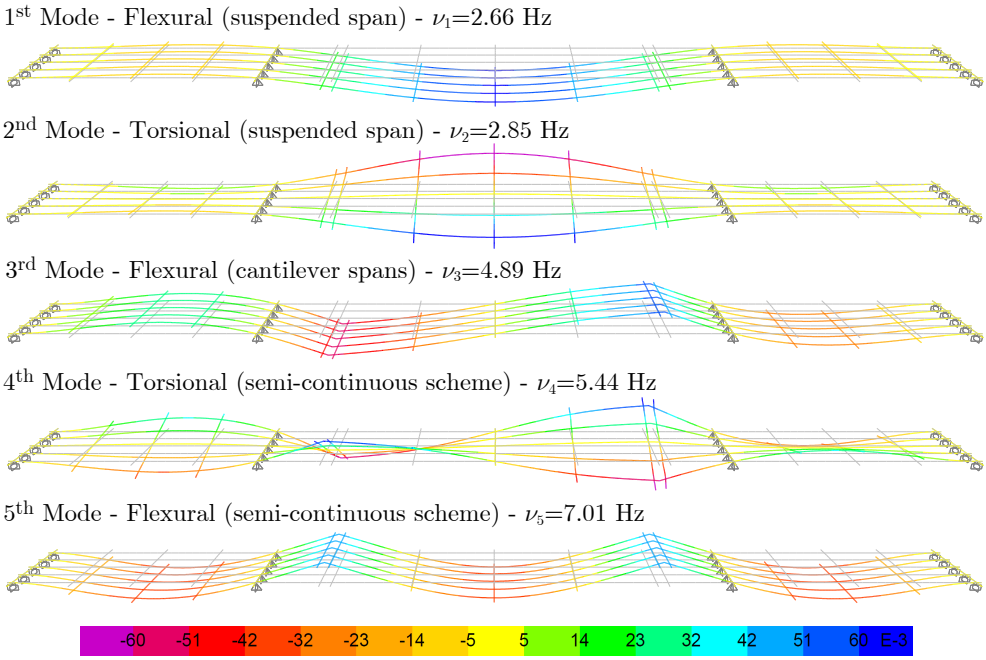

Figure 3.42: First five mode shapes obtained from the refined FE model.

On the evaluation of concrete elastic modulus PDF via PTM

The concrete elastic modulus E_c can be related to its cylindrical compressive strength f_c via the following relation proposed by Eurocode 2 [193]:

$$E_c = 22000 \left(\frac{f_c}{10} \right)^{0.3} \tag{3.22}$$

where f_c can be expressed in terms of cubic compressive strength R_c as follows:

$$f_c = 0.83 R_c \tag{3.23}$$

Eq.(3.22) is a power-law function, differentiable and invertible, in the form $E_c = a R_c^b$ where $a = 10426.7$ and $b = 0.3$. Further, the inverse relation which expresses R_c in terms of E_c is:

$$R_c = g(E_c) = \left(\frac{E_c}{a} \right)^{1/b} \tag{3.24}$$

Since Eq.(3.24) is monotonous it is possible to apply the PTM in the form:

$$\int_{E_{c1}}^{E_{c2}} f_{E_c}(e_c) de_c = \int_{R_{c1}}^{R_{c2}} f_{R_c}(g(E_c)) \cdot g'(e_c) de_c \tag{3.25}$$

where $f_X(x)$ represents the PDF of the considered random variable (i.e, E_c or R_c). Therefore, by exploiting Eq.(3.25), the PDF of the elastic modulus is derived once the

PDF of the cubic compressive strength is known. The latter is determined by fitting the log-normal distribution to the available experimental data once the samples' mean and standard deviation are evaluated. Specifically, the analytical form of the PDF of the elastic modulus has the following form:

$$f_{E_c}(E_c) = f_{R_c}(g(E_c)) \cdot g'(E_c) = f_{R_c}\left[\left(\frac{E_c}{a}\right)^{1/b}\right] \cdot \frac{\left(\frac{E_c}{a}\right)^{-1+a/b}}{ab} \tag{3.26}$$

From the knowledge of $f_{E_c}(E_c)$, it is possible to calculate the corresponding CDF, i.e. $F_{E_c}(E_c)$, and therefore the 5% and 95% fractiles of the elastic modulus. On the other hand, the mean elastic modulus E_{cm} is evaluated as follows:

$$E_{cm} = \mathbb{E}[E_c] = \int_{-\infty}^{\infty} e_c f_{E_c}(e_c) de_c \tag{3.27}$$

where $\mathbb{E}[\cdot]$ is the expected value operator. Using the above-mentioned procedure the elastic moduli of girders and RC slab have been calculated for both the investigated batches and are listed in Tab. 3.12.

Table 3.12: Estimated fractiles of concrete elastic modulus using PTM (values are expressed in GPa).

	Girders			Slab and transverses		
Batch	$E_{5\%}$	E_{cm}	$E_{95\%}$	$E_{5\%}$	E_{cm}	$E_{95\%}$
7	27.39	29.67	32.07	21.53	24.84	28.45
9	28.16	30.77	33.52	25.81	28.41	31.17

CHAPTER 4

AN EFFICIENT MODAL IDENTIFICATION METHOD BASED ON ENHANCED EMPIRICAL FOURIER DECOMPOSITION

4.1 Introductory remarks

In the previous chapter, the performance of the VMD was discussed in the context of the dynamic identification of existing bridges. However, it has been noted that the correct tuning of this method is not always straightforward, thus requiring further investigations into possible alternatives. Further, a very recent decomposition method called the Empirical Fourier Decomposition (EFD) technique [146], showed nice performances when addressing theoretical signals. It operates the extraction of the uni-modal components through an improved segmentation of the frequency spectrum and a zero-phase filter bank.

Both the VMD and the EFD techniques are among the approaches that are rapidly attracting attention in the field of dynamic identification via advanced decomposition methods. In this regard, Civera and Surace [195] have analyzed the performance of different decomposition methods concluding that the VMD technique is most suitable for structural monitoring applications. On the other hand, few applications of the EFD technique are already available in structural monitoring literature and are limited to signal features extraction. [196]. The available evidence suggests that both these techniques can attain very accurate results. Specifically, their performance is influenced by the correct selection of the involved control parameters, which should be possibly set in an automatic fashion, thus not relying on any feedback from the analyst. The feasibility of the VMD technique for the dynamic identification of the modal parameters of bridge structures has been demonstrated by Yang et al. [29] and Mazzeo et al. [30, 177], who also developed suitable strategies towards the automatic optimal tuning of its control parameters. Currently, there is a lack of documented comparative evaluations related to the modal parameters estimation of real structural systems by means of the EFD technique, which is an impediment to understanding its accuracy and reliability in automatic dynamic identification.

This chapter presents the recent results provided by the author on this topic [197, 198]. Specifically in Section 4.2 an enhanced implementation of the EFD technique for automatic dynamic identification purposes is presented. The novel contributions are: i) a smoothing-based improved segmentation of the frequency spectrum; ii) an iterative automatic process for the optimal tuning of the number of frequency spectrum partitions. The whole identification procedure is completed by implementing an area-based approach for modal damping ratios estimation, whereas a time-domain

method based on the phase shift of the free vibration response peaks is employed to identify the mode shapes. Section 4.3 addresses the performance of the proposed framework via synthetic benchmark signals with specific attention to the case of closely spaced modes and minor modes. Further, the precision of the estimates is assessed via a statistical analysis considering the effect of noise. Finally, in Section 4.4 experimental applications are discussed. Specifically, the first case-study deals with the dynamic characterization of the cables in the same stay-cabled bridge analyzed in Chapter 3, comparing the performances of VMD and EFD. The second case-study is concerned with the modal identification of a steel railway bridge deck.

4.2 Automatic modal identification based on the EFD technique

4.2.1 Modal identification by means of the EFD technique

The proposed identification procedure is based on the detection and extraction of the uni-modal components from the free vibrations of a structural system. This is accomplished by means of the EFD technique, which is an adaptive decomposition method introduced recently by Zhou et al. [146] in order to overcome the limitations typically recognized in the other methods based on Fourier transform such as EWT [139] and FDM [147]. The EFD technique allows the decomposition of a multi-modal signal into its uni-modal components via a spectrum segmentation procedure combined with the construction of a zero-phase filter bank. The segmentation procedure aims at producing N frequency partitions of the frequency spectrum of the signal to be analyzed whereas the zero-phase filter bank is required to perform the actual decomposition. Central frequencies of all the segments are extracted as the frequency values in the Fourier spectrum at which the first N highest local maxima are attained. Therefore, the decomposition of the free vibrations allows the identification of all relevant modal parameters of the structure according to the approach described by Mazzeo et al. [30, 177]. Particularly, the component central frequencies are taken as modal frequencies of the structural system whereas modal damping ratios and mode shapes are retrieved according to Eqs.(3.10) and (3.13), respectively.

Although the application of the EFD technique is appealing for modal identification of structures from free vibrations, there are two significant shortcomings that prevent its automatic and robust implementation:

- If the Fourier transform of the signal is noisy, especially close to the peaks, a wrong segmentation is likely to occur. This is due to the fact that trivial peaks not related to modal frequencies occur, which might be wrongly picked up as suitable values of Ω_n. Consequently, trivial local minima points are generated in each frequency partition, thereby misleading the identification of ω_n based on Eq.(2.125).
- The number of frequency partitions N and, as a consequence, the number of components to be extracted must be assigned before the identification starts. If there is not any a priori information, then the proper setting of this parameter might be an issue for automatic applications. This, in turn, might jeopardize the correctness of the decomposition procedure.

Efficient strategies are proposed hereafter in order to cope with both these issues.

4.2.2 Improved segmentation based on smoothed frequency spectrum

Even though the signal might be pre-processed by band-pass filtering to retain only the frequencies falling within the range of interest, the accurate estimation of the frequency spectrum might become challenging due to the residual noise, thereby leading to an incorrect identification of the modal components. This turns out to negatively affect the search for the boundaries of the frequency partitions in the EFD technique according to Eq.(2.125). In order to figure out the detrimental consequences of this issue, a real signal is considered in Fig. 4.1 with $N = 3$ (herein, it is considered the experimental cable response of a cable-stayed bridge that will be thoroughly examined later). It

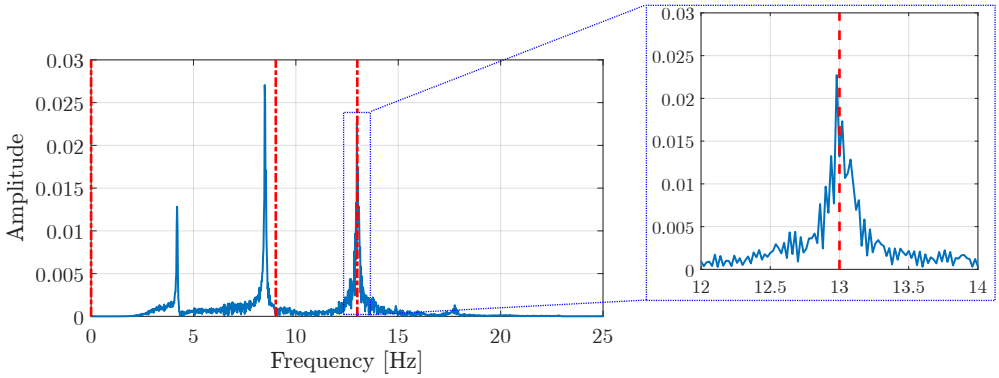

Figure 4.1: Incorrect spectrum segmentation of a real signal (dashed vertical lines denote the boundaries of the frequency segments).

is evident in Fig. 4.1 that the original segmentation process of the signal spectrum wrongly sets a partition boundary at the peak that corresponds to a system frequency representative of a vibration mode. As a result, the first two frequency peaks (i.e., the first two vibration modes) are not separated, and mode-mixing occurs. Spectral smoothing approaches have been adopted previously to mitigate the effect of the noise in other decomposition methods and to assist the proper setting of the boundaries of the frequency partitions. Smoothing approaches based on signal spectrum envelope [199, 200], moving average filters [201] and Savitzky-Golay filter [202, 203] have been adopted in the attempt to improve the spectral representation of the signals.

The proposed solution to improve the segmentation process in the frequency domain for the EFD technique consists of the application of a zero-phase moving average filter in order to smooth the signal spectrum. The moving average filtering operator can be expressed in the following general form:

$$\hat{y}^*[i] = \frac{1}{n^*} \sum_{j=0}^{n^*-1} \hat{y}[i+j] \tag{4.1}$$

where $\hat{y}[i]$ is the sampled input spectrum, $\hat{y}^*[i]$ is the corresponding sampled output (smoothed spectrum) and n^* is the number of samples used in the moving average.

The motivation for using this filter lies in its simplicity of implementation and the minimum number of control parameters. Actually, the only control parameter is the number of samples n^* in the moving average. It is advisable to use a small number of samples n^* in order to avoid too large distortions (i.e., excessive flattening) in the frequency spectrum of the signal. Therefore, the numerical value of this parameter must be related to the frequency resolution adopted for the Fourier transform, which implies that it must depend on the considered number of frequency lines n_{FT} (this latter is usually defined taking into account the recorded signal duration, and it is settled a priori based on the imposed excitation level as well as the expected structural damping). The following rule is thus implemented:

$$n^* = \mathrm{round}[\ln(n_{\mathrm{FT}})/2] \tag{4.2}$$

where round[·] is the rounding operation to the nearest integer. It must be pointed out that the moving average filter in Eq.(4.1) produces a delay between the original and filtered output such that the higher n^*, the larger the delay. In order to remove the delay between input and output, the zero-phase requirement is invoked in the filter construction (in MATLAB programming language, this result can be obtained by means of the built-in function "filtfilt"). Figure 4.2 shows the comparison between the frequency spectrum presented in Fig. 4.1 and its filtered version obtained by means of Eq. (4.1): it is evident that the frequency partitions are properly recognized after smoothing, and mode-mixing is now prevented.

It is important to highlight that the construction of the smoothed frequency spectrum only serves at detecting the frequency boundaries for each partition. This means that, once the number of partitions N has been defined, the zero-phase filter bank involved in the EFD technique is applied on the actual frequency spectrum of the signal using the cut-off frequencies recognized from its smoothed frequency spectrum according to Eq.(2.125).

4.2.3 Tuning of the number of frequency spectrum partitions

The correct choice of the number of frequency segments N is a critical requisite for the EFD technique because it also defines the number of the extracted uni-modal components. A small value of N will cause mode-mixing (i.e., under-decomposition) whereas a large value will split the contribution of a single mode into several components (i.e., over-decomposition). A rough estimate of this parameter might be obtained by counting the number of peaks in the Fourier transform of the signal. However, if residual noise remains after the filtering process and/or the signal exhibits closely spaced modes, then this criterion becomes too subjective and, ultimately, it is not suitable for automatic applications.

In order to overcome this further limitation of the original EFD technique, an automatic three-steps procedure is here proposed for the optimal tuning of the parameter N. Initially, the Fourier Transform is applied to the considered signal and the resulting frequency spectrum is smoothed by means of the moving average filtering as per Eq.(4.1), being the filter order defined according to Eq.(4.2). A few large peaks in the smoothed frequency spectrum will have a physical meaning since they are associated with real modes, whereas the others are small trivial peaks due to the noise. It is evident that the prominence of the peaks plays a major role in this regard: in fact,

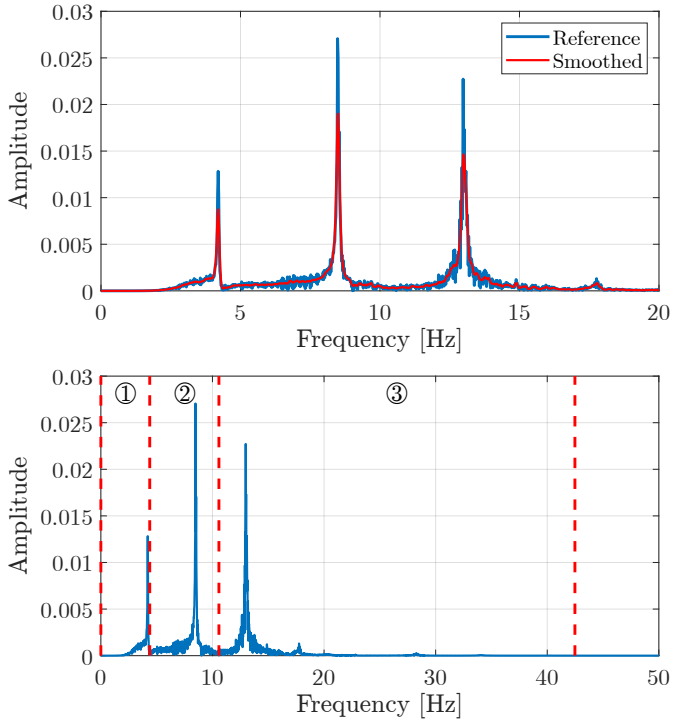

Figure 4.2: Smoothing of the signal frequency spectrum: comparison between original and smoothed frequency spectrum (top); correct segmentation of the frequency spectrum after zero-phase moving average filtering (bottom).

only the peaks whose prominence is larger than a given threshold count towards N while they are trivial peaks otherwise. Keeping this in mind, a tentative value of N is initially established in the first step as the number of peaks of the smoothed frequency spectrum whose amplitude $\hat{F}^*$ fulfills the following condition:

$$\hat{F}^* \geq s_1 \tag{4.3}$$

where s_1 is a threshold parameter. A rational probabilistic criterion is proposed to set the threshold parameter s_1. Let $\hat{F}^*$ be a random variable with non-zero variance $\sigma_{\hat{F}^*}$ and non-zero mean $\mu_{\hat{F}^*}$. Regardless the probabilistic distribution of $\hat{F}^*$, the Chebyshev's inequality [194] states that:

$$\Pr(|\hat{F}^* - \mu_{\hat{F}^*}| \geq k\sigma_{\hat{F}^*}) \leq \frac{1}{k^2} \tag{4.4}$$

where $k \in \mathbb{R}$. Since most of the peaks in the frequency spectrum are due to the noise, those corresponding to real modes are in the tail of the probabilistic distribution of $\hat{F}^*$. For a target probability of exceedance equal to 0.90, it follows from Eq.(4.4) that $s_1 = \mu_{\hat{F}^*} + k\sigma_{\hat{F}^*}$ with $k = 3.162$. It is not recommended to assume a lower target probability of exceedance (i.e., a lower value of k) since this will significantly increase the chance of counting trivial peaks towards N. Conversely, a larger target

probability of exceedance (i.e., a larger value of k) will reduce excessively the number of identifiable modes N. It is highlighted, however, that this first step provides a preliminary estimation of N, whose value can be subjected to adjustments in the further steps of the proposed procedure.

The energy lost in the reconstruction process is evaluated in the second step. To this end, a performance reconstruction factor (PRF) is introduced as follows:

$$\mathrm{PRF} = \frac{\left|\left|y(t) - \sum_{n=1}^{N} y_n(t)\right|\right|^2}{||y(t)||^2} \tag{4.5}$$

where $||\cdot||$ is a suitable norm operator (e.g., Euclidean norm). This parameter is a measure of the accuracy in the reconstruction of the initial signal through the extracted components. The smaller the PRF is, the closer the reconstructed signal $\tilde{y}(t)$ given by Eq.(2.129) is to the original one $y(t)$. Having so done, the following condition is checked:

$$\mathrm{PRF} \leq s_2 \tag{4.6}$$

where s_2 is a threshold parameter. The definition of the threshold parameter s_2 depends on the target fidelity level of the signal reconstruction. A satisfactory trade-off for practical applications is a maximum loss of energy equal to 1%, which implies that $s_2 = 10^{-2}$. If the condition given by Eq.(4.6) is not fulfilled, this means that the signal is under-decomposed and mode-mixing occurs. Therefore, the number of segments must be at least one unit higher than the final value obtained previously (i.e., it must be assumed $N \mapsto N + 1$).

The last step of the proposed procedure aims at checking whether the obtained value of N produces an over-decomposed signal (i.e., the mode-splitting phenomenon occurs). To this end, the signal is decomposed into a number of components equal to N, as it was obtained in the previous step. Hence, the distance between the central frequencies for each couple of consecutive mode functions is evaluated as $\Delta\omega_{n,n+1} = \omega_{n+1} - \omega_n \ \forall n \in [1, N-1]$. Next, it is counted the number of times θ for which the following condition is fulfilled:

$$\Delta\omega_{n,n+1} \leq s_{n,3} \, \forall n \in [1, N-1] \tag{4.7}$$

Following such a check, the number of frequency partitions is updated as $N \mapsto N - \theta$. The definition of the threshold parameter $s_{n,3}$ is related to the frequency resolution of the EFD technique, that is the minimum distance between two consecutive central frequencies that allows the correct extraction of the corresponding components. Taking into account the available studies [204], it is set as $s_{n,3} = 5\omega_n/100$.

The flowchart in Fig. 4.3 illustrates the proposed original procedure for the automatic tuning of the number of frequency partitions N. Once the optimal value of N is obtained at the end of the procedure detailed in Fig. 4.3, the cut-off frequencies are recognized from the smoothed frequency spectrum of the signal as per Eq.(2.125). Finally, the zero-phase filter bank involved in the EFD technique is performed on the actual frequency spectrum of the signal to retrieve the N components.

The proposed procedure for the automatic tuning of N basically looks for its optimal trade-off by preventing both under-decomposition (i.e., mode-mixing) and over-decomposition (i.e., mode-splitting) of the analyzed signal. If the frequency spectrum

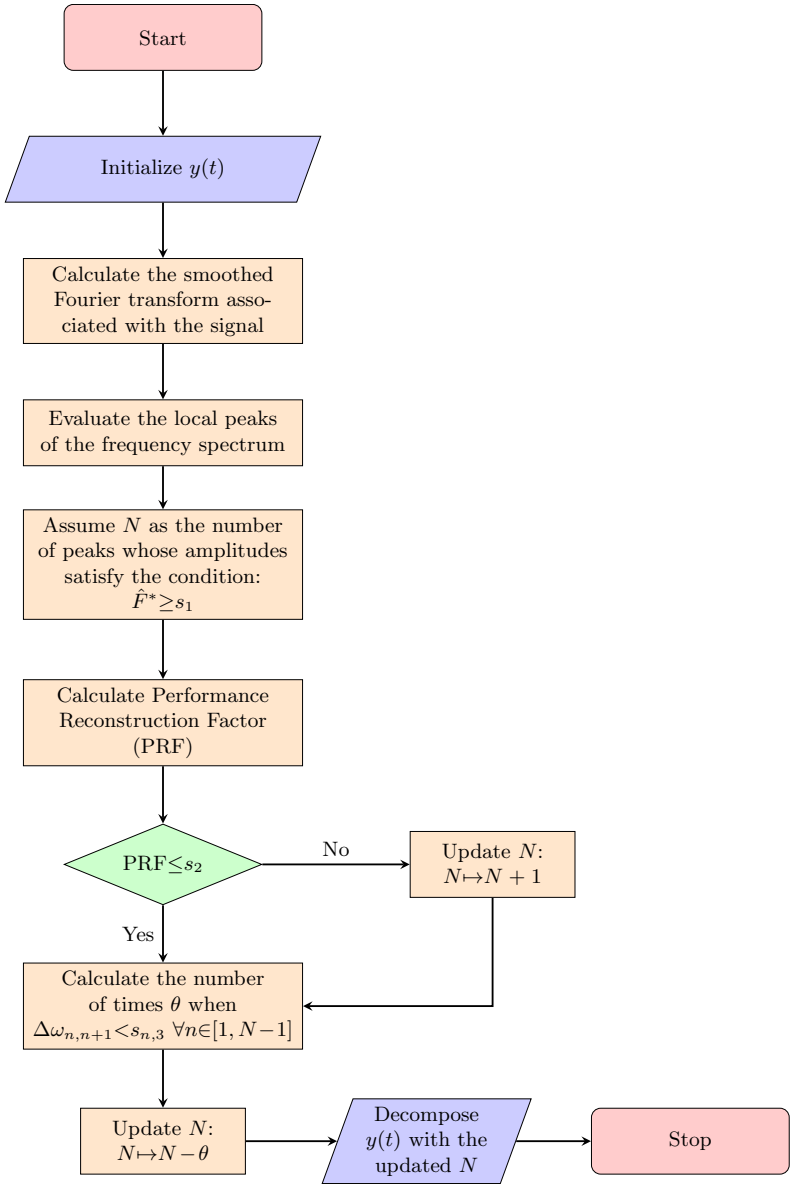

Figure 4.3: Flowchart of the proposed automatic selection procedure for the number of the frequency partitions N.

of the considered signal is smooth enough by itself, then the procedure is likely to converge to the right value of N at the end of the first step whereas the second and the third step holds no influence. This condition, however, is not the most common in practical applications. Consequently, if the frequency spectrum of the signal is rather noisy, then the first step of the procedure will converge to an improper value of N. Unfortunately, the preliminary smoothing of the signal frequency spectrum does not

always fix such a problem. In order to better clarify the existing issues, a real signal with $N = 3$ is investigated in Fig. 4.4 (herein, it is considered the experimental cable response of a cable-stayed bridge that will be thoroughly examined later). On the one hand, if the actual signal frequency spectrum is considered, then the high trivial (i.e., non-physical) peaks near the ones corresponding to the real components will lead to an incorrect estimation of the number of frequency segments N. On the other hand, the selection of the value of N from the smoothed frequency spectrum of the signal only can also produce a wrong spectrum segmentation. In fact, since the application of the smoothing technique on the frequency spectrum makes it more flat, the difference between peaks corresponding to trivial and real modes is reduced and both are wrongly counted towards N, thereby overestimating its value and causing the over-decomposition of the signal. By considering the actual frequency spectrum of the signal, the proposed procedure prevents all these issues taking into account simultaneously the peaks prominence as well as the fidelity of the signal reconstruction and the allowable frequency resolution of the EFD technique. So doing, the number of frequency partitions N and the corresponding boundaries are settled correctly as shown in Fig. 4.4.

4.3 Validation on synthetic signals

4.3.1 Generation of synthetic signals

The proposed improved automatic implementation of the EFD technique is validated against synthetic signals in such a way to quantify objectively its accuracy and robustness. Furthermore, since the reference results are known a priori in case of synthetic signals, the results obtained via the proposed method based on the EFD technique are compared with those carried out by means of the VMD technique [30] in order to assess objectively its performance. To this end, the typical free vibration response of a multi-degree-of-freedom civil structure is considered, which can be generally expressed as follows:

$$y(t) = \sum_{n=1}^{N} A_n e^{-\xi_n \omega_n t} \cos(\bar{\omega}_n t - \varphi_n) + w(t) \tag{4.8}$$

where A_n is the nth component amplitude, ξ_n is the nth modal damping ratio, $\omega_n = 2\pi\nu_n$ is the nth modal circular frequency (ν_n being the modal frequency), $\bar{\omega}_n = \omega_n\sqrt{1-\xi_n^2}$ is the corresponding nth circular damped frequency, φ_n is the nth component phase and $w(t)$ is the measurement noise.

Free-noise data are considered to evaluate the accuracy under reference conditions. Noisy data are taken into account in order to test and evaluate the robustness of the identification under more realistic monitoring conditions. The measurement noise $w(t)$ in Eq.(4.8) is generated as white Gaussian noise with an assigned signal-to-noise ratio (SNR), which is defined as follows:

$$\mathrm{SNR} = 10\log_{10}\left(\frac{P_s}{P_n}\right) \tag{4.9}$$

where P_s and P_n denote the signal and noise average power, respectively. The lower the SNR, the noisier the signal will be. Noisy signals are thus simulated according to the

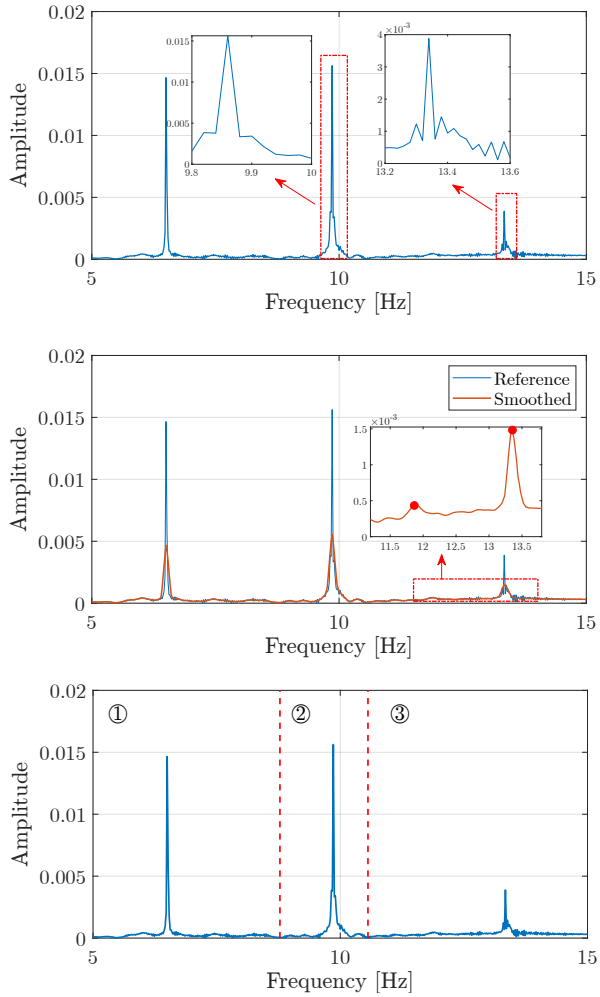

Figure 4.4: Possible issues that can jeopardize the correct estimation of the number of the frequency partitions N for a real signal: occurrence of high trivial peaks near the ones corresponding to the real components of the actual frequency spectrum of the signal (top); ill-conditioned discrimination between trivial and real peaks (both marked with dots) due to the flattening originated by a preliminary smoothing of the signal frequency spectrum (middle). Correct spectrum segmentation according to the proposed automatic procedure (bottom).

targeted SNR level by assuming an additive-type randomly generated white Gaussian noise $w(t)$ as per Eq.(4.8). Three noise levels are considered, namely 0 dB, 5 dB and 15 dB (it is pointed out that the resulting synthetic noisy signals are not subjected to preliminary denoising). Because of the inherent randomness of the noise, a set of 100 independent noisy signals is produced for each noise level to allow a statistical appraisal of the final results. It is remarked that modal frequency and damping ratio maintain their nominal value in each noisy signal simulation whereas the randomness is only related to the additive Gaussian white noise $w(t)$, which is fleshly generated for each run.

4.3.2 Synthetic signal with closely spaced modes

It is considered the free response of a multi-degree-of-freedom system simulated according to Eq.(4.8) and consisting of four superimposed vibrations modes (i.e., $N = 4$). The natural frequency values are taken equal to $\nu_1 = 1.5$ Hz, $\nu_2 = 3.2$ Hz, $\nu_3 = 3.6$ Hz and $\nu_4 = 10$ Hz. It can be observed that the second and the third natural frequency are rather close to each other (i.e., $\Delta\omega_{2,3}/\omega_3$ about 10%) in order to assess the performance of the proposed approach in detecting closely spaced modes. This condition sometimes occurs when dealing with civil structures, even though it is not very common [180]. The modal damping ratio values are $\xi_1 = 3\%$, $\xi_2 = 1.2\%$, $\xi_3 = 0.8\%$ and $\xi_4 = 2\%$. The amplitudes of the modal components are assumed as $A_1 = 3$, $A_2 = 1.8$, $A_3 = 1.6$ and $A_4 = 5$. All components are in phase (i.e., $\varphi_n = 0\ \forall n$) and a sampling frequency $F_s = 1$ kHz is adopted.

To begin with, the case of a free-noise signal is analyzed and thus the measurement noise $w(t)$ in Eq.(4.8) is initially null. Figure 4.5 shows the considered signal and the corresponding frequency spectrum.

It can be inferred from Fig. 4.5 that the proposed algorithm for the selection of N (see Fig. 4.3) enables the extraction of the right number of frequency partitions through the EMD technique. Taking into account the Nyquist-Shannon sampling theorem, the following frequency boundaries are obtained: $\nu_{\mathrm{A}} = 0$, $\nu_{\mathrm{B}} = 2.5$ Hz, $\nu_{\mathrm{C}} = 3.4$ Hz, $\nu_{\mathrm{D}} = 7.7$ Hz and $\nu_{\mathrm{E}} = 499.9$ Hz. Figure 4.6 shows that there exists an almost perfect match between the automatically extracted components of the considered free-noise synthetic signal and the corresponding reference analytical modes.

The same free-noise synthetic signal is now decomposed by means of the VMD technique. To this end, some control parameters must be set in advance to perform the decomposition [125]. Particularly, the two key control parameters governing the performance of the VMD technique, here recalled for clarity's sake, are the number of expected modes K and the quadratic penalty factor α [123,128]. The control parameter K defines the number of uni-modal components to be extracted from the signal. Once again, therefore, an over-decomposition of the signal is obtained for a high value of K while a low value of K can produce mode-mixing effects. The control parameter α rules the amplitude of the bandwidth. If α is small, then the bandwidths will be overestimated and closely spaced modes might be grouped by causing mode-mixing effects. Conversely, a too-high value of α can produce distortions that will compromise the fidelity of the signal reconstruction. The main advantage of the EFD technique over the VMD technique is thus related to the lower number of control parameters to be tuned: while N only must be determined within the EFD technique, K and α must

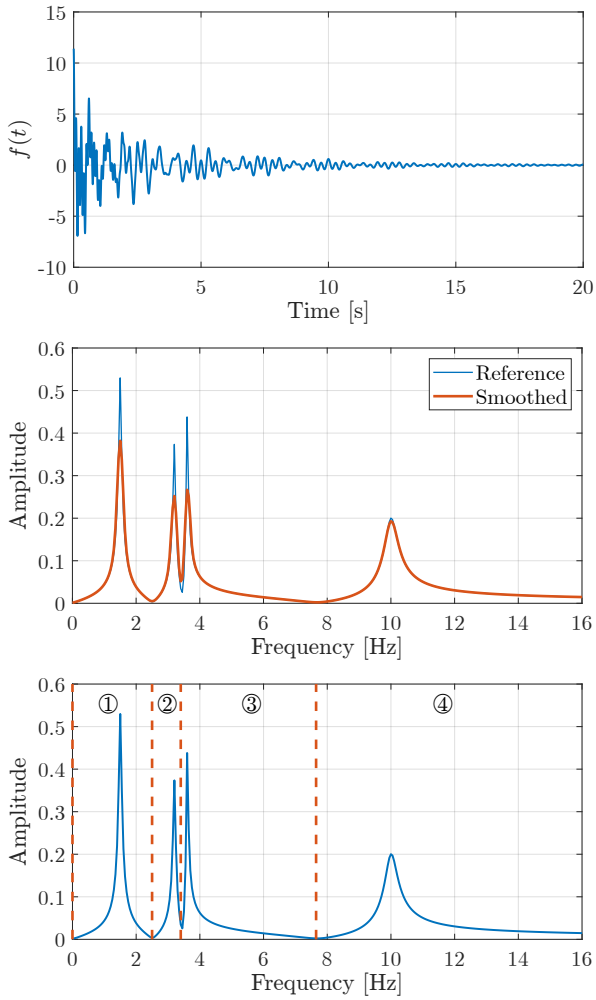

Figure 4.5: Synthetic free vibration response with closely spaced modes: free-noise synthetic signal (top); comparison between original and smoothed frequency spectrum of the signal (middle); frequency spectrum segmentation by means of the proposed automatic implementation of the EFD technique (bottom).

be defined to perform the VMD technique. It must be also remarked that, even if the correct value of K is singled out, the results of the VMD technique are very sensitive to variations of the value of α. Additionally, in view of automatic applications, the proper selection of the parameter N in the EFD technique by means of the proposed procedure is rather straightforward as compared to the optimal tuning of the parameters K and α involved in the VMD technique. In this regard, the optimal tuning of K in the VMD technique according to the procedure proposed by Mazzeo et al. [30] needs the calculation of a stabilization diagram based on the concept of minimum correlation between mode functions. Such a stabilization diagram then provides a feasible set of values for α, from which the optimum is determined taking into account the power

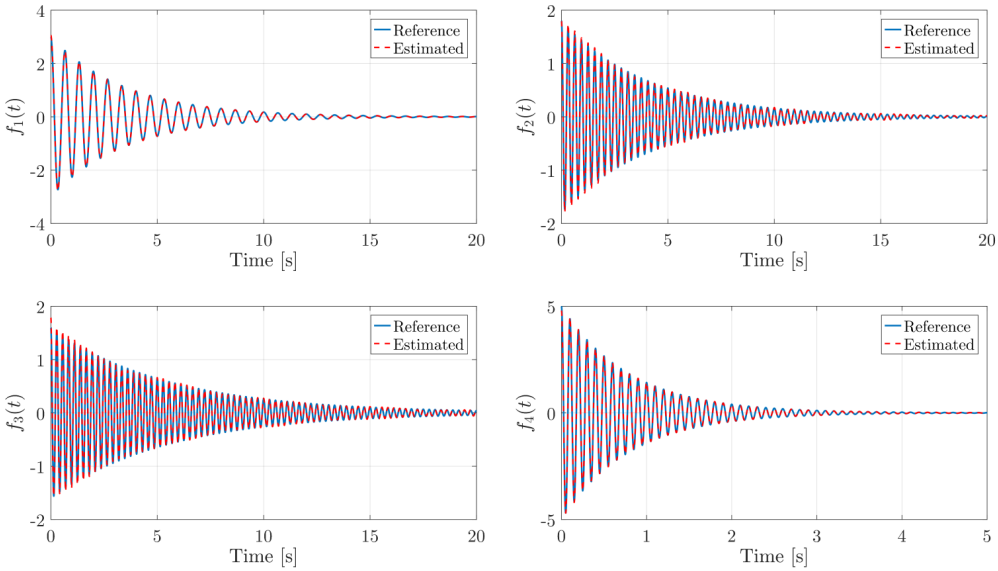

Figure 4.6: Synthetic free vibration response with closely spaced modes: comparison between the reference analytical modes and the components extracted using free-noise data by means of the proposed automatic implementation of the EFD technique.

spectrum of the processed signal and each mode function extracted iteratively by means of the VMD technique. More details about the automatic optimal tuning procedure for the control parameters of the VMD technique are provided in Chapter 3.

Figure 4.7 illustrates the results carried out by applying the VMD technique. The decomposition is initially performed by assuming $K = 4$ and the default value $\alpha = 10^3$. Lastly, the automatic tuning procedure presented by Mazzeo et al. [30] is applied, which provides $K = 4$ and $\alpha = 5.7 \cdot 10^5$. The comparison between the extracted components and the corresponding reference analytical modes demonstrates the correctness of the VMD technique, provided that the numerical values of both K and α are properly selected.

Tables 4.1-4.2 provide the results obtained by implementing the VMD technique with default value of α (i.e., $\alpha = 10^3$, given $K = 4$) and the optimal value of the control parameters estimated according to the results in Chapter 3 and published in Mazzeo et al. [30] (i.e., $\alpha = 5.7 \cdot 10^5, K = 4$). The results obtained by means of the proposed implementation of the EFD technique are also reported.

The analysis of the results listed in Tab. 4.1 demonstrates that the VMD technique as well as the EFD technique are able to identify accurately the natural frequencies of the considered free-noise synthetic signal when they are properly implemented. The exact value of the natural frequencies is retrieved by applying the EFD technique. A negligible error is obtained by estimating the natural frequencies through the VMD technique, provided that the value of α is properly optimized (very large errors can occur for lower modes otherwise). Remarkably, Table 4.2 also demonstrates that the way by which the signal is decomposed has significant effects on the accuracy of the modal damping ratio identification, even though noiseless data are considered. As regards

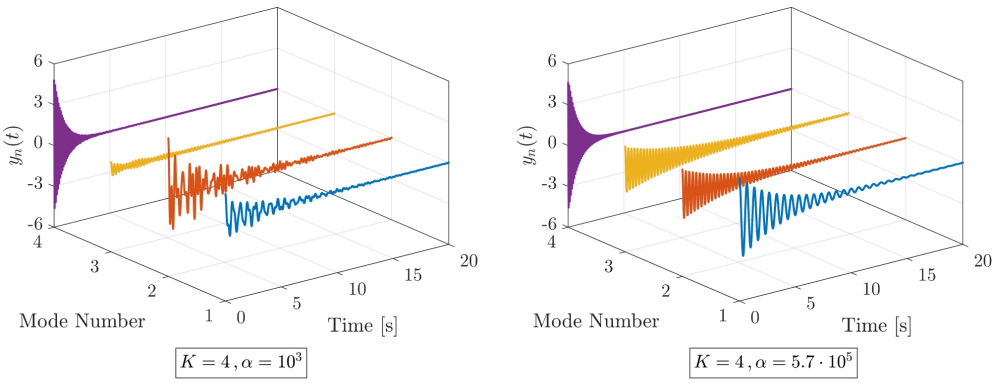

Figure 4.7: Synthetic free vibration response with closely spaced modes: modal components extracted by means of the VMD technique using free-noise data for the default value $\alpha = 10^3$ (left) and $\alpha = 5.7 \cdot 10^5$ as estimated automatically according to Mazzeo et al. [30] (right).

Table 4.1: Synthetic free vibration response with closely spaced modes: identification of the natural frequencies using free-noise data by applying the VMD technique (with both default and optimal values of α and K) and the EFD technique (with N calculated automatically according to the proposed procedure).

Mode	VMD (default α)		VMD ($\alpha = 5.7 \cdot 10^5$)		EFD (proposed)	
	Estimated frequency [Hz]	Relative error [%]	Estimated frequency [Hz]	Relative error [%]	Estimated frequency [Hz]	Relative error [%]
1	1.76	17.33	1.4988	0.08	1.5	0
2	2.54	20.63	3.1988	0.04	3.2	0
3	3.57	0.83	3.5993	0.02	3.6	0
4	9.98	0.20	9.9882	0.12	10	0

the application of the VMD technique, average and maximum value of the relative error in modal damping ratios identification are equal to 2.33% and 7.5%, respectively, after a suitable calibration of α (unacceptable errors are obtained otherwise). Average and maximum value of the relative error in modal damping ratios identification are equal to 0.20% and 0.83% when the EFD technique is applied. The maximum error in modal damping ratio identification is achieved when closely spaced signal components are processed, regardless of the way by which the free-noise signal is decomposed. Hence, although the identification of the modal damping ratios from free-noise data via the VMD technique is still very good, the corresponding average and maximum value of the relative error are about ten times those obtained by applying the EFD, which thus results more accurate.

The robustness against the noise of the identification is now assessed. Figure 4.8 shows some sample noisy signals generated according to different noise levels as well as the frequency spectrum corresponding to the sample noisy signal with the lowest SNR value. Figure 4.8 confirms the feasibility of the proposed procedure (see Fig. 4.3) for the automatic definition of the N components to be extracted by means of the EFD

Table 4.2: Synthetic free vibration response with closely spaced modes: identification of the modal damping ratios using free-noise data by applying the VMD technique (with both default and optimal values of α and K) and the EFD technique (with N calculated automatically according to the proposed procedure).

Mode	VMD (default α)		VMD ($\alpha = 5.7 \cdot 10^5$)		EFD (proposed)	
	Estimated damping [%]	Relative error [%]	Estimated damping [%]	Relative error [%]	Estimated damping [%]	Relative error [%]
1	3.4	13.33	3	0	3	0
2	1.7	41.67	1.19	0.83	1.21	0.83
3	0.43	46.25	0.86	7.5	0.8	0
4	2	0	1.98	1	2	0

technique even in case of noisy data. It is noted that the segmentation procedure detects and removes most of the noise from the partitions in the high-frequency region of the signal spectrum. The comparison between Fig. 4.8 and Fig. 4.5 highlights that the segmentation process reduces the width of the last partition.

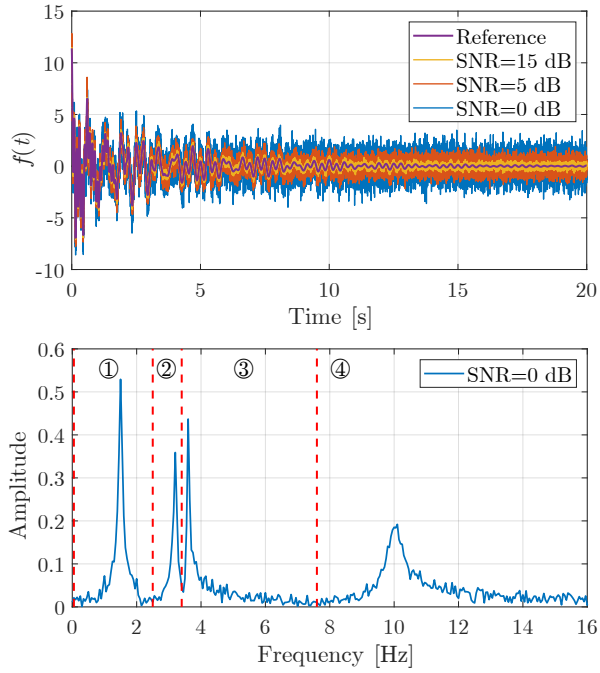

Figure 4.8: Synthetic free vibration response with closely spaced modes: noisy synthetic signals for different values of the SNR (top); frequency spectrum segmentation of the synthetic signal with the highest SNR by means of the proposed automatic implementation of the EFD technique (bottom).

It has been found that the identification of the natural frequencies is not influenced significantly by the decomposition technique even in case of external disturbances.

Therefore, natural frequencies can be properly identified from noisy data for all values of the SNR by using either the VMD technique or the EFD technique. The estimation of the modal damping ratio is instead more sensitive to the measurement noise, as it emerges from the results listed in Tabs. 4.3-4.4.

Table 4.3: Synthetic free vibration response with closely spaced modes: identification of the modal damping ratios using noisy data by applying the EFD technique (with N calculated automatically according to the proposed procedure). Average value and standard deviation of the estimated modal damping ratio are reported. Moreover, mean and maximum value (within brackets) of the relative error are provided.

	SNR=15 dB			SNR=5 dB			SNR=0 dB		
Mode	Estimated damping [%]	Standard Deviation [-]	Relative error [%]	Estimated damping [%]	Standard Deviation [-]	Relative error [%]	Estimated damping [%]	Standard Deviation [-]	Relative error [%]
1	2.99	1.96E−2	0.08 (2.11)	2.98	6.08E−2	0.50 (6.51)	2.97	1.22E−1	0.77 (9.37)
2	1.21	1.17E−2	0.56 (3.82)	1.22	3.81E−2	1.56 (10.21)	1.24	6.83E−2	3.15 (15.77)
3	0.82	9.36E−3	2.55 (5.67)	0.84	3.13E−2	4.89 (15.08)	0.85	5.78E−2	5.80 (23.45)
4	2.01	1.89E−2	0.50 (3.10)	2.04	3.34E−1	2.21 (17.66)	1.94	4.59E−1	3.00 (38.40)

Table 4.4: Synthetic free vibration response with closely spaced modes: identification of the modal damping ratios using noisy data by applying the VMD technique (with α and K calculated automatically according to the procedure proposed by Mazzeo et al. [30]). Average value and standard deviation of the estimated modal damping ratio are reported. Moreover, mean and maximum value (within brackets) of the relative error are provided.

	SNR=15 dB			SNR=5 dB			SNR=0 dB		
Mode	Estimated damping [%]	Standard Deviation [-]	Relative error [%]	Estimated damping [%]	Standard Deviation [-]	Relative error [%]	Estimated damping [%]	Standard Deviation [-]	Relative error [%]
1	2.99	2.20E−2	0.33 (2.20)	2.98	8.31E−2	0.60 (9.26)	2.93	1.51E−1	2.33 (15.88)
2	1.17	2.13E−2	2.41 (6.61)	1.16	6.74E−2	2.50 (15.78)	1.15	1.46E−1	4.17 (35.02)
3	0.85	1.32E−2	6.29 (9.49)	0.84	4.18E−2	5.59 (15.66)	0.75	7.42E−2	6.25 (21.99)
4	1.95	2.58E−2	2.79 (6.33)	1.94	8.17E−2	2.86 (14.01)	1.93	4.70E−1	3.50 (40.01)

The results in Tab. 4.3 demonstrate that the application of the EFD technique based on the proposed automatic segmentation of the signal spectrum provides very good estimates of the modal damping ratios even in case of noisy signals. As expected, the smaller is the SNR value, the larger is the error. This confirms that the proposed automatic implementation of the EFD technique provides a very good and robust frequency spectrum decomposition for modal damping ratio identification. Once again, the accuracy of the automatic procedure based on the VMD technique proposed in Chapter 3 is satisfactory, but slightly larger errors are found. In fact, the highest average and maximum value of the relative errors in damping ratios identification by

means of the EFD technique are equal to 5.80% and 38.40%, respectively, for the highest noise level. The corresponding values of the relative errors obtained via the VMD technique are 6.25% and 40.01%, respectively.

The use of the area-based approach for modal damping ratios as proposed in the present study also plays an important role in this regard. In fact, if the standard logarithmic decrement method is applied after signal decomposition as proposed by He et al. [110], then the accuracy of the modal damping ratios identification reduces significantly. It can be noted in Tab. 4.5 that, if the EFD technique is employed in combination with the standard decrement logarithmic method to identify the relevant modes, then the highest relative error for the highest noise level is about 12.93% whereas the maximum relative error is 81.28%. This confirms that the EFD technique should be implemented together with a suitable modal damping ratio identification procedure in order to obtain the best estimates of the modal characteristics of the structures.

Table 4.5: Synthetic free vibration response with closely spaced modes: identification of the modal damping ratios using noisy data by applying the EFD technique (with N calculated automatically according to the proposed procedure) in combination with the standard decrement logarithmic method. Average value and standard deviation of the estimated modal damping ratio are reported. Moreover, mean and maximum value (within brackets) of the relative error are provided.

	SNR=15 dB			SNR=5 dB			SNR=0 dB		
Mode	Estimated damping [%]	Standard Deviation [-]	Relative error [%]	Estimated damping [%]	Standard Deviation [-]	Relative error [%]	Estimated damping [%]	Standard Deviation [-]	Relative error [%]
1	2.94	4.71E−2	1.85 (5.87)	2.96	1.50E−1	1.16 (13.63)	3.14	2.73E−1	4.66 (22.55)
2	1.33	1.81E−2	11.05 (15.00)	1.32	5.81E−2	10.35 (23.77)	1.33	1.07E−1	10.71 (47.53)
3	0.89	3.47E−2	11.49 (21.72)	0.88	1.04E−1	10.05 (43.98)	0.90	2.26E−1	12.93 (81.28)
4	2.05	3.38E−2	2.25 (5.77)	2.11	2.78E−1	5.29 (18.13)	2.16	9.58E−1	8.18 (57.94)

4.3.3 Synthetic signal with minor mode

It is now considered the free response of a multi-degree-of-freedom system simulated according to Eq.(4.8) and consisting of three superimposed vibrations modes (i.e., $N = 3$). The natural frequencies are equal to $\nu_1 = 1.5$ Hz, $\nu_2 = 3.5$ Hz and $\nu_3 = 7$ Hz whereas modal damping ratios are equal to $\xi_1 = 3\%$, $\xi_2 = 5\%$, $\xi_3 = 3\%$. The amplitudes of the three signal components are equal to $A_1 = 1.5$, $A_2 = 0.95$ and $A_3 = 4$. All components are in phase (i.e., $\varphi_n = 0\ \forall n$). Different noise levels are considered, and a sampling frequency $F_s = 1$ kHz is adopted. Figure 4.9 shows some sample noisy signals generated according to different noise levels as well as the frequency spectrum corresponding to the sample noisy signal with the lowest SNR value. The dynamic identification in the case of a minor vibration mode is the main issue that the present benchmark aims at dealing with. In fact, it is evident from the frequency spectrum in Fig. 4.9 that the peak corresponding to the second mode is much lower than the peaks related to the first and third mode. This condition can

occur when the free vibrations are due to a force or displacement applied close to a nodal point of a highly damped vibration mode. As a consequence, such vibration mode is lowly excited and its accurate identification can be challenging.

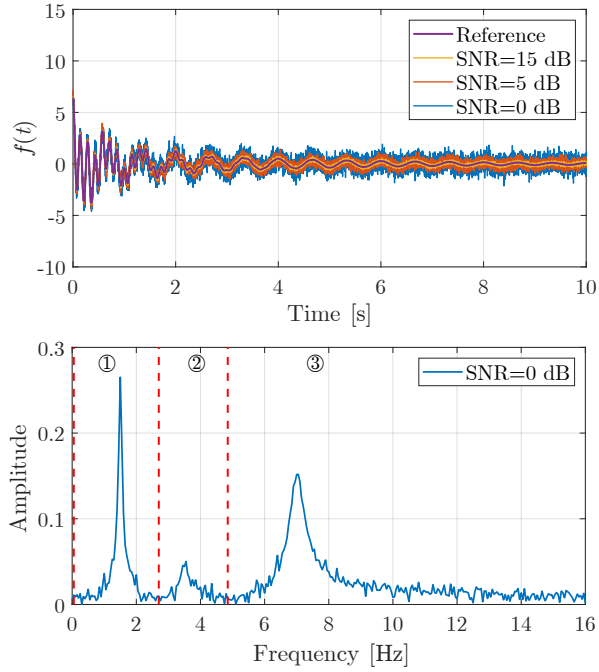

Figure 4.9: Synthetic free vibration response with minor mode: noisy synthetic signals for different values of the SNR (top); frequency spectrum segmentation of the synthetic signal with the highest SNR by means of the proposed automatic implementation of the EFD technique (bottom).

Once again, natural frequencies are well identified by means of either the EFD technique or the VMD technique. The performances of the two approaches diverge significantly when the modal damping ratios identification is examined, as can be observed by comparing the results listed in Tables 4.6-4.7. On average, Tables 4.6-4.7 demonstrate that the implemented identification approaches based on the EFD technique and the VMD technique exhibit almost similar performance in terms of modal damping ratio identification for a low noise level. The accuracy of the VMD technique is still satisfactory on average for mid-high noise levels, but a significant degradation is evidently noted. In fact, the largest value of the average relative error is less than 2% for both signal decomposition techniques at SNR=15 dB, but it is almost equal 15% for SNR=0 dB if the modal damping ratios are obtained through the VMD technique while is still less than 2% if the EFD technique is employed instead. The critical analysis of the results in Tables 4.6-4.7 especially highlights the different robustness between the two approaches. Standard deviations of the modal damping ratios estimated according to the proposed automatic implementation of the EFD technique are lower than the corresponding values obtained through the VMD technique. Furthermore, a deeper inspection of the maximum relative errors demonstrates that the VMD technique sometimes fails to provide satisfactory estimates of the modal damping ra-

Table 4.6: Synthetic free vibration response with minor mode: identification of the modal damping ratios using noisy data by applying the EFD technique (with N calculated automatically according to the proposed procedure). Average value and standard deviation of the estimated modal damping ratio are reported. Moreover, mean and maximum value (within brackets) of the relative error are provided.

	SNR=15 dB			SNR=5 dB			SNR=0 dB		
Mode	Estimated damping [%]	Standard Deviation [-]	Relative error [%]	Estimated damping [%]	Standard Deviation [-]	Relative error [%]	Estimated damping [%]	Standard Deviation [-]	Relative error [%]
1	2.99	2.27E−2	0.03 (1.86)	2.98	7.15E−2	0.31 (5.55)	2.97	1.25E−1	0.81 (9.64)
2	5.03	1.08E−1	0.59 (6.38)	5.09	3.09E−1	1.77 (14.17)	4.90	5.41E−1	1.99 (25.10)
3	3.00	1.78E−2	0.08 (1.44)	3.01	5.08E−2	0.36 (4.48)	2.98	9.37E−2	0.55 (7.92)

Table 4.7: Synthetic free vibration response with minor mode: identification of the modal damping ratios using noisy data by applying the VMD technique (with α and K calculated automatically according to the procedure proposed by Mazzeo et al. [30]). Average value and standard deviation of the estimated modal damping ratio are reported. Moreover, mean and maximum value (within brackets) of the relative error are provided.

	SNR=15 dB			SNR=5 dB			SNR=0 dB		
Mode	Estimated damping [%]	Standard Deviation [-]	Relative error [%]	Estimated damping [%]	Standard Deviation [-]	Relative error [%]	Estimated damping [%]	Standard Deviation [-]	Relative error [%]
1	2.99	3.05E−2	0.08 (3.24)	2.94	1.07E−1	1.95 (12.60)	2.89	2.04E−1	3.63 (17.80)
2	5.10	9.40E−2	1.94 (16.14)	4.83	8.54E−1	3.46 (47.39)	4.43	12.49E−1	11.47 (54.04)
3	2.97	1.84E−2	0.89 (12.38)	2.84	4.51E−1	5.36 (53.83)	2.55	6.89E−1	14.92 (55.75)

tios (i.e., a relative error larger than 25% occurred for the second and the third modal damping ratio in 1%, 5% and 18% of the simulations at SNR=15 dB, SNR=5 dB and SNR=0 dB, respectively). Conversely, the automatic implementation of the EFD technique presented in the current study dramatically reduces the number of failed identifications and is really effective in alleviating the maximum value of the relative error, thereby ensuring a more consistent estimation of the modal damping ratios than the VMD technique. The identification of the minor mode is especially challenging for both signal decomposition techniques. It can be deduced from Tab. 4.7 that the inaccurate identification of the minor mode can affect, to a large extent, the reliable identification of higher modes if the VMD technique is employed. Indeed, it can be inferred from Tab. 4.7 that the identification of the vibration mode following the minor mode is less accurate than the first vibration mode when the VMD technique is adopted. Conversely, it is noteworthy to observe that the proposed implementation of the EFD technique does not facilitate the propagation of the larger errors associated with the identification of the minor mode. This is deduced from the results in Tab. 4.6, which show that the first and the third modal damping ratios are identified with a similar accuracy level when the EFD technique is adopted.

4.4 Experimental application on a roadway bridge

The first experimental application herein addressed deals with the roadway bridge over the Garigliano river which has been already discussed in the previous chapter. The data recorded at the cables (which were tested under free vibrations and previously analyzed in the context of the VMD-based identification approach) have been once again processed adopting the alternative EFD-based approach to compare its performance with respect to a reliable identification approach. The dynamic response has been monitored by means of a couple of uniaxial accelerometers with sensitivity equal to 10 V/g, which were mounted on the two faces of a steel angular element in such a way to record both vertical and horizontal accelerations with respect to the longitudinal axis of each cable. This angular element has been fixed to the bridge cable at an average height equal to 3.8 m by means of nylon straps. The excitation on the cables was induced by applying an impulsive load along two distinct directions (i.e., longitudinal and transversal directions with respect to the longitudinal axis of the cables). Natural frequencies and damping ratios have been identified from the free vibration response of each cable by means of the EFD technique assisted by the proposed procedure for the optimal automatic tuning of the control parameter N. As an example, Fig. 4.10 shows the free vibration response of the shortest bridge cable (Rome direction) due to a vertical impulse load and the corresponding frequency spectrum. The proposed pro-

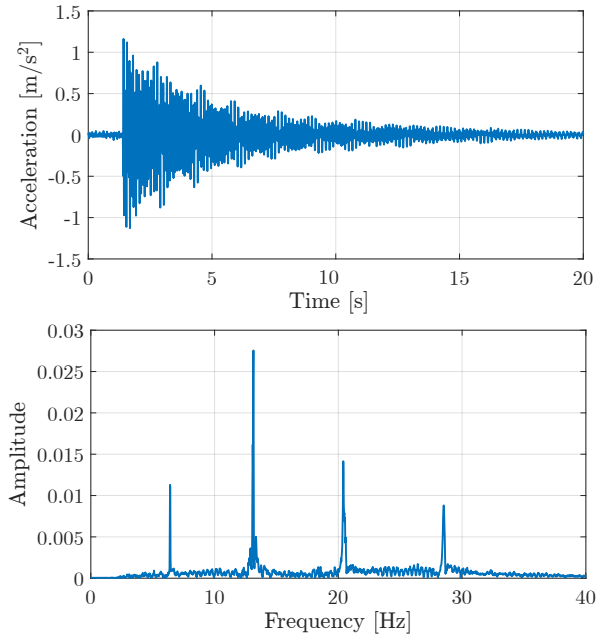

Figure 4.10: Dynamic response of the shortest bridge cable (Rome direction): free vibration due to a vertical impulse load (top); frequency spectrum of the considered signal (bottom).

cedure illustrated in Fig. 4.3 provides the correct value of N for the analyzed signal, as it is shown in Fig. 4.11. A total of $N = 4$ frequency partitions has been identified and the corresponding extracted modes are plotted in Fig. 4.12. For the considered signal,

the estimated natural frequencies are $\nu_1 = 6.42$ Hz, $\nu_2 = 13.16$ Hz, $\nu_3 = 20.52$ Hz, and $\nu_4 = 28.52$ Hz, while the modal damping ratios are equal to $\xi_1 = 0.12\%$, $\xi_2 = 0.16\%$, $\xi_3 = 0.22\%$, $\xi_4 = 0.29\%$.

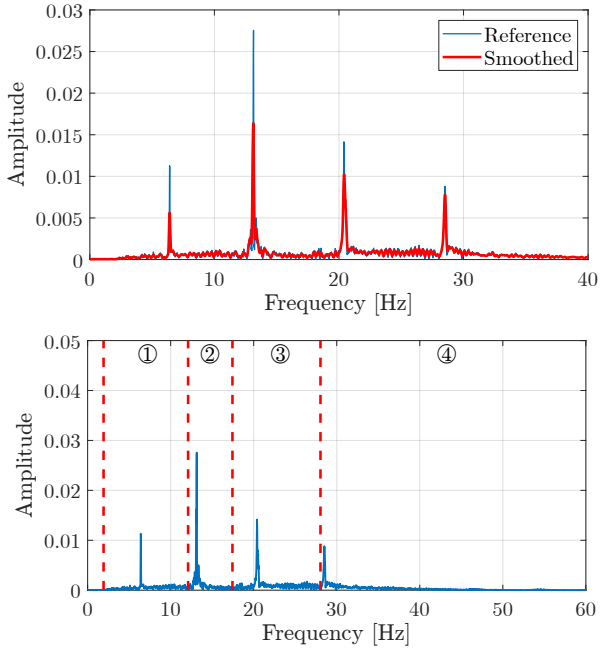

Figure 4.11: Dynamic response of the shortest bridge cable (Rome direction): comparison between original and smoothed frequency spectrum of the considered signal (top); frequency spectrum segmentation of the considered signal (bottom).

The proposed identification procedure has been applied automatically (i.e., without any external feedback) to all the available experimental data. The identified modal frequencies for the first four modes of the bridge cables are listed in Tab. 4.8 (natural frequency values are averaged over all the available signals for the examined cable). It can be observed in Tab. 4.8 that the natural frequencies of the higher modes are approximately integer multiples of the fundamental frequency, in agreement with classical theoretical results about the cable dynamics. These results are also in agreement with previous studies that have exploited ambient vibrations [166, 189].

The natural frequencies of the cables have been also calculated numerically in order to evaluate the general correctness of the experimental estimates obtained by means of the proposed identification procedure; to this aim the Eq.(3.20) proposed by Fang et al. [191] has been adopted, being known the cables tensile force T. Specifically, T is determined according to the original design and includes possible variations due to traffic loads and thermal gradients. Moreover, the actual tensile force of the cables is properly reduced (as compared to the initial value) to also account for tension losses due to steel relaxation according to Eurocode 2 formulation (see Eq.(3.21)) [205]. Figures 4.13-4.14 show the ratio between the natural frequency of the cables estimated by means of the proposed identification procedure $\nu_{n,\mathrm{EFD}}$ and the corresponding reference numerical values $\nu_{n,\mathrm{num}}$ predicted by means of Eqs. 3.20-3.21. These plots demon-

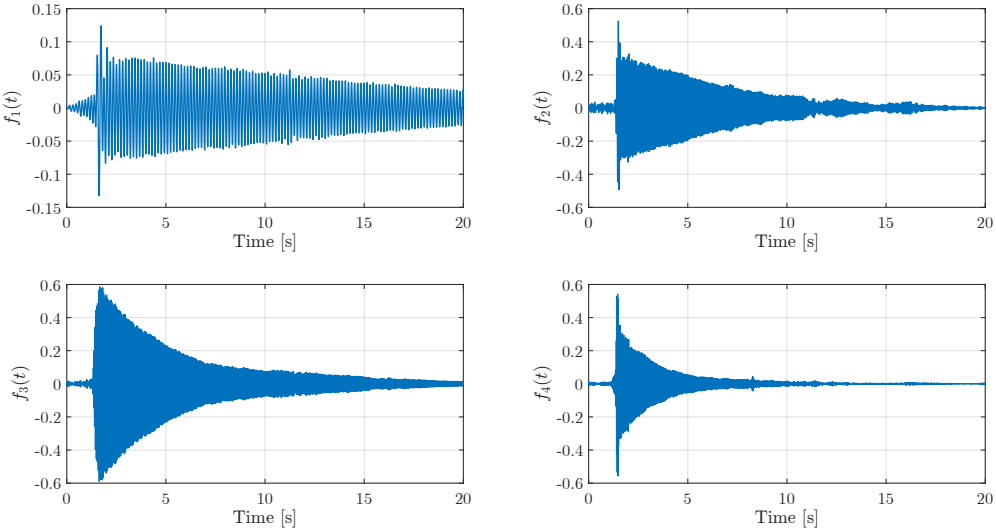

Figure 4.12: Dynamic response of the shortest bridge cable (Rome direction): components extracted from the considered signal via EFD technique.

strate a very good agreement between experimental values and numerical predictions. The maximum relative difference is about 5%, and a small scattering is observed by processing different records. For almost all the cables, numerical predictions of the natural frequencies are slightly larger than the experimental values.

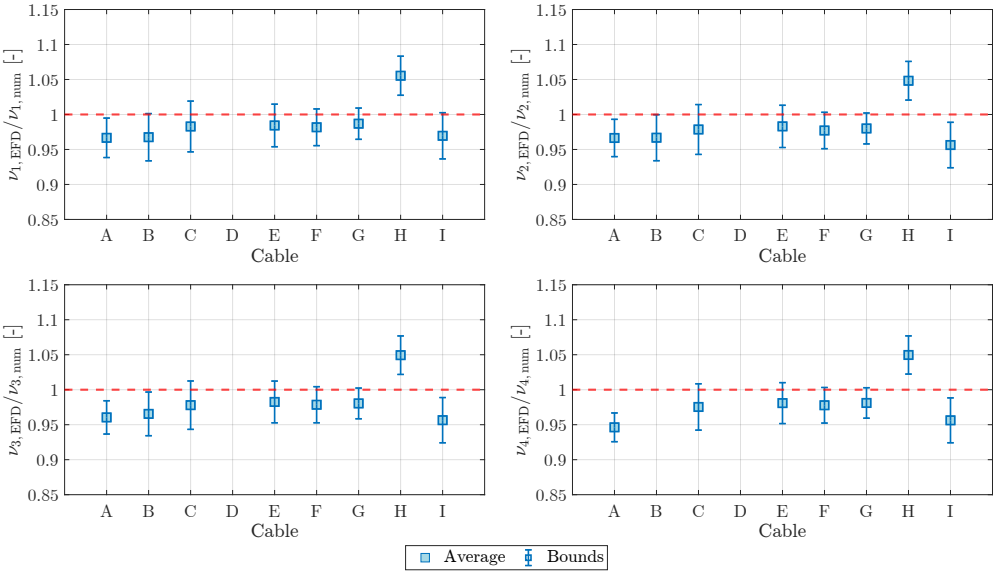

Figure 4.13: Ratio between the natural frequencies of the bridge cables (Rome direction) estimated by means of the proposed identification procedure based on the EFD technique and the corresponding reference numerical values predicted by taking into account the tension losses due to steel relaxation.

Table 4.8: Natural frequencies for the first four vibration modes of the bridge cables estimated by means of the proposed procedure based on the EFD technique.

Cable	Rome direction				Naples direction			
	ν_1 [Hz]	ν_2 [Hz]	ν_3 [Hz]	ν_4 [Hz]	ν_1 [Hz]	ν_2 [Hz]	ν_3 [Hz]	ν_4 [Hz]
A	6.41	13.14	20.48	28.54	6.13	12.57	19.60	-
B	4.21	8.52	13.04	-	4.19	8.48	13.00	17.81
C	3.23	6.51	9.88	13.38	3.21	6.48	9.83	13.32
D	-	-	-	-	2.53	5.06	7.66	10.33
E	2.16	4.34	6.55	8.79	2.16	4.34	6.54	8.78
F	1.87	3.76	5.68	7.61	1.90	3.80	5.72	7.69
G	1.65	3.32	5.00	6.70	1.67	3.37	5.05	6.77
H	1.50	3.00	4.51	6.03	1.49	2.99	4.50	6.02
I	1.26	2.51	3.78	5.06	1.28	2.54	3.83	5.14

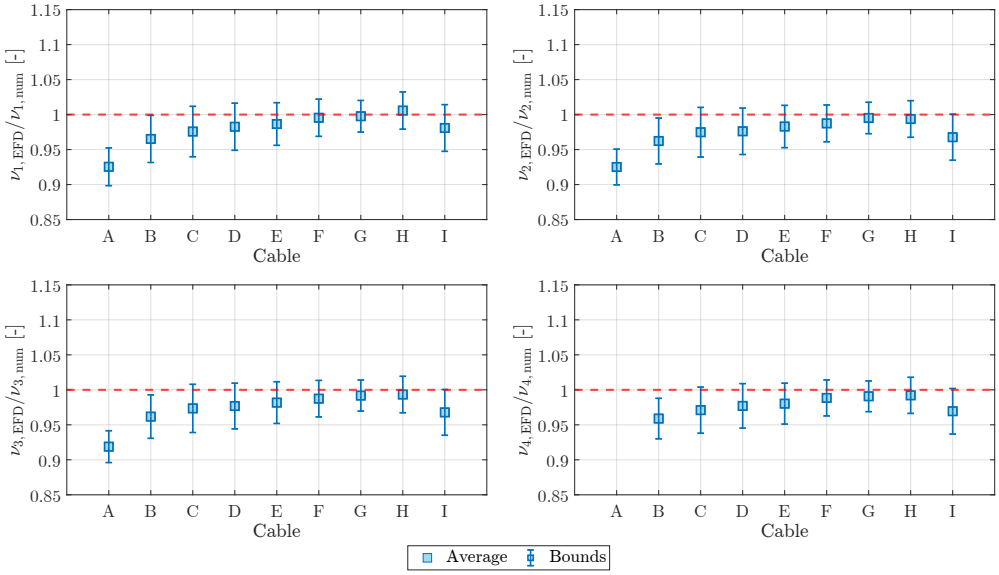

Figure 4.14: Ratio between the natural frequencies of the bridge cables (Naples direction) estimated by means of the proposed identification procedure based on the EFD technique and the corresponding reference numerical values predicted by taking into account the tension losses due to steel relaxation.

To further confirm the accuracy of the identified natural frequency values, all records have been also processed through the VMD technique by implementing the procedure proposed in Chapter 3 (the corresponding natural frequency values are denoted as $\nu_{n,\mathrm{VMD}}$). Results in Fig. 4.15 demonstrate that there exists an excellent agreement on average between the two approaches, as the points settle down close to the quadrant bisector line for both roadway directions and for all the cables. Nonetheless, a more comprehensive statistical analysis performed on the natural frequencies obtained for each cable from all available records confirms that the proposed identification approach based on the EFD technique is more robust. In fact, the maximum

coefficient of variation of the natural frequencies identified by means of the EMD technique and the VMD technique is equal to $7.72 \cdot 10^{-3}$ and $6.47 \cdot 10^{-2}$, respectively.

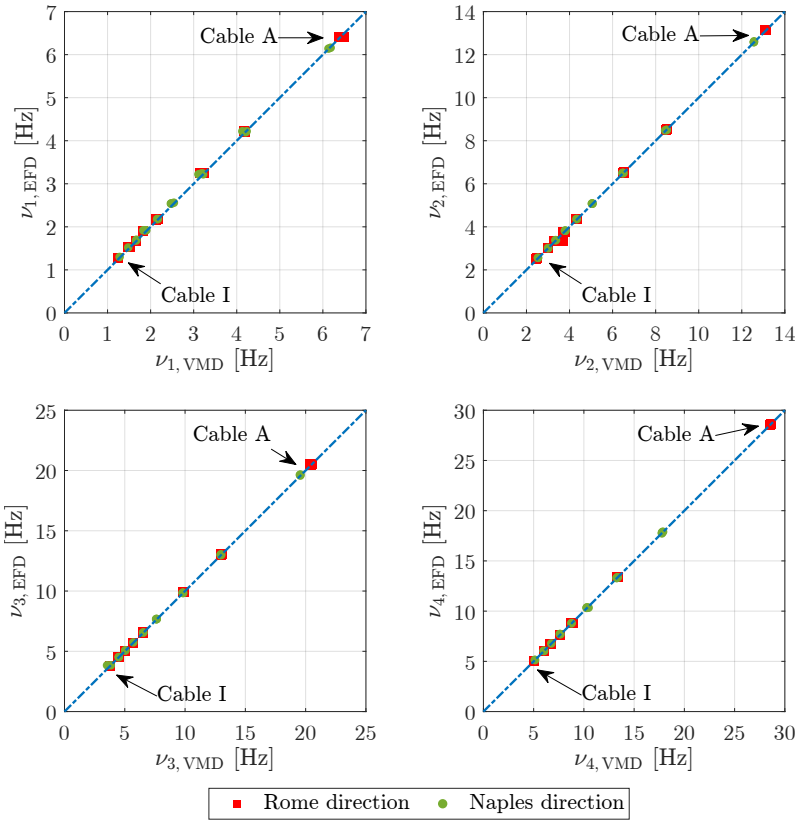

Figure 4.15: Comparison of the natural frequencies of the bridge cables estimated by means of the VMD technique and EFD technique.

The application of the proposed identification approach on the free vibration response of the bridge cables also allowed the modal damping ratios identification up to the fourth vibration mode. The estimated values of the modal damping ratios are listed in Tab. 4.9 (modal damping ratio values are averaged over all the available signals for the examined cable), and they are in line with typical values found in other studies about stay-cabled structures [192].

Two alternative approaches are implemented in the attempt to validate the experimental estimates of the modal damping ratios obtained by means of the proposed procedure. Particularly, free vibration responses are elaborated by means of the VMD technique following the procedure proposed in Chapter 3. Moreover, the cables responses due to ambient vibrations are also considered to estimate their modal damping ratios using the Natural Excitation Technique (NExT) [86] combined with the area-based approach. Figures 4.16-4.17 illustrate the modal damping ratios estimated by means of all these methods. It is remarked that it would be ideal to compare

the results obtained by means of the proposed approach with those carried out from forced vibrations induced by gauged impact hammers or shakers. However, it was not possible to perform none of such vibration tests. Since the ground truth of the modal parameters is not known in real structures, the comparison of alternative approaches makes it possible to evaluate qualitatively the confidence level about the final estimates.

Table 4.9: Modal damping ratios for the first four vibration modes of the bridge cables estimated by means of the proposed procedure based on the EFD technique.

Cable	Rome direction				Naples direction			
	ξ_1 [%]	ξ_2 [%]	ξ_3 [%]	ξ_4 [%]	ξ_1 [%]	ξ_2 [%]	ξ_3 [%]	ξ_4 [%]
A	0.12	0.15	0.21	0.22	0.23	0.27	0.30	-
B	0.19	0.17	0.23	-	0.16	0.33	0.28	0.32
C	0.12	0.14	0.12	0.18	0.19	0.11	0.10	0.13
D	-	-	-	-	0.28	0.11	0.10	0.13
E	0.26	0.14	0.14	0.13	0.1	0.08	0.09	0.08
F	0.22	0.08	0.07	0.17	0.29	0.17	0.13	0.14
G	0.22	0.09	0.14	0.11	0.12	0.13	0.11	0.09
H	0.11	0.21	0.15	0.12	0.12	0.60	0.07	0.15
I	0.17	0.18	0.09	0.1	0.09	0.09	0.14	0.10

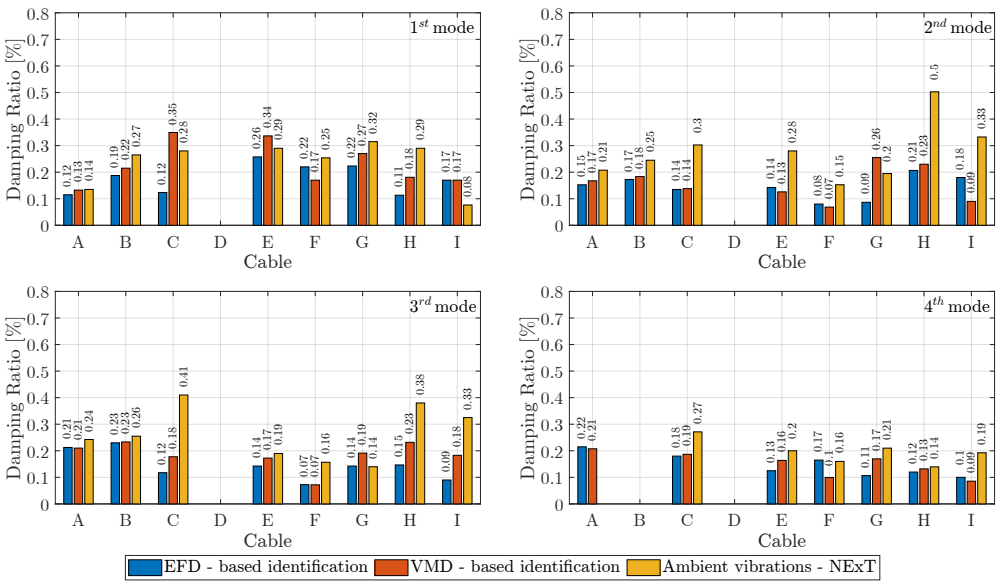

Figure 4.16: Modal damping ratios for the first four vibration modes of the bridge cables (Rome direction) estimated by means of the proposed procedure based on the EFD technique and two alternative methods.

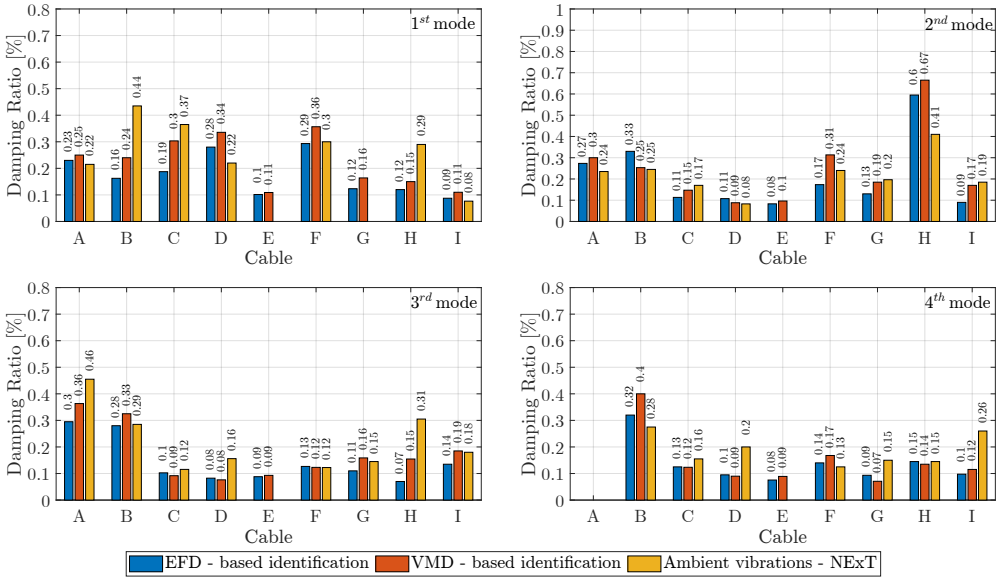

Figure 4.17: Modal damping ratios for the first four vibration modes of the bridge cables (Naples direction) estimated by means of the proposed procedure based on the EFD technique and two alternative methods.

The reasonable agreement among the modal damping ratio values that can be inferred from Figs. 4.16-4.17 substantiates the general correctness of the proposed procedure based on the EFD technique. Furthermore, it can be noted that the experimental estimates of the modal damping ratios obtained under ambient vibrations are, in most cases, slightly larger than those calculated from free vibration tests (both using the EFD technique or the VMD technique). The variability of the modal damping ratios estimated for each cable from all available records further confirms the superior robustness of the proposed identification approach based on the EFD technique for free vibrations-based dynamic identification. In fact, the maximum coefficient of variation of the modal damping ratios estimated by means of the EMD technique and the VMD technique is equal to 0.40 and 0.70, respectively.

4.5 Experimental application on a railway bridge

The last experimental application of the proposed identification framework deals with a typical steel bridge of the Italian railway network (Fig. 4.18). It is a symmetric simply supported truss bridge made up of two lateral spans, each one having length of 28.54 m, and a central span whose length is 34.72 m. The bridge consists of two longitudinal truss girders spaced at 5 m, with transverse frame at the deck. Each truss girder consists of riveted longitudinal parallel top and bottom chords, struts and diagonals. Lower chords are inverse T-shaped sections, diagonals and upper chords are C-shaped built-up elements with stiffening brackets, while the struts have I-section. At the lower chords, the trusses are connected by transverse elements and cross-bracing systems.

Figure 4.18: Overview of steel railway bridge investigated in the present study.

This experimental application aims at identifying natural frequencies, modal damping ratios and mode shapes of one of the lateral spans of the investigated railway bridge from its dynamic response. Six triaxial accelerometers with sensitivity of 1000 mV/g have been installed on the deck. The accelerometers have been placed on both sides of the deck at 1/4, 1/2 and 3/4 of the span (Fig. 4.19). The signal acquisition was performed considering a sampling frequency $F_s = 1.6$ kHz.

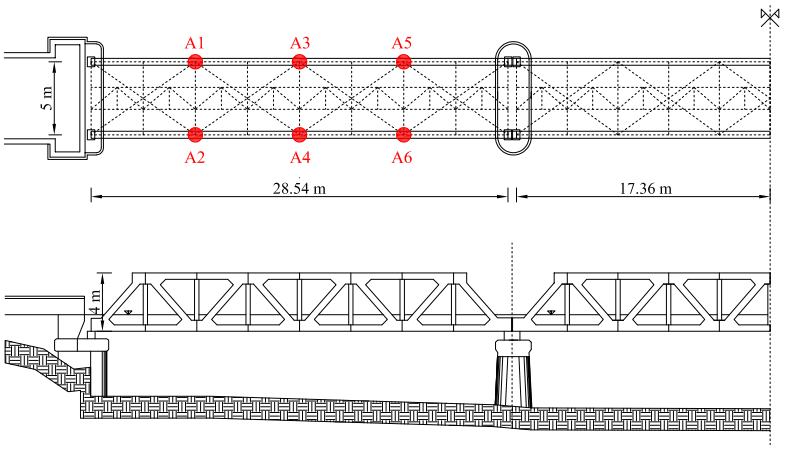

Figure 4.19: Layout of the steel railway bridge and details about the sensors position for monitoring the dynamic response of one lateral span.

The dynamic identification of the bridge is performed by exploiting its free vibrations after the passage of the train. Notably, one dataset consisting of six recordings, one for each sensor installed on the bridge deck, has been exploited to carry out the dynamic identification of the deck. Furthermore, the excitation for the present experimental application has been produced by a high-speed Frecciarossa train with a total length of 317.84 m and a gross weight of 6086.6 kN marching at an average speed equal to 163 km/h. Each recorded signal has been filtered by means of a 3$^{\text{rd}}$ order Butterworth band-pass filter in order to limit the analysis of the frequency range of interest, namely 3-30 Hz. The free vibration part of each signal is employed for the present analysis (Fig. 4.20), and it is extracted automatically according to the guidelines proposed by Yang et al. [29].

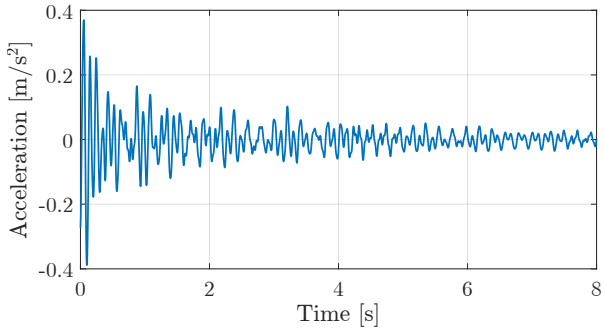

Figure 4.20: Free vibration part extracted from a recorded signal of the steel railway bridge.

The modal characteristics of the monitored span of the railway bridge have been estimated by means of the proposed procedure based on the EFD technique. For the validation of these results, two further methods have been adopted to estimate the modal properties of the railway bridge. Once again, the VMD technique has been employed following the procedure described in Chapter 3. Moreover, the covariance-based stochastic subspace identification (SSI-COV) is adopted[1] [79, 83] since the free vibration responses are proportional to the correlations of the responses to a white noise excitation [206]. Three vibration modes have been identified using all the considered techniques. The natural frequencies (average values over all the available signals) are shown Fig. 4.21 and demonstrate a very good agreement among the considered techniques. The statistical analysis performed on the natural frequencies obtained from each measurement point demonstrates that the proposed identification approach based on the EFD technique turns out to be more robust than that based on the VMD technique. In fact, the maximum coefficient of variation of the natural frequencies identified by means of the EMD technique and the VMD technique is $4.2 \cdot 10^{-3}$ and $1.3 \cdot 10^{-2}$, respectively. It is worth noting that the first and the second natural frequency are close to each other. This is an impediment to an accurate modal identification based on signal components extraction through a bank of band-pass filters with user-defined cut-off frequencies, as usual in common practice. The identified mode shapes are illustrated in Fig. 4.22. First and third vibration modes are representative of vertical flexural mode shapes (first and second bending mode, respectively) whereas the second vibration mode corresponds to a torsional mode shape. Figure 4.22 also provides a comparison between the mode shapes identified through the proposed approach based on the EFD technique and those obtained through the SSI-COV method. MAC can be again employed to assess quantitatively the agreement between the mode shapes carried out by means of these two alternative approaches (i.e., the closer MAC is to 1, the higher the similarity between the mode shapes carried out via EFD technique and the SSI-COV method). As regards the considered railway bridge deck, a MAC value equal to 0.95, 0.97 and 0.94 for the first, second and third mode has been found, respectively. Therefore, the mode shapes obtained by means of the procedure proposed in the present study agree very well with those estimated through the SSI-COV

[1]The identification by means of the SSI-COV technique is performed using the open-source toolkit available at https://code.vt.edu/vibes-lab/modal-analysis.

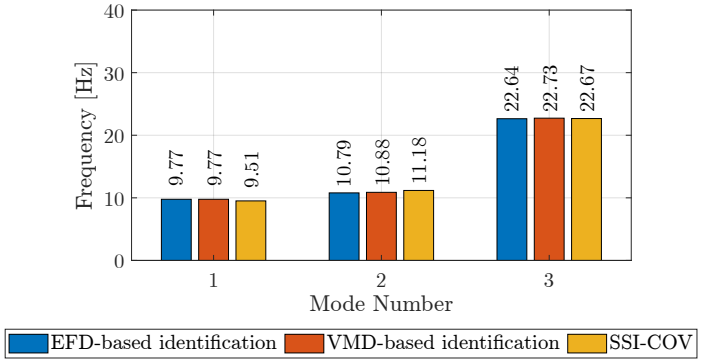

Figure 4.21: Natural frequencies of the railway bridge span estimated according to different identification methods.

technique. This confirms that the proposed procedure based on the EFD technique identifies accurately the mode shapes, with a much lower computational effort than the SSI-COV technique. Indeed, some operations invoked into the SSI-COV technique (such as the preparation of the block Toeplitz matrix of covariances and the singular value decomposition) need a high elaboration time and a large memory usage while the implementation of the proposed approach requires basic operations and a minimum computational effort.

Figure 4.23 is meant at comparing the modal damping ratios obtained by means of the considered alternative identification methods. The results in Fig. 4.23 demonstrate a general good agreement between the estimates obtained by means of the proposed approach and those carried out via the VMD technique. There is, however, a rather significant difference about the modal damping ratio value for the third vibration mode, as estimated at some measurement points. The statistical elaboration of the modal damping ratios obtained from different measurement points further confirms the large robustness of the dynamic identification performed according to the approach presented in the current study. While the maximum coefficient of variation of the modal damping ratios identified by means of the proposed approach is 0.36, the corresponding value obtained via the VMD technique is equal to 0.42.

For the sake of completeness, it is pointed out that the modal damping ratios estimated via the SSI-COV technique are $\xi_1 = 2.3\%$, $\xi_2 = 2.5\%$ and $\xi_3 = 1.4\%$. Hence, the first and the third modal damping ratio values differ significantly from those calculated through the EFD technique and the VMD technique. Actually, this difference is attributable to the fact that SSI methods are not able to identify accurately the damping ratios in case of strongly non-stationary signals [207].

For a critical examination of the obtained estimates of the modal damping ratios, reference values from relevant technical codes and reports are considered. In this regard, Eurocode 1- Part 2 §6.4.6.3.1 [208] provides the lower bound value of the modal damping ratio, which is assumed constant for all modes and is based on the construction material of the bridge as well as on the span length, as reported in Tab. 4.10. Another estimation of the damping ratio is provided by the European Commission in the "Guideline for estimating structural damping of railway bridges" D5.2-S2 [209]. In this case, the constant modal damping ratio can be calculated as

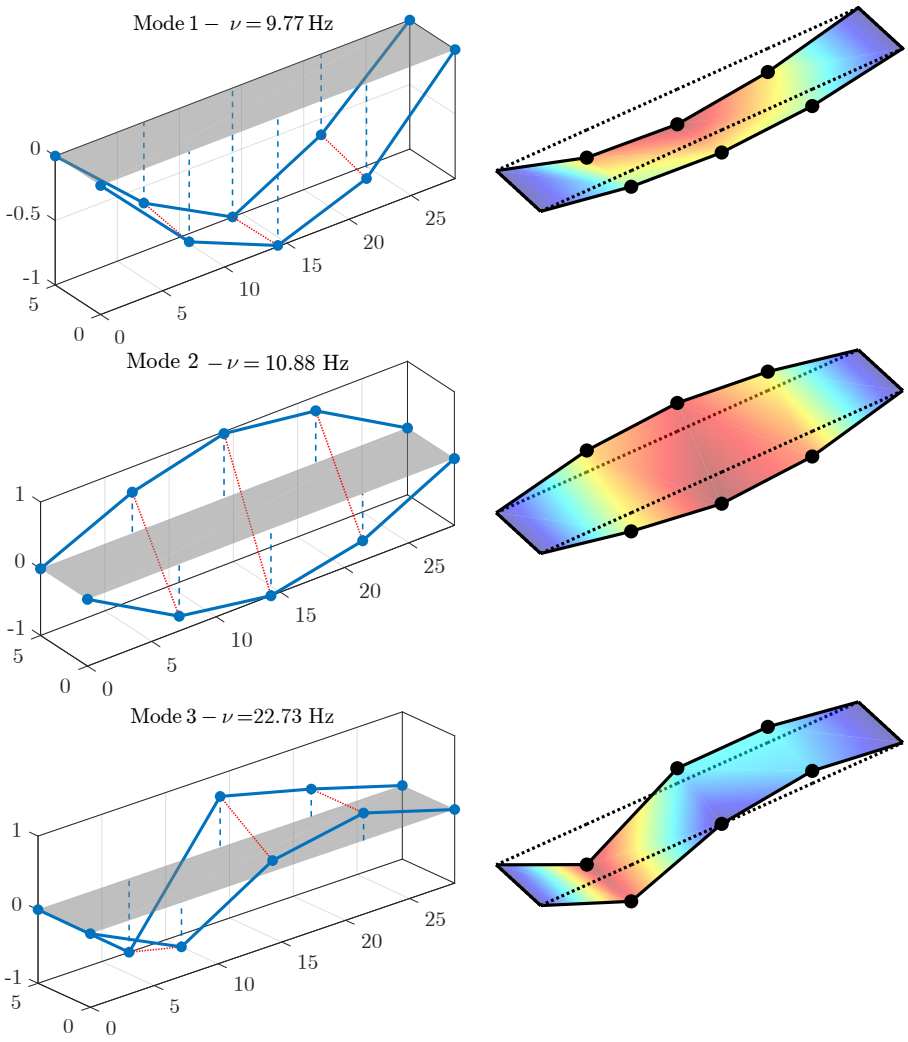

Figure 4.22: Estimated mode shapes of the railway bridge span: identification by means of the proposed approach based on EFD technique (left); identification by means of the SSI-COV technique (right).

the sum of three different contributions depending on the specifics of the structure, namely material, structural type and bearings type. Table 4.11 lists the contributions as named in such guidelines for this specific case. For the examined case study, a constant minimum value of the modal damping ratio equal to $\xi = 0.5\%$ is recommended by Eurocode 1 – Part 2 [208] while a constant modal damping ratio $\xi = 0.64\%$ is calculated following the guidelines into D5.2-S2 [209]. It can be thus concluded that the lower bound recommended by Eurocode 1 – Part 2 as well as the constant modal damping ratio value suggested by D5.2-S2 agree well with the minimum estimates

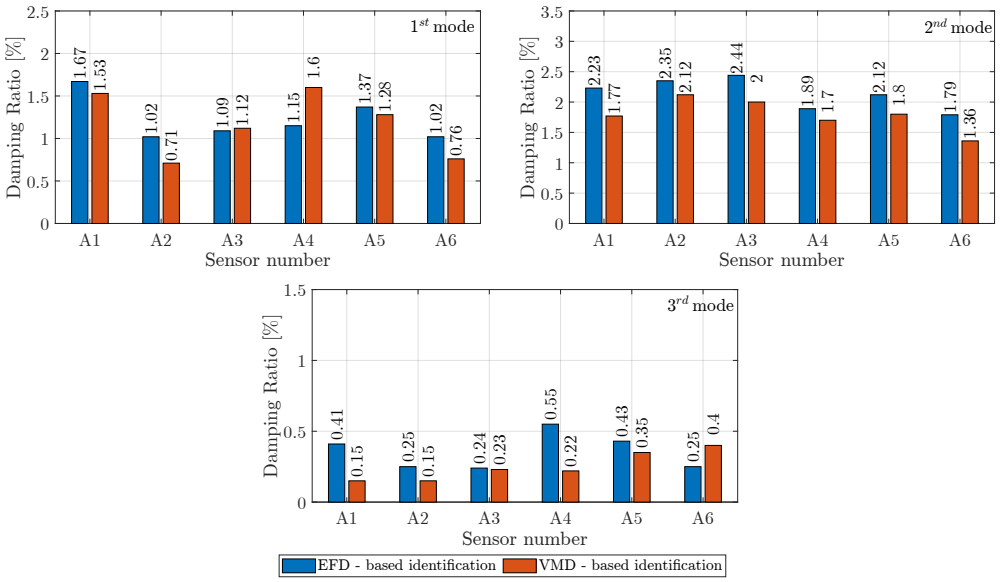

Figure 4.23: Modal damping ratios of the railway bridge span estimated according to different identification methods.

Table 4.10: Lower limit of the modal damping ratio proposed in EC1 – Part 2 [208].

Bridge type	Lower limit of percentage of critical damping [%]	
	Span $L < 20$ m	Span $L > 20$ m
Steel and composite	$\xi = 0.5 + 0.125(20 - L)$	$\xi = 0.5$
Prestressed concrete	$\xi = 1 + 0.07(20 - L)$	$\xi = 1$
Filler beam and reinforced concrete	$\xi = 1.5 + 0.07(20 - L)$	$\xi = 1.5$

of the modal damping ratio found in the present study, which occurs for the third vibration mode as shown in Fig. 4.23. These reference values underestimate the modal damping ratios for the first and the second vibration mode as plotted in Fig. 4.23, being conservative towards the actual overall dissipation capacity of the structure. Finally, it is pointed out that the estimated modal damping ratios are in reasonable agreement with the values reported in other studies [210–212] on steel truss railway bridges with similar materials and static configuration.

Table 4.11: Modal damping ratio value proposed in D5.2-S2 [209]

Damping ratio [%]	
Material damping: steel	0.08
Nonmaterial structural damping: steel riveted bridge	0.32
Interaction damping: standard sliding bearings	0.24

CHAPTER 5

BRIDGES INDIRECT MODAL IDENTIFICATION BASED ON THE DYNAMIC RESPONSE OF MOVING VEHICLES

5.1 Introductory remarks

In the last decades, the development of vibration-based techniques for structural identification has become a relevant area among researchers in the civil and mechanical engineering community, especially for structural health monitoring (SHM) purposes [213]. Vibration-based testing relies on the concept that structural modal parameters depend on several physical characteristics of the structure and change when deterioration or damaging mechanism occurs [214]. Notably, classical direct monitoring approaches typically require the permanent installation of a large network of sensors on the structure. In this manner, the recorded responses due to ambient excitation are processed, and classic methods of Operational Modal Analysis (OMA) are used to estimate the modal parameters. However, due to the large number of sensors generally required for each structure, this strategy is not always feasible. Particularly for medium or short-span bridges, direct vibration monitoring becomes uneconomical to be used consistently, limiting its application only to specific critical infrastructures. In this regard, significant limitations of the direct monitoring approach include the high installation and maintenance costs, the conspicuous volume of raw data to be processed, and the different durability timespan between the monitored structure and monitoring system [215].

On this basis, several research efforts have been focused on the development of different and more economical vibration-based procedures that may lead to the assessment of the conditions of a large number of bridges. In this framework, an indirect approach generally referred to as vehicle scanning method (VSM) has recently gained increasing attention among researchers in the field, due to its ability to possibly overcome classical direct approach main limitations. This procedure, firstly introduced by Yang et al. [216], is based on a drive-by approach where a testing vehicle moves over the bridge, while its vertical acceleration response is recorded via few sensors directly mounted on the car body or its axle. Notably, although both lab-scaled models [217] and in situ testing [218–222] have shown the validity of the VSM in estimating the fundamental frequency of the bridge, some issues may arise when dealing with this procedure. Generally, for instance, the recorded response is affected by the vehicle-related frequency content. In this case, the associated frequency spectrum usually shows a peak related to the vehicle's natural frequency whose magnitude may be significantly higher than the structural ones, thus making it difficult to identify the bridge frequencies. To cope with this issue, the possible use of the acceleration response at the contact point between the vehicle tyre and the surface has been used

and proved to be particularly suitable to identify the bridge dynamic parameters [223]. Further, an additional issue may be represented by the effect of pavement roughness on the quality of the estimated parameters, since the introduced high-frequency noise components can overshadow higher modes frequencies. In this regard, possible solutions have been based on the use of the residual signal from the measurements of two connected vehicles [224] or the vehicle front and rear tyre [225, 226].

It is also worth making some considerations about the effect of the vehicle weight in comparison with the bridge mass as well as the influence of the structural scheme. Specifically, it has been found in [227] that the instantaneous frequencies significantly change as the weight of the moving mass increases whereas are almost invariant if the vehicle mass is negligible. On the one hand, if the vehicle is light in comparison with the bridge, the bridge modal frequencies are the first to be identified since vehicle modal contribution is shifted on high frequencies and mode shapes can be obtained by filtering the vehicle acceleration response and evaluating the envelope of each response modal contribution. On the other hand, if the mass of the vehicle is not negligible time-varying coupled frequencies of the vehicle-beam interaction system are first detected and in this case mode shapes are evaluated considering their relationship with the instantaneous frequencies. Several real case applications of modal frequencies identification considering different vehicle-bridge mass ratios may be found in [218, 228, 229]. Further, it has been observed in [230] that if the vehicle scanning is performed with ongoing traffic, the additional mass exciting the bridge produces a positive effect that balances the noise induced by the pavement roughness helping to identify bridge modal frequencies. With regard to the structural scheme, it is observed that almost all the available literature on VSM considers the typical simply supported boundary condition, however a few studies have investigated alternative support conditions. In this context, Sitton et al. [231] propose a closed-form solution for the identification of modal frequencies of a two-span continuous bridge using the responses of passing vehicles. Demirlioglu et al. [232] compare the performance of three VSM approaches for the estimation of mode shapes of bridges that are seated on elastic supports. It has been found that, using a half-car model, the presence of elastic supports leads to a significant decrease in the mode shape estimates: specifically, the variation of the total load carried by the bridge at the instant of an axle entering or leaving a bridge produces sudden variation in the displacement profile and amplifications in the CP acceleration that leads to inaccurate mode shape estimates at the bridge ends.

Clearly, the performance of both direct and indirect identification approaches is significantly dependent on the adopted signal processing techniques and a crucial role is attributed to the decomposition techniques chosen to retrieve the modal contributions from the multi-modal analyzed signal. To this aim, one of the most adopted methods is the Empirical Mode Decomposition (EMD) [233] which employs an iterative sifting process to extract modal components, generally referred to as Intrinsic Mode Functions (IMFs). The theoretical foundations of this method have been extensively addressed in Chapter 2 showing its inherent strengths and limitations. Specifically, it is recalled that this method suffers from mode mixing problems and weakness against the noise and, thus, improved variants of the EMD have been successively proposed such as Ensemble Empirical Mode Decomposition (EEMD) [121]. In the context of VSM-based monitoring, in [234] the EMD has been used in combination with Fourier

transform to estimate the bridge frequencies from data of a passing vehicle, whereas in [235] an EMD-based damage index has been proposed to assess the bridge health condition. Further, in [236–238] EEMD has been applied to obtain improved bridge modal parameters estimations from drive-by measurements and to capture sudden stiffness changes.

As already mentioned in Chapter 2, in the last decades, several other decomposition methods have been proposed and applied for SHM purposes, among which the Variational Mode Decomposition (VMD) [125] has proved to achieve high decomposition quality in standard direct bridges dynamic identification procedures [123]. As previously seen, this method is based on a variational formulation that yields an adaptive extraction of relevant modal components from a given time series and their corresponding central frequencies. In this context, in Chapter 3 a tuned version of VMD in combination with an area ratio-based approach and a time domain technique was exploited to successfully identify frequencies, damping ratios and mode shapes from different existing bridge typologies.

Notably, the applicability of VMD to the field of indirect dynamic identification has been analyzed to a lesser degree. For instance, in [239] both numerical and experimental studies have assessed the efficiency of the VMD for the modal frequencies estimations and no mode mixing effects have been observed. Further, recently Yang et al. [18] introduced an identification approach combining VMD for the mode extraction with RDT [92] for the free vibration responses generation and Hilbert spectrum (HS) based method for the estimations of both natural frequencies and damping ratios. In this regard, while high accuracy has been achieved in terms of natural frequencies, some discrepancies have been observed in the estimation of damping ratios.

On this basis, it may be argued that further investigations should be carried out for the modal parameters estimation combining the VSM and the VMD approaches. Specifically, note that the free vibrations signals used for the modal parameters estimations may be generated using different techniques once the decomposition is performed, as for instance the RDT and NExT. However, there are no studies comparing the quality of the identified modal parameters varying the free vibration generation technique. Further, there are few applications in the literature regarding modal damping ratios identification, and their estimation is usually imprecise due to the pavement roughness-related noise. Clearly, the use of novel noise-robust methods may be desirable to improve the accuracy of the results. Finally, no studies in the literature have applied the VMD for mode shapes identification. These points will be addressed within the present study.

On the basis of the preceding conspectus, it is evident that further investigation is required for the development of more suitable procedures for the identification of mode shapes and modal damping ratios, in the context of VSM with a single-axis vehicle. To this aim, in this chapter, an enhanced VMD-based procedure is proposed for the accurate modal identification of bridges employing a single-axis vehicle. Specifically, the VMD technique is applied to estimate the IMFs, and the associated central frequencies, directly retrieved via the decomposition procedure, are assumed as the sought structural natural frequencies. Each IMF is then converted into free vibration-like signals using NExT. Further, the procedure involves proceeding to estimate pertinent modal damping ratios from these signals by employing an appropriately developed noise-robust area ratio-based approach. Finally, mode shapes are captured by using

the instantaneous amplitudes of the IMFs, appropriately corrected to account for the influence of the modal damping ratios.

The accuracy of the proposed approach is assessed using several numerical applications that consider the effect of both vehicle damping and pavement roughness, and the estimated modal parameters are compared with the classic Hilbert spectrum-based approach combined with both NExT and RDT for free vibration response generation. The content of this chapter is based on one paper currently under review [240].

5.2 Theoretical formulation

5.2.1 Vehicle-bridge dynamics

For mathematical description purposes, the vehicle-bridge interaction problem is treated by adopting a well-established simplified model which consists of a simply supported Euler-Bernoulli beam (bridge girder) and a Single-Degree-Of-Freedom (SDOF) oscillator (vehicle) moving over the beam with constant velocity v. The simply-supported beam (see Fig. 5.1) has span length L, constant bending stiffness EI, mass per-unit-length μ and damping c. The actual road pavement effect is considered by the definition of a roughness profile $r(x)$ with variable amplitude along the span length, superimposed on the beam smooth surface. The equation of motion for the beam can be therefore written as [241]:

$$EIw^{''''}(x,t) + \mu\ddot{w}(x,t) + c\dot{w}(x,t) = f(x,t) \tag{5.1}$$

where $w(x,t)$ is the beam vertical displacement while $f(x,t)$ is the interaction force between the moving oscillator and the beam at the contact point. Further, note that in Eq.(5.1) the over-dot and the prime over a variable indicate the partial derivatives with respect to time t and abscissa x, respectively.

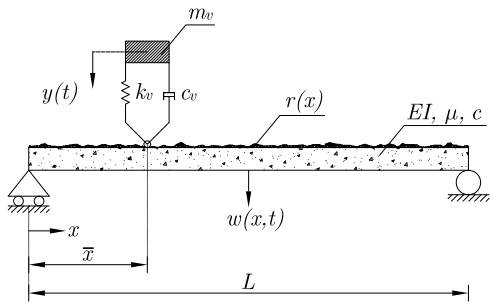

Figure 5.1: Schematic of a SDOF moving oscillator (vehicle) crossing a simply supported beam (bridge).

The moving oscillator is described as a discrete mass-spring-damper system with mass m_v, spring stiffness k_v and damping coefficient c_v, which takes into account the effect of vehicle real suspension system. Under the assumption that the SDOF oscillator crosses the beam with constant velocity v, and its vertical motion is described by the following equation:

$$m_v\ddot{y}(t) + c_v(\dot{y}(t) + \dot{w}(\bar{x},t) + vr'(\bar{x})) + k_v(y(t) - w(\bar{x},t) + r(\bar{x})) = 0 \tag{5.2}$$

where $y(t)$ is the absolute vertical displacement of the oscillator with respect to the static equilibrium position $y_s = m_v g/k_v$ and $r(\bar{x})$ is the amplitude of the roughness profile evaluated at the contact point position $\bar{x}$. In this manner, the contact force $f(x,t)$ between the oscillator and the bridge may be expressed as follows:

$$f(x,t) = [m_v g - c_v(\dot{y}(t) + \dot{w}(\bar{x},t) + v r'(\bar{x})) - k_v(y(t) - w(\bar{x},t) + r(\bar{x}))]\chi(t)\delta(x-\bar{x}) \quad (5.3)$$

where $\delta(x-\bar{x})$ is the Dirac's delta function centered at the contact point $\bar{x}$ and $\chi(t)$ is the window function defined as:

$$\chi(t) = \begin{cases} 1 & \text{for } 0 \leq t \leq L/v \\ 0 & \text{otherwise} \end{cases} \quad (5.4)$$

By combining Eq.(5.2) and Eq.(5.3) the contact force may be expressed in the following compact form:

$$f(x,t) = [m_v g - m_v \ddot{y}(t)]\,\chi(t)\delta(x-\bar{x}) \quad (5.5)$$

According to the modal analysis procedure [22], it is possible to use the modal superposition principle to approximate the beam vertical displacement $w(x,t)$ as the sum of its first n_m modes:

$$w(x,t) \simeq \sum_{k=1}^{n_m} q_k(t)\phi_k(x) \quad (5.6)$$

where $\phi_k(x)$ is the kth mode shape function of the beam and $q_k(t)$ the kth modal displacement. In Eq.(5.6) the mode shape functions $\phi_k(x)$ with $k \in [1, n_m]$ are obtained from the solution of the following eigenproblem:

$$\phi_k^{''''}(x) = \lambda_k^4 \phi_k(x) \text{ with } k \in [1, n_m] \quad (5.7)$$

where $\lambda_k^4 = \mu\omega_k^2/EI$, and ω_k is the circular frequency for the kth mode. Further, considering the orthogonality conditions:

$$\int_0^L \phi_k(x)\phi_j(x)dx = 0 \quad \forall k \neq j \quad (5.8)$$

substituting Eq.(5.6) into Eq.(5.1), pre-multiplying both sides by $\phi_j(x)$, and integrating with respect to x over the length of the beam L, the equations of motion of the beam in modal coordinates are:

$$\ddot{q}_k(t) + 2\xi_k\omega_k\dot{q}_k(t) + \omega_k^2 q_k(t) = \chi(t)\frac{\phi_k(\bar{x})}{\mu\int_0^L \phi_k^2(x)dx}[m_v g - m_v\ddot{y}(t)] \quad \forall k \in [1, N] \quad (5.9)$$

where ξ_k is the kth modal damping ratio under the assumption that the proportionality to the masses condition [242] is respected. Note that, if the following normalization condition is assumed:

$$\int_0^L \phi_k^2(x)dx = L \quad (5.10)$$

Eq.(5.9) can be rewritten in the following form [243]:

$$\ddot{q}_k(t) + 2\xi_k\omega_k\dot{q}_k(t) + \omega_k^2 q_k(t) = \varepsilon\chi(t)\phi_k(\bar{x})[g - \ddot{y}(t)] \quad (5.11)$$

where $\varepsilon = m_v/(\mu L)$.

Similarly, substituting Eq.(5.6) into Eq.(5.2) and dividing by the mass m_v, the equation of motion of the oscillator can be expressed as:

$$\ddot{y}(t) + 2\xi_v\omega_v\dot{y}(t) + \omega_v^2 y(t) = 2\xi_v\omega_v\left[\sum_{k=1}^{n_m}\dot{q}_k(t)\phi_k(\bar{x}) + v\sum_{k=1}^{n_m}q_k(t)\phi_k'(\bar{x}) - vr'(\bar{x})\right] + \omega_v^2\left[\sum_{k=1}^{n_m}q_k(t)\phi_k(\bar{x}) - r(\bar{x})\right] \tag{5.12}$$

where $\xi_v = c_v/(2m_v\omega_v)$ is the vehicle damping ratio, $\omega_v^2 = k_v/m_v$ is the circular frequency of the vehicle and the following relation is exploited:

$$\dot{\phi}_k(\bar{x}(t)) = \frac{d\phi_k(\bar{x})}{d\bar{x}}\frac{d\bar{x}(t)}{dt} = v\phi_k'(\bar{x}) \tag{5.13}$$

It is pointed out that Eq.(5.11) and Eq.(5.12) constitute a system of $N+1$ coupled differential equations which governs the dynamic response of the considered system, taking into account the damping in both the bridge and the vehicle, as well as the effect of the road pavement roughness.

5.2.2 Contact point response estimation

Indirect dynamic identification approaches are usually carried out by elaborating the data recorded by sensors directly mounted on the vehicle body or its axle. However, several studies in the literature [244, 245] have shown that the vehicle frequency may significantly affect the recording spectra, overshadowing higher bridge modes, thus limiting the identification to the first structural mode at most. To overcome this limitation, Yang et al. [244] suggested the use of the contact point (CP) response as a more suitable function for dynamic identification purposes. Specifically, considering Eq.(5.6) the CP displacement $d_{\mathrm{CP}}(t)$ can be expressed as:

$$d_{\mathrm{CP}}(t) = w(\bar{x}, t) = \sum_{k=1}^{n_m} q_k(t)\phi_k(\bar{x}) \tag{5.14}$$

Differentiating Eq.(5.14) with respect to time, the CP velocity $v_{\mathrm{CP}}(t)$ assumes the following expression:

$$v_{\mathrm{CP}}(t) = \dot{w}(\bar{x}, t) = \sum_{k=1}^{n_m}(\dot{q}_k(t)\phi_k(\bar{x}) + vq_k(t)\phi_k'(\bar{x})) \tag{5.15}$$

Finally, differentiating once more Eq.(5.15) with respect to time, the CP acceleration $a_{\mathrm{CP}}(t)$ is obtained as:

$$a_{\mathrm{CP}}(t) = \ddot{w}(\bar{x}, t) = \sum_{k=1}^{n_m}(\ddot{q}_k(t)\phi_k(\bar{x}) + 2v\dot{q}_k(t)\phi_k'(\bar{x}) + v^2q_k(t)\phi_k''(\bar{x})) \tag{5.16}$$

Notably, the CP acceleration is generally adopted in the dynamic identification procedures, due to the higher magnitude of frequency peaks in the Fourier domain in comparison to the other CP response functions. Clearly, however, the contact response cannot be easily measured in practical applications and, therefore, has to be estimated based on the recorded vehicle vertical acceleration $\ddot{y}(t)$. In this regard, it is possible to back-calculate the CP acceleration exploiting the dynamic vertical equilibrium equation of the vehicle once its acceleration $\ddot{y}(t)$ is known [230], as follows:

$$a_{\mathrm{CP}}(t) = \frac{1}{2\xi_v\omega_v} e^{-\frac{\omega_v}{2\xi_v}t} \int_0^t F(\tau) e^{\frac{\omega_v}{2\xi_v}\tau} d\tau \tag{5.17}$$

where it is assumed that:

$$F(t) = \frac{d^2\ddot{y}(t)}{dt^2} + 2\xi_v\omega_v \frac{d\ddot{y}(t)}{dt} + \omega_v^2 \ddot{y}(t) \tag{5.18}$$

Note that, if the vehicle damping is neglected in Eq. (5.17), the CP acceleration simplifies in:

$$a_{\mathrm{CP}}(t) = \ddot{y}(t) + \frac{1}{\omega_v^2}\frac{d^2\ddot{y}(t)}{dt^2} \tag{5.19}$$

In experimental applications, the surface on which the vehicle moves is always not smooth and the recorded vehicle acceleration $\ddot{y}(t)$ implicitly takes into account the effect of surface roughness, thus Eq.(5.17) can be efficiently adopted to determine the CP acceleration. However, when calculating the CP acceleration in the numerical simulations, Eq.(5.17) must be appropriately modified considering the explicit effect of the roughness profile $r(x)$. Specifically, differentiating twice with respect to time Eq.(5.2) the following differential equation is obtained:

$$\begin{aligned} 2\xi_v\omega_v \frac{d\ddot{w}(\bar{x},t)}{dt} + \omega_v^2 \ddot{w}(\bar{x},t) = \frac{d^2\ddot{y}(t)}{dt^2} + 2\xi_v\omega_v \frac{d^2\ddot{y}(t)}{dt^2} + \omega_v^2 \frac{d^2 y(t)}{dt^2} \\ + 2\xi_v\omega_v v^3 r'''(\bar{x}) + \omega_v^2 v^2 r''(\bar{x}) \end{aligned} \tag{5.20}$$

which, for the initial condition $\ddot{w}(\bar{x},t)|_{t=0} = 0$, has the following solution:

$$a_{\mathrm{CP}}(t) = \ddot{w}(\bar{x},t) = \frac{1}{2\xi_v\omega_v} e^{-\frac{\omega_v}{2\xi_v}t} \int_0^t F^*(\tau) e^{\frac{\omega_v}{2\xi_v}\tau} d\tau \tag{5.21}$$

where

$$F^*(t) = \frac{d^2\ddot{y}(t)}{dt^2} + 2\xi_v\omega_v \frac{d\ddot{y}(t)}{dt} + \omega_v^2 \ddot{y}(t) + 2\xi_v\omega_v v^3 r'''(\bar{x}) + \omega_v^2 v^2 r''(\bar{x}) \tag{5.22}$$

Finally, if the vehicle damping is neglected in Eq.(5.2), the CP acceleration simplifies in

$$a_{\mathrm{CP}}(t) = \ddot{w}(\bar{x},t) = \ddot{y}(t) + \frac{1}{\omega_v^2}\frac{d^2\ddot{y}(t)}{dt^2} + v^2 r''(\bar{x}) \tag{5.23}$$

5.3 Proposed modal identification procedure

In this section, a novel modal identification procedure that uses vehicle indirect measurements is introduced. The proposed modal identification approach is based on the

use of the contact response which contains the contributions of the K modes considered in the modal superposition. In this regard, the VMD [125] is exploited to retrieve the uni-modal components. This method also allows the estimation of the central frequency associated with each uni-modal component, which are assumed as the sought modal frequencies in the proposed approach. Subsequently, the NExT [86] method is adopted to convert the extracted uni-modal components into free-decay vibration responses. Further, an area ratio-based procedure is considered for the estimation of modal damping ratios, employing the aforementioned free-decay responses. Finally, mode shapes are constructed by properly correcting the instantaneous amplitudes of the isolated mode functions exploiting the estimated damping ratios. The flowchart in Fig. 5.2 schematically summarizes the proposed identification approach.

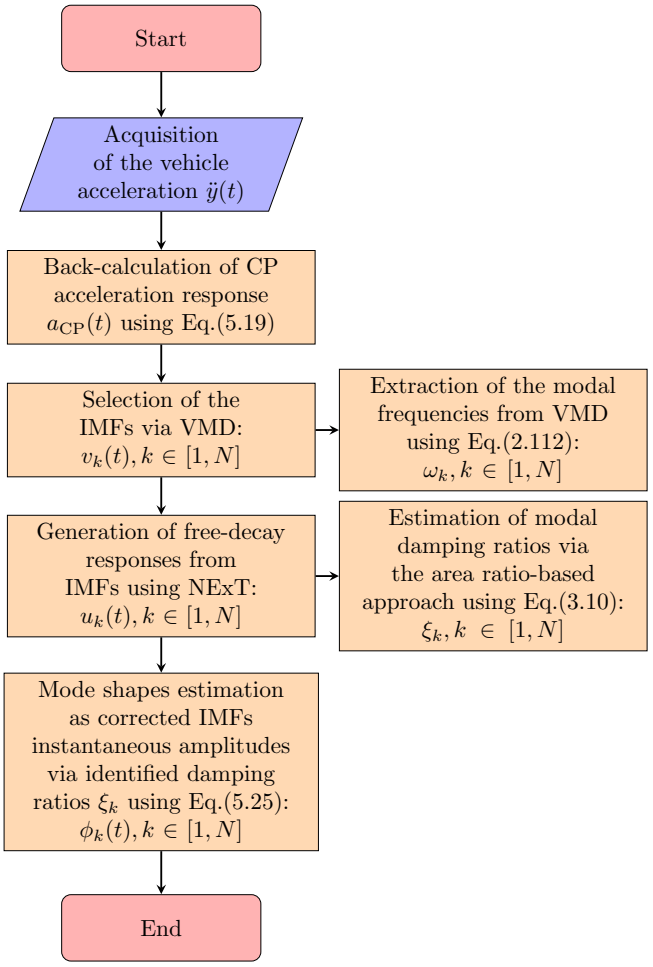

Figure 5.2: Flowchart of the proposed modal identification procedure.

Notably, once each IMF $v_k(t)$ is retrieved by means of the VMD, it is possible to associate the corresponding free-decay response, hereinafter labeled as $u_k(t)$, exploiting the NExT properties [85, 86]. Specifically, this method allows to generate impulse-like

response functions for the analyzed system, based on measured structural responses to white noise excitation. The generated free-decay functions are therefore exploited for the evaluation of the modal damping ratios ξ_k following an approach based on the evaluation of the areas under the system time history response, as originally formulated for a single-degree-of-freedom (SDOF) system by Huang et al. [153]. The main advantage of this approach consists in a strong anti-noise property which leads to more accurate damping estimations. This methodology proved to be effective in direct identification problems as in Mazzeo et al. [30], where the modal damping ratios in existing bridges have been identified exploiting free vibration responses recorded by sensors directly attached to the structure. This study aims to extend the aforementioned procedure to vehicle scanning indirect identification problems under ambient excitation and prove its reliability. In this regard, consider the kth free-decay response function $u_k(t)$ associated with the kth IMF $v_k(t)$; the damping ratio corresponding to the kth mode can be calculated exploiting Eqs.(3.10) and (3.11). This procedure is therefore repeated for all the selected modes, i.e. for each $u_k(t)$ with $k \in [1, N]$, to complete the damping ratios identification process. Once the IMFs $v_k(t)$ and damping ratios ξ_k have been evaluated, a procedure may be followed to estimate mode shapes, appropriately extending an approach firstly introduced in [246]. Specifically, by applying the Hilbert transform operator to each IMF $v_k(t)$, the associated signal can be defined as:

$$\tilde{v}_k(t) = v_k(t) + \mathrm{j}\mathcal{H}[v_k(t)] = \bar{A}_k(t)e^{\mathrm{j}\theta(t)} \quad \text{with} \quad k \in [1, K] \tag{5.24}$$

where $\mathcal{H}[\cdot]$ is the Hilbert transform operator, $\bar{A}_k(t)$ is the instantaneous amplitude function associated with the kth IMF and $\theta(t)$ the corresponding instantaneous phase.

As shown in [246], the instantaneous amplitude function $\bar{A}_k(t)$ which is, by the Hilbert transform properties, the envelope of $v_k(t)$, may represent a first estimate, in absolute value, of the corresponding mode shape function associated with the instantaneous frequency ω_k.

On the other hand, as discussed in [247], the bridge damping ratios effect produces a combined shifting and scaling of the IMFs instantaneous amplitude if compared with the undamped case.

However, it is possible to account for the damping ratio effect on each mode shape estimation by properly correcting it as in [247]. Thus, the estimated mode shapes (in absolute value) can be given as:

$$\phi_k(x) = \frac{\bar{A}_k\left(x/v\right)}{e^{-\xi_k\omega_k x/v}} \quad \text{with} \quad k \in [1, K] \tag{5.25}$$

Notably, the estimated mode shapes according to Eq.(5.25), should be normalized with respect to their corresponding maximum to be compared with their theoretical counterpart.

5.4 Numerical Applications

In this section the proposed dynamic identification procedure is validated on numerical applications, investigating the effects of vehicle damping ratio and pavement roughness. The reliability of the proposed method in estimating the modal parameters is

assessed by comparing different identification approaches: specifically, two procedures for the free vibration response extraction are considered, namely NExT and RDT. Modal frequencies and damping ratios, calculated according to the above-mentioned procedure, are compared to the estimates obtained by Hilbert Spectrum (HS) based identification method.

In this regard, note that the numerical applications presented in the following are based on a vehicle-bridge system whose properties are listed in Table 5.1.

Table 5.1: Properties for the investigated vehicle-bridge system.

Bridge			
Young's modulus	E	$2.8 \cdot 10^{10}$	[N/m^2]
Moment of inertia	I	0.2	[m^4]
Mass-per-unit-length	μ	5400	[kg/m]
Length	L	30	[m]
Modal circular frequency	ω_1	1.78	[Hz]
	ω_2	7.11	[Hz]
	ω_3	16.00	[Hz]
	ω_4	28.44	[Hz]
Modal damping ratio (equal for all the modes)	ξ_k	2	[%]
Vehicle			
Mass	m_v	1000	[kg]
Spring stiffness	k_v	$8 \cdot 10^5$	[N/m]
Velocity	v	4	[m/s]
Circular frequency	ω_v	4.50	[Hz]
Damping ratio	ξ_v	5	[%]

5.4.1 Case 1: Vehicle-bridge system neglecting vehicle damping and road pavement roughness

The first numerical application deals with the most simple-vehicle bridge system; that is a sprung mass moving at a constant velocity v on a simply supported Euler-Bernoulli beam. Further, both the effects of the vehicle damping ξ_v and pavement roughness are neglected ($\xi_v = 0$, $r(x) = 0$), while the bridge damping ratio ξ_k with $k \in [1, K]$ is assumed constant for each mode. Note that a small velocity value in the simulations is employed to avoid the so-called camel hump effect [248], i.e. the splitting in the frequency spectrum of higher modes frequencies into left and right shifted components.

In this regard, the equations of motion (5.11) and (5.12) are solved, evaluating the bridge and vehicle responses in terms of displacement, velocity and acceleration (see Figs. 5.3(a)−(f)). Next, using the approach described in Section 2.2, the contact point response function in terms of displacement, velocity and acceleration, and the corresponding frequency spectra, are determined (see Figs. 5.4).

As it can be seen in Figs. 5.4(a)−(c), the proposed indirect approach (red line)

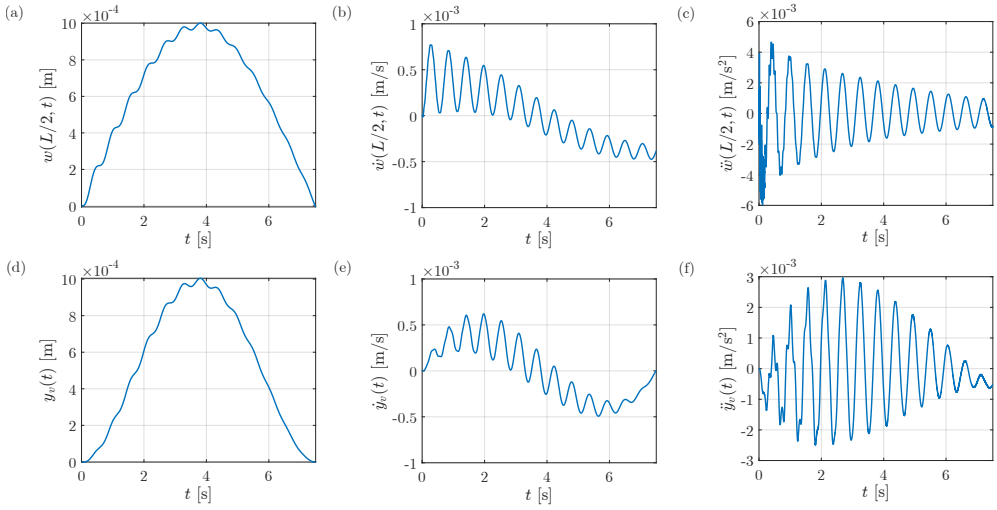

Figure 5.3: Displacement, velocity and acceleration time-histories for the vehicle-bridge system in Figure 5.1 neglecting the vehicle damping and road pavement roughness ($\xi_v = 0$, $r(x) = 0$): (a) bridge response displacement, (b) velocity and (c) acceleration at midspan; (d) vehicle response displacement, (e) velocity and (f) acceleration.

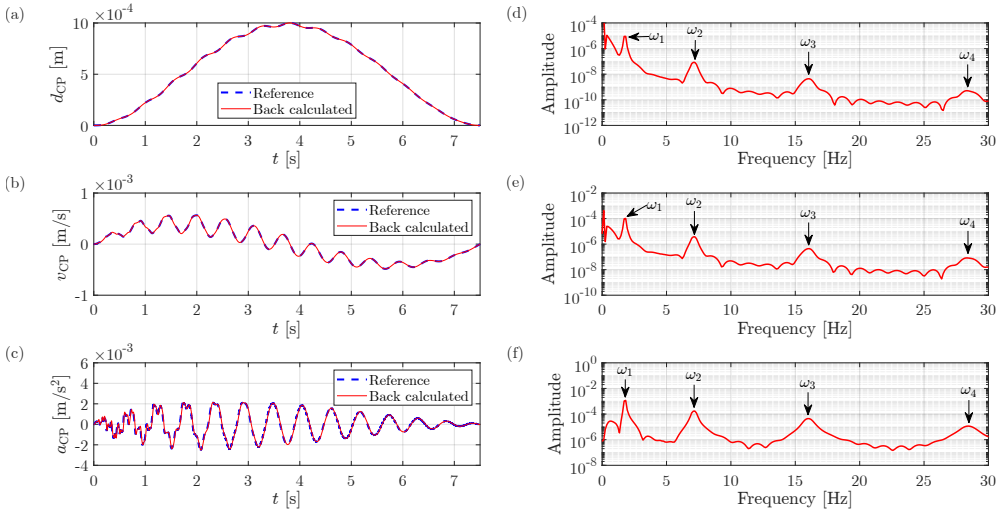

Figure 5.4: Reference and back-calculated CP response functions (from (a) to (c)) and corresponding frequency spectra (from (d) to (f)) for the vehicle-bridge system in Figure 5.1 neglecting vehicle damping and road pavement roughness ($\xi_v = 0$, $r(x) = 0$): CP displacement (top), CP velocity (middle) and CP acceleration (bottom).

yields response functions that perfectly match those obtained using classical modal superposition (blue dashed line), thus underlining the reliability of the back-calculation method. Moreover, it is observed that the contact point acceleration (see Fig. 5.4(f)) is the most suitable response function for indirect dynamic identification purposes due to the highest level of peaks amplitude found for higher modes in comparison with the

CP displacement and CP velocity functions (see Figs. 5.4(d) and 5.4(e)). Therefore, hereinafter the CP acceleration is chosen for the application of the proposed dynamic identification approach. In this manner, applying the VMD procedure, the first four IMFs (see Figs. 5.5(a)−(d)) have been identified, whereas the vehicle frequency was neither observable in the frequency spectrum nor retrieved in the decomposition process. The identified modal frequencies obtained via VMD are listed in Tab. 5.2.

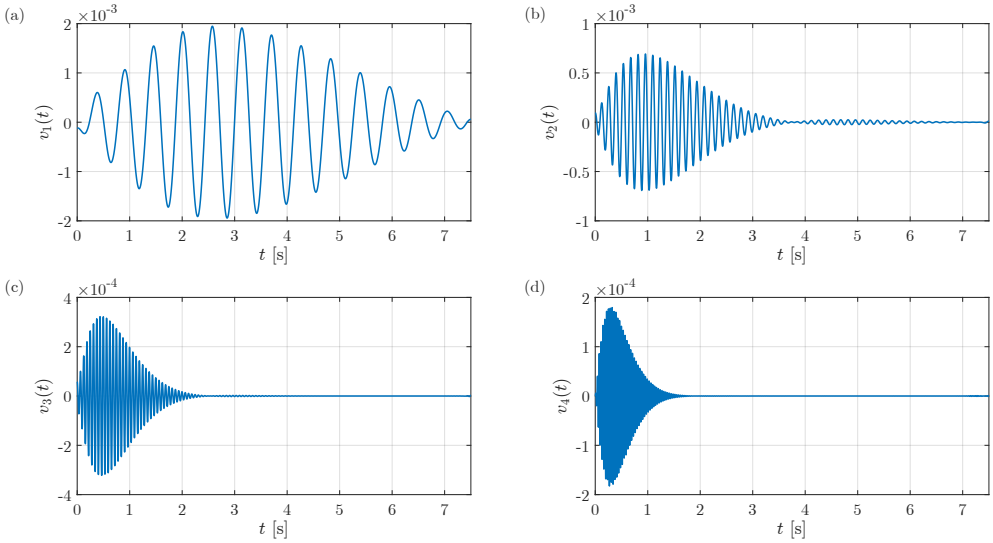

Figure 5.5: IMFs extracted via the VMD from the CP acceleration of the vehicle-bridge system in Figure 5.1 neglecting vehicle damping and road pavement roughness ($\xi_v = 0$, $r(x) = 0$): (a) first IMF, (b) second IMF, (c) third IMF and (d) fourth IMF.

The free vibrations associated with the IMFs have been extracted by means of both NExT and RDT. For further comparison, the natural frequencies have been also estimated from the free vibrations using the HS approach. The identified frequencies obtained with the different approaches and their corresponding relative errors are summarized in Table 5.2. It is observed that the estimated frequencies obtained as VMD central frequencies are overall the most accurate ones with errors of less than 1%.

Table 5.2: Identification of the bridge natural frequencies from the vehicle-bridge system in Figure 5.1 assuming $\xi_v = 0$ and $r(x) = 0$. Comparison of the proposed method with HS-RDT and HS-NExT approaches. The absolute value of relative error is given within brackets.

		Identified frequencies [Hz]		
Mode number	Expected [Hz]	Proposed VMD	HS-based approach NExT	RDT
1	1.777	1.782 (0.26%)	1.791 (1.11%)	1.783 (0.36%)
2	7.109	7.147 (0.51%)	7.150 (0.58%)	7.152 (0.53%)
3	15.996	16.023 (0.17%)	16.023 (0.17%)	15.94 (0.33%)
4	28.438	28.479 (0.15%)	28.419 (0.06%)	28.283 (0.54%)

Similarly, a comparison between damping ratios estimates is carried out as shown in Tab. 5.3. Specifically, for the free-decay functions extracted via NExT and RDT, both the area-ratio based approach and the HS one are considered. As it can be seen, for the free vibrations functions extracted by both NExT and RDT, the proposed area-ratio based approach is preferable, leading to significantly lower errors (less than 5%) in comparison to the HS-based approach.

Table 5.3: Identification of bridge damping ratios from the vehicle-bridge system in Figure 5.1 assuming $\xi_v = 0$ and $r(x) = 0$. Comparison of the proposed method with HS-RDT and HS-NExT approaches. The absolute value of relative error is given within brackets.

		Identified damping ratios [%]			
Mode number	Expected [%]	Area-based approach NExT	RDT	HS- based approach NExT	RDT
1	2	2.06 (2.94%)	2.01 (0.64%)	3.63 (81.40%)	2.79 (39.35%)
2	2	2.04 (1.95%)	2.10 (4.91%)	2.09 (4.33%)	2.42 (20.88%)
3	2	2.03 (1.28%)	2.06 (2.85%)	1.96 (2.02%)	2.10 (5.17%)
4	2	2.02 (1.00%)	2.02 (0.98%)	1.97 (1.65%)	2.05 (2.71%)

Finally, the first two mode shapes of the examined system have been correctly identified through the proposed approach while higher modes have not been estimated satisfactorily due to the lower level of excitation obtainable in indirect identification approaches. Notably, Figs. 5.6(a) and 5.6(b) show that estimated mode shapes are in good agreement with the theoretical counterparts. However, it is also observed a sharp edge effect in both Figs. 5.6, which accentuates as the bridge damping ratios increase: this, in turn, has a detrimental impact on the exploited technique accuracy in constructing mode shapes.

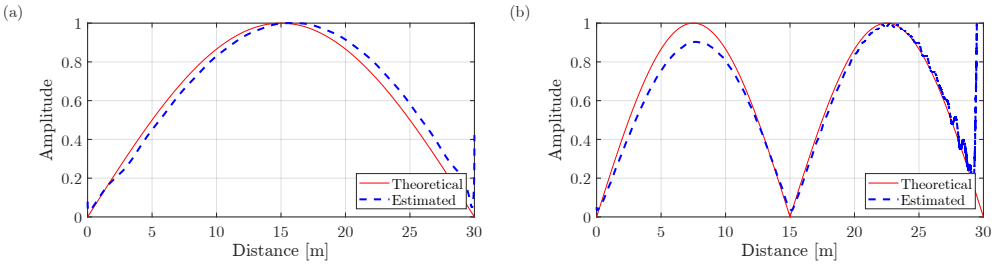

Figure 5.6: Comparison between theoretical and estimated mode shapes for (a) the first and (b) second mode for the vehicle-bridge system in Figure 5.1 neglecting vehicle damping and road pavement roughness ($\xi_v = 0, r(x) = 0$).

5.4.2 Case 2: Vehicle-bridge system considering vehicle damping and neglecting road pavement roughness

In the present application, the same vehicle-bridge system properties of the previous case are adopted. However, since vehicle damping cannot be usually neglected when considering the features of the testing vehicle due to the actual suspensions system, a reasonable damping ratio value, i.e. $\xi_v = 5\%$, is here adopted following other literature studies [249]. For this case study the road pavement roughness is still neglected ($r(x) = 0$). As in the previous case, for dynamic identification purposes, the CP acceleration is here employed (see Figs. 5.7(a) and 5.7(b)). It is observed that the vehicle damping effect slightly alters the CP acceleration response amplitude as well as the peaks magnitude of the frequency spectrum in comparison with the previous case. However, for dynamic identification purposes, no significant alterations have been shown and the first four modes have been accurately determined. The proposed

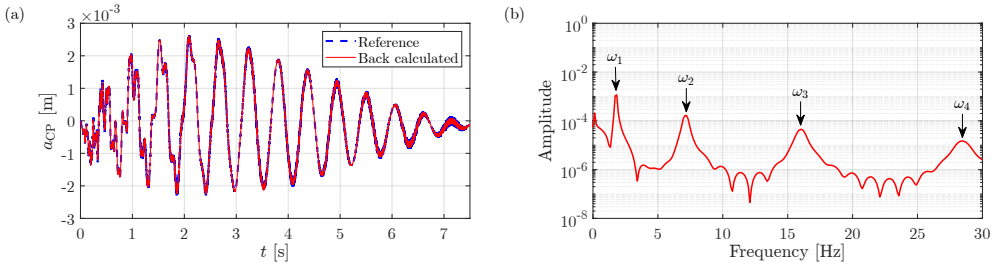

Figure 5.7: (a) Reference and back-calculated contact point acceleration and (b) corresponding frequency spectrum for the vehicle-bridge system in Figure 5.1 in presence of vehicle damping $\xi_v = 5\%$, and neglecting road pavement roughness ($r(x) = 0$).

identification procedure has been therefore applied to the extracted mode functions leading to the estimations of modal frequencies (see Tab. 5.4) and damping ratios (see Tab. 5.5). It may be observed that the slight variations in CP response and its corresponding frequency spectrum are reflected on the estimated modal parameters which show, in general, small discrepancies compared to the results in Section 4.1. Further, it is also observed that damping ratios estimates with all the examined procedures are more sensitive to this effect than the natural frequencies. Notably, again the proposed

area ratio-based approach leads to the most accurate results.

Table 5.4: Identification of bridge natural frequencies from the vehicle-bridge system in Figure 5.1 assuming $\xi_v = 5\%$ and $r(x) = 0$. Comparison of the proposed method with HS-RDT and HS-NExT approaches. The absolute value of relative error is given within brackets.

		Identified frequencies [Hz]		
Mode number	Expected [Hz]	Proposed VMD	Hilbert spectrum based approach NExT	RDT
1	1.777	1.782 (0.27%)	1.791 (0.79%)	1.782 (0.28%)
2	7.109	7.147 (0.53%)	7.151 (0.58%)	7.153 (0.609%)
3	15.996	16.023 (0.17%)	16.024 (0.17%)	15.943 (0.33%)
4	28.437	28.479 (0.15%)	28.419 (0.06%)	28.285 (0.54%)

Table 5.5: Identification of bridge damping ratios from the vehicle-bridge system in Figure 5.1 assuming $\xi_v = 5\%$, and $r(x) = 0$. Comparison of the proposed method with HS-RDT and HS-NExT approaches. The absolute value of relative error is given within brackets.

		Identified damping ratios [%]			
Mode number	Expected [%]	Area-based approach NExT	RDT	HS-based approach NExT	RDT
1	2	2.06 (3.06%)	1.89 (5.65%)	3.07 (53.61%)	2.54 (27.33%)
2	2	2.08 (4.31%)	2.07 (3.78%)	2.13 (6.28%)	2.56 (28.44%)
3	2	2.04 (2.33%)	2.01 (0.12%)	1.98 (0.92%)	2.35 (17.56%)
4	2	2.03 (1.84%)	1.98 (0.72%)	1.99 (0.75%)	2.09 (4.341%)

Similarly to the previous case, the first two mode shapes have been reliably evaluated and compared with theoretical previsions (see Figs. 5.8(a) and 5.8(b)). Further, comparing these results with Figs. 5.6(a) and 5.6(b), slight variations in estimated mode shapes can be observed, proving that a higher accuracy can be reached in appraisals if the vehicle damping is taken into account.

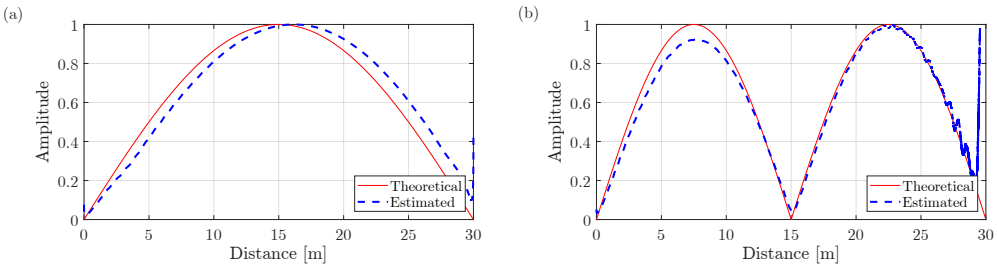

Figure 5.8: Comparison between theoretical and estimated mode shapes for (a) the first and (b) second mode for the vehicle-bridge system in Figure 5.1 assuming $\xi_v = 5\%$ and $r(x) = 0$.

5.4.3 Case 3: Vehicle-bridge system considering road pavement roughness and neglecting vehicle damping

In this section, the vehicle damping is neglected ($\xi_v = 0$) whereas the effect of pavement roughness ($r(x) \neq 0$) is investigated on the vehicle-bridge system responses and the performance of the proposed modal identification procedure is assessed. The construction of the longitudinal road profile can be carried out by exploiting a set of harmonic waves with different amplitudes and phases. The road profile is therefore generated by its spectral description according to the method proposed by Shinozuka et al. [250, 251]; the one-sided PSD spectrum is discretized in bands and for each one of them a fixed number of harmonic samples is generated assuming a uniformly distributed random phase angle θ_i:

$$r(x) = \sum_{i=0}^{N^*} \sqrt{2G_d(n_i)\Delta n}\cos\left(2\pi n_i + \theta_i\right) \tag{5.26}$$

where N^* is the number of harmonics chosen to simulate the profile, n_i is the ith spatial frequency, Δn is the sampling interval of the spatial frequency and θ_i is the random phase angle for the ith harmonic. A possible formulation for the PSD function $G_d(n_i)$ is the one proposed in the ISO 8608 standard [252] as:

$$G_d(n_i) = G_d(n_0)\left(\frac{n_i}{n_0}\right)^w \tag{5.27}$$

where $w = 2$ is a waviness coefficient, $n_0 = 0.1$ cycle/m is the reference spatial frequency, $G_d(n_0)$ is the PSD function value at the reference spatial frequency and n_i is the ith spatial frequency calculated as $n_i = n_l + (i - 0.5)\Delta n$ with $\Delta n = (n_u - n_l)/N^*$, being n_u and n_l the spatial frequency upper and lower bounds. On this base, different roughness classes can be defined, depending on the surface quality, by properly selecting the PSD value $G_d(n_0)$, where higher values correspond to worse pavement roughness conditions.

In that regard the PSD function values proposed in ISO 8608 were derived from data collected on roads: it is neither considered that bridge pavements are usually in much better conditions than road ones nor that this model was developed for transportation engineering applications rather than for vehicle indirect dynamic identification. For these reasons, the PSD function value at the reference spatial frequency $G_d(n_0)$ is properly corrected from the geometric mean provided by ISO 8608 as described in [253] and is therein labeled as $G_d^*(n_0)$. Specifically, three roughness classes are considered assuming three different values of $G_d(n_0)$ to simulate different surface quality, namely $G_d^*(n_0) = 0.001 \cdot 10^{-6}$ m^3 (class A), $G_d^*(n_0) = 8 \cdot 10^{-6}$ m^3 (class B) and $G_d^*(n_0) = 16 \cdot 10^{-6}$ m^3 (class C). The roughness profiles adopted in this study are generated assuming $N^* = 2500$, $n_u = 10$ cycles/m, $n_l = 0.01$ cycles/m, and samples of the generated profiles are shown in Figs. 5.9(a)−(c).

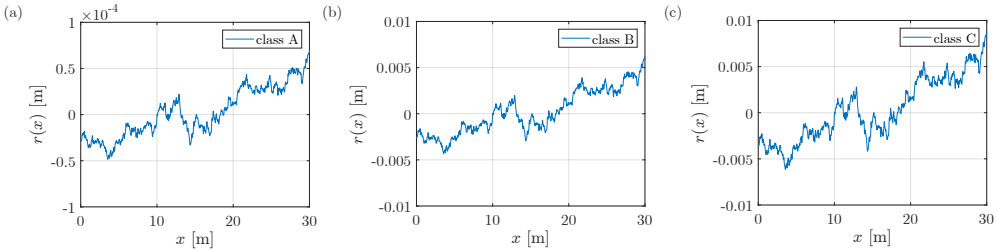

Figure 5.9: Different classes of roughness profiles generated according to ISO 8608 with corrected PSD reference values according to [253]: (a) class A - $G_d^*(n_0) = 0.001 \cdot 10^{-6}$ m^3; (b) class B - $G_d^*(n_0) = 8 \cdot 10^{-6}$ m^3; (c) class C - $G_d^*(n_0) = 16 \cdot 10^{-6}$ m^3.

The contact point response is highly sensitive to the irregularities in the pavement and the use of the generated road profiles leads to highly noisy results. However the tyre, during the passage on the pavement, touches only the point of the surface with higher elevation [223] and the real vehicle-bridge contact is a surface rather than a point. Thus, a moving average filter may be used to smooth the profile [230] and in place of the roughness profile, the smoothed envelope of its local maxima is employed (see Figs. 5.10(a) and 5.10(b)).

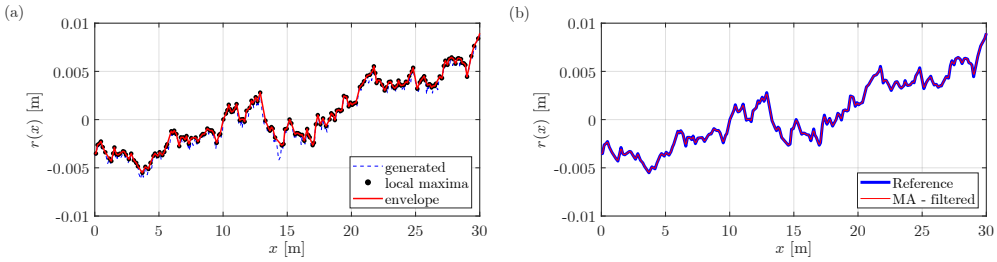

Figure 5.10: Class C roughness profile generation: (a) construction of the envelope of local maximum points and (b) profile smoothing via moving average filtering.

Figures 5.11(a)−(d) show the system response functions considering the highest level of roughness: it is observed that the effect of roughness significantly affects the theoretical response functions of both vehicle and bridge if compared to Figs. 5.3(a)−(f). Further, Figs. 5.12(a)−(f) show the CP responses and their corresponding frequency spectrum considering the roughness profile effect. In this regard, it may be observed that also in this scenario it is preferable to choose the CP acceleration response for identification purposes. As opposed to the previous cases, considering the roughness effect on the CP response, the vehicle frequency appears with significant magnitude in the frequency spectrum. This, however, does not preclude the identification of the first few structural frequencies, which are still easily distinguishable. Further, Figs. 5.13(a)−(f) show how the CP acceleration and the corresponding frequency spectrum change as the roughness class varies. It is observed that, increasing the value of $G_d^*(n_0)$, a wide range of spatial frequencies at increasing magnitudes is introduced in the CP spectrum, thus overshadowing higher order modes (e.g., the fourth mode cannot be detected when higher roughness classes pro-

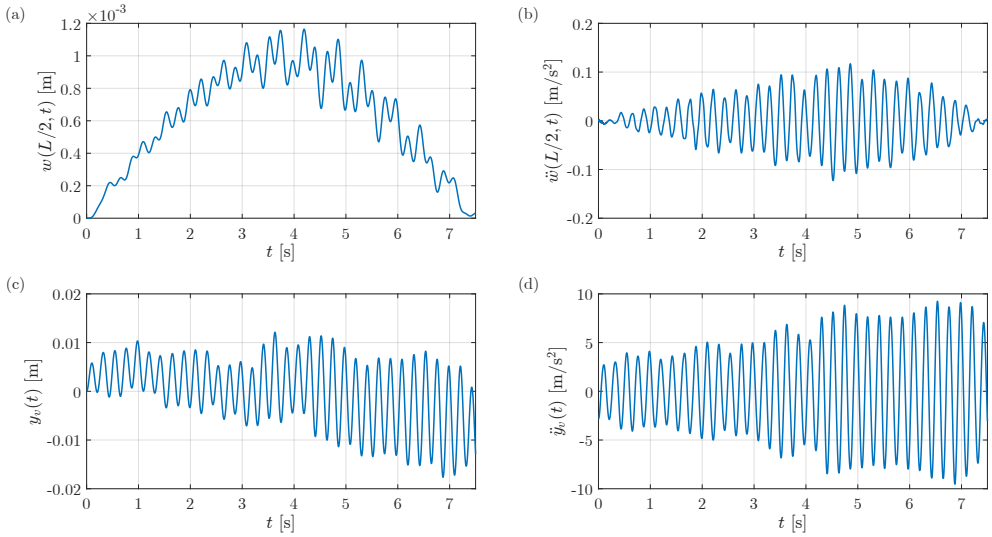

Figure 5.11: Displacement and acceleration time-history for the vehicle-bridge system in Figure 5.1 neglecting the vehicle's damping ($\xi_v = 0$) and considering a class C road pavement roughness profile: (a) bridge response displacement and (b) acceleration at midspan; (c) vehicle response displacement and (d) acceleration.

files are considered). Next, applying the proposed VMD, up to four modes have

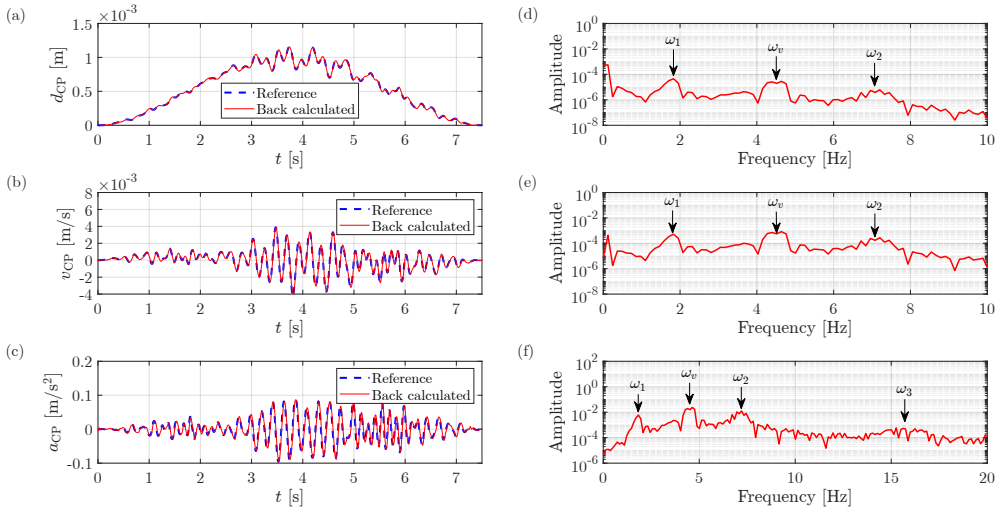

Figure 5.12: Reference and back-calculated contact point response functions (form (a) to (c)) and corresponding frequency spectra (from (d) to (f)) considering the vehicle-bridge system in Figure 5.1 neglecting the vehicle's damping ($\xi_v = 0$) and considering a class C road pavement roughness profile: CP displacement (top), CP velocity (middle) and CP acceleration (bottom).

been identified when a Class A roughness profile has been adopted and up to three in the remaining cases. As an example of the decomposition results, Figs. 5.14(a)−(c)

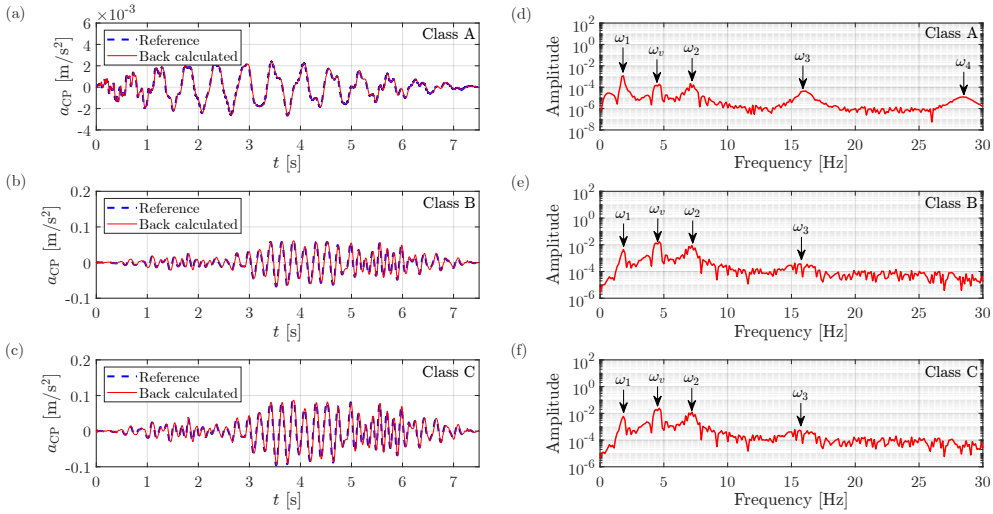

Figure 5.13: CP accelerations (from (a) to (c)) and corresponding frequency spectra (from (d) to (f)) for the vehicle-bridge system in Figure 5.1 neglecting the vehicle's damping ($\xi_v = 0$) and considering three different roughness classes: Class A (top), Class B (middle) and Class C (bottom).

show the three IMFs extracted for class C roughness. The application of the proposed

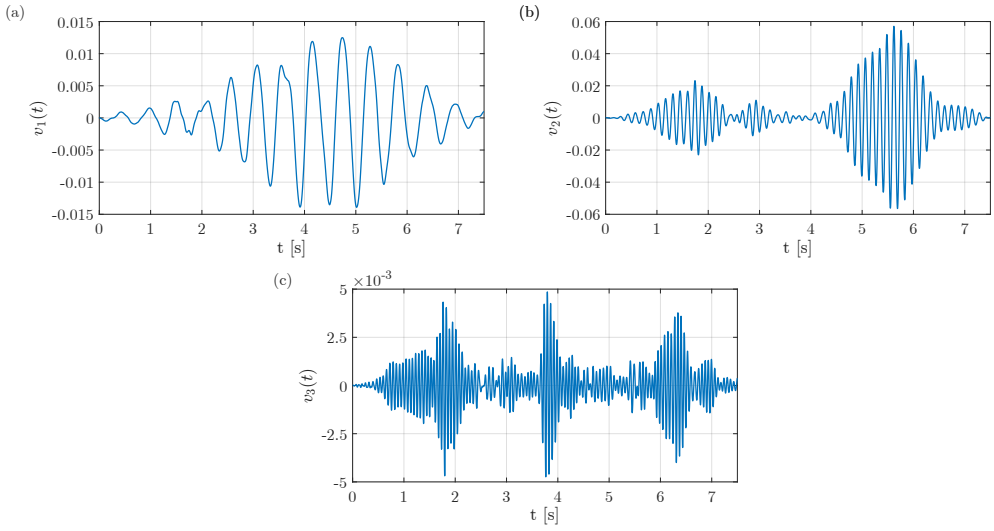

Figure 5.14: IMFs extraction via VMD for the analyzed CP acceleration function considering a class C road pavement roughness class: (a) first IMF, (b) second IMF, (c) third IMF.

procedure led to the natural frequencies and damping ratio estimates summarized in Tables 5.6 and 5.7. Notably, again the natural frequency estimations obtained via the proposed VMD are in general more accurate than the counterpart estimated via the HS approach, with relative errors in most of the cases less than 1%, regardless of the adopted roughness class profile. Further, it may be noted how, for the damping ratios

estimation, the area ratio-based approach yields significantly better results compared to the HS-based approach independently of the technique adopted for the free vibration extraction from the IMFs. This depends on the fact that the area ratio-based approach is a robust method against noise as observed in Section 2.6. In particular, it is noted that the combination of NExT and area-ratio based approach yields the most precise estimates. It is also observed that the quality of estimations for both natural frequencies and damping ratios tends to get worse for increasing roughness classes.

Table 5.6: Identification of bridge natural frequencies from the vehicle-bridge system in Figure 5.1 assuming different classes of road pavement roughness and $\xi_v = 0$. Comparison of the proposed method with HS-RDT and HS-NExT approaches. The absolute value of relative error is given within brackets.

			Identified frequencies [Hz]		
Roughness class	Mode number	Expected [Hz]	Proposed VMD	HS-based approach NExT	RDT
A	1	1.777	1.782 (0.245%)	1.784 (0.35%)	1.775 (0.13%)
	2	7.109	6.795 (4.42%)	7.094 (0.21%)	7.117 (0.10%)
	3	15.996	16.028 (0.20%)	15.929 (0.42%)	16.053 (0.35%)
	4	28.437	28.45 (0.06%)	28.311 (0.44%)	28.316 (0.43%)
B	1	1.777	1.867 (5.04%)	1.841 (3.59%)	1.794 (0.96%)
	2	7.109	7.147 (0.53%)	7.167 (0.80%)	7.185 (1.06%)
	3	15.996	15.916 (0.50%)	16.767 (4.82%)	16.840 (5.26%)
C	1	1.777	1.863 (4.84%)	1.842 (3.62%)	1.817 (2.21%)
	2	7.109	7.145 (0.50%)	7.180 (0.99%)	7.134 (0.34%)
	3	15.996	15.913 (0.52%)	16.31 (1.97%)	16.84 (5.26%)

Table 5.7: Identification of bridge damping ratios from the vehicle-bridge system in Figure 5.1 assuming different classes of road pavement roughness and $\xi_v = 0$. Comparison of the proposed method with HS-RDT and HS-NExT approaches. The absolute value of relative error is given within brackets.

			Identified damping ratios [%]			
Roughness class	Mode number	Expected [%]	Area-based approach NExT	RDT	HS-based approach NExT	RDT
A	1	2	2.13 (6.34%)	1.94 (2.95%)	2.29 (14.67%)	2.65 (32.52%)
	2	2	1.97 (1.31%)	1.73 (13.43%)	1.76 (12.06%)	1.73 (13.66%)
	3	2	1.93 (3.30%)	2.08 (4.44%)	1.94 (3.15%)	2.33 (16.39%)
	4	2	1.96 (1.84%)	1.94 (2.94%)	2.03 (1.60%)	2.14 (7.28%)
B	1	2	2.19 (9.75%)	3.11 (55.99%)	2.81 (40.91%)	2.96 (48.06%)
	2	2	2.11 (5.43%)	2.41 (20.49%)	2.81 (40.68%)	2.76 (38.03%)
	3	2	2.65 (32.94%)	1.83 (8.67%)	3.39 (69.36%)	4.00 (99.20%)
C	1	2	2.23 (11.57%)	3.93 (96.78%)	3.30 (65.21%)	4.70 (137.0%)
	2	2	2.11 (5.60%)	2.38 (19.13%)	2.81 (40.66%)	3.08 (54.40%)
	3	2	2.65 (32.69%)	1.85 (7.23%)	3.43 (71.92%)	3.98 (98.88%)

Further, Fig. 5.15(a) shows the estimated mode shape for the first mode considering the Class A roughness profile. It is noted, however, that for higher roughness and

higher modes, unreliable mode shapes estimations have been obtained and for this reason not represented in the graphics.

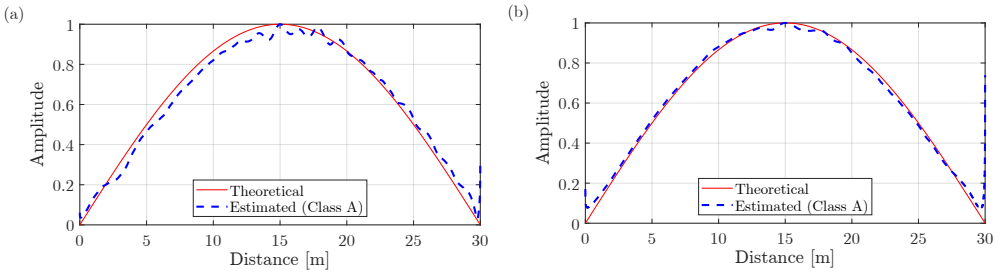

Figure 5.15: Comparison between theoretical and estimated mode shapes for the first mode for the vehicle-bridge system in Figure 5.1 assuming a Class A road pavement roughness and: (a) $\xi_v = 0\%$, (b) $\xi_v = 5\%$.

5.4.4 Case 4: Vehicle-bridge system considering both vehicle damping and road pavement roughness

The last application considered in this study deals with the most general case of vehicle-bridge systems in which neither the vehicle damping nor the road roughness profile is neglected ($\xi_v \neq 0$, $r(x) \neq 0$). The mechanical and geometrical properties are assumed as in Section 4.1, the vehicle damping ratio is assumed $\xi_v = 5\%$ and the same three roughness class profiles are considered as in Section 4.3. Figures 5.16(a)−(f) display the CP acceleration and the corresponding frequency spectrum for different roughness classes. Even though the CP accelerations present only slight differences in their local response peaks if compared to their counterparts in Figs. 5.13(a)−(f), the main differences are observed in the frequency spectra since the magnitude of the peak frequency related to the vehicle in the frequency spectrum significantly reduced regardless of the roughness profile class. This result is consistent with the numerical studies conducted by Yang and Lee [111] where it has been shown that the assumption of a high vehicle damping ratio both reduces the surface roughness-related noise and limits the vehicle frequency peak.

The application of the proposed procedure leads to the identification of the first four modes for a Class A roughness profile, whereas for higher roughness classes the fourth mode was overshadowed and only the first three have been retrieved. Tables 5.8 and 5.9 summarize the identified natural frequencies and damping ratios, respectively, for each corresponding roughness class. It is noted that, consistently with the results of the previous cases, the proposed procedure provides the most accurate estimates. It is also consistently observed that the quality of the estimates tends to worsen as the roughness class increases due to the rising level of noise introduced in the CP response-related frequency spectrum. Once again, a reliable estimation of the first mode shape has been obtained and compared with the theoretical counterpart (see Fig. 5.15(b)). Further, from the comparison with Fig. 5.15(a) it is noted that, for fixed roughness class, the effect of vehicle damping mitigates its detrimental effect improving the precision of the estimated mode shape.

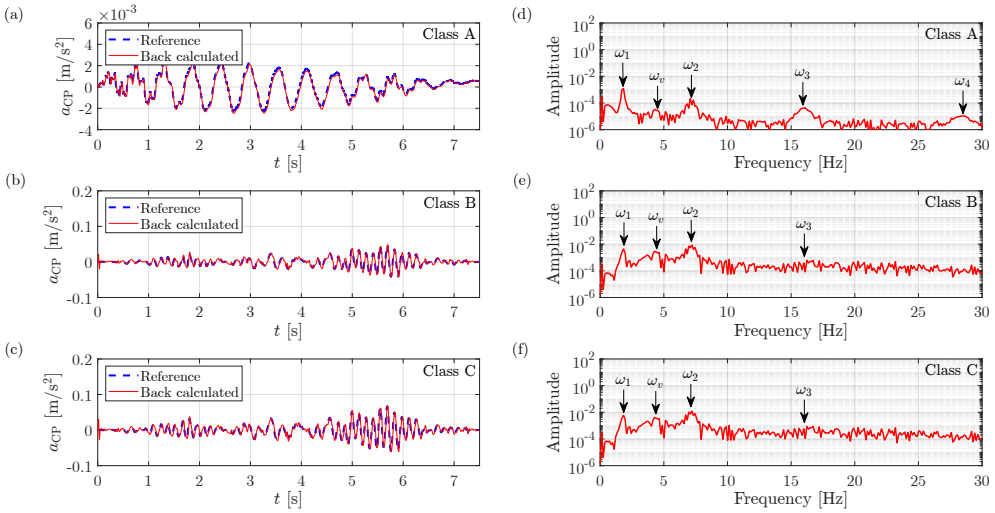

Figure 5.16: CP accelerations (from (a) to (c)) and corresponding frequency spectra (from (d) to (f)) for the vehicle-bridge system in Figure 5.1 assuming $\xi_v = 5\%$ and considering different roughness classes: Class A (top), Class B (middle) and Class C (bottom).

Table 5.8: Identification of bridge natural frequencies from the vehicle-bridge system in Figure 5.1 assuming $\xi_v = 5\%$ and different classes of road pavement roughness. Comparison of the proposed method with HS-RDT and HS-NExT approaches. The absolute value of relative error is given within brackets.

			Identified frequencies [Hz]		
Roughness class	Mode number	Expected [Hz]	Proposed VMD	HS-based approach NExT	RDT
A	1	1.777	1.784 (0.38%)	1.786 (0.47%)	1.780 (0.19%)
	2	7.109	7.150 (0.56%)	7.074 (0.49%)	7.129 (0.27%)
	3	15.996	16.029 (0.20%)	15.949 (0.29%)	16.136 (0.87%)
	4	28.437	28.404 (0.12%)	28.269 (0.59%)	28.24 (0.69%)
B	1	1.777	1.868 (5.09%)	1.841 (3.57%)	1.818 (2.32%)
	2	7.109	7.139 (0.41%)	7.166 (0.79%)	7.163 (0.75%)
	3	15.996	15.949 (0.30%)	16.769 (4.83%)	16.864 (5.42%)
C	1	1.777	1.877 (5.63%)	1.841 (3.61%)	1.787 (0.54%)
	2	7.109	7.139 (0.41%)	7.166 (0.80%)	7.147 (0.53%)
	3	15.996	15.934 (0.39%)	16.77 (4.84%)	16.96 (6.05%)

Table 5.9: Identification of bridge damping ratios from the vehicle-bridge system in Figure 5.1 assuming $\xi_v = 5\%$ and different classes of road pavement roughness. Comparison of the proposed method with HS-RDT and HS-NExT approaches. The absolute value of relative error is given within brackets.

			Identified damping ratios [%]			
Roughness class	Mode number	Expected [%]	Area-based approach NExT	Area-based approach RDT	HS-based approach NExT	HS-based approach RDT
A	1	2	1.90 (5.24%)	1.83 (8.35%)	2.36 (18.07%)	3.71 (85.39%)
	2	2	1.82 (8.78%)	1.96 (2.24%)	1.59 (20.50%)	2.17 (8.53%)
	3	2	1.94 (3.21%)	1.98 (0.93%)	2.02 (0.79%)	1.91 (4.46%)
	4	2	2.00 (0.24%)	2.03 (1.82%)	2.03 (1.55%)	2.14 (7.19%)
B	1	2	2.17 (8.73%)	2.10 (5.15%)	2.83 (41.56%)	1.42 (28.78%)
	2	2	2.03 (1.52%)	2.69 (34.50%)	2.91 (45.46%)	2.87 (43.38%)
	3	2	2.48 (24.08%)	2.03 (1.52%)	3.34 (66.94%)	3.91 (95.80%)
C	1	2	2.19 (9.99%)	2.52 (26.13%)	3.31 (65.51%)	3.44 (71.87%)
	2	2	2.03 (1.40%)	2.18 (9.34%)	2.91 (45.48%)	3.24 (62.22%)
	3	2	2.62 (31.23%)	2.24 (12.01%)	3.39 (69.28%)	1.79 (10.54%)

CHAPTER 6

CONCLUSIONS

In this PhD thesis, the use of advanced decomposition techniques was explored to formulate cost-effective strategies that could be adopted for bridge modal identification and monitoring purposes.

A brief description of the fundamental concepts related to the dynamic characterization of structures and the state of the art on this topic were presented in the introductory chapters, with a focus on operational modal analysis classic approaches and advanced decomposition techniques. Further, the main body of this thesis addressed the formulation of systematic computational strategies for bridge dynamic characterization exploiting cost-effective procedures.

In this context, it was explored the possible applicability of a Variational Mode Decomposition (VMD) based method to identify the significant modal contributions (IMFs) contained in a recorded time series, focusing on its automatization in the tuning procedure phase to facilitate its efficient application at large-scale. Specifically, the latter aimed at selecting the involved control parameters without any subjective user choice, and showed a nice performance even in the case of signal peculiarities such as the occurrence of closely spaced modes. Further, the use of an area ratio-based approach for the identification of modal damping ratios proved to be an accurate tool for the reduction of noise detrimental effect on the measures. Notably, both benchmark validations and experimental applications showed the versatility and reliability of the proposed approach, thus proving that it is a suitable tool for road bridge dynamic characterization. Even though the proposed approach showed a nice accuracy of the estimates, it was observed that the appropriate selection of VMD control parameters was not always straightforward. Therefore, the applicability of dynamic characterization via Empirical Fourier Decomposition (EFD), which depends only on one key parameter, was discussed and its performance was compared with VMD-based one. The original EFD method was improved in two aspects: automatization and robustness. Specifically, a statistical thresholds-based procedure was proposed for the correct setting of the control parameter and the segmentation procedure was improved by adopting a zero-phase moving average smoothing filter to limit the noise effect on the signal frequency spectrum. Statistical comparative analysis on benchmark signals between the EFD and the VMD technique showed that both methods can accurately identify closely spaced modes. However, significantly different results were observed between the two methods when dealing with a lowly excited mode since the VMD technique is affected by error propagation. In contrast, the EFD technique provided much more robust performances. Further, the proposed automatic tuning procedure developed for the EFD technique proved to be more straightforward than the one adopted for the VMD technique. In addition, the analysis of synthetic signals af-

fected by noise proved that the use of traditional approaches, such as the logarithmic decrement method, seldom allows the accurate estimation of the modal damping ratios as opposed to the robust area-based approach. The EFD-based procedure was successfully exploited for the dynamic characterization of two existing bridges, further showing more consistent estimates of the modal parameters in comparison with the VMD-based approach.

Therefore, it is clear that the proposed approach could represent a competitive alternative to ambient vibration tests, where SNR is usually low and amplitude-dependent modal properties cannot be identified. Further, the framework proposed in this thesis, alternatively considering VMD and EFD, could be easily adopted by administration bodies to perform a prompt assessment of bridge health conditions, especially in the case of batches of structures that present similar geometry, static scheme and material properties as shown in Chapter 3. This choice could thus optimize the life cycle management of an infrastructure network.

Finally, in the last part of the dissertation, a theoretical study dealing with the indirect identification of modal parameters was carried out in the context of the Vehicle Scanning Method (VSM). Specifically, the vehicle-bridge system response was obtained in an approximate closed form accounting for the effects of both systems' damping and the road pavement roughness. In addition, the contact-point (CP) acceleration function was adopted for identification purposes due to its enhanced ability to capture higher structural modes. The approach presented in Chapter 3 was extended for dynamic characterization via the CP response. The VMD method was once again adopted to isolate the IMFs and identify the corresponding modal frequencies. In this case, the equivalent free-decay response functions, associated with the VMD's extracted modal components, were generated using the Natural Excitation Technique (NExT). Further, the damping ratios estimation was carried out using the above-mentioned area ratio-based approach. Lastly, mode shapes were obtained from the extracted IMF instantaneous amplitude functions adopting a correction to properly address the effect of the damping ratios. The performance of this identification approach was assessed by comparing NExT and RDT for the generation of the free-decay responses as well as the proposed technique with the Hilbert-based approach for the estimation of modal frequencies and damping ratios. In numerical applications, the roles of both vehicle damping and pavement road roughness were investigated in the CP response function frequency spectrum, as well as in the modal identification performance. Specifically, it was noted that the identification performance worsens as the roughness class increases and that if the vehicle damping is considered, the overshadowing effect due to the vehicle frequency on higher modes in the frequency domain was considerably reduced regardless of the pavement road roughness. Once again, the proposed area ratio-based approach combined with NExT proved to be more accurate in estimating modal damping ratios. It was also noted that the estimated mode shapes are in good agreement with theoretical previsions, highlighting how the effect of vehicle damping improves their estimates.

To sum up, the main contributions of this thesis to the SHM research field are:

- The formulation of an identification framework, which exploits economic free vibration tests, based on the combination of advanced decomposition techniques (i.e., VMD and EFD) for the extraction of modal contribution, a noise-robust area-based approach for the modal damping ratios identification, and a phase-

shift time domain approach for mode shapes construction;

- The proposal of original tuning procedures for both VMD and EFD to automate the extraction of modal components from the investigated signals;
- The extension of the proposed identification approach to the case of indirect monitoring based on VSM also accounting for the effect of vehicle damping and road pavement roughness.

Potential developments for future research, related to the topics addressed throughout this thesis, concern further investigations on the techniques described in Chapters 3 and 4, considering their possible application on highly flexible structures, such as suspended bridges, or on very rigid ones, such as masonry arch bridges, to verify their reliability in the context of a wider range of cases. The real case applications presented throughout this thesis deal only with bridge structure: since the presented approaches, based on free vibration tests, are thought to represent a competitive solution in comparison with traditional OMA approaches, it would be interesting to further extend the investigations to other constructive materials as in the case of composite, masonry or wooden structures as well as to explore their performance for other kinds of civil structures such as buildings, dams and suspended roofs. Another interesting line of research would be the investigation of temperature effects on dynamic identification performance: notably, a limited number of studies are available on this topic and are mainly focused on data recorded in continuous monitoring whereas, to the best knowledge of the author, no investigations have been made considering multiple set of data obtained from periodic and sporadic testing.

With regard to the topic investigated in Chapter 5, the available literature mainly consists of theoretical studies with limited practical application, most of which are based on scaled laboratory models. More research is therefore required to translate this approach into experimental applications concerning the dynamic identifications of full-scale bridges through real signals recorded in situ via instrumented vehicles traveling along the investigated bridge. In this regard, it would be interesting to extend the limited state of the art on how some practical issues may influence the measures such as the ratio of the involved masses in the vehicle-bridge system as well as the influence of the structural scheme, since most of the studies assumes simply supported boundary conditions, neglecting the actual compliance of the supports, whereas continuous and Gerber schemes are rarely investigated. Another interesting aspect to be investigated involves how the sensitivity and accuracy of sensors adopted in the vehicle scanning influence the measure, since it has been shown in the literature how smartphones may also be adopted as measuring devices to retrieve limited information about the modal behavior of bridges.

BIBLIOGRAPHY

[1] P. E. Pinto and P. Franchin, "Issues in the upgrade of italian highway structures," *Journal of Earthquake Engineering*, vol. 14, no. 8, pp. 1221–1252, 2010.

[2] A. Entezami, H. Sarmadi, and B. Behkamal, "Long-term health monitoring of concrete and steel bridges under large and missing data by unsupervised meta learning," *Engineering Structures*, vol. 279, p. 115616, 2023.

[3] F. Marques, C. Moutinho, F. Magalhães, E. Caetano, and Á. Cunha, "Analysis of dynamic and fatigue effects in an old metallic riveted bridge," *Journal of Constructional Steel Research*, vol. 99, pp. 85–101, 2014.

[4] I. Hidayat, M. Suangga, and M. R. Maulana, "The effect of load position to the accuracy of deflection measured with lvdt sensor in i-girder bridge," in *IOP Conference Series: Earth and Environmental Science*, vol. 109, p. 012024, IOP Publishing, 2017.

[5] A. Jamadin, Z. Ibrahim, M. Z. Jumaat, and M. A. Hosen, "Serviceability assessment of fatigued reinforced concrete structures using a dynamic response technique," *Journal of Materials Research and Technology*, vol. 9, no. 3, pp. 4450–4458, 2020.

[6] A. Cunha, E. Caetano, R. Calçada, G. De Roeck, and B. Peeters, "Dynamic measurements on bridges: design, rehabilitation and monitoring," in *Proceedings of the Institution of Civil Engineers-Bridge Engineering*, vol. 156, pp. 135–148, Thomas Telford Ltd, 2003.

[7] C. R. Farrar and K. Worden, "An introduction to structural health monitoring," *Philosophical Transactions of the Royal Society A: Mathematical, Physical and Engineering Sciences*, vol. 365, no. 1851, pp. 303–315, 2007.

[8] W. Ostachowicz and A. Güemes, *New trends in structural health monitoring*, vol. 542. Springer Science & Business Media, 2013.

[9] K. Chang, Z. Shen, and G. Lee, "Modal analysis technique for bridge damage detection," in *Nondestructive testing methods for civil infrastructure*, pp. 1–16, 1995.

[10] C. Rainieri, M. A. Notarangelo, and G. Fabbrocino, "Experiences of dynamic identification and monitoring of bridges in serviceability conditions and after hazardous events," *Infrastructures*, vol. 5, no. 10, p. 86, 2020.

[11] E. Erduran, F. K. Ulla, and L. Næss, "A framework for long-term vibration-based monitoring of bridges," *Sensors*, vol. 21, no. 14, p. 4739, 2021.

[12] S. Ereiz, I. Duvnjak, and J. F. Jiménez-Alonso, "Review of finite element model updating methods for structural applications," in *Structures*, vol. 41, pp. 684–723, Elsevier, 2022.

[13] J. Ko and Y. Q. Ni, "Technology developments in structural health monitoring of large-scale bridges," *Engineering structures*, vol. 27, no. 12, pp. 1715–1725, 2005.

[14] F. Lorenzoni, N. De Conto, F. da Porto, and C. Modena, "Ambient and free-vibration tests to improve the quantification and estimation of modal parameters in existing bridges," *Journal of Civil Structural Health Monitoring*, vol. 9, pp. 617–637, 2019.

[15] C. Rainieri and G. Fabbrocino, "Operational modal analysis of civil engineering structures," *Springer, New York*, vol. 142, p. 143, 2014.

[16] S. S. Saidin, A. Jamadin, S. Abdul Kudus, N. Mohd Amin, and M. A. Anuar, "An overview: The application of vibration-based techniques in bridge structural health monitoring," *International Journal of Concrete Structures and Materials*, vol. 16, no. 1, pp. 1–17, 2022.

[17] Z. Deng, M. Huang, N. Wan, and J. Zhang, "The current development of structural health monitoring for bridges: A review," *Buildings*, vol. 13, no. 6, p. 1360, 2023.

[18] Y. Yang, K. Shi, Z. Wang, H. Xu, B. Zhang, and Y. Wu, "Using a single-dof test vehicle to simultaneously retrieve the first few frequencies and damping ratios of the bridge," *International Journal of Structural Stability and Dynamics*, vol. 21, no. 08, p. 2150108, 2021.

[19] F. Wedel and S. Marx, "Application of machine learning methods on real bridge monitoring data," *Engineering Structures*, vol. 250, p. 113365, 2022.

[20] O. S. Salawu and C. Williams, "Bridge assessment using forced-vibration testing," *Journal of structural engineering*, vol. 121, no. 2, pp. 161–173, 1995.

[21] E. Reynders, J. Houbrechts, and G. De Roeck, "Fully automated (operational) modal analysis," *Mechanical systems and signal processing*, vol. 29, pp. 228–250, 2012.

[22] Z.-F. Fu and J. He, *Modal analysis*. Elsevier, 2001.

[23] J. J. Moughty and J. R. Casas, "A state of the art review of modal-based damage detection in bridges: Development, challenges, and solutions," *Applied Sciences*, vol. 7, no. 5, 2017.

[24] J. Bien and J. Zwolski, "Dynamic tests in bridge monitoring–systematics and applications," in *IMAC-XXV: Conference & Exposition On Structural Dynamics*, 2007.

[25] R. Taleb, F. Bouriche, A. Remas, M. Boukri, and F. Kehila, "Use of ambient and forced vibration tests to evaluate seismic properties of an unreinforced masonry building rehabilitated by dampers," in *15th World Conference on earthquake Engineering*, 2012.

[26] R. Brincker and C. Ventura, *Introduction to operational modal analysis*. John Wiley & Sons, 2015.

[27] F. Magalhães, Á. Cunha, E. Caetano, and R. Brincker, "Damping estimation using free decays and ambient vibration tests," *Mechanical Systems and Signal Processing*, vol. 24, no. 5, pp. 1274–1290, 2010.

[28] J. Rodrigues and M. Ledesma, "Modal identification of railway bridges from ambient and free vibration records," in *Proc. 3rd International Operational Modal Analysis Conference*, 2009.

[29] X.-M. Yang, T.-H. Yi, C.-X. Qu, H.-N. Li, and H. Liu, "Modal identification of high-speed railway bridges through free-vibration detection," *Journal of Engineering Mechanics*, vol. 146, no. 9, p. 04020107, 2020.

[30] M. Mazzeo, D. De Domenico, G. Quaranta, and R. Santoro, "Automatic modal identification of bridges based on free vibration response and variational mode decomposition technique," *Engineering Structures*, vol. 280, p. 115665, 2023.

[31] F. Braga and M. Laterza, "Field testing of low-rise base isolated building," *Engineering Structures*, vol. 26, no. 11, pp. 1599–1610, 2004.

[32] N. D. Oliveto, G. Scalia, and G. Oliveto, "Time domain identification of hybrid base isolation systems using free vibration tests," *Earthquake Engineering & Structural Dynamics*, vol. 39, no. 9, pp. 1015–1038, 2010.

[33] A. Athanasiou, N. D. Oliveto, and F. C. Ponzo, "Identification of first and second order models for the superstructure of base-isolated buildings using free vibration tests: A case study," *Soil Dynamics and Earthquake Engineering*, vol. 135, p. 106178, 2020.

[34] W. Shi, J. Shan, and X. Lu, "Modal identification of shanghai world financial center both from free and ambient vibration response," *Engineering Structures*, vol. 36, pp. 14–26, 2012.

[35] S. Ivorra and F. J. Pallarés, "Dynamic investigations on a masonry bell tower," *Engineering structures*, vol. 28, no. 5, pp. 660–667, 2006.

[36] S. Lagomarsino and C. Calderini, "The dynamical identification of the tensile force in ancient tie-rods," *Engineering Structures*, vol. 27, no. 6, pp. 846–856, 2005.

[37] L. Binda, L. Cantini, C. Tiraboschi, C. Amigoni, *et al.*, "Non destructive investigation for the conservation design of a monastery near bergamo (italy)," in *RILEM Symposium on On Site Assessment of Concrete, Masonry and Timber Structures-SACoMaTiS 2008*, pp. 797–806, RILEM Publications SARL, 2008.

[38] A. Cunha, E. Caetano, and R. Delgado, "Dynamic tests on large cable-stayed bridge," *Journal of Bridge Engineering*, vol. 6, no. 1, pp. 54–62, 2001.

[39] F. Magalhães, E. Caetano, Á. Cunha, O. Flamand, and G. Grillaud, "Ambient and free vibration tests of the millau viaduct: Evaluation of alternative processing strategies," *Engineering Structures*, vol. 45, pp. 372–384, 2012.

[40] J. M. Ko, G. Zheng, Z. Chen, and Y.-Q. Ni, "Field vibration tests of bridge stay cables incorporated with magnetorheological (mr) dampers," in *Smart Structures and Materials 2002: Smart Systems for Bridges, Structures, and Highways*, vol. 4696, pp. 30–40, SPIE, 2002.

[41] K. Van Nimmen, P. Van den Broeck, B. Gezels, G. Lombaert, and G. De Roeck, "Experimental validation of the vibration serviceability assessment of a lightweight steel footbridge with tuned mass damper," in *Proc., ISMA 2012 Int. Conf. on Noise and Vibration Engineering*, pp. 1145–1158, 2012.

[42] A. Quattrone, D. Sabia, F. Tondolo, L. Capacci, A. Lencioni, C. Legramandi, *et al.*, "Dynamic tests and modal identification of corso grosseto viaduct decks before the dismounting," in *Bridge Maintenance, Safety, Management, Life-Cycle Sustainability and Innovations-Proceedings of the 10th International Conference on Bridge Maintenaince, Safety and Management, IABMAS 2020*, pp. 3352–3357, CRC Press/Balkema, 2021.

[43] D. De Domenico, D. Messina, and A. Recupero, "A combined experimental-numerical framework for assessing the load-bearing capacity of existing pc bridge decks accounting for corrosion of prestressing strands," *Materials*, vol. 14, no. 17, p. 4914, 2021.

[44] R. Karoumi and A. Andersson, *Load testing of the New Svinesund Bridge: presentation of results and theoretical verification of bridge behaviour*. 2006.

[45] A. Cunha, E. Caetano, and F. Magalhaes, "Output-only dynamic testing of bridges and special structures," *Structural Concrete*, vol. 8, no. 2, pp. 67–85, 2007.

[46] R. Adams, P. Cawley, C. Pye, and B. Stone, "A vibration technique for non-destructively assessing the integrity of structures," *Journal of mechanical engineering science*, vol. 20, no. 2, pp. 93–100, 1978.

[47] P. Cawley and R. D. Adams, "The location of defects in structures from measurements of natural frequencies," *The Journal of Strain Analysis for Engineering Design*, vol. 14, no. 2, pp. 49–57, 1979.

[48] S. W. Doebling, C. R. Farrar, M. B. Prime, and D. W. Shevitz, "Damage identification and health monitoring of structural and mechanical systems from changes in their vibration characteristics: a literature review," 1996.

[49] C. R. Farrar and S. W. Doebling, "Damage detection and evaluation ii: field applications to large structures," in *Modal analysis and testing*, pp. 345–378, Springer, 1999.

[50] F. Vestroni and D. Capecchi, "Damage evaluation in cracked vibrating beams using experimental frequencies and finite element models," *Journal of Vibration and Control*, vol. 2, no. 1, pp. 69–86, 1996.

[51] A. Pau, A. Greco, and F. Vestroni, "Numerical and experimental detection of concentrated damage in a parabolic arch by measured frequency variations," *Journal of Vibration and Control*, vol. 17, no. 4, pp. 605–614, 2011.

[52] K. Maes, L. Van Meerbeeck, E. Reynders, and G. Lombaert, "Validation of vibration-based structural health monitoring on retrofitted railway bridge kw51," *Mechanical Systems and Signal Processing*, vol. 165, p. 108380, 2022.

[53] A. Messina, A. Jones, E. Williams, *et al.*, "Damage detection and localisation using natural frequency changes," in *1st International Conference on Identification in Engineering Systems*, pp. 67–76, MI Friswell & JE Mottershead, 1996.

[54] O. Salawu, "Detection of structural damage through changes in frequency: a review," *Engineering structures*, vol. 19, no. 9, pp. 718–723, 1997.

[55] J. R. Casas and A. C. Aparicio, "Structural damage identification from dynamic-test data," *Journal of Structural Engineering*, vol. 120, no. 8, pp. 2437–2450, 1994.

[56] A. Jeary and B. Ellis, "Non-destructive in-situ testing using dynamic techniques," in *Proceedings of the 3rd International Conference on Tall Buildings, Hong Kong, China*, pp. 10–15, 1984.

[57] H. Yamaguchi, Y. Matsumoto, K. Kawarai, A. J. Dammika, S. Shahzad, and R. Takanami, "Damage detection based on modal damping change in bridges," 2012.

[58] R. Curadelli, J. Riera, D. Ambrosini, and M. Amani, "Damage detection by means of structural damping identification," *Engineering Structures*, vol. 30, no. 12, pp. 3497–3504, 2008.

[59] M. Frizzarin, M. Q. Feng, P. Franchetti, S. Soyoz, and C. Modena, "Damage detection based on damping analysis of ambient vibration data," *Structural Control and Health Monitoring: The Official Journal of the International Association for Structural Control and Monitoring and of the European Association for the Control of Structures*, vol. 17, no. 4, pp. 368–385, 2010.

[60] C. Williams and O. Salawu, "Damping as a damage indication parameter," in *Proceedings of the 15th international modal analysis conference*, vol. 3089, p. 1531, 1997.

[61] C. R. Farrar, W. E. Baker, and R. C. Dove, "Dynamic parameter similitude for concrete models," *Structural Journal*, vol. 91, no. 1, pp. 90–99, 1994.

[62] J.-H. Kim, H.-S. Jeon, and C.-W. Lee, "Applications of the modal assurance criteria for detecting and locating structural faults," in *Proceedings of the international modal analysis conference*, pp. 536–536, SEM Society for Experimental Mechanics Inc, 1992.

[63] C. Farrar and G. James Iii, "System identification from ambient vibration measurements on a bridge," *Journal of sound and vibration*, vol. 205, no. 1, pp. 1–18, 1997.

[64] R. J. Allemang, "A correlation coefficient for modal vector analysis," in *Proc. of the 1st IMAC*, pp. 110–116, 1982.

[65] O. S. Salawu and C. Williams, "Bridge assessment using forced-vibration testing," *Journal of structural engineering*, vol. 121, no. 2, pp. 161–173, 1995.

[66] R. Salgado, P. J. Cruz, L. F. Ramos, and P. B. Lourenço, "Comparison between damage detection methods applied to beam structures," 2006.

[67] L. Balsamo, S. Mukhopadhyay, R. Betti, and H. Lus, "Damage detection using flexibility proportional coordinate modal assurance criterion," in *Topics in Modal Analysis, Volume 7: Proceedings of the 31st IMAC, A Conference on Structural Dynamics, 2013*, pp. 1–8, Springer, 2014.

[68] J. Zhao and L. Zhang, "Structural damage identification based on the modal data change," *International Journal of Engineering and Manufacturing*, vol. 4, pp. 59–66, 2012.

[69] A. Pandey, M. Biswas, and M. Samman, "Damage detection from changes in curvature mode shapes," *Journal of sound and vibration*, vol. 145, no. 2, pp. 321–332, 1991.

[70] C. R. Farrar and K. Worden, *Structural health monitoring: a machine learning perspective*. John Wiley & Sons, 2012.

[71] A. Pandey and M. Biswas, "Damage detection in structures using changes in flexibility," *Journal of sound and vibration*, vol. 169, no. 1, pp. 3–17, 1994.

[72] T. Toksoy and A. Aktan, "Bridge-condition assessment by modal flexibility," *Experimental Mechanics*, vol. 34, pp. 271–278, 1994.

[73] J. S. Bendat and A. G. Piersol, *Random data: analysis and measurement procedures*. John Wiley & Sons, 2011.

[74] S. W. Smith *et al.*, "The scientist and engineer's guide to digital signal processing," 1997.

[75] N. M. M. Maia and J. M. Montalvão e Silva, *Theoretical and experimental modal analysis*. John Wiley & Sons, 1997.

[76] N. E. Huang, Z. Shen, S. R. Long, M. C. Wu, H. H. Shih, Q. Zheng, N.-C. Yen, C. C. Tung, and H. H. Liu, "The empirical mode decomposition and the hilbert spectrum for nonlinear and non-stationary time series analysis," *Proceedings of the Royal Society of London. Series A: mathematical, physical and engineering sciences*, vol. 454, no. 1971, pp. 903–995, 1998.

[77] J.-N. Juang, *Applied system identification*. Prentice-Hall, Inc., 1994.

[78] B. Peeters and G. De Roeck, "Stochastic system identification for operational modal analysis: a review," *J. Dyn. Sys., Meas., Control*, vol. 123, no. 4, pp. 659–667, 2001.

[79] P. Van Overschee and B. De Moor, *Subspace identification for linear systems: Theory—Implementation—Applications*. Springer Science & Business Media, 2012.

[80] R. Penrose, "On best approximate solutions of linear matrix equations," in *Mathematical Proceedings of the Cambridge Philosophical Society*, vol. 52, pp. 17–19, Cambridge University Press, 1956.

[81] S.-Y. Kung, "A new identification and model reduction algorithm via singular value decomposition," in *Proc. 12th Asilomar Conf. on Circuits, Systems and Computer*, pp. 705–714, 1978.

[82] R. Brincker and P. Andersen, "Understanding stochastic subspace identification," in *Conference Proceedings: IMAC-XXIV: A Conference & Exposition on Structural Dynamics*, Society for Experimental Mechanics, 2006.

[83] B. Peeters and G. De Roeck, "Reference-based stochastic subspace identification for output-only modal analysis," *Mechanical systems and signal processing*, vol. 13, no. 6, pp. 855–878, 1999.

[84] P. Van Overschee and B. De Moor, "Subspace algorithms for the stochastic identification problem," *Automatica*, vol. 29, no. 3, pp. 649–660, 1993.

[85] G. H. James, T. G. Carne, J. P. Lauffer, *et al.*, "The natural excitation technique (NExT) for modal parameter extraction from operating structures," *Modal Analysis-the International Journal of Analytical and Experimental Modal Analysis*, vol. 10, no. 4, p. 260, 1995.

[86] G. H. James III, T. G. Carne, and J. P. Lauffer, "The natural excitation technique (NExT) for modal parameter extraction from operating wind turbines," tech. rep., Sandia National Labs., Albuquerque, NM (United States), 1993.

[87] H. Vold, J. Kundrat, G. T. Rocklin, and R. Russell, "A multi-input modal estimation algorithm for mini-computers," *SAE Transactions*, pp. 815–821, 1982.

[88] S. R. Ibrahim and E. Mikulcik, "A method for the direct identification of vibration parameters from the free response," *The Shock and Vibration Inform. Ctr. Shock and Vibration Bull. Part. 4: Sep. 1977*, 1977.

[89] J. Jer-Nan and S. P. Richard, "An eigensystem realization algorithm for modal parameter identification and model reduction," *Journal of Guidance, Control, and Dynamics*, vol. 8, no. 5, pp. 620–627, 1985.

[90] H. Cole, Jr, "On-the-line analysis of random vibrations," in *9th structural dynamics and materials conference*, p. 288, 1968.

[91] J. Vandiver, A. Dunwoody, R. Campbell, and M. Cook, "A mathematical basis for the random decrement vibration signature analysis technique," 1982.

[92] S. Ibrahim, "Random decrement technique for modal identification of structures," *Journal of Spacecraft and Rockets*, vol. 14, no. 11, pp. 696–700, 1977.

[93] J. C. Asmussen, "Modal analysis based on the random decrement technique: application to civil engineering structures," 1997.

[94] R. Brincker, S. Krenk, P. H. Kirkegaard, and A. Rytter, "Identification of dynamical properties from correlation function estimates," 1992.

[95] J. S. Bendat and A. G. Piersol, "Engineering applications of correlation and spectral analysis," *New York*, 1980.

[96] A. J. Felber, *Development of a hybrid bridge evaluation system.* PhD thesis, University of British Columbia, 1994.

[97] L. Zhang, T. Wang, and Y. Tamura, "A frequency–spatial domain decomposition (fsdd) method for operational modal analysis," *Mechanical systems and signal processing*, vol. 24, no. 5, pp. 1227–1239, 2010.

[98] C. Rainieri, G. Fabbrocino, and E. Cosenza, "Some remarks on experimental estimation of damping for seismic design of civil constructions," *Shock and Vibration*, vol. 17, no. 4-5, pp. 383–395, 2010.

[99] R. Brincker, L. Zhang, P. Andersen, *et al.*, "Modal identification from ambient responses using frequency domain decomposition," in *Proceedings of the 18th international modal analysis conference (IMAC)*, vol. 1, pp. 625–630, San Antonio, TX, USA, 2000.

[100] R. Brincker, L. Zhang, and P. Andersen, "Modal identification of output-only systems using frequency domain decomposition," *Smart materials and structures*, vol. 10, no. 3, p. 441, 2001.

[101] S. Gade, "Frequency domain techniques for operational modal analysis," *The Shock and Vibration Digest*, vol. 38, no. 6, pp. 537–538, 2006.

[102] R. Brincker, C. E. Ventura, and P. Andersen, "Damping estimation by frequency domain decomposition," in *Proceedings of IMAC 19: A conference on structural dynamics: Februar 5-8, 2001, Hyatt Orlando, Kissimmee, Florida, 2001*, pp. 698–703, Society for Experimental Mechanics, 2001.

[103] M. Batel, "Operational modal analysis-another way of doing modal testing," *Sound and Vibration*, vol. 36, no. 8, pp. 22–27, 2002.

[104] A. Entezami and H. Shariatmadar, "Damage localization under ambient excitations and non-stationary vibration signals by a new hybrid algorithm for feature extraction and multivariate distance correlation methods," *Structural Health Monitoring*, vol. 18, no. 2, pp. 347–375, 2019.

[105] N. E. Huang, C. C. Chern, K. Huang, L. W. Salvino, S. R. Long, and K. L. Fan, "A new spectral representation of earthquake data: Hilbert spectral analysis of station tcu129, chi-chi, taiwan, 21 september 1999," *Bulletin of the Seismological Society of America*, vol. 91, no. 5, pp. 1310–1338, 2001.

[106] J. Chen, "Application of empirical mode decomposition in structural health monitoring: some experience," *Advances in Adaptive Data Analysis*, vol. 1, no. 04, pp. 601–621, 2009.

[107] J. N. Yang, Y. Lei, S. Pan, and N. Huang, "System identification of linear structures based on hilbert–huang spectral analysis. part 1: normal modes," *Earthquake engineering & structural dynamics*, vol. 32, no. 9, pp. 1443–1467, 2003.

[108] Z. Shi and S. Law, "Identification of linear time-varying dynamical systems using hilbert transform and empirical mode decomposition method," 2007.

[109] D.-J. Yu and W.-X. Ren, "EMD-based stochastic subspace identification of structures from operational vibration measurements," *Engineering Structures*, vol. 27, no. 12, pp. 1741–1751, 2005.

[110] X. He, X. Hua, Z. Chen, and F. Huang, "EMD-based random decrement technique for modal parameter identification of an existing railway bridge," *Engineering Structures*, vol. 33, no. 4, pp. 1348–1356, 2011.

[111] J. P. Yang and W.-C. Lee, "Damping effect of a passing vehicle for indirectly measuring bridge frequencies by EMD technique," *International Journal of Structural Stability and Dynamics*, vol. 18, no. 01, p. 1850008, 2018.

[112] S. Dhakal and R. B. Malla, "Determination of natural frequencies of a steel railroad bridge using onboard sensors," in *Earth and Space 2018: Engineering for Extreme Environments*, pp. 1034–1046, American Society of Civil Engineers Reston, VA, 2018.

[113] Y. L. Xu and J. Chen, "Structural damage detection using empirical mode decomposition: experimental investigation," *Journal of engineering mechanics*, vol. 130, no. 11, pp. 1279–1288, 2004.

[114] M. Bradley, A. González, and D. Hester, "Analysis of the structural response to a moving load using empirical mode decomposition," *Bridge Maintenance, Safety and Management*, p. 117, 2010.

[115] E. Lofrano, A. Paolone, and F. Romeo, "Damage identification in a parabolic arch through the combined use of modal properties and empirical mode decomposition," in *Proceedings of the 9th international conference on structural dynamics, EURODYN*, 2014.

[116] H. Babajanian Bisheh, G. Ghodrati Amiri, M. Nekooei, and E. Darvishan, "Damage detection of a cable-stayed bridge based on combining effective intrinsic mode functions of empirical mode decomposition using the feature selection technique," *Inverse Problems in Science and Engineering*, vol. 29, no. 6, pp. 861–881, 2021.

[117] R. Rato, M. Ortigueira, and A. Batista, "On the hht, its problems, and some solutions," *Mechanical Systems and Signal Processing*, vol. 22, no. 6, pp. 1374–1394, 2008. Special Issue: Mechatronics.

[118] M. Feldman, "Time-varying vibration decomposition and analysis based on the hilbert transform," *Journal of Sound and Vibration*, vol. 295, no. 3-5, pp. 518–530, 2006.

[119] P. Flandrin, G. Rilling, and P. Goncalves, "Empirical mode decomposition as a filter bank," *IEEE signal processing letters*, vol. 11, no. 2, pp. 112–114, 2004.

[120] Z. Wu and N. E. Huang, "A study of the characteristics of white noise using the empirical mode decomposition method," *Proceedings of the Royal Society of London. Series A: Mathematical, Physical and Engineering Sciences*, vol. 460, no. 2046, pp. 1597–1611, 2004.

[121] Z. Wu and N. E. Huang, "Ensemble empirical mode decomposition: A noise-assisted data analysis method," *Advances in Adaptive Data Analysis*, vol. 01, no. 01, pp. 1–41, 2009.

[122] W. Liu, S. Cao, and Y. Chen, "Applications of variational mode decomposition in seismic time-frequency analysis," *Geophysics*, vol. 81, no. 5, pp. V365–V378, 2016.

[123] W. Yang, Z. Peng, K. Wei, P. Shi, and W. Tian, "Superiorities of variational mode decomposition over empirical mode decomposition particularly in time–frequency feature extraction and wind turbine condition monitoring," *IET Renewable Power Generation*, vol. 11, no. 4, pp. 443–452, 2017.

[124] A. Zeiler, R. Faltermeier, I. R. Keck, A. M. Tomé, C. G. Puntonet, and E. W. Lang, "Empirical mode decomposition-an introduction," in *The 2010 international joint conference on neural networks (IJCNN)*, pp. 1–8, IEEE, 2010.

[125] K. Dragomiretskiy and D. Zosso, "Variational mode decomposition," *IEEE transactions on signal processing*, vol. 62, no. 3, pp. 531–544, 2013.

[126] R. Gu, J. Chen, R. Hong, H. Wang, and W. Wu, "Incipient fault diagnosis of rolling bearings based on adaptive variational mode decomposition and teager energy operator," *Measurement*, vol. 149, p. 106941, 2020.

[127] Q. Huang, Q. Li, M. Ran, X. Liu, and Y. Zhou, "Threshold-optimized swarm decomposition using grey wolf optimizer for the acoustic-based internal defect detection of arc magnets," *Shock and Vibration*, vol. 2021, pp. 1–21, 2021.

[128] T. Liang, H. Lu, and H. Sun, "Application of parameter optimized variational mode decomposition method in fault feature extraction of rolling bearing," *Entropy*, vol. 23, no. 5, p. 520, 2021.

[129] Y.-J. Xue, J.-X. Cao, D.-X. Wang, H.-K. Du, and Y. Yao, "Application of the variational-mode decomposition for seismic time–frequency analysis," *IEEE Journal of Selected Topics in Applied Earth Observations and Remote Sensing*, vol. 9, no. 8, pp. 3821–3831, 2016.

[130] A. Bagheri, O. E. Ozbulut, and D. K. Harris, "Structural system identification based on variational mode decomposition," *Journal of Sound and Vibration*, vol. 417, pp. 182–197, 2018.

[131] M. Zhang and F. Xu, "Variational mode decomposition based modal parameter identification in civil engineering," *Frontiers of Structural and Civil Engineering*, vol. 13, pp. 1082–1094, 2019.

[132] Y. Wang, R. Markert, J. Xiang, and W. Zheng, "Research on variational mode decomposition and its application in detecting rub-impact fault of the rotor system," *Mechanical Systems and Signal Processing*, vol. 60, pp. 243–251, 2015.

[133] H. Yang, S. Liu, and H. Zhang, "Adaptive estimation of VMD modes number based on cross correlation coefficient," *Journal of Vibroengineering*, vol. 19, no. 2, pp. 1185–1196, 2017.

[134] J. Lian, Z. Liu, H. Wang, and X. Dong, "Adaptive variational mode decomposition method for signal processing based on mode characteristic," *Mechanical Systems and Signal Processing*, vol. 107, pp. 53–77, 2018.

[135] Z. Wang, J. Wang, and W. Du, "Research on fault diagnosis of gearbox with improved variational mode decomposition," *Sensors*, vol. 18, no. 10, p. 3510, 2018.

[136] Q. Huang, X. Liu, Q. Li, Y. Zhou, T. Yang, and M. Ran, "A parameter-optimized variational mode decomposition method using salp swarm algorithm and its application to acoustic-based detection for internal defects of arc magnets," *AIP Advances*, vol. 11, no. 6, p. 065216, 2021.

[137] D. E. Goldberg, "Optimization, and machine learning," *Genetic algorithms in Search*, 1989.

[138] M. R. Bonyadi and Z. Michalewicz, "Particle swarm optimization for single objective continuous space problems: a review," *Evolutionary computation*, vol. 25, no. 1, pp. 1–54, 2017.

[139] J. Gilles, "Empirical wavelet transform," *IEEE transactions on signal processing*, vol. 61, no. 16, pp. 3999–4010, 2013.

[140] F. Gougam, C. Rahmoune, D. Benazzouz, and B. Merainani, "Bearing fault diagnosis based on feature extraction of empirical wavelet transform (ewt) and fuzzy logic system (fls) under variable operating conditions," *Journal of Vibroengineering*, vol. 21, no. 6, pp. 1636–1650, 2019.

[141] I. Daubechies, *Ten lectures on wavelets*. SIAM, 1992.

[142] Y. Hu, F. Li, H. Li, and C. Liu, "An enhanced empirical wavelet transform for noisy and non-stationary signal processing," *Digital signal processing*, vol. 60, pp. 220–229, 2017.

[143] Y. Xin, H. Hao, and J. Li, "Operational modal identification of structures based on improved empirical wavelet transform," *Structural Control and Health Monitoring*, vol. 26, no. 3, p. e2323, 2019.

[144] Z. Luo, T. Liu, S. Yan, and M. Qian, "Revised empirical wavelet transform based on auto-regressive power spectrum and its application to the mode decomposition of deployable structure," *Journal of Sound and Vibration*, vol. 431, pp. 70–87, 2018.

[145] A. Bhattacharyya, L. Singh, and R. B. Pachori, "Fourier–bessel series expansion based empirical wavelet transform for analysis of non-stationary signals," *Digital Signal Processing*, vol. 78, pp. 185–196, 2018.

[146] W. Zhou, Z. Feng, Y. Xu, X. Wang, and H. Lv, "Empirical fourier decomposition: An accurate signal decomposition method for nonlinear and non-stationary time series analysis," *Mechanical Systems and Signal Processing*, vol. 163, p. 108155, 2022.

[147] P. Singh, S. D. Joshi, R. K. Patney, and K. Saha, "The fourier decomposition method for nonlinear and non-stationary time series analysis," *Proceedings of the Royal Society A: Mathematical, Physical and Engineering Sciences*, vol. 473, no. 2199, p. 20160871, 2017.

[148] H. Jing, H. Yuan, Y. Zhao, and Y. Yang, "Applying hilbert-huang transform to identifying structural modal parameters," in *2008 International Workshop on Education Technology and Training & 2008 International Workshop on Geoscience and Remote Sensing*, vol. 2, pp. 617–621, IEEE, 2008.

[149] B. Wei, B. Xie, H. Li, Z. Zhong, and Y. You, "An improved hilbert–huang transform method for modal parameter identification of a high arch dam," *Applied Mathematical Modelling*, vol. 91, pp. 297–310, 2021.

[150] G. A. Papagiannopoulos and G. D. Hatzigeorgiou, "On the use of the half-power bandwidth method to estimate damping in building structures," *Soil Dynamics and Earthquake Engineering*, vol. 31, no. 7, pp. 1075–1079, 2011.

[151] B. A. Olmos and J. M. Roesset, "Evaluation of the half-power bandwidth method to estimate damping in systems without real modes," *Earthquake engineering & structural dynamics*, vol. 39, no. 14, pp. 1671–1686, 2010.

[152] J.-T. Wang, F. Jin, and C.-H. Zhang, "Estimation error of the half-power bandwidth method in identifying damping for multi-dof systems," *Soil Dynamics and Earthquake Engineering*, vol. 39, pp. 138–142, 2012.

[153] F.-L. Huang, X.-M. Wang, Z.-Q. Chen, X.-H. He, and Y.-Q. Ni, "A new approach to identification of structural damping ratios," *Journal of Sound and Vibration*, vol. 303, no. 1-2, pp. 144–153, 2007.

[154] F. Magalhães, E. Caetano, and Á. Cunha, "Challenges in the application of stochastic modal identification methods to a cable-stayed bridge," *Journal of Bridge Engineering*, vol. 12, no. 6, pp. 746–754, 2007.

[155] J. Brownjohn, F. Magalhaes, E. Caetano, and A. Cunha, "Ambient vibration re-testing and operational modal analysis of the humber bridge," *Engineering Structures*, vol. 32, no. 8, pp. 2003–2018, 2010.

[156] G. Chen, S. Beskhyroun, and P. Omenzetter, "A comparison of operational modal parameter identification methods for a multi-span concrete motorway bridge," in *Proceedings of the New Zealand Society for Earthquake Engineering Annual Conference*, no. 54, 2015.

[157] F. Magalhães and Á. Cunha, "Explaining operational modal analysis with data from an arch bridge," *Mechanical systems and signal processing*, vol. 25, no. 5, pp. 1431–1450, 2011.

[158] A. Cunha, E. Caetano, F. Magalhães, and C. Moutinho, "Recent perspectives in dynamic testing and monitoring of bridges," *Structural Control and Health Monitoring*, vol. 20, no. 6, pp. 853–877, 2013.

[159] M. J. Whelan, M. V. Gangone, K. D. Janoyan, and R. Jha, "Real-time wireless vibration monitoring for operational modal analysis of an integral abutment highway bridge," *Engineering Structures*, vol. 31, no. 10, pp. 2224–2235, 2009.

[160] A. L. Hong, F. Ubertini, and R. Betti, "Wind analysis of a suspension bridge: identification and finite-element model simulation," *Journal of Structural Engineering*, vol. 137, no. 1, pp. 133–142, 2011.

[161] F. Ubertini, C. Gentile, and A. L. Materazzi, "Automated modal identification in operational conditions and its application to bridges," *Engineering Structures*, vol. 46, pp. 264–278, 2013.

[162] Y. Tamura, A. Yoshida, L. Zhang, T. Ito, S. Nakata, and K. Sato, "Examples of modal identification of structures in japan by fdd and mrd techniques," in *Proceedings of the 1st international operational modal analysis conference, Copenhagen, Denmark*, 2005.

[163] A. Bajric, R. Brincker, and S. Thöns, "Evaluation of damping estimates in the presence of closely spaced modes using operational modal analysis techniques," in *Proceedings of the 6th international operational modal analysis conference, Gijòn, Spain*, vol. 735, 2015.

[164] S. Castellanos-Toro, M. Marmolejo, J. Marulanda, A. Cruz, and P. Thomson, "Frequencies and damping ratios of bridges through operational modal analysis using smartphones," *Construction and Building Materials*, vol. 188, pp. 490–504, 2018.

[165] G. Zini, A. Giachetti, M. Betti, and G. Bartoli, "Vibration signature effects on damping identification of a rc bridge under ambient vibrations," *Engineering Structures*, vol. 298, p. 116934, 2024.

[166] P. Clemente, F. Marulo, L. Lecce, and A. Bifulco, "Experimental modal analysis of the garigliano cable-stayed bridge," *Soil Dynamics and Earthquake Engineering*, vol. 17, no. 7-8, pp. 485–493, 1998.

[167] K. Tomaszkiewicz and T. Owerko, "Estimation of the bridge damping decrement for in-situ recorded signal with unusual features," in *Bridge Safety, Maintenance, Management, Life-Cycle, Resilience and Sustainability* (J.-R. Casas, D. M. Frangopol, and J. Turmo, eds.), pp. 501–508, CRC Press, 2022.

[168] C.-S. Huang, S.-L. Hung, C. Lin, and W. Su, "A wavelet-based approach to identifying structural modal parameters from seismic response and free vibration data," *Computer-Aided Civil and Infrastructure Engineering*, vol. 20, no. 6, pp. 408–423, 2005.

[169] T. Miyashita and M. Nagai, "Vibration-based structural health monitoring for bridges using laser doppler vibrometers and mems-based technologies," *Steel Structures*, vol. 8, no. 4, pp. 325–331, 2008.

[170] X.-l. Li, L.-m. Sun, W. Cheng, and Y. Xia, "Damping analysis on steel strand cables of a cable-stayed bridge based on field tests," in *Proceedings of the 2014*

World Congress on Advances in Civil, Environmental, and Materials Research (C.-K. Choi, ed.), Techno-Press, 2014.

[171] G. Quaranta, C. Demartino, and Y. Xiao, "Experimental dynamic characterization of a new composite glubam-steel truss structure," *Journal of Building Engineering*, vol. 25, p. 100773, 2019.

[172] J. A. Little and B. P. Mann, "Optimizing logarithmic decrement damping estimation through uncertainty propagation," *Journal of Sound and Vibration*, vol. 457, pp. 368–376, 2019.

[173] Y. Liao and V. Wells, "Modal parameter identification using the log decrement method and band-pass filters," *Journal of Sound and Vibration*, vol. 330, no. 21, pp. 5014–5023, 2011.

[174] Ž. Nakutis and P. Kaškonas, "Bridge vibration logarithmic decrement estimation at the presence of amplitude beat," *Measurement*, vol. 44, no. 2, pp. 487–492, 2011.

[175] B. Santoshkumar and F. A. Khasawneh, "Guidelines for optimizing the error in area ratio damping estimation method," in *Proceedings of the ASME 2021 International Design Engineering Technical Conferences and Computers and Information in Engineering Conference* (L. Yu, C. Untaroiu, and L. Munoz, eds.), ASME, 2021.

[176] P. Ni, J. Li, H. Hao, Y. Xia, X. Wang, J.-M. Lee, and K.-H. Jung, "Time-varying system identification using variational mode decomposition," *Structural Control and Health Monitoring*, vol. 25, no. 6, p. e2175, 2018.

[177] M. Mazzeo, D. De Domenico, G. Quaranta, and R. Santoro, "A novel procedure for damping ratio identification from free vibration tests with application to existing bridge decks," in *European Workshop on Structural Health Monitoring: EWSHM 2022-Volume 3*, pp. 699–708, Springer, 2022.

[178] M. Mazzeo, D. De Domenico, R. Santoro, and G. Quaranta, "Informed assessment of structural health conditions of bridges based on free-vibration tests," in *Life-Cycle of Structures and Infrastructure Systems*, pp. 2739–2745, CRC Press, 2023.

[179] M. Barbosh, P. Singh, and A. Sadhu, "Empirical mode decomposition and its variants: A review with applications in structural health monitoring," *Smart Materials and Structures*, vol. 29, no. 9, p. 093001, 2020.

[180] S.-K. Au, J. M. Brownjohn, B. Li, and A. Raby, "Understanding and managing identification uncertainty of close modes in operational modal analysis," *Mechanical Systems and Signal Processing*, vol. 147, p. 107018, 2021.

[181] H. Li, T. Liu, X. Wu, and Q. Chen, "Application of optimized variational mode decomposition based on kurtosis and resonance frequency in bearing fault feature extraction," *Transactions of the Institute of Measurement and Control*, vol. 42, no. 3, pp. 518–527, 2020.

[182] L.-h. Zhi, F. Hu, C. Zhao, and J. Wang, "Modal parameter estimation of civil structures based on improved variational mode decomposition," *Structural Engineering and Mechanics*, vol. 79, no. 6, pp. 683–697, 2021.

[183] J. Feng, B. Zhao, and T. Zhao, "Quantitative identification of near-fault pulse-like ground motions based on variational mode decomposition technique," *Soil Dynamics and Earthquake Engineering*, vol. 151, p. 107009, 2021.

[184] "Decreto 17 gennaio 2018: Aggiornamento delle norme tecniche per le costruzioni," Ministry of Infrastructure and Transport, 2018.

[185] C. SAP2000, "Analysis reference manual; csi berkeley (ca, usa) computer and structures," *Inc.: Berkeley, CA, USA*, 2016.

[186] D. De Domenico, D. Messina, and A. Recupero, "Quality control and safety assessment of prestressed concrete bridge decks through combined field tests and numerical simulation," in *Structures*, vol. 39, pp. 1135–1157, Elsevier, 2022.

[187] E. Cosenza and D. Losanno, "Assessment of existing reinforced-concrete bridges under road-traffic loads according to the new italian guidelines," *Structural Concrete*, vol. 22, no. 5, pp. 2868–2881, 2021.

[188] "Eurocode 4: Design of composite steel and concrete structures – Part 1-1: General rules and rules for buildings," European Committee for Standardization, 2004.

[189] C. Maruccio, G. Quaranta, L. De Lorenzis, and G. Monti, "Energy harvesting from electrospun piezoelectric nanofibers for structural health monitoring of a cable-stayed bridge," *Smart Materials and Structures*, vol. 25, no. 8, p. 085040, 2016.

[190] H. Zui, T. Shinke, and Y. Namita, "Practical formulas for estimation of cable tension by vibration method," *Journal of Structural Engineering*, vol. 122, no. 6, pp. 651–656, 1996.

[191] Z. Fang and J.-q. Wang, "Practical formula for cable tension estimation by vibration method," *Journal of Bridge Engineering*, vol. 17, no. 1, pp. 161–164, 2012.

[192] C.-C. Chen, W.-H. Wu, S.-T. Yu, and G. Lai, "Investigation of modal damping ratios for stay cables based on stochastic subspace identification with ambient vibration measurements," *Advances in Structural Engineering*, vol. 22, no. 16, pp. 3444–3460, 2019.

[193] "Eurocode 2: Design of concrete structures – Part 1-1: General rules and rules for buildings," European Committee for Standardization, 2004.

[194] A. Papoulis, *Random variables and stochastic processes*. McGraw Hill, 1991.

[195] M. Civera and C. Surace, "A comparative analysis of signal decomposition techniques for structural health monitoring on an experimental benchmark," *Sensors*, vol. 21, no. 5, p. 1825, 2021.

[196] W.-B. Gong, A. Li, Z.-H. Wu, and F.-J. Qina, "Nonlinear vibration feature extraction based on power spectrum envelope adaptive empirical fourier decomposition," *ISA Transactions*, 2023.

[197] M. Mazzeo, D. De Domenico, G. Quaranta, and R. Santoro, "Automatic modal identification of bridges based on free vibrations and advanced signal decomposition techniques," *Vibroengineering Procedia*, vol. 50, pp. 49–55, 09 2023.

[198] M. Mazzeo, D. De Domenico, G. Quaranta, and R. Santoro, "An efficient automatic modal identification method based on free vibration response and enhanced empirical fourier decomposition technique," *Engineering Structures*, vol. 298, p. 117046, 2024.

[199] P. Shi, W. Yang, M. Sheng, and M. Wang, "An enhanced empirical wavelet transform for features extraction from wind turbine condition monitoring signals," *Energies*, vol. 10, no. 7, p. 972, 2017.

[200] Y. Xu, Y. Deng, J. Zhao, W. Tian, and C. Ma, "A novel rolling bearing fault diagnosis method based on empirical wavelet transform and spectral trend," *IEEE Transactions on Instrumentation and Measurement*, vol. 69, no. 6, pp. 2891–2904, 2019.

[201] H. Azami, K. Mohammadi, and B. Bozorgtabar, "An improved signal segmentation using moving average and savitzky-golay filter," *Journal of Signal and Information Processing*, pp. 39–44, 01 2012.

[202] J. Luo, K. Ying, and J. Bai, "Savitzky–golay smoothing and differentiation filter for even number data," *Signal processing*, vol. 85, no. 7, pp. 1429–1434, 2005.

[203] G. Betta, D. Capriglione, G. Cerro, L. Ferrigno, and G. Miele, "The effectiveness of savitzky-golay smoothing method for spectrum sensing in cognitive radios," in *2015 XVIII AISEM annual conference*, pp. 1–4, IEEE, 2015.

[204] S. Li, Y. Liu, P. Wang, X. Li, and Z. Li, "Modal parameter identification for closely spaced modes using an empirical fourier decomposition-based method," *Scientia Iranica*, 2022.

[205] P. Code, "Eurocode 2: design of concrete structures-part 1–1: general rules and rules for buildings," *British Standard Institution, London*, 2005.

[206] F. Magalhães, E. Caetano, and Á. Cunha, "Operational modal analysis of the braga sports stadium suspended roof," in *Proceedings of the 24th IMAC, St. Louis*, 2006.

[207] W. Li, V.-H. Vu, Z. Liu, M. Thomas, and B. Hazel, "Extraction of modal parameters for identification of time-varying systems using data-driven stochastic subspace identification," *Journal of Vibration and Control*, vol. 24, no. 20, pp. 4781–4796, 2018.

[208] "Eurocode 1: Actions on structures — part 2: Traffic loads on bridges. EN1991−2," *British Standard Institution , London*, 2003.

[209] G. Feltrin, G. Sedlacek, R. Soorensen, T. Froolund, and B. Luczynski, "Monitoring guidelines for railway bridges, sb-mon: Sustainable bridges guideline, sb d5. 2," 2007.

[210] D. Bacinskas, Z. Kamaitis, D. Jatulis, and A. Kilikevicius, "Field testing of old narrow-gauge railway steel truss bridge," *Procedia Engineering*, vol. 57, pp. 136–143, 2013.

[211] V. Gattulli, E. Lofrano, A. Paolone, and F. Potenza, "Measured properties of structural damping in railway bridges," *Journal of civil structural health monitoring*, vol. 9, pp. 639–653, 2019.

[212] M. Venglár, K. Lamperová, and M. Sokol, "Performance assessment of steel truss railway bridge with curved track," *Acta Polytechnica*, vol. 62, no. 5, pp. 558–566, 2022.

[213] M. Gul and F. N. Catbas, "Ambient vibration data analysis for structural identification and global condition assessment," *Journal of Engineering Mechanics*, vol. 134, no. 8, pp. 650–662, 2008.

[214] B. Gunes and O. Gunes, "Vibration-based damage evaluation of a reinforced concrete frame subjected to cyclic pushover testing," *Shock and Vibration*, vol. 2021, pp. 1–16, 2021.

[215] Y.-B. Yang, J. P. Yang, Y. Wu, and B. Zhang, *Vehicle scanning method for bridges*. John Wiley & Sons, 2019.

[216] Y. Yang and C. Lin, "Vehicle–bridge interaction dynamics and potential applications," *Journal of sound and vibration*, vol. 284, no. 1-2, pp. 205–226, 2005.

[217] D. Cantero, P. McGetrick, C.-W. Kim, and E. OBrien, "Experimental monitoring of bridge frequency evolution during the passage of vehicles with different suspension properties," *Engineering Structures*, vol. 187, pp. 209–219, 2019.

[218] C. Lin and Y. Yang, "Use of a passing vehicle to scan the fundamental bridge frequencies: An experimental verification," *Engineering Structures*, vol. 27, no. 13, pp. 1865–1878, 2005.

[219] A. Miyamoto and A. Yabe, "Bridge condition assessment based on vibration responses of passenger vehicle," in *Journal of physics: conference series*, vol. 305, p. 012103, IOP Publishing, 2011.

[220] A. Di Matteo, D. Fiandaca, and A. Pirrotta, "Smartphone-based bridge monitoring through vehicle–bridge interaction: analysis and experimental assessment," *Journal of Civil Structural Health Monitoring*, vol. 12, no. 6, pp. 1329–1342, 2022.

[221] D. Fiandaca, A. Di Matteo, B. Patella, N. Moukri, R. Inguanta, D. Llort, A. Mulone, A. Mulone, S. Alsamahi, and A. Pirrotta, "An integrated approach for structural health monitoring and damage detection of bridges: An experimental assessment," *Applied Sciences*, vol. 12, no. 24, p. 13018, 2022.

[222] S. Laflamme, F. Ubertini, A. Di Matteo, A. Pirrotta, M. Perry, Y. Fu, J. Li, H. Wang, T. Hoang, B. Glisic, *et al.*, "Roadmap on measurement technologies for next generation structural health monitoring systems," *Measurement Science and Technology*, 2023.

[223] R. Corbally and A. Malekjafarian, "Examining changes in bridge frequency due to damage using the contact-point response of a passing vehicle," *Journal of Structural Integrity and Maintenance*, vol. 6, no. 3, pp. 148–158, 2021.

[224] X. Kong, C. Cai, and B. Kong, "Numerically extracting bridge modal properties from dynamic responses of moving vehicles," *Journal of Engineering Mechanics*, vol. 142, no. 6, p. 04016025, 2016.

[225] H. Wang, T. Nagayama, J. Nakasuka, B. Zhao, and D. Su, "Extraction of bridge fundamental frequency from estimated vehicle excitation through a particle filter approach," *Journal of Sound and Vibration*, vol. 428, pp. 44–58, 2018.

[226] C. Liu, Y. Zhu, and H. Ye, "Bridge frequency identification based on relative displacement of axle and contact point using tire pressure monitoring," *Mechanical Systems and Signal Processing*, vol. 183, p. 109613, 2023.

[227] Y. Zhang, H. Zhao, and S. T. Lie, "Estimation of mode shapes of beam-like structures by a moving lumped mass," *Engineering Structures*, vol. 180, pp. 654–668, 2019.

[228] J. Kim and J. P. Lynch, "Experimental analysis of vehicle–bridge interaction using a wireless monitoring system and a two-stage system identification technique," *Mechanical Systems and Signal Processing*, vol. 28, pp. 3–19, 2012.

[229] S. Urushadze and J.-D. Yau, "Experimental verification of indirect bridge frequency measurement using a passing vehicle," *Procedia engineering*, vol. 190, pp. 554–559, 2017.

[230] H. Xu, C. Huang, Z. Wang, K. Shi, Y. Wu, and Y. Yang, "Damped test vehicle for scanning bridge frequencies: Theory, simulation and experiment," *Journal of Sound and Vibration*, vol. 506, p. 116155, 2021.

[231] J. D. Sitton, Y. Zeinali, D. Rajan, and B. A. Story, "Frequency estimation on two-span continuous bridges using dynamic responses of passing vehicles," *Journal of Engineering Mechanics*, vol. 146, no. 1, p. 04019115, 2020.

[232] K. Demirlioglu, S. Gonen, and E. Erduran, "Efficacy of vehicle scanning methods in estimating the mode shapes of bridges seated on elastic supports," *Sensors*, vol. 23, no. 14, p. 6335, 2023.

[233] N. E. Huang, Z. Shen, S. R. Long, M. C. Wu, H. H. Shih, Q. Zheng, N.-C. Yen, C. C. Tung, and H. H. Liu, "The empirical mode decomposition and the hilbert spectrum for nonlinear and non-stationary time series analysis," *Proceedings of the Royal Society of London. Series A: mathematical, physical and engineering sciences*, vol. 454, no. 1971, pp. 903–995, 1998.

[234] Y. Yang and K. Chang, "Extraction of bridge frequencies from the dynamic response of a passing vehicle enhanced by the EMD technique," *Journal of sound and vibration*, vol. 322, no. 4-5, pp. 718–739, 2009.

[235] K. Kildashti, M. M. Alamdari, C. Kim, W. Gao, and B. Samali, "Drive-by-bridge inspection for damage identification in a cable-stayed bridge: Numerical investigations," *Engineering structures*, vol. 223, p. 110891, 2020.

[236] L. Zhu and A. Malekjafarian, "On the use of ensemble empirical mode decomposition for the identification of bridge frequency from the responses measured in a passing vehicle," *Infrastructures*, vol. 4, no. 2, p. 32, 2019.

[237] S. S. Eshkevari, T. J. Matarazzo, and S. N. Pakzad, "Bridge modal identification using acceleration measurements within moving vehicles," *Mechanical Systems and Signal Processing*, vol. 141, p. 106733, 2020.

[238] H. Aied, A. González, and D. Cantero, "Identification of sudden stiffness changes in the acceleration response of a bridge to moving loads using ensemble empirical mode decomposition," *Mechanical Systems and Signal Processing*, vol. 66, pp. 314–338, 2016.

[239] Y. Yang, H. Xu, X. Mo, Z. Wang, and Y. Wu, "An effective procedure for extracting the first few bridge frequencies from a test vehicle," *Acta Mechanica*, vol. 232, pp. 1227–1251, 2021.

[240] M. Mazzeo, D. De Domenico, G. Quaranta, and R. Santoro, "An enhanced indirect modal identification procedure for bridges based on the dynamic response of moving vehicles," *Journal of Sound and Vibration*, (under review).

[241] L. Fryba, *Vibration of solids and structures under moving loads*. Thomas Telford, 1999.

[242] C. Johansson, C. Pacoste, and R. Karoumi, "Closed-form solution for the mode superposition analysis of the vibration in multi-span beam bridges caused by concentrated moving loads," *Computers & Structures*, vol. 119, pp. 85–94, 2013.

[243] A. Di Matteo, "Dynamic response of beams excited by moving oscillators: Approximate analytical solutions for general boundary conditions," *Computers & Structures*, vol. 280, p. 106989, 2023.

[244] Y. Yang, B. Zhang, Y. Qian, and Y. Wu, "Contact-point response for modal identification of bridges by a moving test vehicle," *International Journal of Structural Stability and Dynamics*, vol. 18, no. 05, p. 1850073, 2018.

[245] Y. Yang and J. P. Yang, "State-of-the-art review on modal identification and damage detection of bridges by moving test vehicles," *International Journal of Structural Stability and Dynamics*, vol. 18, no. 02, p. 1850025, 2018.

[246] Y. Yang, Y. Li, K. C. Chang, *et al.*, "Constructing the mode shapes of a bridge from a passing vehicle: a theoretical study," *Smart Structures and Systems*, vol. 13, no. 5, pp. 797–819, 2014.

[247] C. Tan, N. Uddin, E. J. OBrien, P. J. McGetrick, and C.-W. Kim, "Extraction of bridge modal parameters using passing vehicle response," *Journal of Bridge Engineering*, vol. 24, no. 9, p. 04019087, 2019.

[248] Z. Shi and N. Uddin, "Extracting multiple bridge frequencies from test vehicle–a theoretical study," *Journal of Sound and Vibration*, vol. 490, p. 115735, 2021.

[249] D. Yang and C. Wang, "Modal properties identification of damped bridge using improved vehicle scanning method," *Engineering Structures*, vol. 256, p. 114060, 2022.

[250] M. Shinozuka and C.-M. Jan, "Digital simulation of random processes and its applications," *Journal of sound and vibration*, vol. 25, no. 1, pp. 111–128, 1972.

[251] M. Shinozuka, "Monte Carlo solution of structural dynamics," *Computers & Structures*, vol. 2, no. 5-6, pp. 855–874, 1972.

[252] "ISO 8608:2016 Mechanical vibration - Road surface profiles - Reporting of measured data," International Organization for Standardization, 2016.

[253] Y. Yang, Y. Li, and K. Chang, "Effect of road surface roughness on the response of a moving vehicle for identification of bridge frequencies," *Interaction and multiscale mechanics*, vol. 5, no. 4, pp. 347–368, 2012.